On Coherent Structures and Heat Transfer in Inclined Jets in Turbulent Cross-Flow

A study conducted on film cooling flows at engine-realistic conditions

Zur Erlangung des akademischen Grades eines

Doktors der Ingenieurwissenschaften (Dr.-Ing.)

von der KIT-Fakultät für Maschinenbau des
Karlsruher Instituts für Technologie (KIT)

angenommene

Dissertation

von

Katharina Stichling-Joshi, M. Sc.
aus Stuttgart

Tag der mündlichen Prüfung: 12.10.2023
Hauptreferent: Prof. Dr.-Ing. Hans-Jörg Bauer
Korreferent: Prof. Dr.-Ing. Heinz-Peter Schiffer

On Coherent Structures and Heat Transfer in Inclined Jets in Turbulent Cross-Flow

A study conducted on film cooling flows at engine-realistic conditions

by

Katharina Stichling-Joshi

München 2023

Publisher's Preface

Der schnelle technische Fortschritt im Turbomaschinenbau, der durch extreme technische Forderungen und starken internationalen Wettbewerb geprägt ist, verlangt einen effizienten Austausch und die Diskussion von Fachwissen und Erfahrung zwischen Universitäten und industriellen Partnern. Mit der vorliegenden Reihe haben wir versucht, ein Forum zu schaffen, das neben unseren Publikationen in Fachzeitschriften die aktuellen Forschungsergebnisse des Instituts für Thermische Strömungsmaschinen am Karlsruher Institut für Technologie (KIT) einem möglichst großen Kreis von Fachkollegen aus der Wissenschaft und vor allem auch der Praxis zugänglich macht und den Wissenstransfer intensiviert und beschleunigt.

Flugtriebwerke, stationäre Gasturbinen, Turbolader und Verdichter sind im Verbund mit den zugehörigen Anlagen faszinierende Anwendungsbereiche. Es ist nur natürlich, dass die methodischen Lösungsansätze, die neuen Messtechniken, die Laboranlagen auch zur Lösung von Problemstellungen in anderen Gebieten - hier denke ich an Otto- und Dieselmotoren, elektrische Antriebe und zahlreiche weitere Anwendungen - genutzt werden. Die effiziente, umweltfreundliche und zuverlässige Umsetzung von Energie führt zu Fragen der ein- und mehrphasigen Strömung, der Verbrennung und der Schadstoffbildung, des Wärmeübergangs sowie des Verhaltens metallischer und keramischer Materialien und Verbundwerkstoffe. Sie stehen im Mittelpunkt ausgedehnter theoretischer und experimenteller Arbeiten, die im Rahmen nationaler und internationaler Forschungsprogramme in Kooperation mit Partnern aus Industrie, Universitäten und anderen Forschungseinrichtungen durchgeführt werden.

Es sollte nicht unerwähnt bleiben, dass alle Arbeiten durch enge Kooperation innerhalb des Instituts geprägt sind. Nicht ohne Grund ist der Beitrag der Werkstätten, der Technik-, der Rechner- und Verwaltungsabteilungen besonders hervorzuheben. Diplomanden und Hilfsassistenten tragen mit ihren Ideen Wesentliches bei, und natürlich ist es der stets freundschaftlich fordernde wissenschaftliche Austausch zwischen den Forschergruppen des Instituts, der zur gleichbleibend hohen Qualität der Arbeiten entscheidend beiträgt. Dabei sind wir für die Unterstützung unserer Förderer außerordentlich dankbar.

Hohe Turbineneintrittstemperaturen, die teilweise die zulässigen Materialtemperaturen um mehrere hundert Grad übersteigen, erfordern effektive und effiziente interne konvektive und externe Filmkühlverfahren. Deren zuverlässige Auslegung setzt wiederum eine genaue Kenntnis des lokalen Wärmeübergangs und der lokalen Kühleffektivität voraus. Zur Erzielung höchster Effektivitäten werden vermehrt Filmkühlbohrungen eingesetzt, deren Auslass diffusorförmig verbreitert ist. Es deutet sich an, dass kohärente Strömungsstrukturen, die bei der Ausblasung von Kühlluft in die Heißgasströmung entstehen, einen signifikanten Einfluss auf die Leistungsfähigkeit des Kühlsystems besitzen. Allerdings wurde dieses Phänomen bisher für Diffusorbohrungen weder numerisch noch experimentell im Detail untersucht.

Im vorliegenden Band der Schriftenreihe befasst sich die Autorin folgerichtig mit der experimentellen Untersuchung des Einflusses kohärenter Strömungsstrukturen auf den lokalen Wärmeübergang und die Effektivität der Kühlung für Filmkühlsysteme mit Diffusorbohrungen. Dabei berücksichtigt sie insbesondere auch den Einfluss der internen Anströmung der Kühlluftbohrungen. Für die aerodynamischen Untersuchungen wurde ein am Institut für Thermische

Strömungsmaschinen des KIT vorhandener Aufbau einer generischen Filmkühlkonfiguration für den Einsatz von stereoskopischen PIV-Messungen erweitert. Der Versuchsaufbau ermöglicht das relevante Volumen im Nah- bzw. Fernfeld der Einblasung vollständig dreidimensional aufzulösen. Die umfangreiche Messmatrix bezüglich Ausblaserate, Quer- bzw. Parallelanströmung und Strömungsreynoldszahl im internen Kühlkanal umfasst insgesamt 12 Konfigurationen. Aus den gewonnenen Strömungsdaten konnten wesentliche kohärente Strukturen identifiziert und ihre Auswirkungen auf das thermische Verhalten der Filmkühlung analysiert werden. Besonders die komplexen Zusammenhänge die sich für eine interne Queranströmung der Filmkühlbohrungen ergeben, wurden sehr anschaulich herausarbeitet. Gerade diese Konfiguration besitzt für die Filmkühlung von thermisch hochbelastete Turbinenschaufeln eine große Relevanz und ist in ihrer Leistungsfähigkeit gegenüber der Anströmung aus einem – generischen – Plenum oder einer Parallelanströmung deutlich reduziert. Aus dem Verständnis der Mechanismen, die zur Entstehung von kohärenten Strukturen führen, lassen sich nun Ansätze ableiten, um ihre negativen Auswirkungen zu mindern oder zu beseitigen. Darüber hinaus hat die Autorin eine umfassende Datenbasis geschaffen, um numerische Werkzeuge zur Berechnung und Auslegung von Filmkühlströmungen unter realistischen Geometrie- und Strömungsrandbedingungen validieren und gegebenenfalls weiter verbessern zu können.

Karlsruhe, November 2023 Prof. Dr.-Ing. Hans-Jörg Bauer

Kurzfassung

Stationäre Gasturbinen und Flugtriebwerke sind nach wie vor wichtige Bestandteile in der Energiewandlung beziehungsweise dem Transportwesen. Die Steigerung des thermischen Wirkungsgrades durch eine Erhöhung der Turbineneintrittstemperatur erfordert Verbesserungen im Kühlsystem der Hochtemperaturkomponenten. Die Filmkühlung ist eine wesentliche Methode in diesem Kühlsystem. Die Filmkühlbohrungen verbinden die inneren Kühlkanäle mit der Schaufeloberfläche. Das resultierende Strömungsfeld stellt einen Spezialfall des generischen Strahls in einer Querströmung dar. Um die Filmkühlung gezielt weiter zu verbessern und die wesentlichen Unterschiede zum generischen Strömungsfall zu verstehen, ist eine detaillierte experimentelle Untersuchung des Strömungsfeldes im Mischungsbereich zwischen Heißgas und Kühlluftstrahl erforderlich.

In der vorliegenden Arbeit werden erstmals die kohärenten Strömungsstrukturen für eine sogenannte laidback fan-shaped Bohrung bei maschinenähnlichen Betriebsbedingungen experimentell quantitativ detailliert charakterisiert. Dabei werden maschinenähnliche Temperaturverhältnisse, Ausblaseraten, Heißgasturbulenzgrade und eine parallele und orthogonale kühlluftseitige Anströmung berücksichtigt. Detaillierte Messungen mittels stereoskopischer Particle Image Velocimetry werden durchgeführt, um die bereits verfügbaren thermischen Filmkühlgrößen durch hochaufgelöste quasi-volumetrische Geschwindigkeitsdaten am Filmkühlbohrungsaustritt zu ergänzen. Die Messungen werden für drei Ausblaseraten und zwei Kühlluftkanalreynoldszahlen pro Anströmrichtung durchgeführt, woraus sich 12 verschiedene Fälle ergeben.

Für jeden Fall wird das Nah- und Fernfeld des Filmkühlstrahls analysiert, ein detailliertes Verständnis der kohärenten Strömungsstrukturen abgeleitet und der Ursprung dieser Strömungsstrukturen diskutiert. Anhand der vorliegenden Arbeit wird deutlich, dass quasi-volumetrische Strömungsfelddaten erforderlich sind, um die resultierenden kohärenten Strukturen und ihre Entstehung korrekt zu charakterisieren, insbesondere bei orthogonaler Kühlluftanströmung. Nicht alle kohärenten Strukturen, die aufgrund der Ergebnisse aus generischen Untersuchungen erwartet werden, finden sich tatsächlich bei der Filmkühlausblasung unter maschinenähnlichen Randbedingungen wieder.
Darüber hinaus wird der lokale Zusammenhang zwischen den thermischen Filmkühlgrößen und den kohärenten Strömungsstrukturen analysiert. Teils unerwartete Zusammenhänge zwischen der lokalen Verteilung des Verhältnisses der Wärmeübergangskoeffizienten mit und ohne Filmkühlung und den dominanten kohärenten Strömungsstrukturen werden beobachtet. In Verbindung mit den vorangegangenen Forschungsarbeiten legt die vorliegende Arbeit nahe, dass die bedeutendste Steigerung des Wärmeübergangs mit einer instationären Komponente des Nierenwirbelpaares zusammenhängt. Die allgemein diskutierten Gründe für die Erhöhung des Wärmeübergangs spielen eine weniger bedeutende Rolle. Basierend auf diesen Ergebnissen wird der quasi-stationäre Modellierungsansatz für die Änderungen im Wärmeübergang durch Filmkühlung in Frage gestellt. Des Weiteren wird der Einfluss der kohärenten Strukturen auf die lokale Wärmestromminderung und dessen Relevanz für die Auslegung des Kühlsystems diskutiert.
Die vorliegende Arbeit leistet neben dem anwendungsorientierten Forschungsfeld der Filmkühlung auch einen Beitrag zum grundlegenden Verständnis der treibenden Faktoren des Wärmeübergangs stromab der Strahlausblasung.

Abstract

Stationary gas turbines and jet engines remain crucial components in today's energy conversion and transport systems, respectively. Enhancing the thermal efficiencies by an increase in turbine entry temperatures, demands improvements in the cooling system of the high-temperature components. Film cooling is an essential method in this cooling system, relying on small holes connecting the inner cooling channels to the outer surface of the turbine blades or vanes. The resulting flow field constitutes a special case of the generic jet in cross-flow. To further improve this cooling method and understand the differences to the generic jet in cross-flow, an experimental investigation of the flow field in the mixing region between the hot gas and the coolant jet is required.

In the present work, for the first time the coherent flow structures are experimentally characterised for a laidback fan-shaped cooling hole geometry at scaled, engine-realistic operating conditions. This includes engine-realistic temperature and blowing ratios, hot gas turbulence intensities and the mostly neglected effects of parallel and orthogonal coolant cross-flow. Extensive measurements are carried out using stereoscopic Particle Image Velocimetry to complement the available thermal film cooling quantities with highly resolved quasi-volumetric velocity data of the entire mixing region around the film cooling hole exit. The measurements are conducted for three blowing ratios and two coolant channel Reynolds numbers for each coolant cross-flow direction, yielding 12 different cases.

For each case, the near and far field of the jet in cross-flow is analysed, a detailed understanding of the coherent flow structures is derived and the origin of these flow structures is discussed. It is clearly shown that quasi-volumetric flow field data is required to correctly characterise the resulting coherent structures and their formation, especially for the cases with orthogonal coolant cross-flow configuration. Not all coherent structures expected based on the results from generic jet in cross-flow research are present in film cooling jets in cross-flow.
Furthermore, the local relation between the thermal film cooling quantities and the coherent flow structures is analysed. Partially unexpected relations between the local distribution of the ratio of heat transfer coefficients with and without film cooling and the dominant coherent flow structures are observed. In conjunction with research leading up to this work, the present work suggests that the most significant heat transfer augmentation is related to an unsteady component of the counter-rotating vortex pair. The commonly discussed reasons for heat transfer augmentation are observed to play a less significant role. Based on these results, the quasi-steady modelling approach for the heat transfer augmentation due to film cooling should be revisited. Furthermore, the significance of understanding the impact of the dominant coherent flow structures on the heat flux reduction for the design of film cooled airfoils is outlined to provide impulses for the design process of film cooling.
The present work contributes not only to the application oriented film cooling research field, but also to the fundamental understanding of the significant drivers for heat transfer augmentation.

Contents

Symbols

Symbol	Unit	Description
Latin symbols		
C	–	confidence level
D	m	cooling hole diameter
D_I	px	linear dimension of interrogation area
L	m	length
M	–	magnification factor
N_m	–	number of measurements
T	K	temperature
U	a.u.	expanded uncertainty
b_X	a.u.	systematic standard uncertainty
c_p	J/(kg K)	specific heat capacity
h	W/(m² K)	heat transfer coefficient
k	–	coverage factor
k_t	m²/s²	turbulent kinetic energy
l_i	m	image distance
l_o	m	object distance
s_X	a.u.	random standard uncertainty
u_c	a.u.	combined standard uncertainty, $u_\mathrm{c} = \sqrt{b_X^2 + s_X^2}$
u, v, w	m/s	streamwise (x-), lateral (y-), wall-normal (z-)velocity component
Greek symbols		
Γ	–	heat flux reduction acc. to Baldauf et al. (2002b)
Δt	s	time between the double images of a PIV recording
β	°; a.u.	camera angle; systematic error
δ	a.u.	total error
ϵ	m²/s³; a.u.	dissipation rate; random error
η	Pa s	dynamic viscosity
γ	°	Scheimpflug angle
κ	–	isentropic exponent
λ	W/(m K); m	thermal conductivity; wavelength
μ	a.u.	mean value
ω	1/s	vorticity

ρ	kg/m³	density
σ	a.u.	standard deviation; uncertainty
ϑ	–	coefficient relating h_w to the external heat transfer without film cooling h_0
θ	°; –	viewing angle; dimensionless temperature ratio

Similarity parameters

BR	–	blowing ratio, $BR = \frac{\rho_\mathrm{c} u_\mathrm{c}}{\rho_\mathrm{h} u_\mathrm{h}}$
DR	–	density ratio, $DR = \frac{\rho_\mathrm{c}}{\rho_\mathrm{h}}$
IR	–	momentum ratio, $IR = \frac{\rho_\mathrm{c} u_\mathrm{c}^2}{\rho_\mathrm{h} u_\mathrm{h}^2}$
$NHFR$	–	net heat flux reduction
Nu	–	Nußelt number, $Nu = \frac{\alpha l_\mathrm{char}}{\lambda}$
Re	–	Reynolds number, $Re = \frac{\rho v d_\mathrm{char}}{\eta}$
St	–	Strouhal number, $St = \frac{f D}{U_\mathrm{j}}$
TR	–	temperature ratio, $TR = \frac{T_\mathrm{h}}{T_\mathrm{c}}$
θ	–	dimensionless temperature ratio, $\theta = \frac{T_\mathrm{h} - T_\mathrm{c}}{T_\mathrm{h} - T_\mathrm{w}}$
VR	–	velocity ratio, $VR = \frac{u_\mathrm{c}}{u_\mathrm{h}}$
VR_inlet	–	inlet velocity ratio, $VR = \frac{u_\mathrm{cc}}{u_\mathrm{c}}$

Indices

$\square_0$	without film cooling; along principal optical axis
$\square_\mathrm{a}$	adiabatic
$\square_\mathrm{bl}$	boundary layer
$\square_\mathrm{c}$	coolant in film cooling hole
$\square_\mathrm{cc}$	cooling air in cooling air channel
$\square_\mathrm{f}$	with film cooling
$\square_\mathrm{fl}$	fluid
$\square_\mathrm{h}$	hot gas in hot gas channel
$\square_\mathrm{rec}$	recovery
$\square_\mathrm{thermal}$	thermal
$\square_\mathrm{w}$	wall
$\square_\mathrm{x}$	streamwise (x-)direction
$\square_\mathrm{y}$	lateral (y-)direction
$\square_\mathrm{z}$	wall-normal (z-)direction

Abbreviations

2D2C	two-dimensional-two-component
2D3C	two-dimensional-three-component
bc.	because
ACV	anti-counter-rotating vortex/vortices
CC	cross-correlation
CFD	computational fluid dynamics
CV	counter-rotating vortex/vortices
CYL	cylindrical
DEHS	di-ethyl-hexyl-sebacate
DES	detached eddy simulation
DNS	direct numerical simulation
FEM	finite element method
FH	fan-shaped
FOV	field of view
HV	horseshoe vortex/vortices
IA	interrogation area
IRT	infrared thermography
JiC	jet in cross-flow
KHI	Kelvin-Helmholtz instability
LFH	laidback fan-shaped
LiF	laser induced fluorescence
PEEK	Polyether ether ketone
PIV	Particle Image Velocimetry
RV	ring vortex/vortices
SNR	signal-to-noise ratio
SPIV	stereoscopic Particle Image Velocimetry
SV	shear-layer vortex/vortices
UQ	uncertainty quantification
VOV	volume of view
WV	wake vortex/vortices

Figures

Tables

1 Introduction

Stationary gas turbines still contribute largely in converting the primary energy sources to satisfy the final energy requirement every day. In Germany in 2022, the contribution of renewable energy to the gross electricity demand was below 50 %. Given that the gross electricity demand makes up around 20 % of the final energy demand in Germany, renewable energy sources covered no more than 10 % of the final energy demand in 2022 and no more than 10 % to 15 % at any time in history (BMWK, 2022). Compared to the rest of the world, the contribution of renewable energy in Germany is high. While European and world-wide agreements are formulated to emphasise the relevance of energy solutions with low climate impact (UN, 2016), Europe itself and much more so the majority of the world will continue to rely on conventional energy conversion requiring turbomachinery for covering the final energy demand reliably at all times. According to Brandes et al. (2021), the required installed capacity of gas power plants in Germany will approximately double until 2045 to compensate the shut-down of coal power plants and cover the increasing electricity demand in any of the modelled scenarios towards a climate-neutral energy system. This is despite the fact, that the final energy demand, which has been more or less constant over the past decades in Germany, is predicted to reduce by at least 30 % until 2045 (Brandes et al., 2021)[1].

In terms of aviation, jet engines remain the only propulsion system for all military and medium to large capacity civil aviation. Entering the post COVID-19 era, the growth of the aviation industry is predicted to recover quickly (Gelhausen et al., 2021; ICAO, 2022) and latest by 2024 (ACARE, 2022). Aviation currently contributes 2 % to 3 % of CO_2 emissions globally and 4 % in Europe. When accounting for non-CO_2 related anthropogenic climate impact, the contribution of aviation might increase significantly (D. Lee et al., 2021). Facing the challenges of climate change, political and legislative efforts are made to reduce the climate impact of jet engines. For Europe's aviation, the short-term goal until latest 2030 is to reduce the net CO_2 emissions by 55 % compared to the 1990 baseline. In the long-term until latest 2050, the goal is to reduce the CO_2 emissions to net-zero and the absolute amount of CO_2 and NO_x emissions by 90 % compared to the year 2000 (ACARE, 2022). Given the growing demand for jet engines, reducing the climate impact is challenging. While hydrogen is an appealing fuel in aviation, it requires a drastic redesign of the engine and airframe, and entirely new safety regulations and infrastructure around it. Compared to battery electric vehicles for ground transport, small short-haul full-electric flights might gain traction in the near-term, but the current energy density of batteries is way below the requirements for medium- and long-haul full-electric aviation (Bauen et al., 2020). Sustainable aircraft fuels (SAFs) are another attractive decarbonisation option, but currently significantly more costly and the production infrastructure is lacking. Recent studies further show, that the particle mitigation potential of SAF blends tend to decrease with increasing power settings of the engine (Schripp et al., 2022).

Continuously improving the thermal efficiency of gas turbines and jet engines is, therefore, essential. For fossil fuels, this will lead to reduced emissions and for sustainable aviation fuels, simply reducing the fuel burn is advantageous as it will ease challenges related to fuel transport

[1] This reduction in final energy demand is expected to be achieved by technological progress in general but mainly an increase in process efficiencies.

and infrastructure. Improving the efficiency will remain specifically relevant as the long-term goals for gas turbines and jet engines consider net-zero and not absolute-zero CO_2 emissions (ACARE, 2022).

Increasing the thermal efficiency of the underlying thermodynamic process can be achieved by either improving the component efficiencies, or increasing the pressure ratio or turbine entry temperature (TET). The specific work also increases with increasing TET, enhancing the power density which is specifically relevant for jet engines. Since the introduction of the first cooled turbine blades in the late 1960s, a continuous upward trend of the TET can be observed. Modern high pressure turbine blades are manufactured using single-crystal materials made of nickel-based superalloys and sustain TETs beyond 2000 K (Hada et al., 2012). Sophisticated cooling concepts combining multiple cooling methods are used to protect the high-temperature components from the hot gas and prevent component failure.

One essential cooling method is film cooling. The main goal of film cooling is to protect the blade surface from the hot gas exiting the combustion chamber and reduce the heat flux into the blade material (Bogard and Thole, 2006), to achieve a reduction of blade metal temperatures. Depending on the required pressure level, primary air from the compressor is channelled into the secondary air system to bypass the combustion chamber. It is then fed into the turbine blade's internal coolant channels to exit on the blade surface via discrete film cooling holes. The air used for cooling no longer takes part in the thermodynamic cycle, constitutes a loss and its usage has to be minimized.

The coolant exiting the film cooling hole into the hot gas main stream essentially constitutes a special case of the generic jet in cross-flow (JiC). The structure and mixing characteristics of a jet in cross-flow (JiC) are fundamental to its understanding and immensely significant to the efficiency and effectiveness of connected processes. Due to the generally vast areas of application, JiCs have been a focal point of research for decades. A direct consequence of the variety of applications are the large regimes of relevant operating conditions, which significantly influence the jet and cross-flow interaction. While being broadly used in industry, the exact purpose of the JiC varies significantly and its applications in the field of gas turbines may even be contradicting. For external cooling such as film cooling, the main purpose is decreasing the heat flux into the component by reducing the surface temperature and preventing heat transfer augmentation. To achieve a long lasting external near-wall cooling film, mixing between the hot gas cross-flow and the coolant jet has to be minimised. With the goal of improving the cooling performance, most experimental research has centred around determining the cooling performance for specific geometries and operating conditions. Fundamental research on JiCs has been more focused on understanding the flow field and specifically the coherent structures in the flow to understand the mixing process. These results are frequently referred to when describing effects observed in film cooling performance at significantly different operating conditions while few or no flow field measurements are conducted. New geometries are regularly proposed with the aim of altering the flow field to reduce the downstream surface temperature while minimising heat transfer augmentation. Despite the massive generic and film cooling related research on JiCs, the impact of specific operating conditions on the jet's coherent structures in combination with the cooling performance has never been experimentally reported at operating conditions transferable to real

engines.

Such data is required for various purposes. From a fundamental perspective it allows insights into understanding the formation process of coherent structures and the connection between coherent structures and cooling performance. Detailed aero-thermal data sets further extend the possibilities for benchmarking or improving modelling approaches in numerical flow simulations. For JiC applications as film cooling in gas turbines and jet engines, a comprehensive aero-thermal data set will further improve the understanding of the flow field enabling educated geometry alterations.

Improvements in flow field measurement techniques and advancements in hardware over the past decade enable capturing flow field quantities at both relatively high temporal and spatial resolution (Beresh, 2021). In the present work, such flow field measurements will be systematically employed for jets in cross-flow at operating conditions tailored to gas turbines and jet engines to fully explore the coherent structures in the flow and their relation to the cooling performance.

2 Generic and Application-Oriented Jets in Cross-Flow

The countless applications and the associated large range of operating conditions, compounded with geometry variations pose a great challenge for conducting exhaustive research on the flow field of a JiC. No single parameter set can be derived that describes the characteristic behaviour of the JiC for all applications with acceptable accuracy and precision. In the fundamental JiC research, certain flow characteristics are repeatedly associated with jets in cross-flow (JiCs). In order to analyse the JiC for a specific application, it is necessary to understand these flow characteristics first. This enables the reader to comprehend the discriminating features of the JiC for the application in film cooling discussed in the present work compared to the results from the fundamental research. Being able to classify the relevance of the typically observed flow characteristics will enable more targeted development of film cooling hole geometries and an improved overall design process.

In the following sections, the most recent consensus on typically expected flow structures in a generic JiC and the effects on the downstream heat transfer from a fundamental perspective are provided (section 2.1). Despite the large amount of flow field investigations on JiCs, no standardised hole geometry or operating conditions for a JiC exist. Certain commonalities are present and used as a basis for the definition of the *generic*[1] JiC in the present work. The inclination angle of a generic JiC is 90° relative to the main stream cross-flow. The hole cross section is cylindrical with a flush hole exit to the cross-flow. The hole length and diameter may vary but the jet to cross-flow density ratio is unity. Unless specified otherwise, inlet-sided cross-flow is neglected and plenum conditions are used.
The state of the art of the JiC for film cooling applications is provided in section 2.2. This includes an aero-thermal characterisation of the film cooling ejection (subsection 2.2.1), followed by an overview of the relevant dimensionless parameters (subsection 2.2.2). This section is concluded with a detailed literature review on previous experimental flow field investigations on film cooling flows (see subsection 2.2.3).
Finally, a detailed description of the intentions of the present work is provided in section 2.3.

2.1 Coherent Structures in the Generic Jet in Cross-Flow

Understanding the aerodynamics of a JiC has been a topic of research for many decades, as shown in early reviews (Hancock, 1987; Sherif and Pletcher, 1990; Margason, 1993). Widespread applications have led to continued interest in this fundamental flowfield, which is confirmed by recent topical reviews (Mahesh, 2013; Karagozian, 2014; Dai et al., 2016; Taherian and Mohammadian, 2021). The majority of research on JiC is focused on the coherent structures developing in the near- or far-field of the jet. Coherent structures are organised spatial features which repeatedly appear and undergo a characteristic temporal life cycle (Berkooz et al., 1993). They may or may not constitute a vortical structure. The aim of this section is to provide an overview of the current consensus on which coherent structures are typically observed and how they are formed.

[1] In the fundamental JiC research, the generic JiC is frequently referred to as *canonical* JiC.

The interaction between jet and cross-flow leads to a complex set of coherent structures. An early but seemingly complete and widely accepted experimental description of the coherent structures in a generic JiC is provided by Fric and Roshko (1994) based on previous publications (Fric and Roshko, 1994, 1991, 1988; Fric, 1990) using flow visualisations. Kelso et al. (1996) expand the observations by Fric and Roshko (1994) and create detailed topological maps of the coherent structures.

A schematic of the coherent structures typically observed in a generic JiC is presented in Figure 2.1. Some of the coherent structures have a mean flow definition in terms of velocity as schematically shown in Figure 2.1a, but may also present with unsteady components. These unsteady components and all exclusively unsteady coherent structures are schematically shown in Figure 2.1b.

For a large variety of operating conditions, the dominating structure is the counter-rotating vortex pair, where each vortex leg is indicated by Ω_{CV} in Figure 2.1a. The existence of the Ω_{CV} pair leads to an entrainment of cross-flow fluid and thereby cross-flow momentum beneath and into the jet. This entrainment majorly contributes to the bending of the jet trajectory in cross-flow direction (Fric and Roshko, 1994). The jet trajectory based on the centre streamline typically penetrates deeper into the cross-flow than the trajectory of the dominant coherent structure, as noted by Fearn and Weston (1974). This is indicated in Figure 2.1 by the dashed line as the centre streamline, which is located slightly above the trajectories of the Ω_{CV} pair. While its true genesis is disputed (Peterson, 2003; Mahesh, 2013; Taherian and Mohammadian, 2021), the general consensus is that the Ω_{CV} pair formation is initiated in the near-field. It is thought to be associated with the evolution of vorticity in the shear-layer and pressure differences between the windward (upstream) and leeward (downstream) side of the jet resulting in a downstream and downward movement along the lateral sides of the jet. The ring vortex Ω_R is initiated by the in-hole vorticity caused by the hole boundary layer. For high jet to cross-flow velocity ratios it may propagate along the windward side of the bent jet contributing to the windward shear-layer vortices Ω_{WSV}. Along the lateral hole edges, the ring vortex Ω_R contributes but is not required

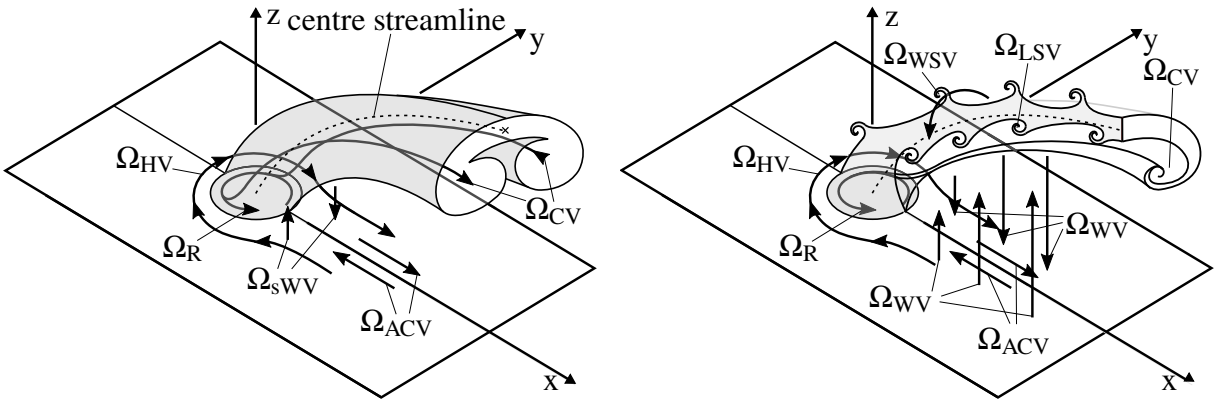

(a) Steady coherent structures based on Fric and Roshko (1994) and Kelso et al. (1996)

(b) Unsteady coherent structures based on Fric and Roshko (1994) and Cambonie and Aider (2014)

Figure 2.1: Coherent structures in a generic JiC with orthogonal ejection from a cylindrical orifice; adapted from Baldauf (2001) and Cambonie and Aider (2014)

for the formation of the Ω_{CV} pair. As Muppidi and Mahesh (2007) show, the Ω_{CV} pair formation can be driven purely by the pressure-difference. They generalise by considering the near-field of the jet as pressure-driven and the far field as momentum-driven. Instantaneously, the Ω_{CV} pair is highly unsteady and asymmetric (Mahesh, 2013). A detailed overview of the proposed mechanisms for the Ω_{CV} pair genesis can be found in Taherian and Mohammadian (2021). Below the Ω_{CV} pair, an anti-counter-rotating vortex (Ω_{ACV}) pair may form.

The jet obstructing the cross-flow leads to a local adverse wall-normal pressure gradient upstream of the jet. The cross-flow boundary layer separates yielding either a single horseshoe vortex Ω_{HV} or a system of Ω_{HV}. Depending on the jet to cross-flow velocity ratio, the lateral legs of the Ω_{HV} can be steady, oscillate or coalesce. In the latter case, they are either lifted away merging with the Ω_{CV} pair or are incorporated into the wake vortices Ω_{WV} (Kelso and Smits, 1995; Peterson, 2003), depending on the sign of the streamwise vorticity.

The wake vortices Ω_{WV} are upright vortices observed downstream of the jet as shown in Figure 2.1b. Their appearance is similar to those in a Kármán vortex street downstream of a solid cylinder. In contrast to the Kármán vortex street, the wake vortices Ω_{WV} in a JiC originate from separation events observed in the cross-flow boundary layer downstream of the jet and are mainly comprised of boundary layer fluid (Fric and Roshko, 1994). An intuitive understanding of the Ω_{WV} formation is the roll-up of wall-normal vorticity in the near-jet wake as the boundary layer fluid sweeps around the issuing jet (Hale et al., 2000). As the Ω_{WV} are advected downstream, they instantaneously appear as a system of wake vortices Ω_{WV} in a staggered alignment, as indicated in Figure 2.1b. Cross-flow fluid may be incorporated in the Ω_{WV} depending on the vorticity direction (Kelso et al., 1996). The system of wake vortices is roughly oriented in the same direction as the initial jet (Peterson, 2003) and eventually combines with the Ω_{CV} pair. In most of the literature, wake vortices Ω_{WV} are considered entirely unsteady, suggesting they are not detectable in the mean flow field.

Brizzi (1994) and Hale (1999), however, report steady nodes in the immediate jet wake. They classify these nodes as the steady remainder of the unsteady wake vortices Ω_{WV}, as they correspond to their time-averaged separation in the wake. In the present work, they are referred to as steady wake vortices Ω_{sWK} as shown in Figure 2.1a to distinguish them from the unsteady wake vortices Ω_{WV} identified by Fric and Roshko (1994).

Another exclusively unsteady coherent structure are the shear-layer vortices that are typically observed on the windward side (Ω_{WSV}) but can also occur on the leeward side of the jet (Ω_{LSV}) as indicated in Figure 2.1b. They are highly unsteady and are thought to resemble Kelvin-Helmholtz instabilities (KHI). At high velocity ratios, recent studies suggest formation processes different from the KHI. (Mahesh, 2013)

At low velocity ratios $VR \lessapprox 1$, the interaction of the jet with the cross-flow tends to be dominated by hairpin vortices Ω_{HpV} (Mahesh, 2013). A schematic of a JiC at low jet to cross-flow velocity ratios is schematically shown in Figure 2.2. The displayed scenario corresponds to when the interaction between jet and cross-flow is entirely dominated by hairpin vortices Ω_{HpV}. They form as the approaching cross-flow boundary layer vorticity at low velocity ratios can overwhelm the windward vorticity of the ring vortex Ω_R at the hole exit. Vorticity is then shed from the leeward

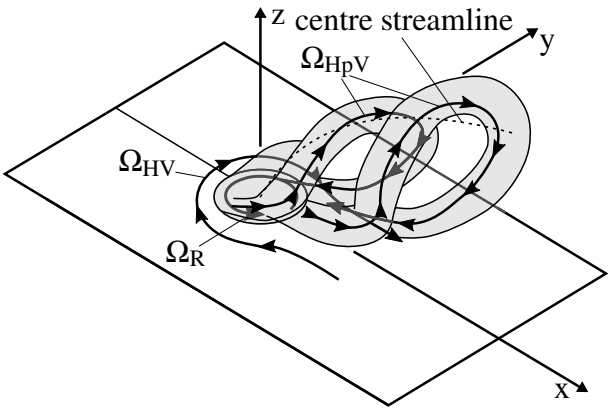

Figure 2.2: Unsteady coherent structures in a generic JiC with orthogonal ejection from a cylindrical orifice at low jet to cross-flow velocity ratios

side of Ω_R in the hole. Hairpin vortices are not necessarily apparent if the flow is visualised in a 2D plane alone as they might appear to be a Ω_{CV} pair or traces of shear-layer or wake vortices, Ω_{WV} or Ω_{SV}. They may or may not be accompanied by a horseshoe vortex Ω_{HV}. (Acarlar and C. R. Smith, 1987; Tyagi and Acharya, 2003; Sau and Mahesh, 2008; Mahesh, 2013; Fawcett et al., 2013)

To characterise unsteady coherent structures, the Strouhal number

$$St = \frac{fD}{U_j}, \tag{2.1}$$

is used, where f is the shedding frequency of the instability of interest, D the hole or orifice diameter and U_j the jet mean velocity at the hole exit. No general tendencies with regard to shedding frequencies and corresponding strength are available. Details on frequency content of the unsteady coherent structures for specific velocity ratio regimes can be found in Megerian et al. (2007), Dai et al. (2016), and Shoji et al. (2020).

With regard to the formation of the presented vortex structures, it can be summarised that the counter-rotating vortex pair and the ring vortex, Ω_{CV} and Ω_R, respectively, are issued by the jet, whereas the horseshoe vortex Ω_{HV} and the wake vortices Ω_{WV} originate from cross-flow boundary layer fluid (Leboeuf and Sgarzi, 2001). The anti-counter-rotating vortex Ω_{ACV} pair may originate from the jet or the cross-flow fluid as will be discussed in the course of this work. Shear-layer vortices and hairpin vortices Ω_{HpV} contain both, jet and cross-flow fluid.

2.2 Inclined Jets in Cross-Flow for Application in Film Cooling

In order to determine optimal operating conditions for a specific application, a thorough understanding of the structural and mixing flow characteristics at a range of operating conditions is required (Karagozian, 2014). One highly relevant application is film cooling, in which a relatively cold air jet is ejected into a relatively hot cross-flow at various different operating conditions. To understand the relevant features of the JiC for the application in film cooling, an overview of the

aero-thermal characterisation of the film cooling ejection is given in subsection 2.2.1. The relevant operating conditions are detailed in subsection 2.2.2 and an extensive review of previous aerodynamic film cooling flow investigations is provided in subsection 2.2.3.

2.2.1 Aero-Thermal Characterisation of the Film Cooling Ejection

The main goal of film cooling is to reduce the wall temperature by introducing a cold film close to the wall which acts both as a protective layer as well as a heat sink. To characterise the film cooling performance, the aerodynamic and thermal effects of the film cooling ejection on the wall temperature have to be quantified.

In Figure 2.3, the mean temperature and velocity profiles without (left) and with (right) film cooling and the resulting heat fluxes are schematically shown. The hot gas cross-flow direction is from left to right. The direction of the coolant cross-flow in gas turbines and jet engines varies and is indicated in parallel and orthogonal direction relative to the hot gas cross-flow in Figure 2.3. $\dot{q}_\mathrm{h}$ is the heat flux from the hot gas to the cooling film, $\dot{q}_\mathrm{f}$ is the heat flux convected

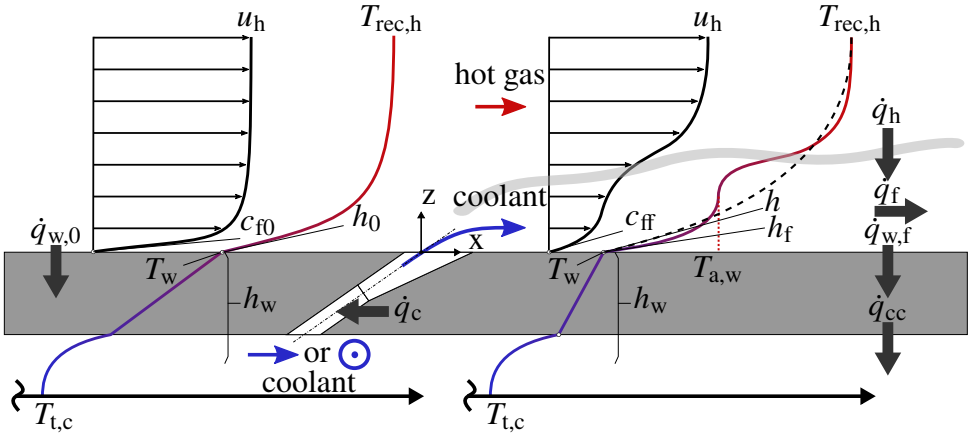

Figure 2.3: Temperature and velocity profiles without (left) and with (right) film cooling ejection on a flat plate and resulting heat fluxes; based on Baldauf (2001)

downstream by the cooling film, $\dot{q}_\mathrm{w,f}$ is the heat flux into the wall, $\dot{q}_\mathrm{c}$ the heat flux from the wall to the coolant passing through the cooling hole and $\dot{q}_\mathrm{cc}$ is the heat flux from the wall to the internal cooling passages. Depending on the coolant flow direction and the hole placement, these heat fluxes are interdependent.

Without film cooling, the local wall-normal heat flux $\dot{q}_\mathrm{w,0}$ can be derived from the local temperature boundary layer profile such that

$$\dot{q}_\mathrm{w,0}(z) = \lambda_\mathrm{fl} \left.\frac{\partial T}{\partial z}\right|_{z=0} . \tag{2.2}$$

In most applications, the local thermal conductivity λ_fl of the fluid and the local near-wall temperature profile is unknown. Hence, the construct of a heat transfer coefficient characterising

the heat transfer from the fluid to the wall is introduced as

$$h_0 = \frac{\lambda_{\mathrm{fl}}}{\Delta T} \left.\frac{\partial T}{\partial z}\right|_{z=0} = \frac{\dot{q}_{\mathrm{w},0}}{\Delta T}, \quad \text{such that} \quad \dot{q}_{\mathrm{w},0} = h_0 \Delta T, \tag{2.3}$$

where $\dot{q}_0$ is the wall-normal heat flux without film cooling. ΔT is the temperature difference between the hot gas recovery temperature and the wall temperature, yielding $\Delta T = T_{\mathrm{rec,h}} - T_{\mathrm{w}}$. The heat transfer coefficient without film cooling h_0 is dependent on the velocity boundary layer shape and state and the fluid properties. If changes in the fluid properties caused by temperature changes of the fluid are considered negligible, a decoupling of the heat transfer characteristics due to the flow field and the temperature field is achieved. (R. J. Goldstein, 1971)

Due to the coolant jet, the aerodynamic and thermal characteristics of the near-wall flow field on the flat plate are modified. The temperature boundary layer with film cooling shown on the right in Figure 2.3 is qualitatively representative for most operating conditions relevant to film cooling. The temperature of the coolant jet is lower compared to the temperature of the hot gas. The driving temperature difference in Equation 2.3 is decreased, such that the wall heat flux with film cooling $\dot{q}_{\mathrm{w,f}}$ is defined as

$$\dot{q}_{\mathrm{w,f}} = h_{\mathrm{f}}(T_{\mathrm{a,w}} - T_{\mathrm{w}}), \tag{2.4}$$

where $T_{\mathrm{a,w}}$ is the cooling film temperature. $T_{\mathrm{a,w}}$ is also the wall temperature in case of an adiabatic wall, hence the name adiabatic wall temperature $T_{\mathrm{a,w}}$. For the velocity boundary layer, no single qualitative distribution is representative for all operating conditions. The change in near-wall velocity gradient and corresponding friction coefficients (from c_{f0} without film cooling to c_{ff} with film cooling) affects the convective heat transfer. The configuration shown in Figure 2.3 is representative for an operating condition, where the coolant jet's mean exit velocity is lower compared to the local hot gas velocity. The near-wall hot gas cross-flow is decelerated due to the coolant ejection.

To fully quantify the cooling performance of a specific film cooling hole geometry, the local adiabatic wall temperature $T_{\mathrm{a,w}}$ and the local heat transfer coefficient with film cooling h_{f} have to be determined. Due to practical constraints, experimental investigations cannot be conducted at operating conditions of real engines. Hence, dimensionless numbers are used to ensure transferability of the results. The dimensionless numbers including $T_{\mathrm{a,w}}$ and h_{f} are the adiabatic film cooling effectiveness

$$\eta_{\mathrm{a,w}} = \frac{T_{\mathrm{rec,h}} - T_{\mathrm{a,w}}}{T_{\mathrm{rec,h}} - T_{\mathrm{t,c}}} \tag{2.5}$$

and the ratio of heat transfer coefficients with and without film cooling

$$\frac{h_{\mathrm{f}}}{h_0}. \tag{2.6}$$

The adiabatic film cooling effectiveness $\eta_{\mathrm{a,w}}$ is the ratio of the achieved temperature decrease on the wall (difference between the hot gas recovery temperature $T_{\mathrm{rec,h}}$ and the adiabatic wall temperature $T_{\mathrm{a,w}}$) upon the maximum possible temperature difference (difference between $T_{\mathrm{rec,h}}$ and the total coolant temperature $T_{\mathrm{t,c}}$). For ideal cooling, a value of $\eta_{\mathrm{a,w}} = 1$ and, hence, $T_{\mathrm{a,w}} = T_{\mathrm{t,c}}$

is present. In reality, the values of $\eta_{a,w}$ range between $\eta_{a,w} \in [0, 1]$ and generally decline downstream of the ejection due to mixing and conduction between coolant and hot gas dominated by steady and unsteady coherent structures.
Currently, a direct measurement of the adiabatic wall temperature $T_{a,w}$ and the heat transfer coefficient with film cooling h_f is not possible. Instead, the superposition principle of film cooling is used. According to this approach, the heat flux $\dot{q}_{w,f}$ can be described using the heat transfer coefficient h of the fictitious temperature profile indicated by the dashed line in Figure 2.3 such that

$$\dot{q}_{w,f} = h(T_{rec,h} - T_w). \tag{2.7}$$

Introducing the dimensionless temperature ratio

$$\theta = \frac{T_h - T_c}{T_h - T_w}, \tag{2.8}$$

and equating Equation 2.7 to Equation 2.4, the following linear relationship between the heat transfer coefficient h and the dimensionless wall temperature θ is deduced:

$$h(\theta) = h_f(1 - \eta_{a,w}\theta). \tag{2.9}$$

This linearity is in principal valid for incompressible flows, as the energy and momentum equation are decoupled, and was experimentally verified by Metzger et al. (1968), Metzger and Fletcher (1971), Metzger et al. (1973), and Choe et al. (1974). From Equation 2.9, the adiabatic film cooling effectiveness $\eta_{a,w}$ and the heat transfer coefficient with film cooling h_f can be calculated for each point on a surface as

$$\eta_{a,w} = \frac{1}{\theta_{a,w}} \quad \text{with} \quad h(\theta_{a,w}) = 0 \quad \text{and} \quad h_f = h(\theta = 0), \tag{2.10}$$

respectively. From an experimental perspective, two measurements at identical flow conditions, varying only the dimensionless temperature θ deliver the information to calculate $\eta_{a,w}$ and h_f/h_0. Gritsch et al. (1999) have shown that the superposition principle remains valid even at engine-realistic temperature ratios violating the initial assumption of constant fluid properties.

To draw a conclusion on the film cooling performance based on the adiabatic film cooling effectiveness and the ratio of heat transfer coefficients with and without film cooling, the net heat flux reduction

$$NHFR = 1 - \frac{h_f}{h_0}(1 - \eta_{a,w}\theta) \tag{2.11}$$

is introduced (Sen et al., 1996). The wall temperature with film cooling and therefore the dimensionless temperature θ is unknown in the design process and has to be estimated. To avoid the flaw of generating arbitrary $NHFR$ values by estimating θ, Baldauf et al. (2002b) introduced the heat flux reduction Γ in analogy to Equation 2.11 as

$$NHFR \approx \Gamma = 1 - \frac{(1 + \vartheta)(h_f/h_0)}{\vartheta + (h_f/h_0)}(1 - \eta_{a,w}). \tag{2.12}$$

This is an approximation, as it underlies the following assumptions: the wall normal heat flux is dominant; the heat transfer coefficient h_w through the wall and into the internal cooling air (see Figure 2.3) is invariant with and without film cooling; h_w can be approximated with a fraction of the external heat transfer coefficient without film cooling h_0 as $h_w = \vartheta h_0$. According to Baldauf et al. (2002b) and Baldauf (2001), $h_w \approx h_0$, yielding $\theta = 1$ is valid for real applications, such that the heat flux reduction Γ is only dependent on the adiabatic film cooling effectiveness $\eta_{a,w}$ and the ratio of heat transfer coefficients with and without film cooling h_f/h_0. A complete performance review of film cooling requires all three of these parameters (Bogard and Thole, 2006).

2.2.2 Dimensionless Operating Parameters Relevant to Film Cooling Jets in Gas Turbines and Jet Engines

Experimental investigations yielding the adiabatic film cooling effectiveness $\eta_{a,w}$ and the heat transfer coefficient with film cooling h_f at operating conditions of modern gas turbines or aero engines are currently not possible. They are either too costly or not feasible at all due to the high temperatures and pressures. By scaling the test section based on the relevant dimensionless parameters, transferability of the results to real engines is provided. For film cooling, a detailed analysis of all relevant operating conditions and a dimensionality analysis based on the Buckingham Π-theorem can be found in Baldauf and Scheurlen (1996) and Baldauf (2001). Hereafter, the dimensionless parameters relevant to characterise the film cooling ejection in the test section used for the present work are introduced. More details on how these parameters are derived can be found in Fraas et al. (2017) and Fraas (2019).

To achieve engine-realistic hot gas and cooling channel cross-flow, the respective hot gas and cooling channel air Reynolds numbers

$$Re_{D,h} = \frac{(\rho u)_h D}{\mu_h} \quad \text{and} \quad Re_{D,cc} = \frac{(\rho u)_{cc} D}{\mu_{cc}}, \tag{2.13}$$

respectively, have to be maintained. The densities ρ_h, ρ_{cc}, the velocities u_h, u_{cc} and the dynamic viscosities μ_h, μ_{cc} refer to those of the hot gas and the cooling channel air, respectively. To characterise the coolant ejection, the blowing ratio BR is most prominently used as a scaling parameter in literature. It is defined as the ratio of the mass flux densities of coolant and hot gas

$$BR = \frac{\rho_c u_c}{\rho_h u_h} = DR \cdot VR, \tag{2.14}$$

where $\square_c$ refers to quantities related to the coolant in the cooling hole. The blowing ratio BR can also be described as the product of the density ratio DR and the velocity ratio VR. In many experimental studies on film cooling, the density ratio DR is maintained rather than the temperature ratio TR by using foreign gas injection. The effect of how well the coolant is able to maintain its temperature as thermal diffusion and conduction occur between hot gas and coolant is lost when using foreign gas injection (McNamara, 2019). Wiese and Rutledge (2021) show that maintaining the density ratio DR by using foreign gas injection is insufficient to ensure adequate scaling

of the aero-thermal characteristics of a film cooling flow. The resulting adiabatic film cooling effectiveness is dependent on the foreign gas properties. Hence, rather than the density ratio *DR*, the temperature ratio *TR* is the relevant dimensionless quantity. This has been shown in previous studies and early dimensionless analysis by Foster and Lampard (1975) and Rydholm (1998), respectively. Assuming constant heat capacities, the temperature ratio *TR* and its relation to the density ratio *DR* for film cooling flows is as follows:

$$TR = \frac{T_\mathrm{c}}{T_\mathrm{h}} = \frac{1}{DR}. \tag{2.15}$$

For relatively low blowing ratios, the adiabatic film cooling effectiveness $\eta_{\mathrm{a,w}}$ and the ratio of heat transfer coefficients with and without film cooling h_f/h_0 increase with an increase in blowing ratio. Due to the simultaneous increase of coolant momentum, a plateau is reached, after which the adiabatic film cooling effectiveness decreases again due to jet lift-off (Baldauf et al., 1999a,b). When lift-off occurs, the momentum ratio

$$IR = \frac{\rho_\mathrm{c} u_\mathrm{c}^2}{\rho_\mathrm{h} u_\mathrm{h}^2} = \frac{BR^2}{DR} \tag{2.16}$$

or the velocity ratio *VR* are found to be more suitable for scaling, however, this is highly controversial (Schroeder and Thole, 2014; B. Johnson et al., 2014). Using realistic temperature ratios in experimental investigations is therefore essential to achieve transferability of the results to real engine applications.

With respect to the in-hole aerodynamics, the Reynolds number of the coolant $Re_{D,\mathrm{c}}$ is relevant and related to the hot gas Reynolds number $Re_{D,\mathrm{h}}$ and the blowing ratio *BR* as follows:

$$Re_{D,\mathrm{c}} = \frac{(\rho u)_\mathrm{c} D}{\mu_\mathrm{c}} = Re_{D,\mathrm{h}} \cdot BR \cdot \frac{\mu_\mathrm{c}}{\mu_\mathrm{h}}. \tag{2.17}$$

The ratio of dynamic viscosities is approximately constant for a constant temperature ratio *TR*. For generic JiC and their application in film cooling, entry-related effects play an important role as previously shown by Plesniak (2005), Gritsch et al. (2003), and Fraas et al. (2019a). Flow phenomena at the hole inlet influence the in-hole flow propagating artefacts of the entry-related effects into the coolant hot gas interaction regime, especially for short holes. The inlet velocity ratio between cooling channel air and in-hole cooling air (coolant) is defined as

$$VR_\mathrm{inlet} = \frac{u_\mathrm{cc}}{u_\mathrm{c}} = \frac{DR}{BR} \cdot \frac{u_\mathrm{cc}}{u_\mathrm{h}} \approx \frac{1}{BR} \cdot \frac{Re_{D,\mathrm{cc}}}{Re_{D,\mathrm{h}}} \cdot \frac{\mu_\mathrm{c}}{\mu_\mathrm{h}}. \tag{2.18}$$

Assuming that density and temperature are equal between cooling channel air and coolant, the approximation in Equation 2.18 is valid. For an engine-realistic temperature ratio, the viscosity ratio is also engine-realistic with an error of within 10 %. Given that the ratio of Reynolds numbers of the hot gas and cooling channel air are engine-realistic, the inlet velocity ratio $u_\mathrm{cc}/u_\mathrm{c}$ is too. (Fraas et al., 2017)

This is relevant when investigating film cooling hole flows under engine-realistic operating con-

ditions with coolant channel cross-flow.

2.2.3 Previous Flow Field Investigations on Film Cooling Jets in Cross-Flow with Focus on Coherent Structures and their Relation to the Heat Transfer

Film cooling of turbine airfoils was introduced in the 1970s and has allowed for tremendous increase in turbine entry temperatures. The research landscape spanning the past five decades is vast. The focus was mainly on the adiabatic film cooling effectiveness and the ratio of heat transfer coefficients with and without film cooling. Analysing these thermal film cooling parameters ($\eta_{\mathrm{a,w}}$ and h_{f}/h_0), studies have repeatedly shown the significance of maintaining engine-realistic operating conditions. This includes engine-realistic temperature ratios or at least density ratios (Foster and Lampard, 1975; Rydholm, 1998; Baldauf et al., 1999a; Schroeder and Thole, 2014; B. Johnson et al., 2014), hot gas turbulence intensities (Saumweber et al., 2003; Saumweber and Schulz, 2008b), boundary layer thicknesses (Saha and Yaragani, 2011; Anderson et al., 2016) and realistic cooling air inflow conditions (Saumweber et al., 2001; Gritsch et al., 2003; Saumweber and Schulz, 2008a, 2012; Fraas et al., 2019a). Maintaining engine-realistic dimensionless parameters when transferring film cooling problems into a laboratory environment is, therefore, essential. Despite this consensus (Bogard and Thole, 2006), the majority of experimental studies compromises on at least one and often more of these parameters, likely due to the significant experimental effort.
Information on the flow field of a JiC for film cooling applications is sparse compared to the data available on the thermal film cooling quantities and the research on generic JiCs. Apart from a few exceptions, investigations using flow field measurement techniques started to emerge around the turn of the millennium. The available studies at operating conditions tailored to film cooling flows exclusively treat the interaction regime between hot gas cross-flow and coolant jet. A method for in-hole measurements at engine-realistic conditions has not yet been established. In the following, a mostly chronological overview of the existing studies is presented. Most of them were conducted using Particle Image Velocimetry (PIV) or stereoscopic PIV (SPIV) for flow field measurements. The overview is limited to those studies contributing new insights into the coherent structures themselves or their relation to the thermal film cooling quantities. The main findings are briefly summarised with an emphasis on whether the relevant dimensionless parameters satisfy engine-realistic conditions. An exhaustive list containing all additional publications related to experimental investigations of the flow field of film cooling JiCs is provided in section A.1

From this literature review, it will become clear how little generalisable information can be obtained from most of the flow field measurements of the past two to three decades. Assumptions about vortex structures mentioned once in previous publications using single-plane data are subsequently often considered as ground truth by other authors. The data in those and newer publications is frequently inconclusive in characterising whether and which coherent structures are actually present at engine-realistic conditions.

Early flow field investigations were conducted by Gogineni et al. (1995). Using two-colour PIV techniques and reactive Mie scattering, the overall flow field and molecular mixing for an unforced and a streamwise forced JiC from a square duct were compared. Forcing refers to the deliberate introduction of low frequency instabilities into the jet column. The penetration depth increased up to 30 % for the forced jet. Mixing between jet and cross-flow fluid started earlier and was substantially enhanced. Streamwise periodic structures observed in instantaneous flow fields exhibited very similar wavelengths for the forced and unforced jet. A low-velocity domain in the wake of the unforced jet disappeared due to streamwise forcing. According to Gogineni et al. (1995), the diminution of this wake region combined with an increased entrainment of cross-flow fluid below the jet due to secondary flows suggests an increased heat transfer for the forced jet. Measurements of the heat transfer coefficient were not conducted. Coolant cross-flow, as well as engine-realistic turbulence levels and temperature ratios were neglected.

Gogineni et al. (1996) investigated the effect of turbulence intensity on a JiC from cylindrical holes, while also neglecting engine-realistic coolant cross-flow and temperature ratios. They observed a doubling of wall-normal jet spreading from Tu =1 % to 17 %. Increasing the blowing ratio BR yielded higher shear-layer shedding frequencies with decreasing scale sizes. The roll-up frequency for the shear-layer downstream of the film cooling hole decreases while the scale size increases with both increasing blowing ratio BR and turbulence intensity Tu.

Peterson and Plesniak (2002), Peterson (2003), and Peterson and Plesniak (2004) reported that regions of increased heat transfer coefficient downstream of the jet are not caused by wake vortices Ω_{WV}, as those are inherently unsteady (Fric and Roshko, 1994). Instead, using PIV measurements at the hole inlet, in the hole and at the hole outlet combined with numerical simulation, a different vortex pair was identified. The authors referred to it as downstream spiral separation node Ω_{DSSN}. This definition is, however, not found in any other literature. Aside from the vortex definition, Peterson and Plesniak (2002), Peterson (2003), and Peterson and Plesniak (2004) observed a significant difference in the flow field when comparing parallel coolant co-cross-flow and counter-cross-flow. For the specific, not engine-realistic operating conditions and the short-hole cylindrical geometry, counter cross-flow proved to be beneficial for film cooling. It reduced the jet trajectory and the strength of the Ω_{CV} pair due to an in-hole vortex pair of opposite rotational sense.

David et al. (2004) investigated a square hole ejection at different velocity ratios. A clear, steady horseshoe vortex Ω_{HV} with an approximate diameter of $0.15D$ was observed in the velocity field upstream of the ejection for the highest velocity ratio $VR = 0.63$. The upstream boundary layer thickness was not reported specifically, but appears to be $\approx 0.3D$. This is large for applications in film cooling and might explain why David et al. (2004) was the only one so far to conclusively set out the presence of a Ω_{HV}. They further reported the unsteady merging of two Ω_{CV} pairs at a frequency equivalent to the shedding frequency of the shear-layer vortices. With regard to the latter, it should be mentioned that the explanation and data presentation seemed incomplete. While the investigation was intended for film cooling flows, the operating conditions were not engine-realistic.

Bernsdorf et al. (2005) investigated the flow field of cylindrical film cooling holes at two inclination angles (30° and 50°) and different temperature ratios using SPIV. They associated patches

of streamwise vorticity in a plane parallel and near to the wall with the horseshoe vortex Ω_{HV}. The streamwise vorticity had the opposite direction compared to that of the Ω_{CV} pair but no secondary flow structures in the flow field upstream of the ejection were presented to confirm this claim. Engine-realistic turbulence intensities and coolant cross-flow of any sort were not considered in their investigation.

While investigating the effect of hole imperfection of flow field and adiabatic film cooling effectiveness, Jovanović et al. (2006) observed a strong interdependence between the formation of large coherent structures and cooling effectiveness. According to them, the large vortical structures have the biggest influence on momentum and heat exchange. The study was unspecific as to how the coherent structures impact heat transfer. It was conducted in water, neglecting engine-realistic temperature ratios, coolant cross-flow and with nearly no turbulence intensity in the free stream cross-flow.

Jessen et al. (2007) investigated the influence of the density ratio *DR* on the flow field and the turbulence intensities of cylindrical holes using air and foreign gas injection. The flow field was observed to change much less when the velocity ratio was maintained rather than the blowing ratio for a change in density ratio. The flow field data was further compared to results of a large eddy simulation (LES) by Renze et al. (2007a). Qualitative differences in velocity data of up to 10 % and in turbulence intensities of up to 20 % were observed. In the study, engine-realistic hot gas turbulence intensities and coolant cross-flow were not considered.

Using the same film cooling test facility as Bernsdorf et al. (2005), Aga et al. (2008) investigated the flow field of a 45° compound angled inclined cylindrical hole under consideration of realistic temperature ratios. For the given operating conditions, a single coherent structure with positive, streamwise vorticity was observed instead of a Ω_{CV} pair. Thinning of the boundary layer associated with an increased heat transfer augmentation was reported. An increase in temperature ratio *TR* at constant blowing ratio *BR* resulted in an increased lateral spreading, significantly changing the velocity and vorticity field. As in Bernsdorf et al. (2005), realistic turbulence intensities and coolant cross-flow were not considered.

In Bernsdorf et al. (2008), the same test facility was further used to evaluate the effect of pulsating coolant flow on the flow field and instantaneous as well as time-averaged coolant jet trajectories. While the facility can run at engine-realistic temperature ratios, the flow field and jet trajectory analyses were exclusively conducted for $1/TR = DR \approx 1.0$. The steady coolant ejection was compared with the unsteady ejection at two different pulsating frequencies. For the higher pulsating frequency, small differences in instantaneous and phase-averaged flow fields were observed. The low pulsation frequencies yielded larger corresponding fluctuations in the blowing ratio and larger deviations from the steady case. The authors therefore deducted that a quasi-steady description of the ejection was sufficiently accurate only for high pulsation frequencies and low pulsation amplitudes. For low frequency pulsations with larger blowing ratio modulation, the quasi-steady assumption was quite limited and inaccurate. This is relevant when models for the steady-state flow fields are to be derived. A wider variation in pulsation frequency and amplitude to define the limits in quasi-steady modelling of such flows was not provided. The impact of the pulsation on the thermal film cooling quantities was not reported.

A combined experimental and numerical study was conducted by Renze et al. (2008) for cylindrical holes with and without a trench. An Ω_{CV} pair was observed for both hole configurations but the lateral spreading was significantly increased for the trenched hole. An overall consensus between numerical and experimental data was found, with deviations in peak values of up to 15 %. Thermal film cooling quantities, which are typically challenging for numerical simulations, were not investigated and the connection between the observed flow field and the thermal film cooling quantities was left unresolved. While the numerical study was conducted for two temperature ratios, the comparison between LES and experiment was conducted for $TR = 1.0$ only. Coolant cross-flow and engine-realistic turbulence intensities were also neglected.

Takeishi et al. (2010) investigated the influence of swirl in the coolant hole on the flow field and film cooling effectiveness using PIV, LiF and PSP with nitrogen as the coolant. According to their results, the film cooling effectiveness increases for both cylindrical and laidback fan-shaped cooling holes when swirl is introduced, as the tendency to lift-off was reduced. Similarly to the compound angled cylindrical holes in Aga et al. (2008), the Ω_{CV} pair was suppressed by the swirl and the jet was biased towards a lateral side. Heat transfer coefficients were not presented and the density ratio was not engine-realistic.

Combining PIV and PSP measurements, Wright et al. (2011a) investigated the effect of free stream turbulence on jet structure and film cooling effectiveness for a cylindrical cooling hole geometry. For attached jets at low turbulence intensities, an increase in turbulence intensity had a detrimental effect on the corresponding adiabatic film cooling effectiveness. For higher blowing ratios, at which the coolant jet tends to lift off for the given operating conditions, an increase in turbulence intensity has little effect on the adiabatic film cooling effectiveness in the near-hole region. In streamwise direction, the increased turbulence intensity reduces the adiabatic film cooling effectiveness due to the increased vertical and lateral mixing with the main flow. Maxima in turbulent kinetic energy thickness and turbulent shear stress thickness were associated with minima and local maxima in centreline adiabatic film cooling effectiveness, respectively. Coolant cross-flow and engine-realistic density ratios and turbulence intensities were not discussed.
Claims about a horseshoe vortex Ω_{HV} were made based on the jet velocity field not being clearly defined and increased velocity fluctuations in certain lateral planes. The measurement quality was overall limited as only the cooling air was seeded. Global validation rates were around 50 % and locally reduced to as low as 10 %. Given the overall flow field measurement quality, the spatial resolution and the fact that more convincing evidence of the Ω_{HV} in other studies suggest a diameter of $D \approx 0.1$ to $0.15D$ (Hale et al., 2000; David et al., 2004), these claims are highly speculative.

A similar investigation but for fan-shaped cooling holes with a lateral opening angle of 10° was conducted by Wright et al. (2011b). According to the authors, the effect of the Ω_{HV} observed for the cylindrical holes was diminished for the fan-shaped hole due to the lateral spreading. The authors further claim to observe a reversal of the Ω_{CV} pair reasoned by an elevated adiabatic film cooling effectiveness immediately downstream of the film cooling hole exit. Since no attributes of a reversed Ω_{CV} pair can be seen in the presented flow field data, the results should be treated with caution. Additionally, the approach in measurement techniques and data evaluation as well

as the global operating conditions were equivalent to Wright et al. (2011a). Hence, the previously mentioned concerns with respect to the data quality remain.

Aga and Abhari (2011) combined infrared thermography (IRT) for acquisition of adiabatic film cooling effectiveness and ratio of heat transfer coefficients with and without film cooling using the superposition approach of film cooling (Choe et al., 1974) with SPIV measurements. They investigated cylindrical holes at three different compound angles at engine-realistic temperature ratios. Corroborating the results in Aga et al. (2008), an increasing asymmetry between the Ω_{CV} legs was observed for increasing compound angles. Eventually, the Ω_{CV} pair fully transformed into a single streamwise vortex.
An increase in adiabatic film cooling effectiveness and ratio of heat transfer coefficients with and without film cooling was observed for increasing compound angles. Interestingly, local maxima in wall-normal vorticity associated with wake vortices Ω_{WV} were observed to not overlap with local maxima in ratio of heat transfer coefficients with and without film cooling. Coolant cross-flow and engine-realistic turbulence intensities were not considered in this study.

Jessen et al. (2011) investigated staggered multi-row film cooling using laidback fan-shaped holes with lateral and streamwise opening angles of 10° and 8°, respectively. Their focus was on zero and adverse cross-flow pressure gradients as well as density ratios of $DR = 1$ and 1.5 using CO_2 injection. Due to the staggered alignment, the Ω_{CV} pair of each consecutive row of holes interacted with the previous one reducing their overall strength. As in Jessen et al. (2007), engine-realistic turbulence intensities as well as coolant cross-flow was neglected and no experimental data was provided to quantify the thermal film cooling parameters.

Fawcett et al. (2011) investigated the flow field of cylindrical and laidback fan-shaped film cooling holes on a blade pressure side of a large scale linear cascade using PIV and high-speed photography for velocity measurements and analysis of unsteadiness, respectively. A Ω_{CV} pair developed for all blowing ratios in case of the cylindrical hole, while for the LFH hole it was only present at low blowing ratios and much weaker compared to the cylindrical hole at the same blowing ratio.
A spectral analysis of the pixel intensity time-series yielded Strouhal numbers $St \approx 1$ in the shear-layer. Coolant cross-flow and engine-realistic turbulence intensities and density ratios were not considered and no information on the thermal film cooling quantities was presented.

A combination of PIV, LIF and DES was used by Takeishi et al. (2011) to analyse the flow field and mixing process for cylindrical, fan-shaped and laidback fan-shaped geometries. They observed a premixing of coolant in the diffuser for the laidback fan-shaped geometry due to cross-flow ingestion. Coolant cross-flow and engine-realistic turbulence intensities and temperature ratios were not considered. Furthermore, the boundary layer thickness of five hole diameters is unreasonably large for gas turbine applications. The jet and cross-flow boundary layer thicknesses, however, have a major impact on the flow structures and therefore the mixing process in JiC (Saha and Yaragani, 2011).

Kampe et al. (2012) were the first to investigate flow field and thermal data, as well as numerical simulation data all from the same test facility. They analysed a cylindrical and a laidback fan-shaped geometry using SPIV, LDA, IRT and RANS simulations at low and medium density ratios

and elevated turbulence intensity for low blowing ratios. The laidback fan-shaped geometry was further investigated at higher blowing ratios but with a reduced density ratio close to unity.
An Ω_{CV} pair was only observed for the cylindrical hole, whereas for the diffuser geometry, the lateral spreading was considered to be the dominant flow structure. The double peak of lateral and wall-normal velocity was observed to increase with the blowing ratio and attributed to a flow separation in the central laidback part of the diffuser as suggested in Saumweber (2005). Only lateral averages of the adiabatic film cooling effectiveness were presented and it is unclear, whether a single or double lateral maximum of $\eta_{a,w}$ occurred. Heat transfer coefficients were not provided and coolant cross-flow was neglected entirely. A semi-realistic density ratio was only considered for the low blowing ratio.

Wright et al. (2013) investigated the benefits of laidback fan-shaped over cylindrical geometries at a high turbulence intensity but an unrealistically low density ratio and in neglect of coolant cross-flow. The formation of a Ω_{CV} pair was observed to be overall much weaker for the laidback fan-shaped geometry but increasing in strength with the blowing ratio for both the cylindrical and the laidback fan-shaped geometry. With the intention to further mitigate the Ω_{CV} pair, they suggested a double-hole cylindrical geometry. Due to the single jets merging closely downstream of the coolant ejection, the strength of the Ω_{CV} pair was, however, enhanced rather than reduced. In terms of laterally averaged adiabatic film cooling effectiveness, the double-hole concept outperformed the simple cylindrical geometry for the higher blowing ratios for a certain streamwise extent. For the laidback fan-shaped geometry, which presented with the weakest Ω_{CV} pair, the highest adiabatic film cooling effectiveness was observed. Data on the heat transfer coefficient with film cooling was not provided.

Eberly and Thole (2013) investigated the influence of the density ratio on the flow field and adiabatic film cooling effectiveness of a cylindrical cooling hole with coolant plenum conditions using PIV, IRT and LDV. Time-averaged and instantaneous flow fields were analysed. In contrast to Kampe et al. (2012), the PIV and LDV measurements agreed well, even in the near-wall region. The authors assume the presence of a Ω_{CV} pair based on changes in the near-wall flow field in a central compared to a laterally shifted streamwise plane. Flow fields orthogonal to the main flow direction are not presented. Strength and position of the Ω_{CV} pair are therefore not defined and the connection to the adiabatic film cooling effectiveness was not investigated.
Using instantaneous flow fields, opposite lateral vorticities were observed for high blowing ratio at low density ratios, indicating an upper and lower shear-layer. At low blowing ratios, only negative vorticity was observed. Increasing the density ratio at constant blowing ratio resulted in the negative-vorticity regions moving closer to the wall. This signifies the importance of maintaining engine-realistic density ratios when considering mixing between hot gas and coolant as well as the influence of film cooling on the turbine aerodynamic losses.
Heat transfer coefficients were not provided, and coolant cross-flow as well as engine-realistic turbulence intensities were neglected.

Combined investigations of flow field and adiabatic film cooling effectiveness were conducted by Takeishi et al. (2013) using PSP, PIV and LiF for a cylindrical and a laidback fan-shaped hole, analysing the influence of swirl in the coolant plenum. Depending on the swirl number, they observed both, beneficial and adverse effects on the adiabatic film cooling effectiveness. For both

geometries, an optimum swirl leading to a maximum in adiabatic film cooling effectiveness was found. At this optimum swirl number, the penetration depth of the coolant jet reduced, and the shape and strength of the Ω_{CV} pair was altered and reduced, respectively. A jet deflection towards the lateral direction with positive streamwise component of the coolant swirl was observed. The investigations were not conducted at engine-realistic temperature ratios and turbulence intensities, coolant cross-flow was neglected, and no information on heat transfer coefficients were provided.

Zhou and Hu (2015, 2016a,b, 2017) investigated variations of a so-called Barchan-dune-shaped ramp located upstream or downstream of a cylindrical cooling hole with the intention of decreasing the lift-off tendency of cylindrical cooling holes towards increased blowing ratios. For the cylindrical hole reference case, Zhou and Hu (2016b) observed a Ω_{CV} pair and an alleged comparatively weak horseshoe vortex Ω_{HV} in a plane orthogonal to the hot gas cross-flow. The presented streamwise planes including the upstream edge of the hole did not indicate a horseshoe vortex Ω_{HV} upstream of the cooling hole. It is, therefore, not clear, whether the observed vorticity is due to a Ω_{HV}.
Including the shaped ramp lead to a Ω_{CV} pair similar as for the cylindrical hole, but with increased lateral distance of the Ω_{CV} pair legs, yielding an increase in adiabatic film cooling effectiveness. The ramp further caused a second vortex pair which the authors referred to as an anti-counter rotating vortex Ω_{ACV} pair replacing the allegedly observed Ω_{HV}. Using an elongated dune-shaped ramp, Zhou and Hu (2017) reported an increase in area-averaged adiabatic film cooling effectiveness by up to a factor of three over a range of small to medium blowing ratio. Aside from the nearly-tangential discharge of coolant into the mainstream caused by the dune-shaped ramp, the Ω_{CV} pair observed for the cylindrical cooling hole was weakened significantly. The previously mentioned Ω_{ACV} pair was reported as the most dominant flow structure leading to an additional downwash of coolant towards the wall.
As in B. Johnson et al. (2013, 2014), in the studies by Zhou et al. (2014), Zhou and Hu (2015, 2016a,b, 2017), and Zhou et al. (2017), coolant cross-flow was not considered and the turbulence intensity was far from engine-realistic. Heat transfer coefficients with film cooling were not reported.

Using a thermocouple rake, IRT and PIV, Schroeder and Thole (2016c) investigated the effect of free stream turbulence intensity on the time-averaged velocity and temperature fields and the adiabatic film cooling effectiveness of a laidback fan-shaped cooling hole at engine-realistic density ratios and varying blowing ratios. While they conducted a combined analysis, the results for adiabatic film cooling effectiveness and flow fields stem from Schroeder and Thole (2014) and Schroeder and Thole (2016a), respectively.
For high blowing ratios and low turbulence intensities, a delayed coolant lift-off was observed due to the Ω_{CV} pair entraining increasing amounts of cross-flow hot gas below the jet. No such lift-off was observed for high turbulence intensities, as the Ω_{CV} pair became less relevant compared to the fluctuations caused by the free stream turbulence intensity. Lift-off of the coolant jet was defined in terms of whether the minimum temperature in wall-normal direction was found at the wall or away from the wall.
Increasing the turbulence intensity caused little changes in the velocity fields and the vertical ex-

tent of the jet, but enhanced dilution and lateral spreading of the coolant, promoting jet merging with neighbouring jets that would otherwise remain discrete. For attached coolant jets, which are usually present at low blowing ratios, an increased turbulence intensity yielded a lower laterally averaged adiabatic film cooling effectiveness. For high blowing ratios, no decrease in laterally averaged adiabatic film cooling effectiveness was observed, which the authors attributed to the fact that the delayed lift-off was prevented due to the higher turbulence intensity.
While temperature fields were required to determine the coolant distribution, the turbulent shear-stresses in the flow field yielded more insights into the reasons for the increased lateral spreading at high turbulence intensities. The authors attributed this to two main factors: First, a tendency of near-wall eddies preferentially directed laterally due to the damping effect imposed on the wall-normal fluctuations by the wall. Secondly, the fact that near-wall fluid subjected to lateral fluctuations was generally colder, implying a higher coolant concentration compared to fluid at the top of the jet which was subject to wall-normal fluctuations. Fluctuations of the near-wall fluid, therefore, simply had more impact on the overall temperature distribution in the flow.
Coolant cross-flow was not considered in any of these studies.

Abram et al. (2016) and Schreivogel et al. (2016) used thermographic PIV for the first time to investigate the instantaneous and time-averaged velocity and temperature fields in the hot gas coolant interaction regime of cylindrical and trenched cylindrical cooling holes at engine-realistic density ratio. While a detached jet with a pronounced upper and lower shear-layer was observed for the cylindrical hole, adding a trench resulted in an attached jet containing only an upper shear-layer. Somewhat wall-normal angled cold streaks between the jet core and the wall were attributed to wake vortices Ω_{WV} (referred to as "tornado" vortices) for the cylindrical hole. It should be mentioned, though, that wake vortices Ω_{WV} originate from the cross-flow (hot gas) boundary layer (Fric and Roshko, 1994). They should, therefore rather entrain hot gas. Hairpin vortices, which are typically observed at velocity ratios $VR \leq 1.0$, are, given their origin in the upstream shear-layer, comprised of hot gas with mixed in cooling air.
For the cylindrical hole, the jet was observed to become unstable downstream, showing a meandering motion, releasing lumps of coolant into the hot gas cross-flow. According to Abram et al. (2016) and Schreivogel et al. (2016), due to the faster moving coolant lumps, the mixing of coolant and hot gas main flow would be driven not only by the shear-layer instabilities, but also by the inherent intermittency of the coolant jet. The coolant lumps might also be the reason for the fact that the streamwise turbulent heat flux term was negative in both mixing layers, thereby contradicting the gradient diffusion hypothesis commonly used in RANS simulations. A frequency analysis was conducted for the cylindrical hole in the upper and lower shear-layer yielding frequencies of 2.3 kHz and 2.6 kHz in acceptable agreement with an LES conducted by Kalghatgi and Acharya (2014). Further downstream, lower frequencies dominated the flow field as the shear-layers merged and became less relevant compared to the free stream fluctuations. Similar observations were made by Kohli and Bogard (1998), who observed an initial dominance of higher frequency turbulence associated with the shear-layer, followed further downstream by a dominance of low-frequency turbulent structures associated with free stream turbulence. The investigations were conducted without coolant cross-flow and at low turbulence intensities.

Wernet et al. (2016) investigate cylindrical holes and claim to see a horseshoe vortex Ω_{HV} in

their PIV data. However, to the best knowledge of the author, no Ω_{HV} is visible in the presented data.

Song et al. (2017) investigated the change in adiabatic film cooling effectiveness by placing a vortex generator immediately downstream of a cylindrical cooling hole at various inclination angles to induce an anti-counter-rotating vortex Ω_{ACV} pair. They observed a significant increase in adiabatic film cooling effectiveness and for attached coolant jets due to the "downwash" effect of the Ω_{ACV} pair. The robustness of the adiabatic film cooling effectiveness towards a change in inclination angle was also improved. Engine-realistic temperature ratios and turbulence intensities were not maintained and coolant cross-flow was not considered.

Takeishi (2017) investigated the effects of in-hole swirl on the adiabatic film cooling effectiveness and the flow field of cylindrical and shaped cooling holes. They observed an increase in adiabatic film cooling effectiveness for most of the swirl angles and claimed to observe a connection between the suppression of the Ω_{ACV} pair and the increase in adiabatic film cooling effectiveness. For the cases without swirl, no Ω_{ACV} pair was, however, visible in the PIV data to start with. Engine-realistic operating conditions were not maintained.

Haydt and Lynch (2018) and Haydt et al. (2018) investigated laidback fan-shaped cooling holes at various compound angles and area ratios by increasing the hole lengths. An increase of blowing ratio at zero compound angle yielded a larger Ω_{CV} pair. With increasing compound angle, an increasing asymmetry was observed in the Ω_{CV} pair, which eventually turned into a single vortex. Increasing area ratio yielded a much weaker Ω_{CV} pair. For the largest area ratio, hardly any secondary flows were observed downstream of the coolant ejection. Engine-realistic temperature ratios and turbulence intensities were not maintained and coolant cross-flow was not considered.

Based on the same test facility as in Abram et al. (2016) and Schreivogel et al. (2016), high frequency velocity field measurements were conducted by Straußwald et al. (2018) to investigate the effect of turbulence intensity on film cooling jets at high and low momentum ratios. While at low momentum ratios, cross-flow eddies had considerable influence on the jet trajectory, eddies of the same size did not affect the trajectory of jets at high momentum ratios. The fluctuations caused by the shear-layer instabilities exceeded those in the approaching cross-flow. Judged by the variability of the jet trajectory decreasing with increasing momentum ratios, the coolant jets were observed to be more stable at higher momentum ratios. The most significant influence on the jet trajectory was caused by increasing turbulence intensities. Similarly to Kohli and Bogard (1998), the authors postulated that even when similar velocity fields are present at different turbulence intensities, the adiabatic film cooling effectiveness may be higher for high-turbulence main flow due to coolant intermittently reaching the surface to be cooled.
Compared to the previous studies, the density ratio was reduced and thereby not within an engine-realistic regime.

McClintic et al. (2019) investigated a laidback fan-shaped cooling hole with coolant channel cross-flow orthogonal to the hot gas cross-flow at various inlet velocity ratios. For the largest inlet velocity ratio, they were able to capture the remainder of the in-hole swirl in a measurement plane orthogonal to the hole axis coinciding with the upstream edge of the diffuser outlet. Temperature fields in a similar plane confirmed the hot gas ingestion into the diffuser. Downstream of the film

cooling hole, an asymmetric Ω_{CV} pair was observed. The lateral bias was observed to scale with the inlet velocity ratio. The density ratio was, however, not engine realistic and the turbulence intensity was low at $Tu = 4.8\,\%$.

For detached jets at engine-realistic density ratios, Straußwald et al. (2020) further observed that increased turbulence intensities enhance the velocity, but not the temperature fluctuations in the shear-layer. The streamwise and wall-normal heat flux was increased everywhere except for the wall-normal component in the lower shear-layer, indicating a reduction in heat-flux away from the wall for increased turbulence intensities. In contrast to Schroeder and Thole (2016c), who observed little influence of turbulence intensity on the vertical jet spread, Straußwald et al. (2020) observed a broadening of the jet in wall-normal direction caused by large, instantaneous deviations in jet trajectory, rendering a less stable jet at high turbulence intensities. Due to apparent shorter coolant jets in the streamwise plane, a lateral meandering motion of the jet was anticipated.
No information on the thermal film cooling quantities was provided and the unsteady effects of the coolant jet were, hence, not related to the adiabatic film cooling effectiveness and the ratio of heat transfer coefficients with and without film cooling. Coolant cross-flow was also not considered in this study.

Haydt and Lynch (2021) complement the flow field data of Haydt and Lynch (2018) by providing information on the adiabatic film cooling effectiveness and the ratio of heat transfer coefficients with and without film cooling for the laidback fan-shaped film cooling hole at various compound angles. At zero compound angle, a single peak was observed in adiabatic film cooling effectiveness for low and high velocity ratios. The trend in the ratio of heat transfer coefficients with and without film cooling is different. For low blowing ratios, a double peak in the ratio of heat transfer coefficients with and without film cooling was seen, while for high blowing ratios, a single peak was observed. While the authors make no efforts at explaining their observations, the double peak at low blowing ratios is likely due to the Ω_{CV} pair leaving imprints of the vortex legs when attached to the wall. According to Baldauf et al. (1999b), the transition from a double to a single peak is related to wake vortices Ω_{WV} at high blowing ratios. Haydt and Lynch (2021) also associate an increased heat transfer augmentation downstream of the ejection with the impinging, single vortex developed at increasing compound angles.
Haydt and Lynch (2021) also observe a heat transfer augmentation upstream of the film cooling hole outlet. Based on the observations by Wright et al. (2005), they associate this increase in the ratio of heat transfer coefficients with and without film cooling with a horseshoe vortex Ω_{HV}. Wright et al. (2005), however, only discussed thermal film cooling quantities with no information on the flow field. Their claim of a horseshoe vortex Ω_{HV} was also based only on the increased heat transfer coefficient upstream of the film cooling hole. Wright et al. (2011b) presented flow field data with alleged proof of a horseshoe vortex Ω_{HV}. As previously mentioned, the quality of the presented data was seriously lacking and, to the best knowledge of the author, no horseshoe vortex Ω_{HV} was present.
While providing an interesting combination of flow field data and thermal film cooling quantities, the investigation was conducted at unit density ratio with negligible turbulence intensity and no coolant cross-flow.

A graphical summary of the steady and unsteady coherent structures in a film cooling JiC containing references to the previously discussed experimental flow field investigations is shown in Figure 2.4 and 2.5 for a cylindrical (CYL) and a shaped cooling hole, respectively. The results for the shaped cooling hole include both, fan-shaped (FH) and laidback fan-shaped (LFH) cooling holes. In the figures, the previous flow field studies are indicated in accordance to the coherent structures that the authors observe or claim to observe. Entries are greyed out if the contained conclusions about the coherent structures are debatable. That is the case, if the presented flow field data is inconclusive or ambiguous or, to the best knowledge of the author, wrongly interpreted with respect to whether and which coherent structures are present in the flow. Entries are also considered debatable if flow field data was available, but the conclusions about the coherent structures were purely based on the thermal film cooling quantities.
While a distinction is made between the different cooling hole cross-sectional shapes, too few studies exist to assess the influence of other geometrical parameters such as the inclination angle of the cylindrical part of the holes or the opening angles of the shaped holes. As previously discussed, all investigations mentioned in the current section were intended to replicate film cooling flows in gas turbines and jet engines but not all relevant engine-realistic operating conditions were met. Most of the investigations are, hence, not directly comparable to each other.

For the cylindrical cooling hole (Figure 2.4), the presence of the steady counter-rotating vortex Ω_{CV} pair and the unsteady shear layer vortices Ω_{WSV} and Ω_{LSV} is conclusively demonstrated in the referenced flow field investigations. The steady wake vortex Ω_{sWV} (or Ω_{DNNS}) is discussed less frequently and the available investigations are less representative in terms of the engine-realistic operating parameters. Traces of unsteady wake vortices Ω_{WV} are also mentioned in previous literature. So far, their presence in film cooling JiCs is only suggested based on wall-normal vorticity in the mean flow field. The definite presence of a steady horseshoe vortex Ω_{HV} is stated several times but shown in flow field data only once at operating conditions barely representative for gas turbines or jet engines. The presence of the Ω_{WV} is, hence, debatable for cylindrical cooling holes.

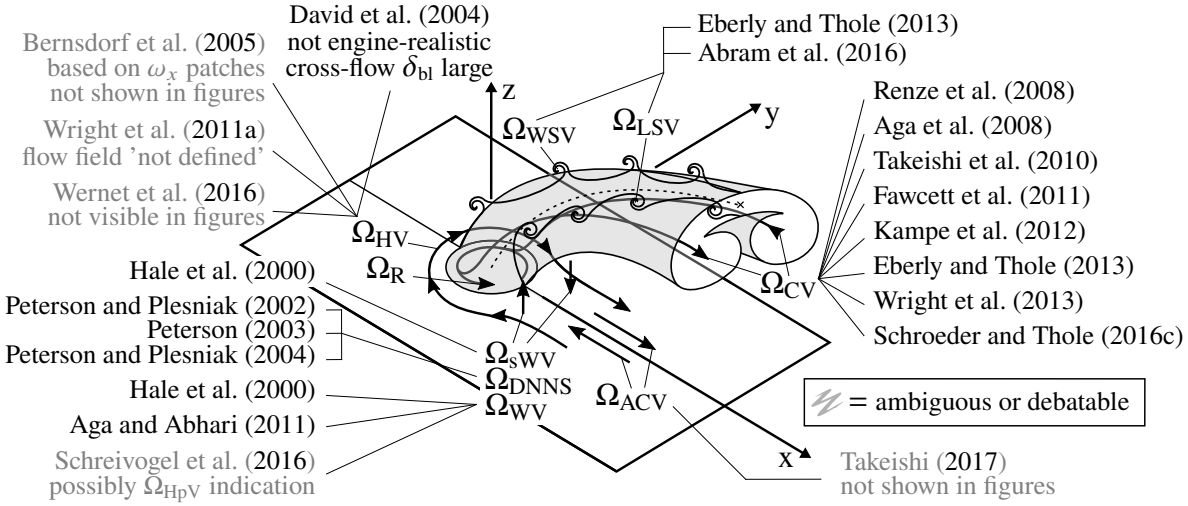

Figure 2.4: Graphical summary of the literature review on steady and unsteady coherent structures observed in a cylindrical film cooling JiC

For shaped cooling holes (Figure 2.5), fewer flow field investigations are available. The information provided on the counter rotating vortex Ω_{CV} pair stems exclusively from studies using LFH cooling holes. The results are inconclusive in that contrary observations are made. In some studies, the presence of the Ω_{CV} is clearly demonstrated and an increase in size or vorticity magnitude with an increase in blowing ratio *BR* is reported. In another study, the Ω_{CV} pair is observed for low blowing ratios only and in one study, the absence of the Ω_{CV} pair is explicitly demonstrated. With respect to the horseshoe vortex Ω_{HV}, the absence of such is clearly shown in one study, while another claims to observe a Ω_{HV} but only based on the thermal film cooling quantities. Given that, for cylindrical cooling holes, no conclusive proof of the presence of a Ω_{HV} is found at engine-realistic operating conditions, the presence of a Ω_{HV} seems even less likely in a shaped cooling hole.

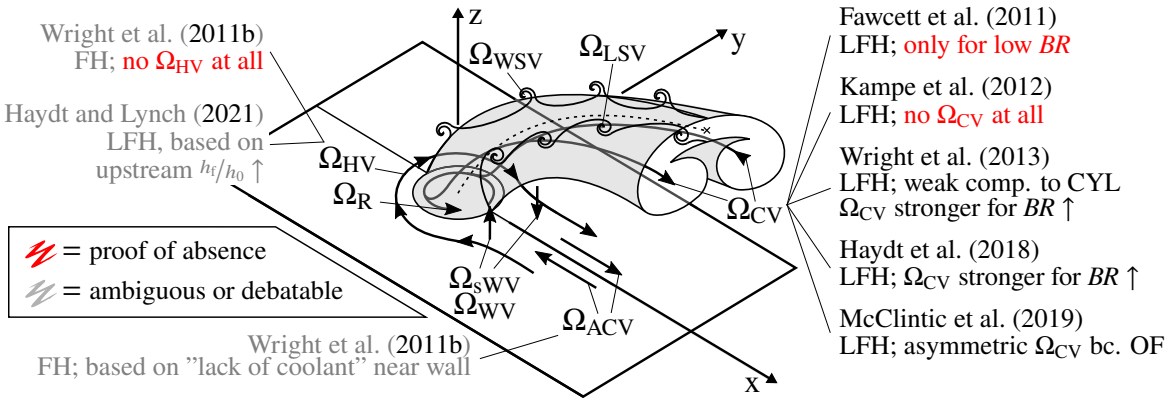

Figure 2.5: Graphical summary of the literature review on steady and unsteady coherent structures observed in fan-shaped (FH) and laidback fan-shaped (LFH) film cooling JiCs

Given the previously discussed, partially contrary results, more research into the coherent structures is clearly required. Furthermore, the impact of the coherent structures on the heat transfer coefficient is not discussed in any of the previously mentioned studies.

2.2.4 Influence of Coherent Structures on Heat Transfer

As part of the present work, the relation between the coherent flow structures and the resulting local heat transfer coefficients is of interest. In this regard, the information from the previously discussed flow field measurements for the film cooling JiC is limited. Despite the immense interest in the flow field of the JiC, only a handful of either fundamental or application-oriented studies investigate the connection between the prevailing coherent structures and the changes in heat transfer coefficients downstream of the jet.

An early fundamental study into this connection was conducted by Cardone et al. (1998). They used infrared scanning radiometry on heated thin-foil technique to measure convective heat transfer enhancement on a flat plate subjected to a JiC. Immediately downstream of the hole, a low heat transfer zone is observed and ascribed to the stagnation region caused by the ejection. The observation of a single maximum or in some cases double maxima along the symmetry

line in downstream direction is associated with eddy formation in the wake of the jet. Increasing jet to cross-flow velocity ratios lead to a deeper jet penetration into the cross-flow. Despite the mean jet trajectory being further away from the wall, increases in heat transfer coefficients are observed as the jet wake and associated vortex formation is thought to be enhanced. Wake vortices Ω_{WV} that increasingly occur for higher jet to cross-flow velocity ratios are thought to entail specifically high local heat transfer. For increases in cross-flow velocity and turbulence intensity, the heat transfer peaks are attenuated or vanish as wake vortices Ω_{WV} are thought to be swept away more quickly. Two lateral local minima closely downstream of the ejection are associated with what the authors refer to as trailing vortices accompanying the issuing jet. By the description, these trailing vortices have similarities to what Peterson and Plesniak (2002), Peterson (2003), and Peterson and Plesniak (2004) described as downstream spiral separation node (DNNS) and what Brizzi (1994), Hale (1999), and Hale et al. (2000) described as steady wake vortices (Ω_{sWV}, see Figure 2.1a).

Hale et al. (2000) connected surface heat transfer with coherent flow structures for cylindrical holes under consideration of co- and counter-cross-flow at the hole inlet. They used surface streak experiments, flow visualisations with smoke and measurements of surface heat transfer coefficients. Flow visualisations using smoke yielded weak horseshoe vortices Ω_{HV} with diameters $\leq 0.1D$ at the leading edge of the coolant hole exit, which were expected to dissipate quickly. Surface topology maps around and downstream of the film cooling hole exit were deduced using surface streak experiments. According to the authors, the observed time-averaged separation regions at the lateral sides downstream of the hole exit are caused by the time-averaged separation related to the wake vortices Ω_{WV}. As previously mentioned, Hale et al. (2000) suggested a pair of steady wake vortices Ω_{sWV}. In combination with surface heat transfer measurements, separation events were associated with reduced heat transfer coefficients, while reattachment caused an increase in heat transfer coefficients. According to the authors, the heat transfer coefficients for a JiC, in general, depend on the jet trajectory, the effective jet coverage and the resulting blockage, separation and attachment regions, as well as the strength of the wake vortices Ω_{WV}.

Carlomagno et al. (2004b,a) and Carlomagno (2006) investigated the change in heat transfer coefficients in proximity of the jet using heated thin-foils as in Cardone et al. (1998) and PIV to estimate the flow fields. Their aim was to find connections between the turbulent statistics of the JiC and the convective heat transfer along the wall. Upstream of the jet, an increase of heat transfer coefficients was observed which was attributed to the strong curvature of the streamlines and the sucking action of the jet on the boundary layer. Some correspondence between maxima/minima in turbulent kinetic energy and the ratio of heat transfer coefficients with and without the jet was found in the wake region. A definite conclusion was not made as the turbulent statistics were not available directly on the wall but in a near-wall parallel plane at the edge of the boundary layer[2]. For increasing velocity ratios between 2.0 to 5.0, the overall increase in heat transfer in the wake region was associated with the "upward motion" in the jet wake which grows stronger. The simultaneous decrease of upstream heat transfer was associated with the strong deceleration of the cross-flow. The impact of the Ω_{CV} pair on heat transfer was assumed

[2]The bending of the jet is different for different velocity ratios and therefore the downstream distance at which to expect similarities in the maxima/minima patterns varies.

to reduce as the formation was delayed for increasing velocity ratios.

2.3 Intentions of the Present Work

Many decades of research on film cooling flows have provided plenty of insights into the thermal film cooling quantities $\eta_{a,w}$ and h_f/h_0 for a variety of geometries and operating conditions. Fundamental research efforts into jets in cross-flow, on the other hand, offer detailed insights into the flow field of generic JiCs, which are often used as a basis to explain the trends observed in $\eta_{a,w}$ and h_f/h_0. The operating conditions of these experiments are, however, very different from what is required for film cooling. Specifically, the fundamental research on JiC is nearly exclusively using equal-temperature flows. As shown in the literature review in subsection 2.2.3 and 2.2.4, the current understanding of the relations between the coherent flow structures and the thermal film cooling parameters at engine-realistic experimental conditions is lacking. The extrapolations from the thermal film cooling quantities to the flow field are frequently vague and inconsistent. To correctly interpret the separation, mixing and heat transfer phenomena in film cooling flows, detailed understanding of the coherent structures is required.
Significant improvements in hardware and software components have encouraged increasing efforts into understanding the underlying flow field of JiCs at operating conditions tailored to applications in gas turbines and aero engines. A quantitative understanding of the flow field and its connection to the local thermal film cooling quantities will enable targeted geometry optimisation and contribute to the fundamental research in terms of the understanding of heat transfer augmentation on the adjacent wall. Experimental data of the JiC at engine-realistic operating conditions is required to cover both, the thermal film cooling quantities as well as the flow field in the mixing zone between hot gas main stream and coolant jet. This combination of experimental data also constitutes a unique dataset for validation and further development of numerical simulation methods. To make the interpretation of the combined data set as indubitable as possible, it should be gathered at the same test facility at well-defined operating conditions using well-understood, established measurement techniques.

The present work aims at gathering, understanding and providing such a combined data set. For this purpose, a unique film cooling test facility at the Institute of Thermal Turbomachinery (ITS) is used. It was previously built and used for extensive experimental investigations on the thermal film cooling quantities. The focus in the construction of the test section was to provide fully engine-realistic scaled operating conditions. Most importantly, this includes engine-realistic temperature and blowing ratios, turbulence intensities and the mostly neglected effects of parallel and orthogonal coolant cross-flow. For the specific geometry investigated in the present work, the previously gathered thermal film cooling quantities from the same test facility are used. The test facility is adopted to accommodate a stereoscopic Particle Image Velocimetry (SPIV) setup to gather highly resolved two-dimensional three-component (2D3C) velocity data. Quasi-3D velocity information is achieved in the entire mixing region of the film cooling jet and the hot gas cross-flow by shifting the SPIV-setup in lateral and streamwise direction. A detailed overview of the film cooling test facility, is provided in chapter 3.
For the first time, experimental data is provided at engine-realistic operating conditions giv-

ing insights into the coherent structures of the film cooling flow and possible unsteady effects. A variation of coolant cross-flow direction and Reynolds number as well as blowing ratio is conducted to emphasise the influence of these parameters on the coherent structures. Beyond describing the observed coherent structures, the aim of this work is to discuss in detail their relation to the thermal film cooling quantities $\eta_{a,w}$ and h_f/h_0. Details of this analysis can be found in chapter 4.

Thereby, the present work contributes not only to the application oriented film cooling research field, but also to the fundamental understanding of the significant drivers for heat transfer augmentation. Furthermore, it should raise awareness for questioning widely accepted explanations that are based only on the time-averaged flow field.The concluding remarks and future implications of this work are summarised in chapter 5.

3 Test Facility, Experimental Methods and Previous Flow Field Investigations

The measurement data presented throughout this thesis is gathered at a complex wind tunnel test facility designed for investigating jets in cross-flow at operating conditions relevant to industrial applications in aero engines and gas turbines. Details regarding the test facility, the infrastructure in which it is embedded, the investigated geometry and operating conditions will be discussed in the following sections. Furthermore, the measurement principles and the measurement setup will be explained in detail.

3.1 Experimental Setup of the Film Cooling Test Facility

For the experimental investigations, a test facility first introduced by Fraas et al. (2017) is modified to facilitate stereoscopic Particle Image Velocimetry (SPIV) measurements (Stichling et al., 2021). A schematic of the test facility including the relevant infrastructure is shown in Figure 3.1. The facility consists of a hot gas (top) and a coolant strand (bottom). For the hot gas strand, the air is delivered by a radial low pressure compressor and heated by an electrical heater using 40 separate heating elements. The temperature downstream of each heating element is measured and the heating power adapted using a PID controller to meet the target temperature, achieving an overall homogeneous temperature distribution. Mixer and sieves are used to further

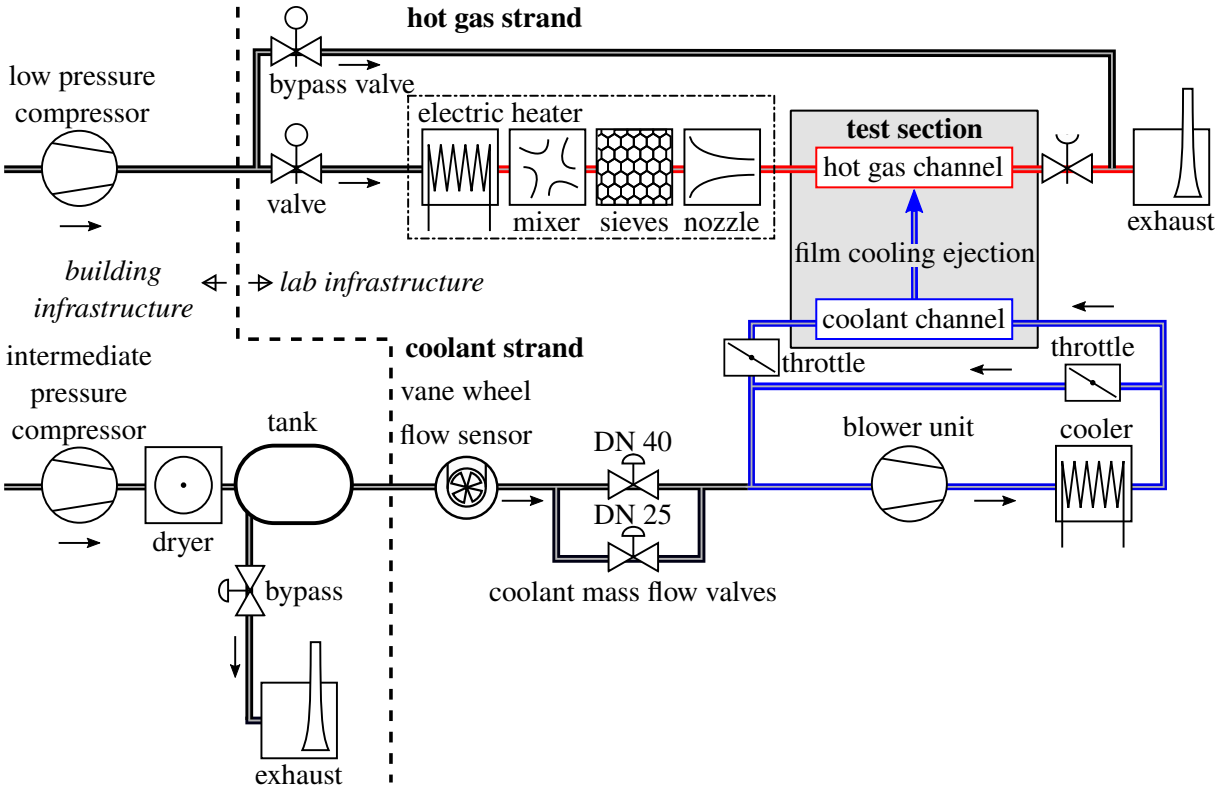

Figure 3.1: Schematic of the test facility including relevant laboratory and building infrastructure

homogenise the temperature profile and settle the flow, respectively. While transitioning from a circular to a rectangular cross section in the nozzle, the flow is accelerated by a factor of 13 to meet the target flow parameters in the hot gas channel of the test section. After passing through the test section, the air exits the test facility through the exhaust chimney. Detailed descriptions of the velocity and temperature homogeneity can be found in Fraas et al. (2017).

Replicating engine realistic flow conditions is essential, as it ensure transferability of the experimental results to real engines. Rather than using a plenum as frequently found in literature, the coolant is fed from a designated coolant channel. The coolant channel can be oriented either in parallel to the hot gas channel or rotated by 90°. These two configurations are henceforth referred to as parallel and orthogonal coolant cross-flow configuration, PF and OF configuration, respectively. The coolant is provided by an intermediate pressure screw compressor, passes through a dryer and provides a specified pressure in the tank. Two valves are available to adjust the coolant mass flow ejected via the film cooling holes. Except for the film cooling ejection, the coolant channel is a closed-circuit wind tunnel. Therefore, in steady-state condition, the mass flow added to the coolant channel via the coolant mass flow valves is equivalent to the mass flow ejected via the film cooling holes. The volume flow is measured using a vane wheel flow sensor upstream of the coolant mass flow valves. From that, the mass flow is calculated using additional temperature and pressure data from the same location. Excess air is blown off via the bypass valve into the exhaust chimney.

The blower unit is used to circulate the cooling air in the channel and a heat exchanger removes the heat added to the system by the blower unit. The coolant Reynolds number can be varied by one order of magnitude and is coarsely adjusted using two throttles and a bypass in the closed-circuit coolant channel. The fine-tuning of the Reynolds number is conducted via the speed controller of the blower unit.

A streamwise cross-section of the test section is shown in Figure 3.2 for parallel coolant cross-flow configuration. The test section is designed such that the target operating conditions are achieved at the film cooling hole inlet and exit for the coolant and hot gas channel, respectively[1]. For normalisation of the measurement data, the undisturbed streamwise hot gas cross-flow velocity is used and referred to as u_{ref}. Both channels are $50D$ wide (y-direction), where D is the cooling hole diameter, ensuring no interaction with the channel side-walls. In orthogonal coolant cross-flow configuration, an upstream (with respect to the hot gas flow) distance of $20D$ is maintained between coolant channel sidewall and cooling hole inlet. A turbulence grid (1) $22.9D$ upstream of the cooling hole exit is used to ensure the target turbulence intensity at the film cooling hole exit. The turbulence grid and its placement in the hot gas channel are designed based on Roach (1987). According to Stripf (2007), the design guidelines by Roach (1987) yield isotropic turbulence of the correct turbulence intensity. No measurements of the turbulence intensity were conducted in previous works by Fraas et al. (2017, 2019a,b), Fraas (2019), and Stichling et al. (2020, 2021) in the presented test section. In the current work, an accurate estimation of the turbulence intensity will be discussed in subsection 3.3.3. As shown in Saha

[1]The cooling hole inlet and exit are defined as the intersection of the axis of the cylindrical part of the cooling hole with the bottom and top surface of the blowing module, respectively. The origin of the right-handed coordinate system coincides with the cooling hole exit of the central hole.

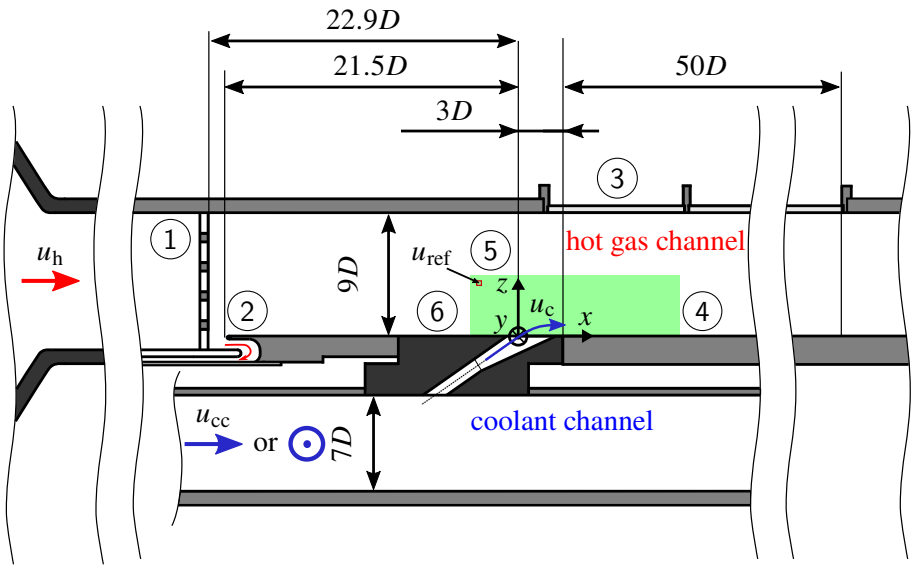

Figure 3.2: Schematic of test section including: (1) turbulence grid, (2) boundary layer bleed, (3) sapphire windows, (4) test plate, (5) PIV field of view (FOV), (6) blowing module; adapted from Fraas et al. (2019a)

and Yaragani (2011) using direct numerical simulation (DNS), coherent structures in a generic JiC change when altering the velocity profile of the main flow or in-hole jet from a block profile to a more realistic boundary layer profile. Anderson et al. (2016), too, state the significance of a correctly scaled boundary layer thickness in experimental investigations. They quantify the influence of the displacement thickness on the adiabatic film cooling effectiveness. Therefore, a boundary layer thickness in the correct order of magnitude is crucial for transferability of the results to real engines. In the film cooling test section, a boundary layer bleed (2) is placed $21.5D$ upstream of the film cooling hole exit such that the displacement thickness is $\delta_1 = 0.05D$ at the film cooling hole exit. As can be seen in Fraas et al. (2017) and Stichling et al. (2021), the displacement thickness is in the correct order of magnitude.

For the thermal measurements, an optical access in the top wall of the channel is provided using five sapphire windows (3) separated by narrow metal frames. Three different measurement plates (4) exist. For thermal measurements as conducted in Fraas et al. (2019a,b), Fraas (2019), and Stichling and Bauer (2022b), two differently constructed plates with embedded thermocouples in the top and bottom are used to impose two different surface temperature conditions. Based on two thermal measurements for one operating point using each plate once, the superposition principle of film cooling (Choe et al., 1974) is applied to derive the adiabatic film cooling effectiveness and the ratio of heat transfer coefficients with and without film cooling (see subsection 2.2.1). For simplicity, these quantities will be referred to as thermal film cooling quantities. Details on the measurement principle of infrared thermography (IRT), the construction of the thermal measurement plates, and the evaluation chain can be found in Ochs et al. (2009, 2010) and Fraas et al. (2017, 2019a), respectively. Using this method, meaningful results for the thermal film cooling quantities can be gathered in the range of $5 \leq x/D \leq 50$.

For the flow field measurements, stereoscopic Particle Image Velocimetry (SPIV) is chosen and

a simple steel plate is used as measurement plate (4). The field of view (FOV) for the SPIV measurements (5) is a streamwise, wall-normal plane indicated by the green area covering the flow in $-2,5 \leq {}^{x}/_{D} \leq 8,5$ and $0 \leq {}^{z}/_{D} \leq 3,5$.

The interchangeable blowing module (6) shown in Figure 3.2 is manufactured from polyether ether ketone (PEEK), a semi-crystalline high-temperature resistant thermoplastic with a low thermal conductivity of $\lambda_{\text{th}} \approx 0.27\,\text{W}/(\text{m K})$. It thus minimises the temperature change of the coolant while passing through the cooling hole.

For the present work, a 10°-10°-10° laidback fan-shaped hole is used and a schematic is shown in Figure 3.3. The hole is scaled up such that the diameter of the cylindrical part of the cooling hole is $D = 10\,\text{mm}$. As indicated by the name, the diffuser opening angle in lateral and streamwise direction is 10° each. The cylindrical inlet section is $L_{\text{cyl}} = 3.8D$ long and the cooling hole is inclined by 35° yielding a total hole length of $L = 7.5D$. The streamwise edges of the diffuser are rounded by $0.5D$ and the area ratio of cooling hole outlet and inlet is ${A_{\text{outlet}}}/{A_{\text{inlet}}} = 3.71$.

To ensure periodicity, five film cooling holes of the geometry depicted in Figure 3.3 are placed in the blowing module laterally spaced at a pitch of $P = 8D$. This yields a coverage factor of 0.35 at the cooling hole outlet. All measurements discussed in the course of this work were conducted on the central cooling hole.

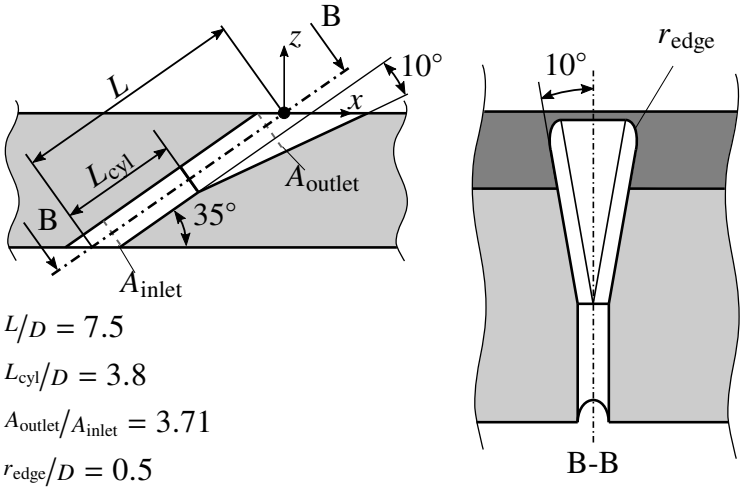

Figure 3.3: 10°-10°-10° laidback fan-shaped cooling hole (Fraas et al., 2019a)

3.2 Operating Conditions of the Film Cooling Test Section

The test section described in section 3.1 was designed to meet all of the dimensionless parameters most relevant to film cooling described in subsection 2.2.2. In Table 3.1, the resulting operating conditions are summarised. Given the two different coolant channel orientations and coolant channel Reynolds numbers, four different configurations were investigated. For each of them, the blowing ratio was varied such that $BR = 1.0,\ 2.0$ and 3.0 yielding 12 different cases.

[2]Two values are provided. The first value refers to the turbulence intensity measured based on a method proposed by Scharnowski et al. (2018) detailed in subsection 3.3.3. The second value is the design point turbulence

Table 3.1: Operating conditions of the test section in Figure 3.2

Parameter	Variable	Value
Reynolds number hot gas	$Re_{D,\mathrm{h}}$	13×10^3
Reynolds number coolant	$Re_{D,\mathrm{cc}}$	5×10^3 and 30×10^3
Cooling channel air to hot gas velocity ratio	$u_{\mathrm{cc}}/u_{\mathrm{h}}$	≈ 0.15 and 0.92
Density ratio	DR	1.7
Turbulence intensity hot gas[2]	Tu_{h}	≈7.1 % (8.2 %)
Blowing ratio	BR	1.0, 2.0 and 3.0
Total temperature hot gas	$T_{\mathrm{t,h}}$	510 K
Total temperature coolant	$T_{\mathrm{t,c}}$	300 K
Turbulent length scale	l_ϵ	$0.73D$
Boundary layer displacement thickness	δ_1	$0.05D$

3.3 Three-Component Velocity Fields from Stereoscopic Particle Image Velocimetry

Particle Image Velocimetry (PIV) is a non-intrusive optical flow measurement technique by which instantaneous velocity fields can be estimated. In its simplest form, a PIV setup includes seeding, a light source for illuminating the tracer particles of the seeding in the FOV and a single camera to capture the light scattered by the tracer particles. A calibration method is used to determine the relation between particle image displacement in the image plane (camera sensor) ΔX and the tracer particle displacement in the object plane (FOV in the flow) Δx. Two camera frames are acquired with a short time interval Δt in between and a cross-correlation (CC) algorithm is used to estimate the particle image displacement ΔX in subsets of the FOV at a point (x, y) in space. These subsets are called interrogation areas (IA).The local flow velocity u in each IA can be calculated from the displacement estimate as

$$u = \frac{\Delta x}{\Delta t} = \frac{\Delta X}{M \Delta t}, \tag{3.1}$$

with M being the local magnification factor. This simplest form of PIV is referred to as 2D2C PIV, where two components (2C) of the displacement vector are acquired in a 2-dimensional (2D) plane of the flow. In the present work, a 2D3C system is used, which can gather all three components of the displacement vector and is commonly referred to as stereoscopic or stereo PIV (SPIV). Since both cameras capture the same particle images from two different perspectives, the two 2D displacement fields can be used to reconstruct the 3D displacement field (Raffel et al., 2018, p. 289). The subsequent section will give a detailed overview of the hardware and software setup and the measurement chain used for the SPIV measurements in the film cooling test facility. For a detailed description of PIV basics and the required (S)PIV subsystems, the

[2] intensities according to Roach (1987)

reader is referred to Raffel et al. (2018) and Adrian and Westerweel (2011).

3.3.1 SPIV Setup in the Film Cooling Test Facility

Due to the complex three-dimensional flow fields typically associated with jets in cross-flow, a time-correlated[3] stereoscopic PIV system is used for the experimental investigation of the mixing between hot gas and coolant in the film cooling test facility. A schematic of the hardware setup for the SPIV measurements is presented in Figure 3.4 as a top view with the test section at its centre.

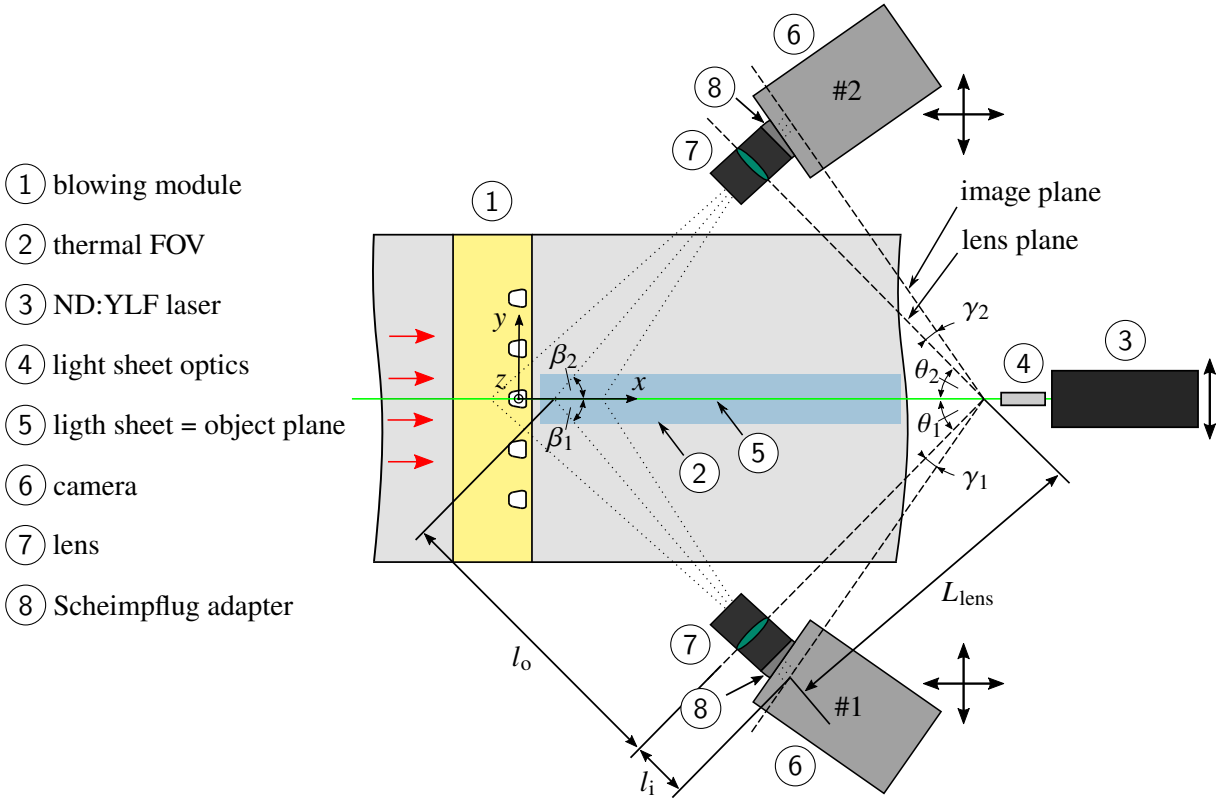

Figure 3.4: Schematic SPIV setup as top view on test section, adapted from Stichling et al. (2021)

The region of interest is the central film cooling hole exit in the blowing module (1). The origin of the coordinate system coincides with the exit of the central film cooling hole. x, y and z denote the streamwise, lateral and wall-normal main flow direction of the hot gas, respectively. The FOV of the thermal measurements (2) extends downstream of the central film cooling hole from $5 \leq {}^{x}/_{D} \leq 50$.
Using a green ($\lambda = 527$ nm) dual pulse ND:YLF laser (3) (*Darwin-Duo* by *Quantronix*) with an attached light sheet optics (4) (*iLA5150 GmbH*), a light sheet (5) with a thickness of $\delta_z \approx 0.08D$ is produced. The light sheet constitutes the object plane and is positioned such that streamwise,

[3]In the PIV community, the terminology used more frequently is *high frequency* or *time-resolved* (TR)PIV. As stated in Beresh (2021), this terminology is not accurate, as it does not specify the underlying characteristic of temporal sequencing of correlated vector fields.

wall-normal ($x - z$) planes in the test section can be investigated. Two cameras (6) (model *Fastcam SA5* CMOS by *Photron*) with a sensor size of 1024 px × 1024 px each are placed symmetrically about the light sheet plane in a backward scattering angular displacement configuration. The cameras can be moved in streamwise and lateral direction to change the position of the FOV. For the laser, only the lateral position is adapted accordingly. A change in the streamwise position of the laser is not required as the change in light sheet thickness is negligible. Optical access for the laser and the cameras is granted via three fused silica windows (not displayed). Each camera is equipped with a 130 mm focal length camera lens (7) (*Canon 130 mm EF 2.0 L USM*) connected via a Scheimpflug adapter (8) (by *iLA5150 GmbH*) to compensate for the oblique viewing angle of $\theta_1 = \theta_2 \approx 46°$. The Scheimpflug angle γ describes the angle subtended by lens and image plane. According to the Scheimpflug criterion, an object in the object plane can be reproduced fully focused on the image plane only if object, lens and image plane intersect in a common line as indicated by the dashed lines in Figure 3.4 (Raffel et al., 2018).

The choice of the lens and of the object and image distances, l_o and l_i, respectively, are determined to achieve a target FOV size and spatial resolution at optimal camera angles and minimum Scheimpflug angles γ_1 and γ_2. For a single thin lens, the magnification factor along the principal optical axis M_0 is defined as

$$M_0 = \frac{l_\mathrm{i}}{l_\mathrm{o}} = \frac{h_\mathrm{i}}{h_\mathrm{o}} \quad \text{with} \quad l_\mathrm{o} = \frac{L_\mathrm{lens}}{\tan(\beta)} \quad \text{and} \quad l_\mathrm{i} = L_\mathrm{lens}\tan(\gamma), \tag{3.2}$$

where h_i and h_o are the image and object height. L_lens is the shortest distance between the camera lens centre and the intersection line between object, lens and image plane as mandated by the Scheimpflug criterion. The relationship between camera angle β and Scheimpflug angle γ for each camera is thus given as

$$\gamma = \arctan\left(\frac{M_0}{\tan(\beta)}\right). \tag{3.3}$$

In Figure 3.5, the theoretical relationship between camera angle β and Scheimpflug angle γ along the optical axis (see Equation 3.3) is visualised for three different magnification factors. For any SPIV setup, the uncertainties of the in-plane and out-of-plane displacement, $\sigma_{\Delta X}$ and $\sigma_{\Delta Z}$, respectively, are dependent on the stereo viewing angle β such that (Raffel et al., 2018)

$$\sigma_{\Delta Z} = \frac{\sigma_{\Delta X}}{\tan(\beta)}. \tag{3.4}$$

For a camera angle of $\beta = 45°$, this yields an uncertainty ratio of unity between in-plane and out-of-plane displacement components. Since all displacement components are considered equally relevant to the experimental investigations in this work, a ratio of unity is desirable, and a camera angle of $\beta = 46°$ is chosen. Smaller camera angles would lead to a significant increase in uncertainty of the out-of-plane component (Raffel et al., 2018, p. 235) and as shown in Figure 3.5, a larger camera angle reduces the Scheimpflug angle for a given magnification factor. For the current test section, it is observed that exceedingly large Scheimpflug angles ($\gamma \gtrapprox 18°$) lead to a reduced imaging quality since lens aberrations become more significant and the illumination less homogeneous over the image plane. If larger magnification factors are desired, the camera

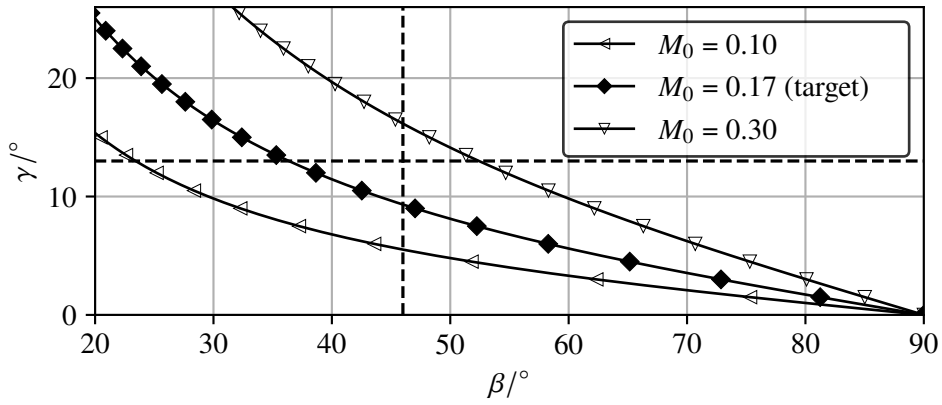

Figure 3.5: Theoretical relationship between camera angle β and Scheimpflug angle γ along the optical axis for three different magnification factors M_0; adapted from Mersch (2020)

angle β has to be increased rather than increasing the Scheimpflug angle.

According to Equation 3.3 and Figure 3.5, the resulting Scheimpflug angle γ for a target magnification factor of $M_0 = 0,17$ should be $\approx 9.6°$. For the SPIV setup in the film cooling test facility (see Figure 3.4), increasing the Scheimpflug angle γ until a fully focused image is achieved yields a Scheimpflug angle of $\gamma_1 = \gamma_2 \approx 13°$. A deviation of the real Scheimpflug angle from the theoretical angle is expected due to a variety of reasons. Modern camera lenses always consist of a system of single lenses. Gaussian and Newtonian thin lens equations as used in Equation 3.2 merely approximate the optical setup using an ideal single (thin) lens of the same focal length as the camera lens. Lens aberrations are not considered. For the theoretical calculation, it is assumed that the optical centre of the camera lens is in the centre which is atypical for telephoto camera lenses. Furthermore, the local magnification factor varies along the image plane so that $M_{\max}/M_{\min} \approx 1.18$.

Both, cameras and laser, are mounted on a traverse system. As indicated by the black arrows in Figure 3.4, the laser can be moved in lateral direction and the cameras in both, lateral and streamwise direction, with a bidirectional repeatability of $\leq$ 15 µm. For the measurements in this work, two streamwise positions are required and the focus of the light sheet optics is moved in the respective streamwise direction to ensure close to identical light sheet conditions.

For the calibration, a two-sided two-level calibration target, as suggested in Raffel et al., 2018, p. 294, with circular markers is used. Two levels are required for each camera view, as the camera viewing angles have to be calculated aside from the mapping between image and object space only. The marker diameter is 1 mm, the marker spacing 5 mm and the level offset 1 mm.

For seeding, silicon oil and di-ethyl-hexyl-sebacate (DEHS) particles with a mean diameter of $d = 1$ µm are seeded in the hot gas and coolant channel, respectively. The hot gas seeding is added immediately downstream of the electrical heater in Figure 3.1 and the coolant seeding is added in the closed loop coolant channel sufficiently upstream of the film cooling hole inlet. The double images are acquired at a frequency of $f = 5$ kHz to 7 kHz in frame-straddling mode

with a time delay of $\Delta t = 10\,\mu s$ to $30\,\mu s$ at multiple lateral y/D positions. For camera and laser synchronization a synchronizer by *iLA5150 GmbH* is used. For data evaluation, a multi-pass scheme with an overlap of 50 % and a final interrogation window size of 12 px is used during evaluation (*PIVview3C* by *PIVTEC GmbH*), yielding a spatial in-plane resolution of 13.3 vec/D.[4]

3.3.2 Uncertainty Quantification in Particle Image Velocimetry for Film Cooling Flows

The basic principle of PIV as a flow field measurement technique is more than 100 years old. Today, PIV has become the most important field measurement technique in fluid flows. Uncertainty Quantification (UQ) in PIV is, however, a much more recent research topic and the most significant contributions where made in the past ten years. The following will elaborate on the important definitions and give a brief overview of the relevant methods.

Random and Systematic Error, Uncertainty and Uncertainty Quantification

According to JCGM (2008), the error of a measurement is defined as the difference between the true value X_{true} and the measured value X such that

$$X = X_{\text{true}} + \delta, \quad \text{with} \quad \delta = \epsilon + \beta, \tag{3.5}$$

where the total error δ is generally composed of a random error ϵ and a systematic error β. Random errors are unpredictable and by definition the expected value of the random error over repeated measurements tends towards zero. Systematic (or bias) errors are a relatively fixed function of their source (B. L. Smith and Oberkampf, 2014) and predictable if correctly identified. According to Coleman and Steele (2018), a systematic error is constant over time, however, the systematic error as commonly understood in PIV may vary over time with the input source. It should be pointed out that a measurement can be accurate (low systematic error), while not being precise at all (high random error) and vice versa. (Raffel et al., 2018, p. 210)

For a number of measurements N_{m}, measurement errors δ will yield a sample population distribution rather than the identical measurement value N_{m} times. According to JCGM (2008) and Sciacchitano (2019), this distribution is characterised by its mean value $\bar{X}$ and its standard deviation s_X. For $N_{\text{m}} \to \infty$, the sample population approaches the parent population distribution, whose mean μ systematically deviates from X_{true} by β. The random standard uncertainty is therefore simply the standard deviation s_X. If the same set of N_{m} measurements is repeated sufficiently often to form a sample population distribution of the mean values $\bar{X}$ of each set of measurements, the systematic standard uncertainty equates to the standard deviation b_X of the new sample population distribution. The combined standard uncertainty is then defined as (JCGM, 2008)

$$u_{\text{c}} = \sqrt{b_X^2 + s_X^2}. \tag{3.6}$$

[4]The evaluation parameters vary in the given ranges and will be specified exactly in the respective subsections if relevant.

Uncertainty quantification (UQ) is used to estimate an interval, wherein the magnitude of the total error δ lies with a certain probability. Since no explicit or implicit assumptions on the shape of the probability distribution are made for u_c, the probability of the error falling within the interval $\pm u_c$ is unknown and the expanded uncertainty U is introduced as

$$\left|\bar{X} - X_{\text{true}}\right| \leq U \quad \text{with a confidence level of } C, \quad \text{with} \quad U = k u_c, \tag{3.7}$$

where the coverage factor k depends on the underlying probability distribution. For the frequently applicable Gaussian error distribution, coverage factors of $k = 1,\ 2$ and 3 yield confidence levels C of 68.0 %, 95.0 % and 99.7 %, respectively (Kline, 1953).

Uncertainty Quantification in PIV

While a typical figure reported for PIV uncertainty is 0.1 px (Scarano and Riethmuller, 2000; Adrian and Westerweel, 2011; Raffel et al., 2018) or 0.2 px (Li et al., 2014), the actual uncertainty of a PIV measurement is known to vary significantly in a single experiment, depending on the image acquisition, the velocity estimation and the flow physic itself. A detailed analysis of PIV error sources and their classification in either mainly random or mainly systematic error sources is given in Wieneke (2017) and Sciacchitano (2019), respectively.

To obtain the uncertainty of the estimated velocity u, a Taylor series propagation (Coleman and Steele, 2018) is used with the particle displacement ΔX, the local magnification factor M and the time interval Δt as independent variables, yielding

$$\left(\frac{U_u}{u}\right)^2 = \left(\frac{U_{\Delta X}}{\Delta X}\right)^2 + \left(\frac{U_{\Delta t}}{\Delta t}\right)^2 + \left(\frac{U_M}{M}\right)^2. \tag{3.8}$$

According to Sciacchitano (2019), the uncertainty $U_{\Delta t}$ of the laser pulse separation and the uncertainty of the local magnification factor $U_{\Delta M}$ are negligible. This assumption is valid, provided the Δt is large compared to the errors associated with the timing unit and the calibration is conducted carefully with a subsequent disparity correction when using SPIV.

Available methods for quantifying the remaining uncertainty of the displacement $U_{\Delta X}$ in PIV measurements can be split into *a-priori* and *a-posteriori* UQ methods. *A-priori* methods usually return a general figure for the uncertainty of a PIV algorithm, while *a-posteriori* methods can quantify the local and instantaneous uncertainty of a specific dataset. *A-posteriori* methods can be further divided into direct and indirect methods (Sciacchitano et al., 2013). A thorough review of methods proposed for *a-priori* and *a-posteriori* UQ in PIV so far is provided in Sciacchitano (2019).

Uncertainty Quantification for PIV Measurements in the Film Cooling Test Facility

While there are quite a few methods theoretically available for UQ in PIV, to the knowledge of the author, only the correlation statistics method proposed by Wieneke (2015) is implemented in a commercially available software for PIV evaluation. As discussed in Sciacchitano (2019),

the level of difficulty for implementation of the methods for UQ varies significantly. Apart from publications directly related to the topic of UQ in PIV, the research community has only recently started to include useful estimates of the uncertainty when providing PIV data in their research.

For the literature related to this work, a short review on the methods used for UQ is conducted. The content of the publications directly relevant to this work was already discussed in subsection 2.2.3. For the sake of completeness, all available experimental studies using PIV or SPIV on film cooling test facilities are considered for the review of UQ methods in this section. A comprehensive list of all studies not explicitly discussed in subsection 2.2.3 can be found in section A.1. If available, the UQ methods used are identified and the estimated uncertainties are quantified relative to the respective flow velocities. The information gathered is summarised in Figure 3.6.

Each bar represents one publication and the height of each bar corresponds to the relative uncertainty of the measurement of the respective publication. Since the measurement uncertainty is a function of the instantaneous local flow and imaging conditions, in some publications more than one value is provided. In such cases, the minimum and maximum values are visualised by the differently shaded regions in the same bar. Whenever no explicit value for the relative uncer-

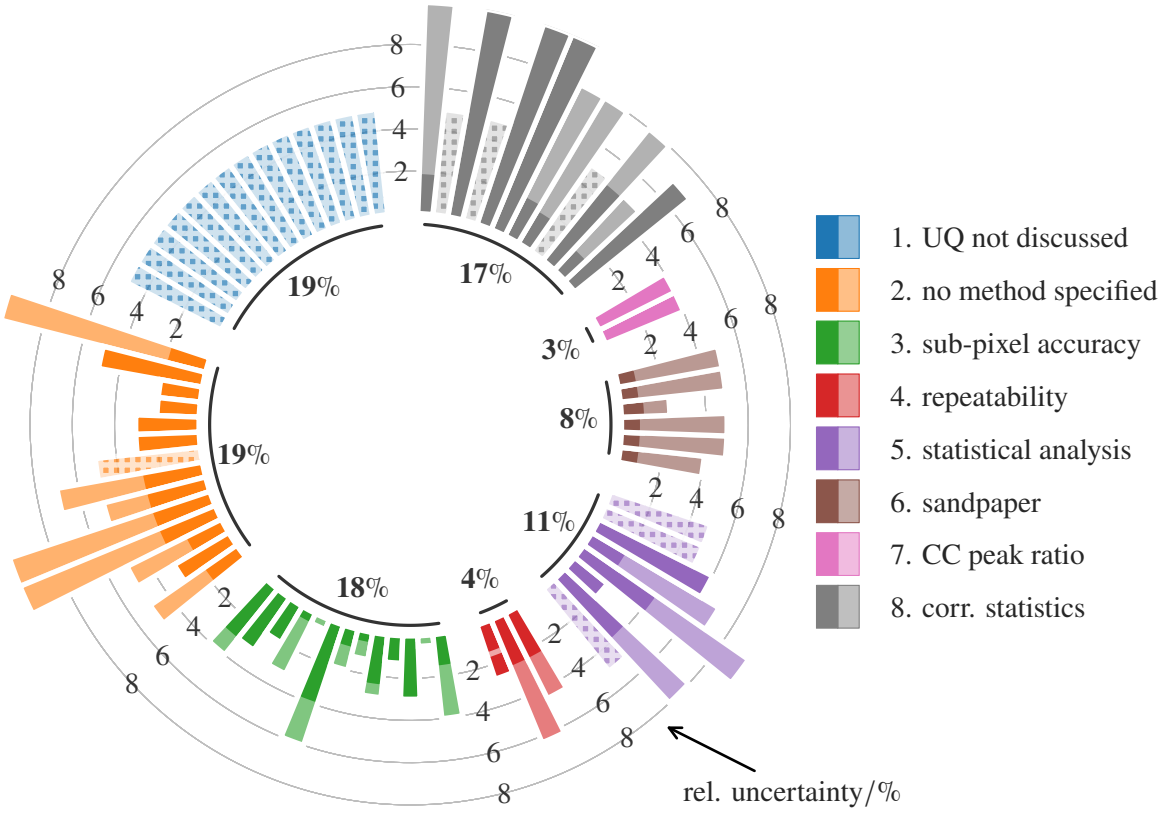

Figure 3.6: Prevalence of different methods for uncertainty quantification in literature related to (S)PIV measurements in film cooling test facilities. Each bar represents one publication.

tainty is provided or quantifiable from the data[5] , the bar is hashed and the relative uncertainty is set to 5 %.

Amongst all 72 publications related to (S)PIV measurements in film cooling, eight different methods of UQ are identified and the publications are grouped by these methods of UQ. The percentage value within the inner circle corresponds to the prevalence of the respective methods in film cooling literature. It should be mentioned that, in 97 % of the relevant publications, systematic errors and the systematic uncertainty are neglected entirely, bearing the assumption of being either removed entirely beforehand or negligible compared to the random uncertainties. The latter assumption is reasonable given a careful calibration, an appropriate choice of interrogation algorithm (Adrian and Westerweel, 2011) and no peak locking. In such cases, the systematic error is, while much harder to quantify if unknown, usually an order of magnitude smaller compared to the random error as shown by Sciacchitano et al. (2015) and Wieneke (2015).

It can be observed in Figure 3.6 that the predicted uncertainties vary largely depending on the applied method. For the literature relevant to film cooling, in 19 % of publications, the uncertainty of the (S)PIV measurement is not discussed at all and hence no uncertainty is provided. In another 19 %, the uncertainty is quantified, but the method used for UQ is not specified. While it is well known that the uncertainty in PIV can vary largely even in a single measurement (Raffel et al., 2018), in 18 % of the relevant literature, a typical figure for the sub-pixel accuracy ranging from 0.01 px to 0.1 px is assumed. The sub-pixel accuracy depends on the peak finding algorithm which determines the location of the particle image centre in a pixel. The ratio of sub-pixel accuracy and mean or local particle image displacement is then used as a measure for the (local) uncertainty. As can be seen in Figure 3.6, the estimates for the uncertainty are comparatively low and are known to underestimate the true uncertainty of the measurement significantly (Sciacchitano et al., 2015). Repeatability of the measurement is translated to uncertainty in 4 % of the relevant publications, but repeatable mean quantities do not stipulate a low uncertainty in the instantaneous data. In 11 % of publications, a statistical analysis is performed to derive an uncertainty. While the parent population chosen for the analyses varies, the derived uncertainty always includes the random turbulent velocity fluctuations which as such do not constitute an uncertainty. Using the standard deviation of the fitted parent population as a measure of uncertainty is therefore inherently flawed, irrespective of the choice of parent population, unless applied to laminar flows only. Alternatively, in 8 % of the publications, a method based on placing sandpaper in the FOV to appear as a field of seeding particles is used. By taking two images of the FOV, once before and once after shifting the camera(s), a fictitious displacement field can be calculated using the same PIV algorithm as for the actual measurement. The deviation compared to the imposed shift length is used to calculate the local error and global uncertainty of the measurement. Aga et al. (2008) claim that this method incorporates all potential error sources. However, based on the extensive list of error sources provided in Wieneke (2017), this is clearly not the case. Furthermore, no disparity[6] correction can be conducted for sandpaper images. If

[5]By some authors, information on the method used for UQ of their measurement is provided, but only absolute values of uncertainty are stated and insufficient information is provided to derive relative uncertainties.

[6]In PIV measurements, a misalignment between the laser light sheet and the position of the calibration target,

no disparity between sandpaper and calibration plate exists, this method gives a good insight in the quality of the stereo camera alignment and calibration. In just 3 % of the relevant literature, the cross-correlation peak ratio method proposed by Charonko and Vlachos (2013) is used to estimate the measurement uncertainty of the velocity magnitude. This a-posteriori method relies on the uncertainty being directly related to the peak ratio in the respective correlation plane. The peak ratio is defined as the ratio of the largest detectable peak and the second largest peak in the correlation plane, where the latter occurs due to spurious particle image pairing (Keane and Adrian, 1990). The correlation statistics method proposed by Wieneke (2015) also belongs to the a-posteriori methods. It is used in 17 % of the relevant literature and, according to Sciacchitano et al. (2015), delivers the most accurate results for the uncertainty. According to Sciacchitano et al. (2015), when compared to the correlation statistics method (Wieneke, 2015), the cross-correlation peak ratio method (Charonko and Vlachos, 2013) is less sensitive to variations in the error as the peak ratio is not directly related to the measured displacement. Furthermore, the CC peak ratio method is highly dependent upon the dynamic range of the signal-to-noise ratio (SNR) and therefore on the correlation approach. In a comparative assessment of four different methods, the correlation statistics method (Wieneke, 2015) provided the most accurate estimate of uncertainty while also exhibiting exceptional sensitivity.

Stating the uncertainty of the velocity estimation in (S)PIV measurements is imminent in general but specifically when the data shall also serve as reference data for numerical simulations to improve modelling approaches. Due to the high accuracy of the correlation statistics method reported in Sciacchitano et al. (2015), this method is used for the UQ of the PIV measurements in this work. The uncertainty analysis is conducted in *DaVis Version 8.4* by *LaVision GmbH*.

The method utilises the differences between the corresponding interrogation windows of one double image as they are mapped back onto each other based on the computed displacement vector field. Ideally, all particle images match perfectly, producing a symmetric cross-correlation peak. The disparity of these particle images in realistic and, hence, imperfect images is reflected in an asymmetric cross-correlation peak. The uncertainty is quantified based on the standard deviation of the pixel-wise contributions to the peak shape of each correlation window with a 68 % confidence interval assuming an underlying Gaussian error distribution. The correlation statistics method delivers good agreement when tested with synthetic data. The results of this method is the random standard uncertainty (s_x in Equation 3.6) and it is unable to estimate bias errors like peak locking[7]. (Wieneke, 2015; Sciacchitano et al., 2015; Sciacchitano, 2019)

For the measurements in the present work, bias errors due to peak locking are ruled out by an appropriate choice of aperture and magnification factor and by monitoring the probability density function of the displacement fields of each measurement. Based on the correlation statistics method, the magnitude of uncertainty is below 7 % in 95 % of the flow field for all measurement planes. The uncertainty increases to $\approx$ 10 % in near-wall regions with coolant ejection down-

is referred to as disparity. In SPIV measurements, this disparity can be corrected for based on a cross-correlation of the individual frames of both cameras (Raffel et al., 2018).

[7] *Peak-locking* occurs when the particle image diameter spans less than 2 px. The discretised camera sensor is unable to resolve the continuous intensity distribution of the particle image, the sub-pixel-position of the particle images is lost and the displacement is biased towards full integer displacements. Raffel et al. (2018, p. 219)

stream of the cooling hole exit ($z \leqq 0.5D$, $0D \leqq x \leqq 4.3D$). This is expected as the uncertainty of a PIV measurement correlates with the out-of-plane motion (Wieneke, 2015). The highest uncertainties of up to 20 % are observed very close to the wall ($z \leqq 0.1D$) upstream of the ejection due to reflections of the laser light sheet on the measurement plate.

3.3.3 Estimation of Turbulence Quantities and the Random Measurement Uncertainty from Particle Image Velocimetry

For the analysis of steady and unsteady coherent structures and their impact on the thermal film cooling quantities, well-defined boundary conditions are required, including the turbulence intensity. Accurate knowledge of the hot gas turbulence intensity is also required to make the data gathered at the film cooling test section valuable for validation and further development of numerical flow simulations. As described in Figure 3.2, a turbulence grid is used in the test section of the present work. The turbulence grid was designed by Fraas et al. (2017) according to the guidelines in Roach (1987) to achieve a turbulence intensity of $Tu = 8.2\,\%$ at the cooling hole exit plane. Prior to the present work, the turbulence intensity in the test section has not been measured. The content of this section will use a method suggested in Scharnowski et al. (2018) to accurately estimate the turbulence intensity in the hot gas channel.

For a sufficiently large discrete time series, the turbulence intensity Tu is defined as the population standard deviation of the velocity fluctuations normalised by the mean velocity magnitude such that

$$Tu = \frac{\sqrt{\langle u'^2 \rangle}}{\langle u \rangle}, \qquad \text{with} \qquad \sqrt{\langle u'^2 \rangle} = \sqrt{\frac{1}{N} \sum_n \left(u_n - \langle u \rangle\right)^2}. \tag{3.9}$$

$\langle u \rangle$ is the mean velocity of an ensemble of independent and uncorrelated measurements.

If the loss-of-correlation due to out-of-plane motion and the streamline curvature[8] are small, the random measurement uncertainty is independent of the magnitude of the displacement vector (Raffel et al., 2018). In contrast to what is stated in Scharnowski et al. (2018), the systematic error of a PIV measurement does affect the calculated turbulence intensity Tu (see Equation 3.9). However, as mentioned previously, the systematic measurement error in PIV is usually an order of magnitude smaller compared to the random error (Sciacchitano et al., 2015; Wieneke, 2015). The mean measured displacement fluctuation $\langle \Delta x'^2 \rangle_{\text{meas}}$ at every point in space is, hence, a combination of the true mean turbulent displacement fluctuation $\langle \Delta x'^2 \rangle_{\text{turb}}$ and the random measurement error characterised by the square of its standard deviation $\sigma^2_{\Delta x}$, such that (Scharnowski et al., 2018)

$$\langle \Delta x'^2 \rangle_{\text{meas}} = \langle \Delta x'^2 \rangle_{\text{turb}} + \sigma^2_{\Delta x}, \qquad \text{yielding} \qquad \frac{\langle \Delta x'^2 \rangle_{\text{meas}}}{\langle \Delta x \rangle^2} = Tu^2 + \frac{\sigma^2_{\Delta x}}{\langle \Delta x \rangle^2}. \tag{3.10}$$

[8]The volume-averaged mean particle displacement vector calculated using multi-pass schemes is located at the centre of the interrogation window. For non-constant gradients within an interrogation window, the deviation from the mean displacement does not cancel out and produces a bias error. In the PIV context, these non-constant gradients are more commonly referred to as *streamline curvature*. (Raffel et al., 2018, p. 231)

The estimation of turbulence intensities from PIV measurements is subject to multiple types of bias errors. As seen from Equation 3.10, the random uncertainty of the measurement increases the measured turbulence intensity compared to the true turbulence intensity. While, given the previous assumption, the absolute random uncertainty can be considered constant for a specific PIV setup, the relative contribution to the displacement vector increases with decreasing displacement vector magnitude. In contrast, the PIV-inherent spatial filter decreases the measured turbulence intensity with increasing final interrogation window size. This bias error tends to zero when the final interrogation window size approaches the size of the smallest turbulent structures in the flow. When several value pairs of the variation of the mean particle image displacement Δx and the measured turbulence intensity are available, the true turbulence intensity Tu and the random measurement uncertainty $\sigma_{\Delta x}$ can be estimated using Equation 3.10 as the fit function. (Scharnowski et al., 2018)

For the hot gas channel in Figure 3.2, a variation of the time between the double images Δt is conducted for a constant operating condition. While the local mean velocity is close to identical for all data sets, the displacement vector and the derived turbulence intensity is dependent on the time between the double images Δt. The turbulence intensity of the x-component along with the mean x-displacement are spatially averaged in a region of interest (ROI) of $-4.0D \leqq x \leqq 0.0D$ and $2.6D \leqq z \leqq 3.0D$. The ROI is chosen as it is upstream of the ejection and sufficiently far from the wall as to be considered independent of upstream ejection effects. Due to the small size, the values for the true turbulence intensity Tu and the random uncertainty $\sigma_{\Delta x}$ in the ROI are expected to be constant in space.

The results of this procedure are presented in Figure 3.7. For the specified ROI, the measured local mean turbulence intensity is plotted along the local mean displacement in x-direction. The vertical error bar represents the standard deviation of the measured turbulence intensity arising in the averaging process in the ROI.

For each Δt, several different evaluations are performed using an increasing final interrogation window size ranging from 8 px to 24 px indicated by a different symbol each. Fitting all data points from identical evaluation procedures according to Equation 3.10 yields the fit parameters $\sigma_{\Delta x}$ and the true turbulence intensity Tu. The fit is indicated by a dashed line and the standard deviation of the displacement $\sigma_{\Delta x}$ is equivalent to the random measurement uncertainty as detailed in subsection 3.3.2. The respective values of $\sigma_{\Delta x}$ and the true turbulence intensity Tu for each data set with identical evaluation procedure are given in Figure 3.7.

For the test section used in the present work, a number of implications on the cross-flow can be made based on the data in Figure 3.7:

- For the selected FOV, the resolution of the camera is insufficient to spatially resolve all turbulent structures even at the smallest possible final interrogation window size of $D_\mathrm{I} = 8\,\mathrm{px} = 0.1D$. Further increasing the final interrogation window size leads to an increased spatial filtering of the flow introducing an even stronger bias towards underpredicted turbulence intensities.
- The decrease in the rate of change in turbulence intensity for $D_\mathrm{I} \leqq 16\,\mathrm{px}$ for large mean displacements $\langle \Delta x \rangle \geq 10\,\mathrm{px}$ suggests an actual true turbulence intensity of approximately

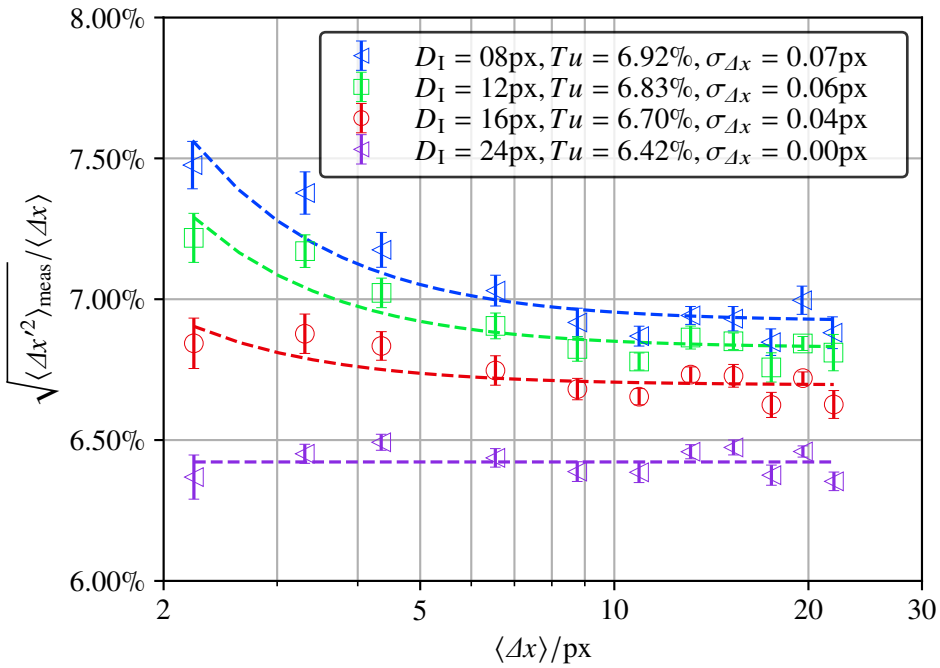

Figure 3.7: Estimated turbulence intensity Tu in the hot gas channel as a function of the mean displacement $\langle \Delta x \rangle$ for different final interrogation window sizes D_I averaged in the ROI $x/D \in -4.0$ to 0.0 and $y/D \in 2.6$ to 3.0

7.1 %. This value is derived by fitting a second-order polynomial function and extrapolating towards $D_I = 0$. In contrast to the findings of Stripf (2007), the target turbulence intensity of 8.2 % based on the design of the turbulence grid according to Roach (1987) (see (1) in Figure 3.2) is not met.

- For $D_I \leqq 16$ px a convergent behaviour towards smaller turbulence intensities is observed with increasing displacements ΔX. The contribution of the random uncertainty to the calculated turbulence intensity reduces with increasing ΔX as the relative error decreases (see Equation 3.10).
- The random uncertainty tends to increase with decreasing final interrogation window size D_I. The maximum random uncertainty determined based on this method is $\sigma_{\Delta x} = 0.07$ px at $D_I = 8$ px for the specified ROI.
- For the largest interrogation window size of $D_I = 24$ px $= 0.3D$, no trend can be observed for a change in the mean displacement. This is most likely because the spatial resolution is insufficient to avoid streamline curvature, violating at least one of the initial assumptions to the approach according to Scharnowski et al. (2018). When the initial assumptions are not fulfilled, the predicted random uncertainty is not meaningful.

By fitting the ”true” turbulence intensities of all final interrogation window sizes in Figure 3.7 using a polynomial of second degree, the bias of spatial filtering remaining for $D_I = 8$ px can be removed to find the closest estimate of the actual true turbulence intensity. In Figure 3.8, the result of this procedure is displayed for various x/D locations in the hot gas channel. For the ROI

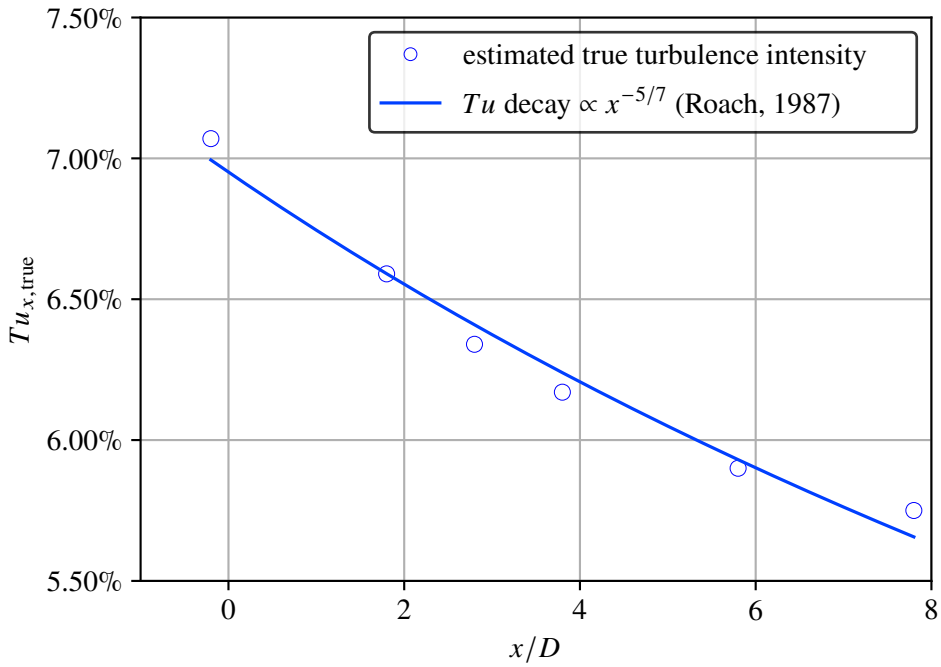

Figure 3.8: Estimated true turbulence intensity with spatial filtering bias removed for multiple streamwise positions in the hot gas channel and comparison to correlation of Roach (1987). The ROI size and y/D position is identical for all streamwise positions.

discussed earlier, the turbulence intensity is 7.1 %. All downstream ROIs are of the same size and at the same y-position. In Figure 3.8, a decay of the turbulence intensity in streamwise direction can be observed. Fitting the turbulence intensity decay using the fit function suggested in Roach (1987) yielded acceptable results. It should be noted that the film cooling ejection is likely influencing the turbulence intensity estimation at the downstream positions. The turbulence intensity decay is expected to be steeper without the influence of the film cooling ejection which would reduce the fitting error.

The interaction between coolant jet and hot gas cross-flow introduces additional turbulent fluctuations of unknown time and length scales. The smallest interrogation window size of 8 px would be preferable due to the higher spatial resolution, but increases the data size and processing time drastically. Additionally, the random uncertainty is higher. Unless specified otherwise, all measurement data in the present work is, therefore, evaluated using a final interrogation window size of $D_\mathrm{I} = 12\,\mathrm{px} = 0.15D$ with an overlap of 50 %, yielding a spatial resolution of 13.3 vec/D in the x-z plane.

Compared to the turbulence intensity estimated based on the correlation provided in Roach (1987) for the turbulence grid used in the present work, the turbulence intensity calculated from the PIV data is 13.4 % lower. In Roach (1987), the correlation is compared to measurement data from previous literature. The level of scatter is not quantified but shows discrepancies of up to approximately ±11 %. Turbulence intensity measurements conducted in Stripf (2007) using hot wire anemometry have shown that for a solidity of 64 % the measured turbulence intensity is sys-

tematically lower by up to approximately 12.5 % compared to the correlation in Roach (1987). Solidities of the turbulence grid greater than 50 % are not recommended in Roach (1987). The solidity of the turbulence grid used in the present work designed in Fraas et al. (2017) is 49.6 %. Given this information, it is plausible to assume that the turbulence intensity calculated from the PIV data in the present work based on the method proposed in Scharnowski et al. (2018) is closer to the true turbulence intensity compared to the estimate based on the correlation in Roach (1987).

3.4 Flow Field Investigations leading up to the Present Work

Aside from the flow field investigations discussed in subsection 2.2.3, a number of studies using SPIV were conducted in the test facility in section 3.1, leading up to the present work. The differences between the measurement data in the present work and that of previous SPIV studies on the same test facility are highlighted in the following and the results of the previous studies are briefly discussed. Some of these results are referred to in the course of the present work.

Stichling et al. (2021) investigated a laidback fan-shaped cooling hole at engine-realistic temperature ratios, turbulence intensities and parallel coolant cross-flow. The same geometry as in the current study was used (see Figure 3.3) but the measurements were limited to the streamwise symmetry plane. No horseshoe vortex Ω_{HV} was observed upstream of the cooling hole. An analysis using a method called Proper Orthogonal Decomposition (POD) suggested a fluctuation of the coolant ejection that was most significant at the lowest blowing ratio. The decreasing sensitivity of the coolant jet, e.g. to disturbances due to the hot gas cross-flow turbulence, towards increasing coolant mass flow is consistent with the observations in Straußwald et al. (2018). Orthogonal coolant cross-flow was not considered in this investigation and other than the absence of the Ω_{HV}, no information on the coherent structures was provided, as no quasi-volumetric data was available.

Stichling and Bauer (2022b) compared results of the same laidback fan-shaped film cooling hole but with a narrower pitch to diameter ratio of $p/D = 3$ to a slot geometry at parallel coolant co-cross-flow and counter-cross-flow, respectively. The coolant mass flow per downstream area was set to be equivalent for corresponding operating points of the different geometries. For the slot geometry, a Ω_{CV} pair with large lateral spreading was present, while for the laidback fan-shaped cooling hole with narrow pitch, no significant secondary flows were observed. No horseshoe vortex Ω_{HV} was present for either of the geometries at any of the investigated operating points. Despite the presence of the Ω_{CV} pair, a much larger adiabatic film cooling effectiveness was observed for the slot geometry compared to the laidback fan-shaped geometry. The ratio of heat transfer coefficients with and without film cooling was higher for the slot geometry compared to the laidback fan-shaped cooling hole. Two lateral maxima in the ratio of heat transfer coefficients with and without film cooling and the adiabatic film cooling effectiveness were observed for the slot, one in proximity of each Ω_{CV}. For the laidback fan-shaped cooling hole, only one peak in lateral direction was present for both the adiabatic film cooling effectiveness and the ratio of heat transfer coefficients with and without film cooling. The higher adiabatic film cooling

effectiveness of the slot cooling hole correlated with a much more stable coolant ejection. For the laidback fan-shaped cooling hole, coolant lumps periodically releasing into the hot gas were observed much like the intermittency of the jet in Schreivogel et al. (2016) and Abram et al. (2016). Orthogonal coolant cross-flow was not considered in this investigation.

For the same laidback fan-shaped film cooling hole as in the present work, Stichling and Bauer (2022a) provided more insights into the unsteady coherent structures observed at engine-realistic operating conditions using the POD. As in Stichling et al. (2021), the measurements were limited to the streamwise symmetry plane. A lateral unsteadiness of the Ω_{CV} pair and shear-layer instabilities as well as lateral fluctuations indicating unsteady Ω_{WV} or hairpin vortices Ω_{HpV} were documented using the spatial POD modes. A frequency analysis of the time coefficients from the POD yielded no definite dominant frequencies. This is in agreement with Zamiri et al. (2020), who conducted a LES for the same laidback fan-shaped cooling hole. Only minor peaks in the frequency analysis were observed. Given these results, it is reasonable to assume that unsteady coherent structures in laidback fan-shaped cooling holes at high hot gas cross-flow turbulence intensities fluctuate over a range of frequencies.

4 Coherent Structures in Film Cooling Flows at Engine-Realistic Operating Conditions

The main goal of this work is to characterise the coherent structures observed in a JiC at engine-realistic operating conditions and understand their relation to the local heat transfer augmentation. Based on the observed steady and unsteady coherent structures, connections between the thermal film cooling quantities[1] and the coherent structures are analysed. The combination of thermal and aerodynamic measurement data provides a valuable reference for validation and further development of numerical flow simulations. Aside from an improved understanding of the flow field of a JiC from a laidback fan-shaped film cooling hole, the present work contributes to the fundamental understanding of the jet morphology and the significant drivers for heat transfer augmentation.

Engine-realistic coolant cross-flow is still frequently neglected in many recent studies on thermal film cooling quantities. This is despite the fact that studies have repeatedly reported the significance of the inlet conditions for the adiabatic film cooling effectiveness and the ratio of heat transfer coefficients with and without film cooling (Saumweber et al., 2001; Gritsch et al., 2003; Saumweber and Schulz, 2008a, 2012; Fraas et al., 2019a). In terms of flow field investigations, the scarcity is prevalent with nearly no contributions considering coolant cross-flow, except for Hale et al. (2000), Peterson and Plesniak (2002), Peterson (2003), Peterson and Plesniak (2004), and McClintic et al. (2019). The present work aims at providing a detailed flow field analysis maintaining all relevant engine-realistic parameters, including coolant cross-flow.

As laid out in section 3.2, 12 different cases are considered, six at parallel coolant cross-flow (PF) and six at orthogonal coolant cross-flow (OF). Depending on the blowing ratio BR and coolant channel Reynolds number $Re_{D,\mathrm{cc}}$, the resulting absolute values of the dimensionless parameters described in subsection 2.2.2 vary. In Table 4.1, an overview of the nominal dimensionless parameters relevant to the subsequent discussions are shown. All of them are calculated for the cylindrical part of the cooling hole based on the quantities provided in Table 3.1.

[1]The thermal film cooling quantities are the adiabatic film cooling effectiveness and the ratio of heat transfer coefficients with and without film cooling, as described in subsection 2.2.1

Table 4.1: Evaluated dimensionless parameters of the test section in Figure 3.2 for all test cases. The values are valid for both, parallel and orthogonal coolant cross-flow, as the cross-flow direction does not impact the nominal dimensionless parameters.

BR	IR	VR	$VR_{\mathrm{inlet}} = u_{\mathrm{cc}}/u_{\mathrm{c}}$		$u_{\mathrm{cc}}/u_{\mathrm{h}}$	
			$Re_{D,\mathrm{cc}}$	5×10^3	$30{\times}10^3$	5×10^3	$30{\times}10^3$
1.0	0.59	0.59		0.26	1.58		
2.0	2.35	1.18		0.13	0.78	0.15	0.92
3.0	5.29	1.76		0.09	0.51		

Since the dimensionless parameters are independent of the coolant channel cross-flow direction, a maximum of six different values results for each dimensionless parameter. The nominal dimensionless parameters blowing ratio BR, momentum ratio IR and velocity ratio VR at the cooling hole exit are independent of the coolant channel Reynolds number $Re_{D,\mathrm{cc}}$ resulting in just three values each. Flow separations and other steady and unsteady flow phenomena in the cooling hole impact the effective local values of these quantities. As an example, a strong single-sided flow separation in the diffuser could dramatically increase the local velocity ratio VR_{local} in the unblocked diffuser area. As the blowing ratio, the momentum ratio and the velocity ratio are interdependent, the true local values of each of these quantities varies correspondingly. A local over-prediction is, for example, accompanied by a local under-prediction of the dimensionless parameters in opposing parts of the diffuser exit cross section.

The inlet velocity ratio VR_{inlet} is a less frequently reported dimensionless parameter as most studies disregard inlet effects entirely by using plenum conditions, likely due to the experimental effort. The inlet velocity ratio VR_{inlet} is defined as the ratio of the coolant channel air velocity upon the coolant air velocity, $u_{\mathrm{cc}}/u_{\mathrm{c}}$. It is naturally dependent on the coolant channel Reynolds number and the blowing ratio BR. The ratio of cooling channel air velocity and hot gas cross-flow velocity $u_{\mathrm{cc}}/u_{\mathrm{h}}$ is only dependent on the cooling channel air Reynolds number $Re_{D,\mathrm{cc}}$.

In the following sections, the characteristics of the coherent structures are discussed for all configurations and operating conditions listed in Table 3.1. Furthermore, a detailed analysis of the relation between the local coherent structures and the local ratio of heat transfer coefficients with and without film cooling is conducted.

4.1 Fundamental Differences in the Jet Morphology between Parallel and Orthogonal Coolant Cross-Flow

As discussed in section 2.1 and summarised in Figure 2.1a, the steady coherent structures frequently observed in a generic JiC are the counter-rotating vortex pair (Ω_{CV} pair) and the horseshoe vortex (Ω_{HV}). In certain cases, they are complemented by an anti-counter-rotating vortex pair (Ω_{ACV} pair), a ring vortex (Ω_{RV}) and in rare cases by a steady wake vortex pair (Ω_{sWV} pair). In the following, the coherent structures observed for the parallel and orthogonal coolant cross-flow configuration at two different coolant channel Reynolds numbers $Re_{D,\mathrm{cc}} = 5 \times 10^3$ and 30×10^3 and three different blowing ratios $BR = 1.0,\ 2.0$ and 3.0 each, are discussed. As shown in Figure 3.3, the cooling hole geometry has a cylindrical hole inlet connected to a diffuser-shaped exit with opening angles of 10° in lateral and streamwise direction and an overall inclination angle of 35°. This laidback fan-shaped (LFH) cooling hole geometry significantly differs from the generic cylindrical hole with 90° inclination considered in all of the fundamental JiC research. A large portion of the experimental flow field investigations conducted for film cooling applications is related to inclined cylindrical holes. It is, therefore, a reasonable assumption that the observed steady and unsteady flow structures differ compared to what is described in section 2.1.

In the following sections, the coherent structures observed for all PF and OF cases are discussed.

The focus is on which coherent structures are observed, how they are formed and how they are related to the trends observed in the thermal film cooling quantities based on the data in Fraas et al. (2019a) and Fraas (2019).
To provide a basic intuition of the time-averaged jet morphology for all PF and OF cases, an iso-surface of the turbulent kinetic energy normalised by the kinetic energy of the hot gas cross-flow ($k_t/\left(0.5u_{ref}^2\right) = 2.5\,\%$) is visualised in Figure 4.1 and 4.2 for all PF and OF cases, respectively. It should be mentioned that iso-surfaces based on the Q-criterion are qualitatively similar. However, coherent structures of the hot gas cross-flow turbulence cause additional 'noise' that blurs

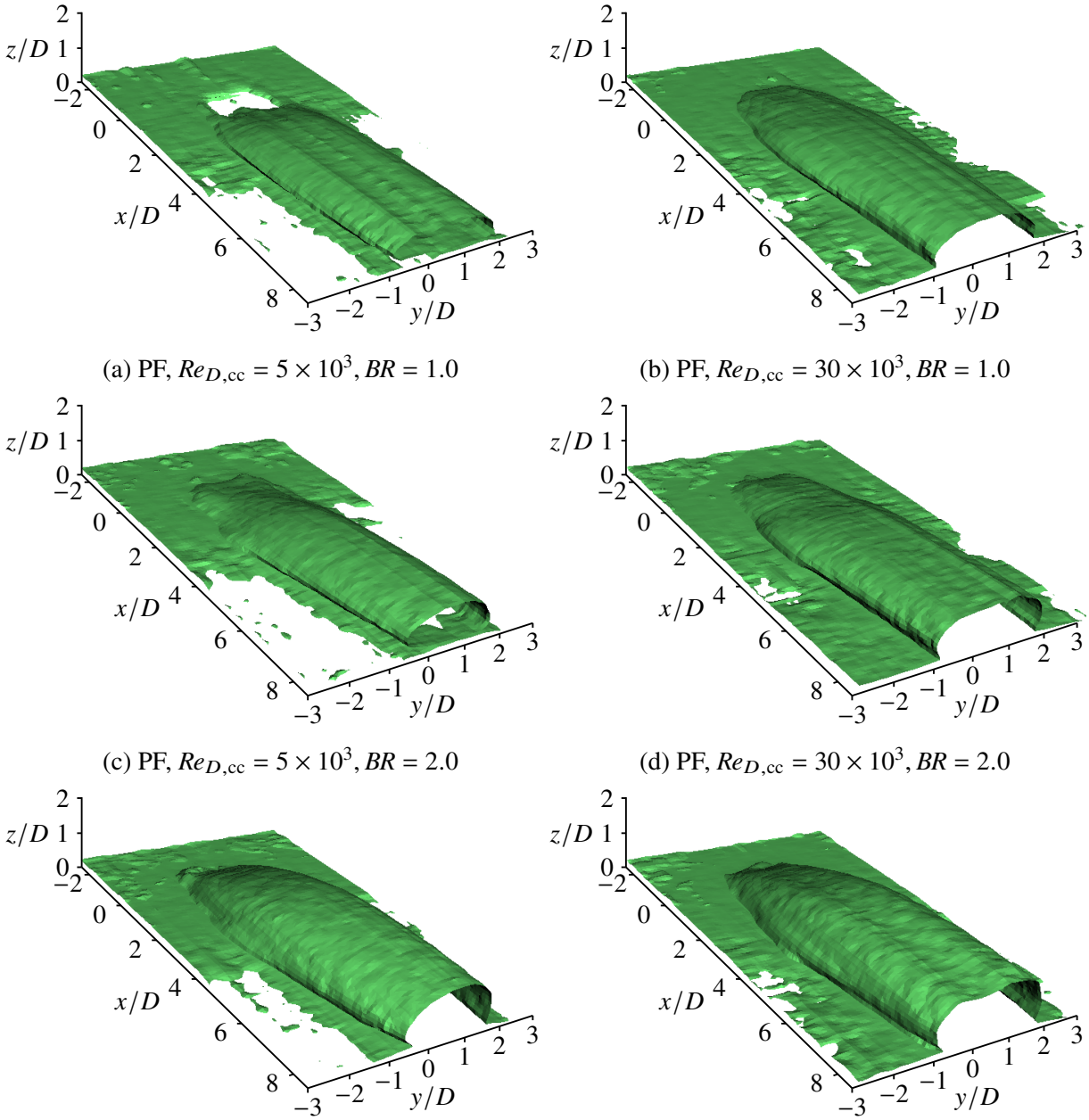

(a) PF, $Re_{D,cc} = 5 \times 10^3$, $BR = 1.0$

(b) PF, $Re_{D,cc} = 30 \times 10^3$, $BR = 1.0$

(c) PF, $Re_{D,cc} = 5 \times 10^3$, $BR = 2.0$

(d) PF, $Re_{D,cc} = 30 \times 10^3$, $BR = 2.0$

(e) PF, $Re_{D,cc} = 5 \times 10^3$, $BR = 3.0$

(f) PF, $Re_{D,cc} = 30 \times 10^3$, $BR = 3.0$

Figure 4.1: Iso-surfaces of normalised turbulent kinetic energy $k_t/\left(0.5u_{ref}^2\right) = 2.5\,\%$ for parallel coolant cross-flow configuration

the actual jet morphology when using the Q-criterion. Hence, k_t is chosen instead. The specific value of the normalised turbulent kinetic energy was chosen as $k_t/\left(0.5u_{ref}^2\right) = 2.5\,\%$ and provides a characteristic representation of the jet morphology. The blowing ratio BR increases from top to bottom and the coolant channel Reynolds number $Re_{D,cc}$ increases from left to right.
While the coolant jet remains relatively symmetric for all PF cases (Figure 4.1), strong and varying asymmetries can be observed for the OF cases (Figure 4.2). This is in good qualitative agreement with the symmetry and asymmetry observed in the adiabatic film cooling effective-

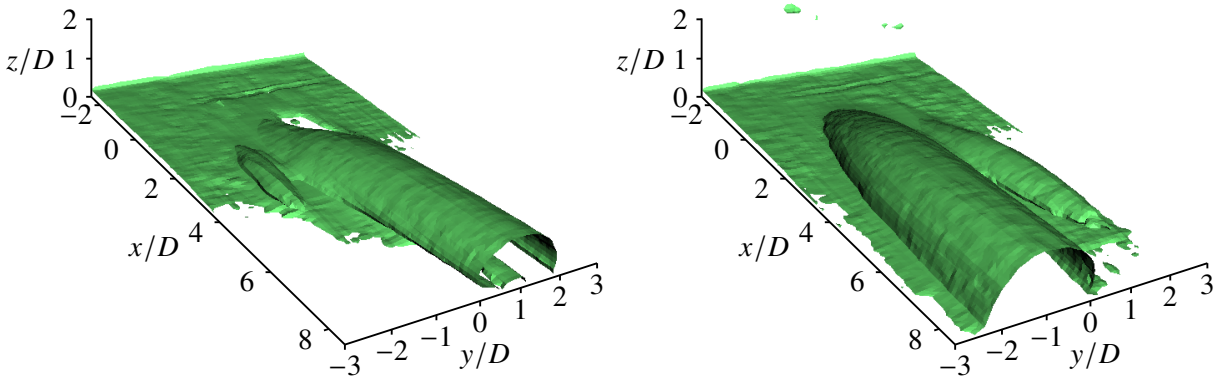

(a) OF, $Re_{D,cc} = 5 \times 10^3$, $BR = 1.0$

(b) OF, $Re_{D,cc} = 30 \times 10^3$, $BR = 1.0$

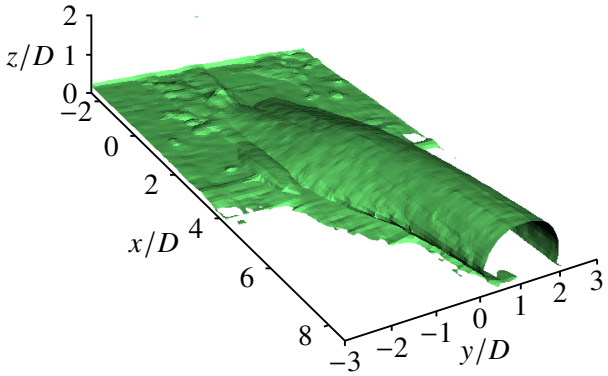

(c) OF, $Re_{D,cc} = 5 \times 10^3$, $BR = 2.0$

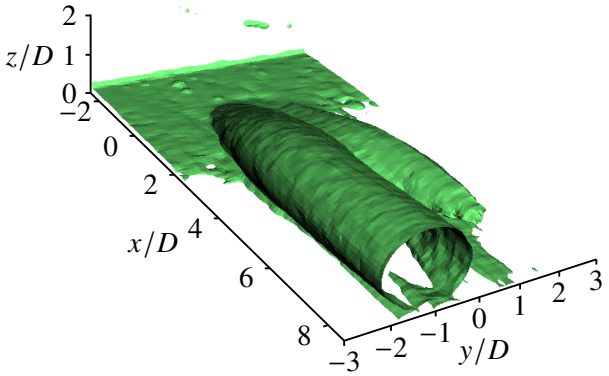

(d) OF, $Re_{D,cc} = 30 \times 10^3$, $BR = 2.0$

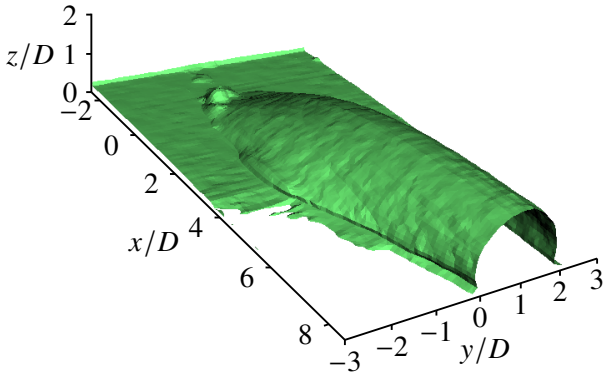

(e) OF, $Re_{D,cc} = 5 \times 10^3$, $BR = 3.0$

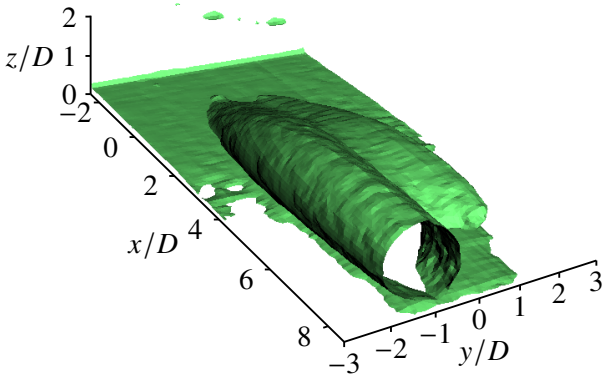

(f) OF, $Re_{D,cc} = 30 \times 10^3$, $BR = 3.0$

Figure 4.2: Iso-surfaces of normalised turbulent kinetic energy $k_t/\left(0.5u_{ref}^2\right) = 2.5\,\%$ for orthogonal coolant cross-flow configuration. Coolant cross-flow direction is in negative y/D direction.

ness distributions in Fraas (2019) (for details, see Figure A.37 and A.40). For all PF and OF cases, the coolant appears attached to the wall. This is confirmed by the spatial distributions of the adiabatic film cooling effectiveness, where no interruption of the cooling film can be observed immediately downstream of the cooling hole exit (Fraas et al., 2019a; Fraas, 2019). The overall morphology of the jet is much flatter for the PF cases, especially at the low coolant channel Reynolds number. For the OF cases, the jet is more circular and a drastic change in jet appearance can be observed from low to high coolant channel Reynolds number.

While the iso-surfaces already provide a generic idea of the jet morphology and penetration depth[2] of the different PF and OF cases, a more detailed analysis of the coherent structures is necessary. This is required to understand the local relation between the coherent structures and the thermal film cooling quantities which, in turn, allows for targeted improvements of the film cooling hole geometries and operating conditions.
For this purpose, the near and far field of the JiC have to be investigated. Thereby, not only the dominant coherent structures are characterised, but their formation process is analysed as well. At engine-realistic operating conditions, the hot gas cross-flow is expected to quickly divert the coolant jet and the corresponding dominant coherent structures in hot gas main stream direction. Therefore, z-planes parallel to the wall and close to the cooling hole exit are suitable to analyse the near field. For the far field, x-planes orthogonal to the hot gas cross-flow direction downstream of the cooling hole exit are suitable.

To get meaningful data in the x- and z-planes, the data acquisition detailed in subsection 3.3.1 has to be briefly revisited. As schematically shown in Figure 3.4, the FOV of the SPIV measurement is a y-plane. This FOV is chosen as the dominant hot gas cross-flow velocity component is in x-direction. Compared to measuring in the x- or z-plane the relative error of the measurement is reduced as a larger mean particle image displacement is permitted while still minimizing the in-plane loss of particle image pairs. An acceptable spatial resolution in lateral direction in the desired x- and z-planes is achieved by laterally traversing the camera and laser setup with a step length of $\Delta y = 0.25D$ as indicated in Figure 3.4. Based on the thermal film cooling quantities provided in Fraas et al. (2019a), the volume of view (VOV) is chosen as $-3D \leqq y \leqq 3D$, covering slightly less than a full cooling hole pitch. Given the number of cases, further increasing the lateral spatial resolution or measurement range entails a disproportionately longer measurement time and an unfeasible increase in data storage space requirements and raw data processing time.
As will be demonstrated in the subsequent discussions, the selected VOV and lateral resolution is more than sufficient to capture the vortical structures in the interaction region of hot gas cross-flow and coolant jet.

The subsequent analysis contains a variety of figures containing in-plane velocity vectors. It should be noted that the vector resolution is reduced by a factor of 2 to 3 compared to the available spatial resolution depending on the specific figure to improve legibility. Beyond the details on

[2]The penetration depth describes the Euclidean distance of the jet core to the adjacent wall. However, no singular definition of the jet core for film cooling JiCs exists. Frequently, the penetration depth is quantified based on the jet centre streamline (see Figure 2.1) or, if temperature field data is available, based on the location in the JiC with the lowest temperature.

the out-of-plane resolution provided above, the reader is referred to subsection 3.3.1 and 3.3.3 for detailed information on the spatial and temporal in-plane resolution of individual measurement planes.

4.2 Coherent Structures with Parallel Coolant Cross-Flow

In the following sections, the coherent structures observed in the far field of the coolant JiC are explored to understand the most dominant secondary flow features downstream of the ejection. The near field is analysed to understand how it influences the formation process of the far field structures and to explore additional near field structures. Finally, the adiabatic film cooling effectiveness and the ratio of heat transfer coefficients with and without film cooling are included in this analysis to understand the connection between the coherent flow structures and the thermal film cooling quantities.

4.2.1 Far Field Coherent Structures

In Figure 4.3 and 4.4, the time-averaged lateral and wall-normal velocity components are shown in an x-plane at $x/D = 5.0$ with a background contour of normalised x-vorticity ω_x for the low and high coolant channel Reynolds number $Re_{D,\mathrm{cc}}$, respectively. The location of the reference velocity u_{ref} used for normalisation is indicated in Figure 3.2. The white iso-line of turbulent kinetic energy corresponds to the respective iso-surface depicted in Figure 4.1. The black lines below the horizontal axis indicate the downstream edges of the cooling hole exit geometry. The blue line represents the lateral distribution of the ratio of heat transfer coefficients with and without film cooling h_{f}/h_0 at $x/D = 5.0$ based on data from Fraas (2019). The x-axis corresponds to $h_{\mathrm{f}}/h_0 = 1.0$. For the first part of the discussion, the focus is on the velocity and vorticity field, and h_{f}/h_0 can be ignored.

The relatively dominant steady coherent structure observed for all PF cases in Figure 4.3 and 4.4 is the Ω_{CV} pair. In x-planes further upstream in the flow (not shown), it can be seen that the Ω_{CV} pair starts to develop closely downstream of the hole and near to the lateral edges of the hole exit. For the low coolant channel Reynolds number, the Ω_{CV} pair develops slightly earlier compared to the high coolant channel Reynolds number and is generally initiated earlier towards higher blowing ratios. The same trend with a change in blowing ratio is observed for the high coolant channel Reynolds number but less pronounced.
The lateral and wall-normal position of the Ω_{CV} legs varies depending on the coolant channel Reynolds number, the blowing ratio and the streamwise position. An increase in blowing ratio or downstream distance correlates with a slight increase in wall-normal distance of the Ω_{CV} legs for all PF cases. This increase is significantly more pronounced for $BR = 3.0$ and $Re_{D,\mathrm{cc}} = 30 \times 10^3$ (Figure 4.4c). A change in coolant channel Reynolds number, however, generally yields a much stronger change in the position of the Ω_{CV} legs, specifically in lateral direction. In case of the low coolant channel Reynolds number (Figure 4.3), the Ω_{CV} legs are significantly further apart (e.g. at $BR = 1.0$: $y/D \approx \pm 1.0$ for $Re_{D,\mathrm{cc}} = 5 \times 10^3$ versus $y/D \approx \pm 0.5$ for $Re_{D,\mathrm{cc}} = 30 \times 10^3$).

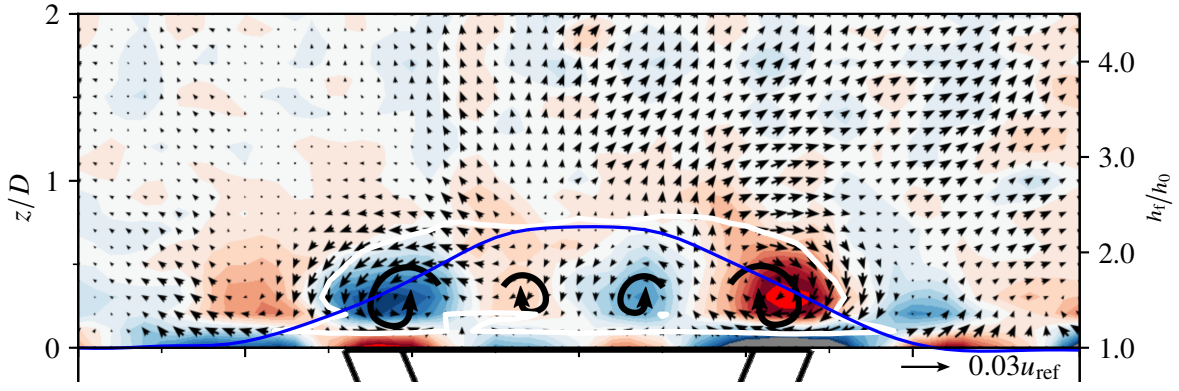

(a) PF, $Re_{D,\mathrm{cc}} = 5 \times 10^3$, $BR = 1.0$

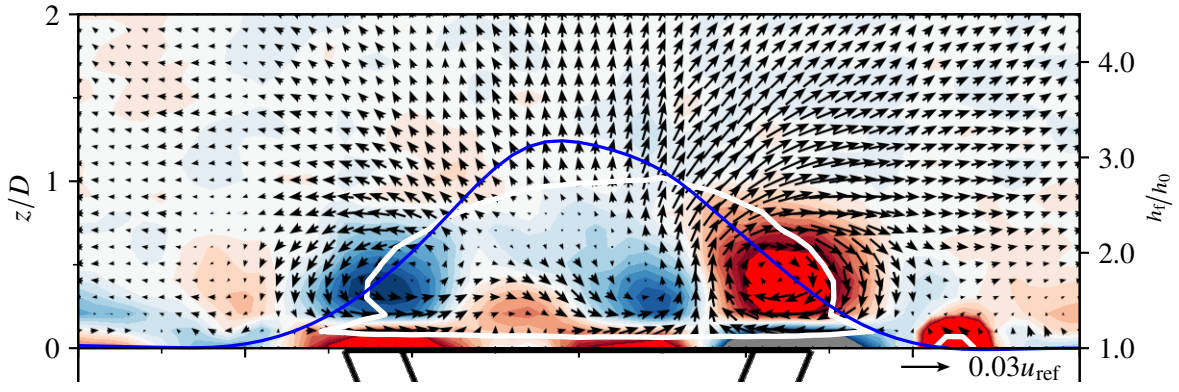

(b) PF, $Re_{D,\mathrm{cc}} = 5 \times 10^3$, $BR = 2.0$

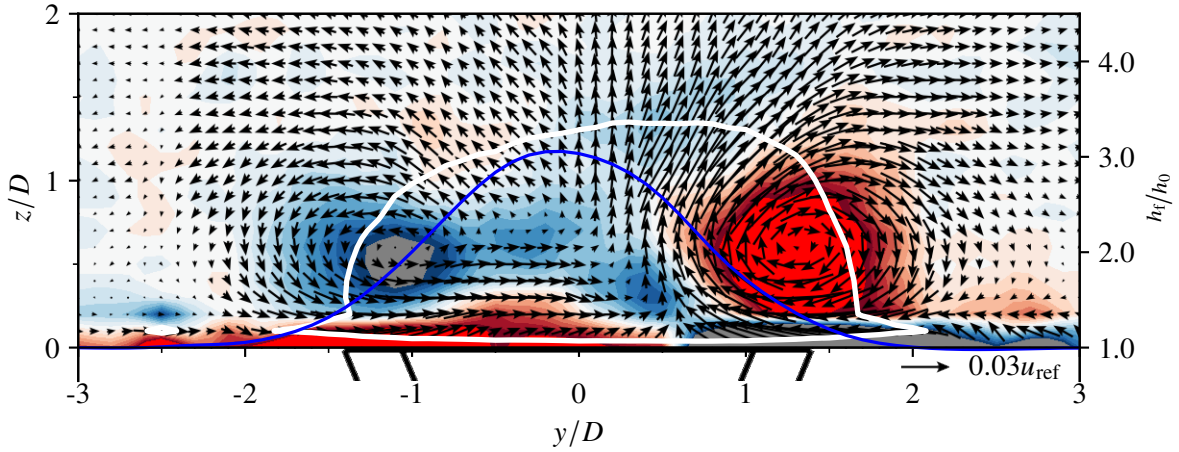

(c) PF, $Re_{D,\mathrm{cc}} = 5 \times 10^3$, $BR = 3.0$

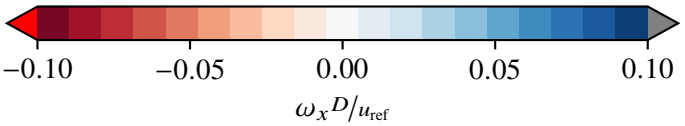

Figure 4.3: Steady coherent flow structures and their relation to h_f/h_0 at $x/D = 5.0$ and $Re_{D,\mathrm{cc}} = 5 \times 10^3$. White iso-line corresponds to the iso-surface of k_t shown in Figure 4.1.

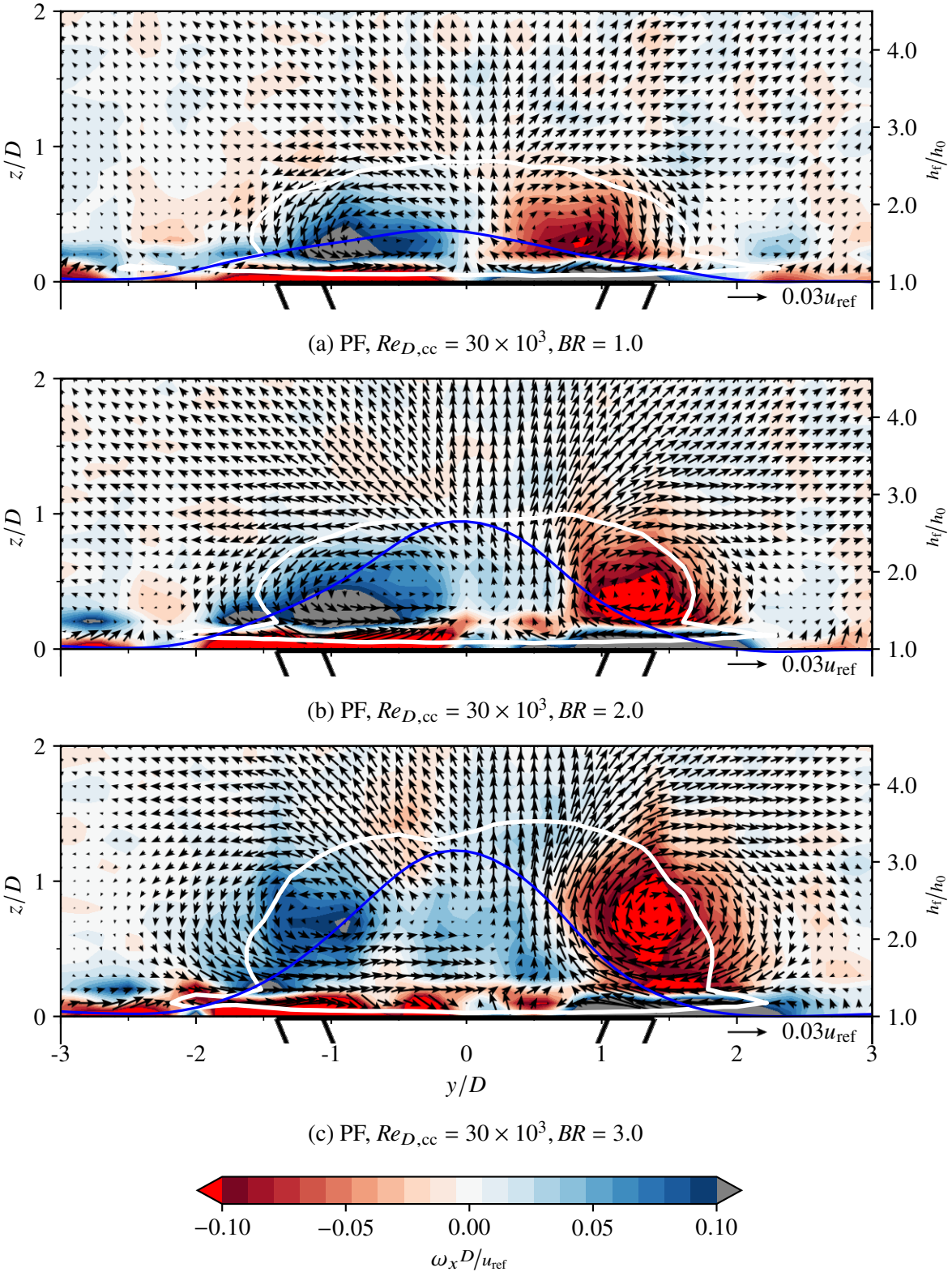

(a) PF, $Re_{D,\mathrm{cc}} = 30 \times 10^3$, $BR = 1.0$

(b) PF, $Re_{D,\mathrm{cc}} = 30 \times 10^3$, $BR = 2.0$

(c) PF, $Re_{D,\mathrm{cc}} = 30 \times 10^3$, $BR = 3.0$

Figure 4.4: Steady coherent flow structures and their relation to h_f/h_0 at $x/D = 5.0$ and $Re_{D,\mathrm{cc}} = 30 \times 10^3$. White iso-line corresponds to the iso-surface of k_t shown in Figure 4.1.

An additional anti-counter-rotating vortex pair (Ω_{ACV} pair) is found in between the dominant Ω_{CV} pair for all cases of the low coolant channel Reynolds number. For clarification, the Ω_{CV} and Ω_{ACV} pair are exemplarily indicated by black arrows in Figure 4.5a for the low blowing ratio, where the Ω_{ACV} pair is most significant. In previous flow field investigations, an Ω_{ACV} pair was induced using a vortex generator to achieve an increased lateral spreading (Song et al., 2017). Brittingham and Leylek (1997) suggested that the lift produced by the interaction of the two Ω_{CV} legs is hindered by the increased spreading. The reduced spreading and the absence of the Ω_{ACV} pair for the high coolant channel Reynolds number, therefore, explain the increased wall-normal distance of the Ω_{CV} legs for these PF cases (Figure 4.4). Whether the Ω_{ACV} pair is the reason for the larger lateral spreading or develops because of it, is discussed in the subsequent section about the near-field structures.

As indicated by the unit vectors in Figure 4.3 and 4.4, the secondary flow velocities of the dominant coherent structures observed in the x-planes contain approximately 1 % to 5 % of the cross-flow reference velocity u_{ref}. In all PF cases, except for the high blowing ratio $BR = 3.0$ at the high coolant channel Reynolds number, the Ω_{CV} pair dissipates nearly entirely within the PIV VOV until $x/D \approx 8.8$ (not shown). Nearly no significant x-vorticity ω_x remains visible for the applied value range (not shown).

4.2.2 Near Field Coherent Structures

To better understand the Ω_{CV} and Ω_{ACV} pair formation and to provide insights into the flow field at the hole exit in a laidback fan-shaped film cooling jet at engine-realistic operating conditions, the velocity and x-vorticity fields in a z-plane parallel to the wall are analysed. In Figure 4.5 and 4.6, the normalised x-vorticity field is shown at $z/D = 0.3$ for $BR = 1.0$ and 3.0, respectively, for the low and high coolant channel Reynolds number each. This plane is chosen, since the qualitative data does not change for $0.1 \leq z/D \leq 0.3$, but the vorticity fields are significantly less noisy at $z/D = 0.3$. The corresponding data for $BR = 2.0$ is qualitatively similar to $BR = 1.0$ and can be found in Figure A.11.
In all figures, the in-plane velocity components are indicated by black arrows. The undisturbed, laterally averaged streamwise component of the hot gas cross-flow velocity upstream of the ejection $u_{ref,z}$ at the wall-normal location $z/D = 0.3$ is subtracted from the local streamwise velocity component $u(x, y)$. Thereby, the local impact of the coolant ejection on the hot gas cross-flow is emphasised.

To understand the origin of the x-vorticities and, by extension, the Ω_{CV} pair formation, additional information on the local velocities is required. Therefore, white iso-lines in Figure 4.5 and 4.6 qualitatively indicate contours of wall-normal velocity. A detailed overview of the velocity distributions close to the hole exit at $z/D = 0.3$ are provided in section A.2, A.3 and A.4 for the u, v and w velocity components.
As specified in Table 4.1, the nominal dimensionless parameters at the cooling hole exit are constant despite a change in coolant channel Reynolds number. The local velocity distributions at the hole exit, however, vary strongly depending on the coolant channel Reynolds number and the nominal blowing ratio, altering the effective dimensionless hole exit parameters.

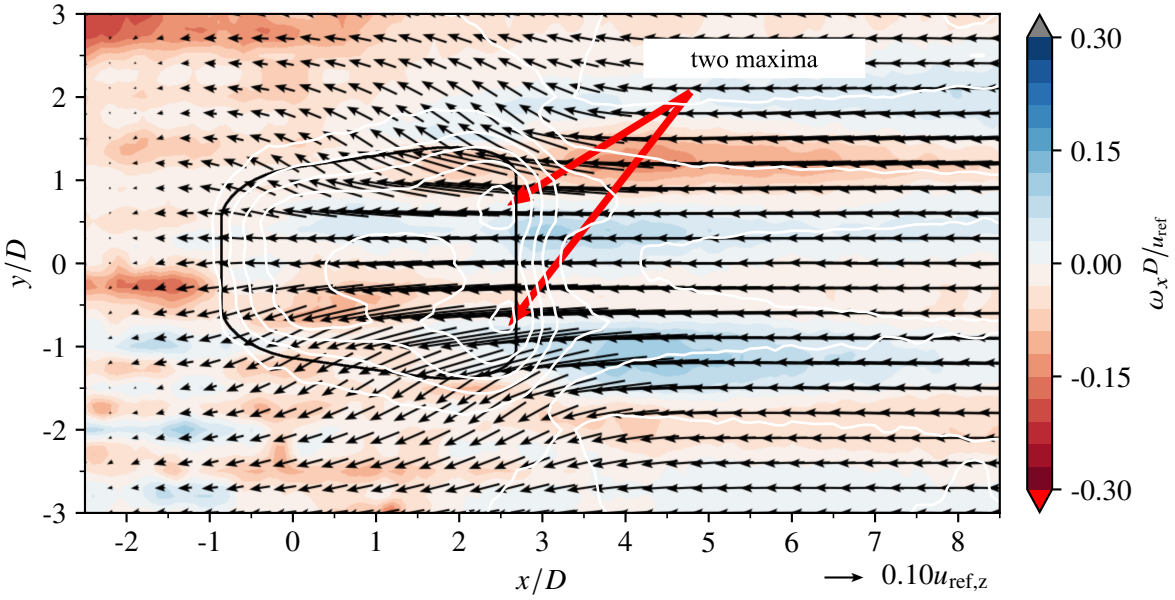

(a) PF, $Re_{D,\mathrm{cc}} = 5 \times 10^3$, $BR = 1.0$

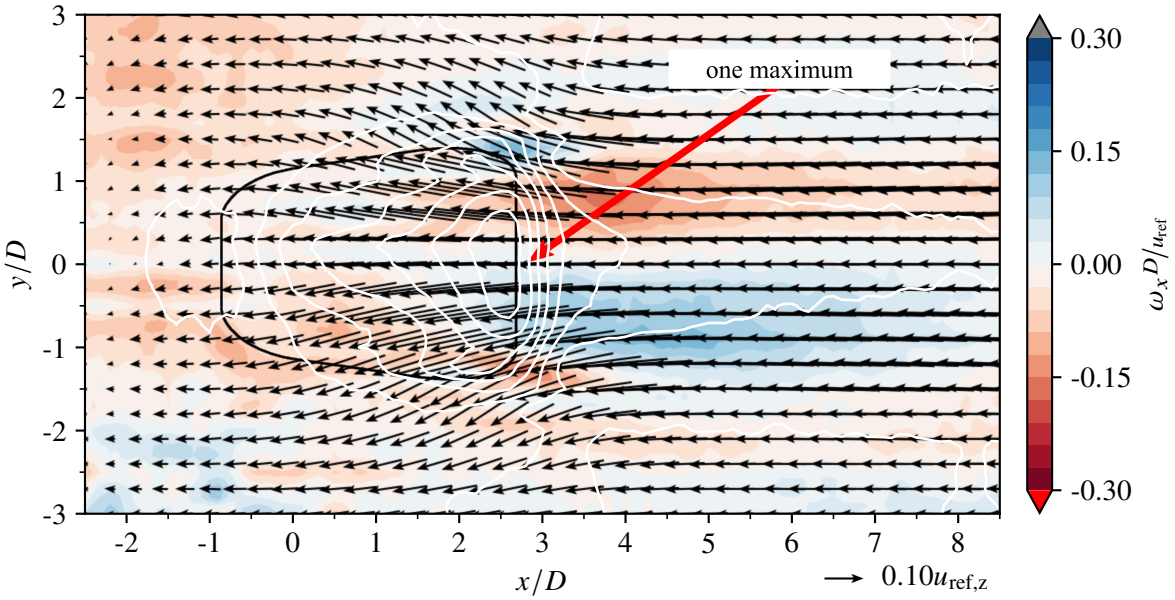

(b) PF, $Re_{D,\mathrm{cc}} = 30 \times 10^3$, $BR = 1.0$

Figure 4.5: Impact of the coolant ejection on the near-wall x-vorticity, ω_x, and in-plane velocity field, $\left(\left(u - u_{\mathrm{ref,z}}\right), v\right)$, at $z/D = 0.3$. The white lines correspond to the contours of wall-normal velocity (for details see Figure A.7 and A.9).

For the low coolant channel Reynolds number at $BR = 1.0$ (see Figure 4.5a or A.7a), comparatively homogeneous wall-normal velocities are observed over the entire cooling hole exit. Two weak local velocity maxima are observed close to the downstream edge of the hole exit at $y/D = \pm 0.75$. For an increase in nominal blowing ratio to $BR = 2.0$, these local maxima are still present (see Figure A.8a), but two additional and more significant local maxima of the wall-normal velocity develop near the upstream edge of the cooling hole exit. At the highest blowing

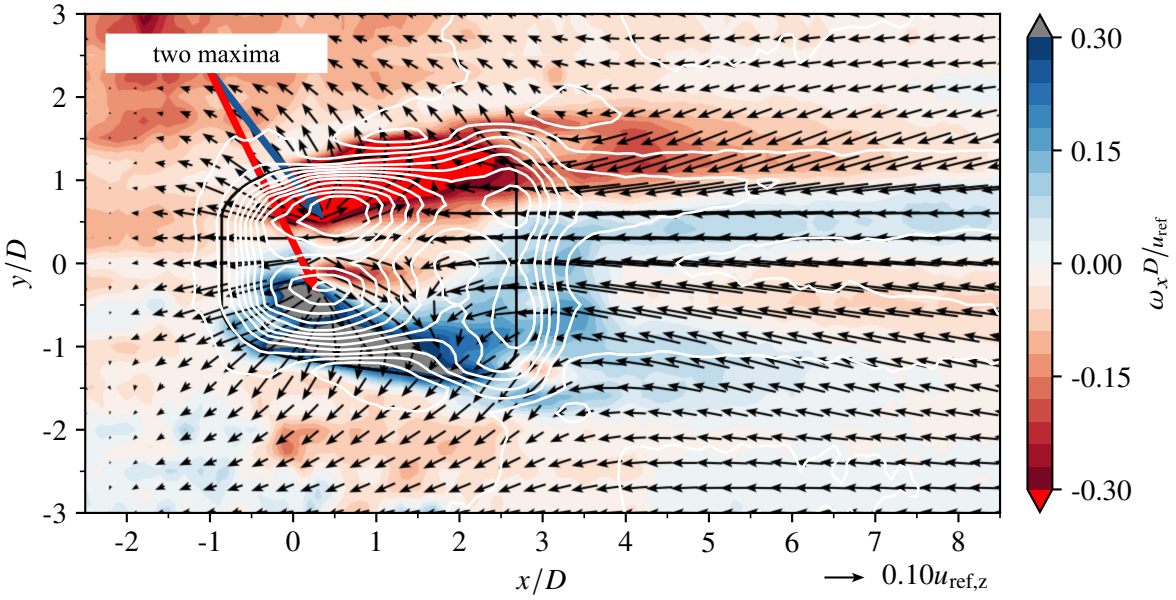

(a) PF, $Re_{D,\mathrm{cc}} = 5 \times 10^3$, $BR = 3.0$

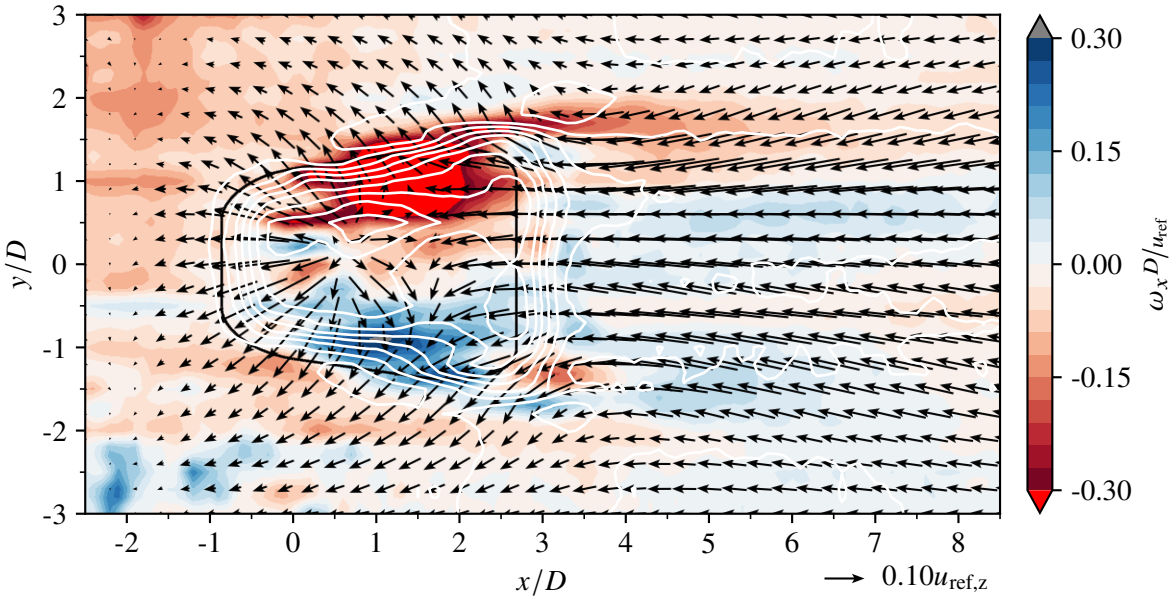

(b) PF, $Re_{D,\mathrm{cc}} = 30 \times 10^3$, $BR = 3.0$

Figure 4.6: Impact of the coolant ejection on the near-wall x-vorticity, ω_x, and in-plane velocity field, $\left(\left(u - u_{\mathrm{ref,z}}\right), v\right)$, at $z/D = 0.3$. The white lines correspond to the contours of wall-normal velocity (for details see Figure A.7 and A.9).

ratio $BR = 3.0$ (see Figure 4.6a and A.9a), the two local maxima close to the upstream edge become even more dominant compared to the much weaker local maxima downstream.
For the high coolant channel Reynolds number and $BR = 1.0$ (see Figure 4.5b or A.7b), a clear global maximum of wall-normal velocity is observed close to the downstream edge of the hole exit. Towards higher blowing ratios at $BR = 2.0$ (see Figure A.8b), the single maximum splits into two distinct local maxima and at the highest blowing ratio $BR = 3.0$ (see Figure 4.6b or

A.9b) a wall-normal velocity distribution similarly homogeneous as for the low coolant channel Reynolds number at $BR = 1.0$ is achieved.

A schematic overview of possible inlet flow phenomena explaining the observed velocity distributions close to the cooling hole exit for all PF cases is given in Figure 4.7. The relevant scaling parameter is the inlet velocity ratio VR_{inlet}. Assuming no swirl in the hole given parallel coolant cross-flow, an increase in inlet velocity ratio VR_{inlet} from (1) to (3) for $Re_{D,\text{cc}} = 5 \times 10^3$ (left column) leads to a decrease in the downstream separation at the hole inlet. Further increasing the inlet velocity ratio VR_{inlet} from (3) to (6) for $Re_{D,\text{cc}} = 30 \times 10^3$ (right column) leads to an increasingly significant upstream separation at the hole inlet. The respective location of the velocity maximum at the inlet of the diffuser contributes to the streamwise position of the ve-

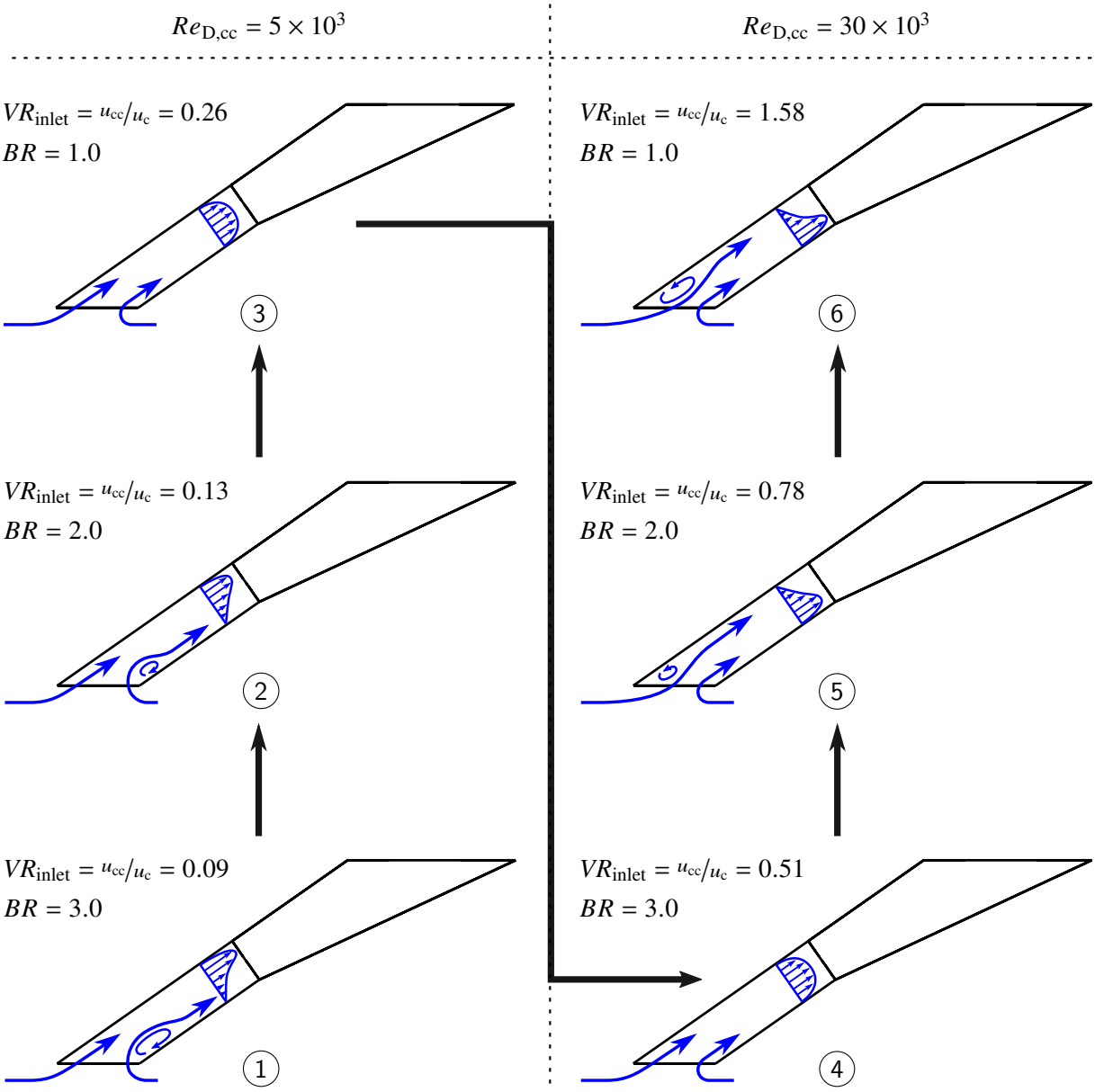

Figure 4.7: Possible inlet flow phenomena for the PF configuration based on the local hole exit velocities observed in Figure A.4 to Figure A.9.

locity maxima at the diffuser exit. From (1) to (6), the location of the global velocity maximum transitions from the upstream to the downstream region of the diffuser exit.
For a cylindrical cooling hole, Thole et al. (1997) similarly show the influence of the position of the inlet flow separation on the hole exit velocity field. Using LES, Acharya and Leedom (2012) replicate this flow phenomenon for cylindrical cooling holes achieving good agreement with comparable experimental data. The SPIV measurement data in the present work, hence, constitutes a valuable data basis for validation of numerical simulations of laidback fan-shaped film cooling holes.

Combined with the local streamwise and wall-normal velocity distributions for the different PF cases, the resulting x-vorticity fields in Figure 4.5 and 4.6 provide insights into what drives the Ω_{CV} pair formation for the different PF cases.
As previously discussed, the Ω_{CV} legs show significant differences in lateral and wall-normal position for the low blowing ratio $BR = 1.0$ when comparing low and high coolant channel Reynolds number (compare Figure 4.3a and 4.4a). As indicated by the white contour lines in Figure 4.5, two local maxima in the wall-normal velocity w are present for the low coolant channel Reynolds number. For the high coolant channel Reynolds number, a single global maximum is observed. In both cases, the maxima are located towards the downstream edge of the cooling hole exit. Multiple maxima in wall-normal velocity essentially constitute separate jet cores.
For the low coolant channel Reynolds number, it appears that each jet core located at $y/D = \pm 0.75$ and $x/D = 2.5$ is accompanied by its own Ω_{CV} pair. This is indicated by the laterally alternating x-vorticities observed in Figure 4.5a around and downstream of each jet core. The inner legs of both Ω_{CV} pairs seem to attenuate each other and are perceived as a comparatively weak Ω_{ACV} pair in the x-plane observed in Figure 4.3a.
The initial observation of a delay in the Ω_{CV} pair formation for the high compared to the low coolant channel Reynolds number can now be explained. As mentioned in the discussion of Figure 4.7, the in-hole velocity maximum is shifted in hot gas downstream direction for all cases with high coolant channel Reynolds number compared to the low coolant channel Reynolds number at the same blowing ratio. Irrespective of whether one or two lateral jet cores are present, and irrespective of the formation process, for the high coolant channel Reynolds number the formation of the Ω_{CV} pair starts around the jet core and is, hence, shifted in downstream direction as well.
For the high coolant channel Reynolds number, the single jet core centred at $y/D = 0$ and $x/D = 2.5$ initiates a single Ω_{CV} pair with reduced spreading as seen in Figure 4.4a. For the high blowing ratio $BR = 3.0$, the differences in lateral and wall-normal position of the Ω_{CV} pair for the low and high coolant channel Reynolds number are much less pronounced (compare Figure 4.3c and 4.4c). As previously discussed, the wall-normal distance of the Ω_{CV} legs in downstream direction increases more for the high compared to the low coolant channel Reynolds number. This is due to the reduced lateral spreading at the high coolant channel Reynolds number.

A deciding factor for the formation and downstream location of the dominant coherent structures in the x-plane is the effective local velocity ratio VR_{local} at the cooling hole exit. As discussed in section 2.1, Mahesh (2013) shows that $VR_{local} \approx 1.0$ is a critical velocity ratio, below or above which the observed coherent structures for JiCs and their formation may change. As the nominal

VR is calculated based on the cylindrical part of the cooling hole, the effective local velocity ratio at the hole exit of the laidback fan-shaped hole is expected to be smaller.

For $BR = 1.0$, the nominal velocity ratio is $VR = 0.59 \leq 1.0$. As indicated by the in-plane velocity vectors in Figure 4.5, the exiting coolant jet leads to a deceleration of the approaching cross-flow velocity $u_{\mathrm{ref,z}}$ across the entire hole exit area, irrespective of the coolant channel Reynolds number.
For $BR = 2.0$, despite a nominal velocity ratio of $VR = 1.18 \geq 1.0$, the velocity and x-vorticity field (see Figure A.14) is qualitatively similar compared to $BR = 1.0$. Again, a deceleration of the approaching cross-flow across the entire hole exit is observed for both coolant channel Reynolds numbers.
As described in Figure 2.2, unsteady hairpin vortices can form at low velocity ratios $VR \leq 1.0$ when the boundary layer vorticity of the cross-flow dominates the jet. The observed Ω_{CV} and Ω_{ACV} pair at $BR = 1.0$ and 2.0 are, in fact, most likely the steady remainder in the x-plane of unsteady hairpin vortices shedding either across the single, or the double jet core at the cooling hole exit. Tyagi and Acharya (2003) and Fawcett et al. (2013) reported similar observations for numerical and experimental investigations, respectively, for a laidback fan-shaped film cooling hole at low velocity ratios.

For $BR = 3.0$, regions with $VR_{\mathrm{local}} > 1.0$ are present at the cooling hole exit for both coolant channel Reynolds numbers. Significant x-vorticities are observed to emerge from within the cooling hole as shown in Figure 4.6. In both cases, the in-hole vorticity is oriented such that it supports or even initiates the Ω_{CV} pair formation. For both blowing ratios, an acceleration of the hot gas cross-flow due to the coolant ejection can be observed in the downstream vicinity of the respective jet cores, suggesting local velocity ratios $VR_{\mathrm{local}} > 1.0$.
For the low coolant channel Reynolds number (Figure 4.6a), the two most significant local maxima in wall-normal velocity (white iso-lines) appear closer to the upstream edge of the hole exit. Due to this double jet core, the known, alternating pattern of x-vorticities can be observed, leading to a weak but existent Ω_{ACV} pair in between the much stronger Ω_{CV} pair. For the blowing ratios $BR = 1.0$ and 2.0, the streamwise vorticity downstream of the cooling hole exit appears to be the most significant impact of the coolant jet on the flow field. In contrast to that, for the $BR = 3.0$, the previously mentioned 'in-hole' x-vorticities are significantly more relevant.
For the high coolant channel Reynolds number (Figure 4.6b), the wall-normal velocity distribution is significantly more homogeneous and the local maxima are much less distinct. Due to this homogeneity, the magnitudes of wall-normal velocity are much lower compared to the low coolant channel Reynolds number. The global maximum of wall-normal velocity is slightly shifted in downstream direction. The maxima in x-vorticity along the inner lateral diffuser edges are equally shifted in downstream direction but the maxima in lateral velocity are not (see Figure A.6 for lateral velocity distribution). Also, the magnitude of the local maxima of the lateral velocity is slightly lower for the high coolant channel Reynolds number. Due to the absence of the Ω_{ACV} pair compared to the low coolant channel Reynolds number, the Ω_{CV} pair can lift further away from the wall (see Figure 4.6b). At $x/D = 5.0$ and the high blowing ratio $BR = 3.0$, the lateral spreading is very similar for the low and high coolant channel Reynolds number.

For all cases with an Ω_{ACV} pair (low coolant channel Reynolds number), the lift produced by the

Ω_{CV} pair is comparatively lower and the lateral position of the Ω_{CV} legs does not change very much at all. For all cases without an Ω_{ACV} pair (high coolant channel Reynolds number), the lift produced by the Ω_{CV} pair continuously increases the hot gas entrainment and, thereby, the lateral spreading in streamwise direction.

Regarding the exact formation of the Ω_{CV} pair at $VR_{local} > 1.0$ it is unclear how the frequently reported 'tilting and folding' of vorticity (Andreopoulos and Rodi, 1984; Kelso et al., 1996; Fric, 1990) plays a role. The intuitive notion of vortices being associated with extrema in vorticity is misleading, as vorticity arises from shear and swirling motion. Based on vorticity only, it is not possible to distinguish between shear and swirling motion (Lugt, 1985). The extrema in x-vorticity observed in the x-planes (see Figure 4.5 and 4.6) do, however, align very well with the Ω_{CV} and Ω_{ACV} pair locations. In contrast to that, the significant z-vorticities observed for all PF cases in the z-plane trailing the lateral edges of the hole (see section A.6) do not translate into x-vorticities and secondary flow structures in the far field, despite the bending of the jet trajectory due to the cross-flow.

In Figure 4.8, the effect of local velocity ratios $VR_{local} > 1.0$ is emphasised using the PF case with low coolant channel Reynolds number and high blowing ratio $BR = 3.0$. The presented data is from a lateral y-plane at $y/D = 0.6$, such that it passes through one of the two lateral jet

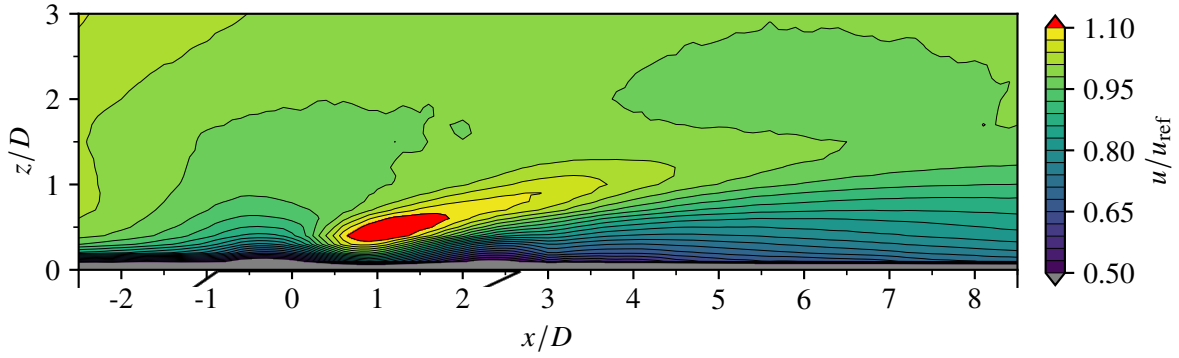

(a) Normalised streamwise velocity u at $y/D = 0.6$

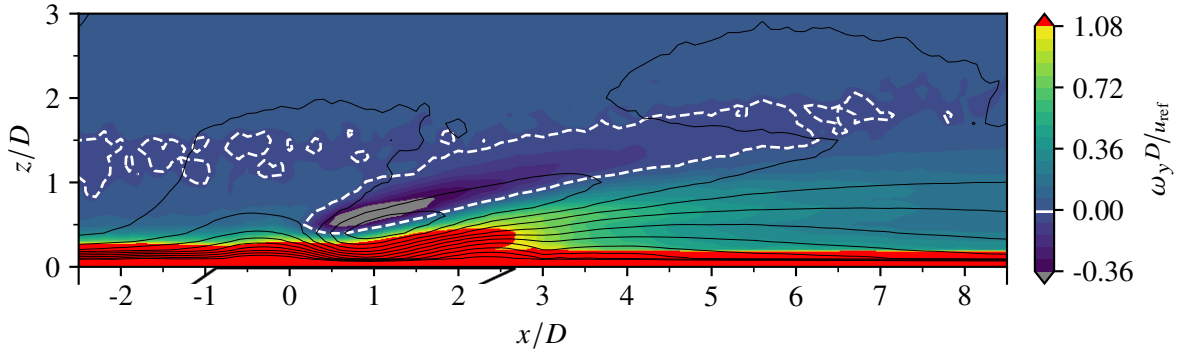

(b) Normalised y-vorticity and black contour lines of u-velocity from (a) at $y/D = 0.6$

Figure 4.8: Example for $VR_{local} > 1$ at the low coolant channel Reynolds number $Re_{D,cc} = 5 \times 10^3$ for blowing ratio $BR = 3.0$ at $y/D = 0.6$ where one of the two wall-normal velocity maxima occurs (see Figure A.9a)

cores where the maximum in wall-normal velocity occurs for this case. In Figure 4.8a, the normalised streamwise velocity u is shown. In Figure 4.8b, a background contour of the normalised y-vorticity ω_y can be seen. The switch from positive to negative y-vorticities is emphasised by adding the dashed white line at $\omega_y = 0$. The contours of the normalised streamwise velocity from Figure 4.8a are added to point out the relative location of the streamwise velocity maxima compared to the switch between the positive and negative y-vorticity regions.
As previously discussed, the acceleration of the hot gas cross-flow is observed for the high blowing ratio only. The resulting y-vorticity in Figure 4.8b implies the presence of two separate shear layers as indicated in Figure 2.1b with unsteady windward and leeward shear-layer vortices, Ω_{WSV} and Ω_{LSV}, respectively. This confirms that hairpin vortices Ω_{HpV} do not play a significant role in the Ω_{CV} pair formation for $BR = 3.0$. For locally high velocity ratios, the Ω_{CV} pair formation is likely driven by coherent structures from within the film cooling hole as suggested by Dai et al. (2016) indicated by the 'in-hole' streamwise vorticities in Figure 4.6.
For local velocity ratios $VR \leq 1.0$ ($BR = 1.0$ and 2.0), purely positive y-vorticities are observed (not shown) suggesting only leeward shear-layer vortices Ω_{LSV} in the unsteady flow field. This confirms the presence of unsteady hairpin vortices Ω_{HpV} as suggested by Tyagi and Acharya (2003) and Fawcett et al. (2013) and indicated in Figure 2.2. The Ω_{CV} pair or Ω_{CV}-Ω_{ACV} pair observed in the x-planes for $BR = 1.0$ and 2.0 in Figure 4.3 and 4.4, hence, constitutes the steady remainder of the streamwise component of the Ω_{HpV}.
The switch in y-vorticity direction depending on the local velocity ratio is also observed in Eberly and Thole (2013). Due to the much lower density ratios of $DR = 1.2$, negative y-vorticities were observed at a blowing ratio of $BR = 2.0$ already.

Apart from the Ω_{CV} and Ω_{ACV} pair and the changes in the shear-layer vortices Ω_{WSV} and Ω_{LSV}, one more interesting observation is made. For $BR = 3.0$ and the low coolant channel Reynolds number, the near-wall z-vorticity distribution at $z/D = 0.3$ is shown in Figure 4.9 as it is significantly different compared to all other PF cases (see section A.6). Directly downstream of the wall-normal velocity maxima, two regions of opposite z-vorticity appear at $x/D \approx 2.3$ and $y/D \approx \pm 0.8$. For all other PF cases, the maxima in z-vorticity lie beyond the indicated film cooling hole exit geometry close to the downstream end of the lateral edges. As mentioned before, the relation between vorticity maxima and vortices is ambiguous, as vorticity is caused by both, rotation and shear. For the z-vorticity regions observed in Figure 4.9, however, the wake produced by the upstream wall-normal velocity maxima is likely associated to a pair of steady wake vortices Ω_{sWV} (see Figure 2.1a). According to Hale et al. (2000), the Ω_{sWV} constitute the time-averaged separation due to unsteady Ω_{WV}. Such a wake is neither expected not found in any other PF cases, as the wall-normal hole exit velocities are much more homogeneous and the magnitudes of the maxima are much lower.

4.2.3 Influence of Coherent Structures on Thermal Film Cooling Quantities $\eta_{\mathrm{a,w}}$ and h_{f}/h_0

In the following, the relation between the coherent structures in the flow field and the thermal film cooling quantities is analysed. The data of the thermal film cooling quantities was gathered by

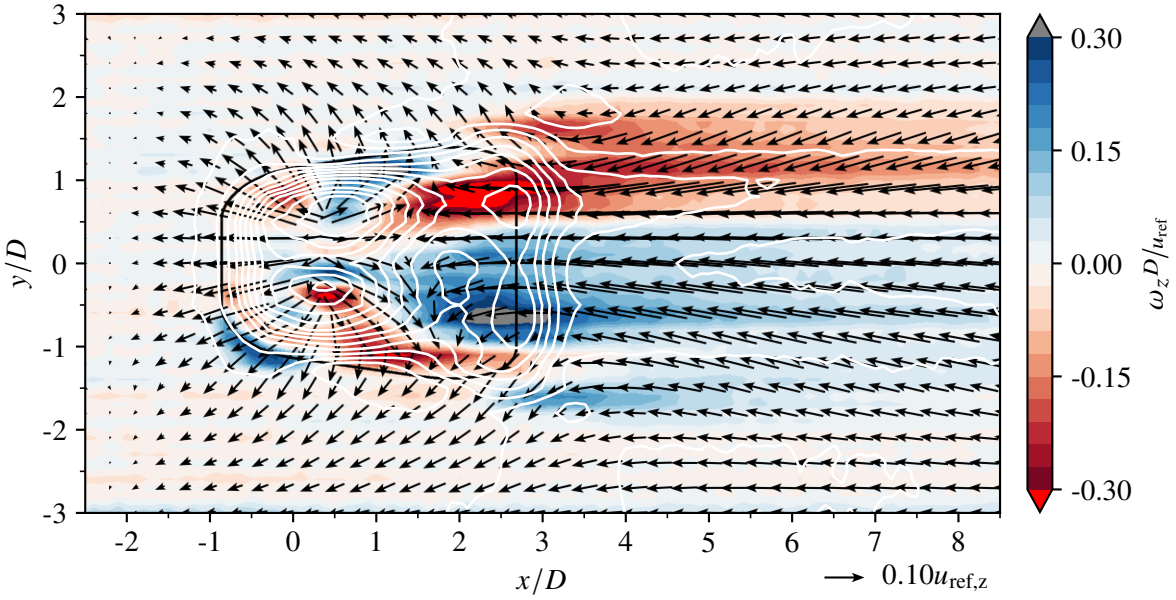

Figure 4.9: Impact of the coolant ejection on the near-wall z-vorticity, ω_z, and the in-plane velocity field, $\left(\left(u - u_{\mathrm{ref,z}}\right), v\right)$, for $Re_{D,\mathrm{cc}} = 5 \times 10^3$ and $BR = 3.0$ at $z/D = 0.3$. The white lines correspond to the contours of wall-normal velocity (for details see Figure A.7 and A.9).

Fraas et al. (2019a) and Fraas (2019) on the same test section as in the present work schematically shown in Figure 3.2. The operating conditions for all PF and OF cases are identical to the present work and listed in Table 3.1 and 4.1. An introduction to the thermal film cooling quantities $\eta_{\mathrm{a,w}}$ and h_{f}/h_0 can be found in subsection 2.2.1. Details on the data acquisition using infrared thermography (IRT) and the data processing based on the superposition principle of film cooling can be found in Fraas et al. (2017).

For all PF cases, the adiabatic film cooling effectiveness and the ratio of heat transfer coefficients with and without film cooling show a single, symmetric maximum in lateral direction. The spatial distributions of $\eta_{\mathrm{a,w}}$ and h_{f}/h_0 are, therefore, omitted but can be found in Figure A.37 and A.38, respectively. For h_{f}/h_0, the lateral distributions in Figure 4.3 and 4.4 at $x/D = 5.0$ will be referred to in a later part of the discussion.

In Figure 4.10, the laterally averaged adiabatic film cooling effectiveness $\bar{\eta}_{\mathrm{a,w}}$ (Figure 4.10a) and the laterally averaged ratio of heat transfer coefficients with and without film cooling $\bar{h}_{\mathrm{f}}/\bar{h}_0$ (Figure 4.10b) are shown. Overall, a lower $\bar{\eta}_{\mathrm{a,w}}$ is observed along the streamwise direction for the high compared to the low coolant channel Reynolds number for all PF cases. For the blowing ratio $BR = 1.0$, the laterally averaged adiabatic film cooling effectiveness $\bar{\eta}_{\mathrm{a,w}}$ of both cases converges in downstream direction; for $BR = 2.0$ the laterally averaged values have a more or less constant offset and for $BR = 3.0$, they are identical at $x/D = 5.0$ and diverge in downstream direction. This change in trend is related to the size, spread and wall-normal position of the Ω_{CV} pair observed in Figure 4.3 and 4.4. While the streamwise overlap of the SPIV and IRT data is limited to $5.0 \leq x/D \leq 8.8$, this overlap is sufficient to understand the relation between the flow field and the thermal film cooling quantities. Significant qualitative changes in the flow field are observed in streamwise direction between $-2.5 \leq x/D \leq 5.0$. Further downstream, between

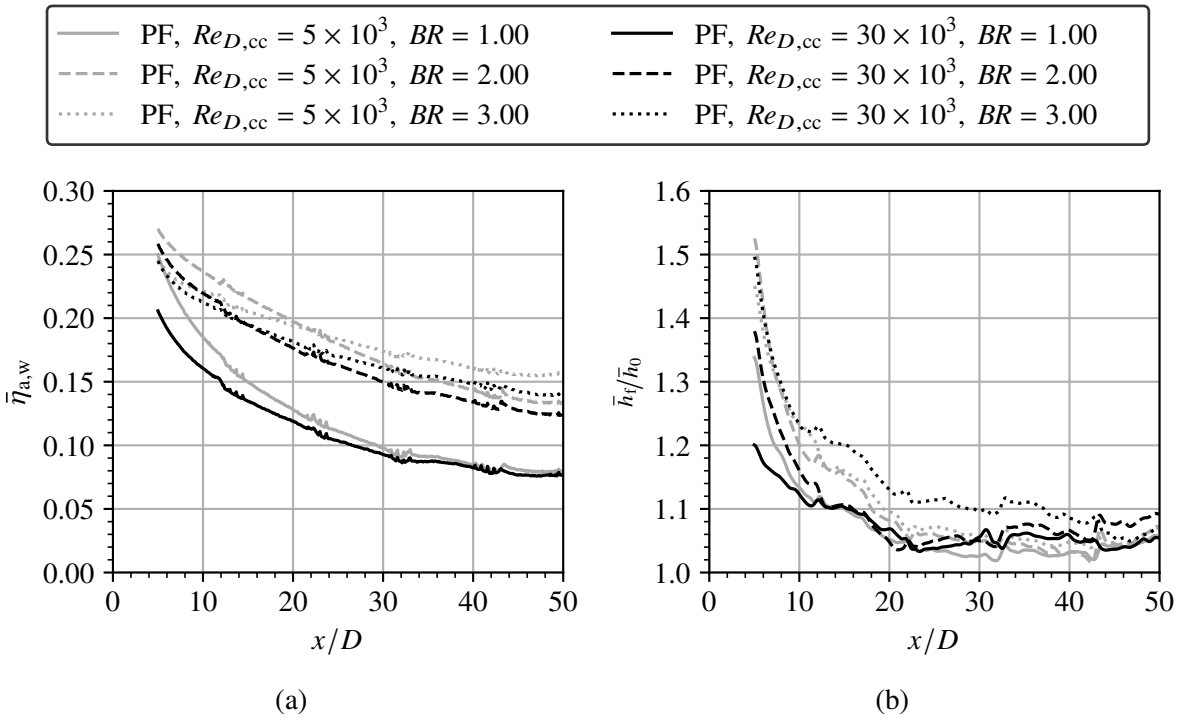

Figure 4.10: Laterally averaged (a) adiabatic film cooling effectiveness $\bar{\eta}_{a,w}$ and (b) ratio of heat transfer coefficients with and without film cooling $\bar{h}_f/\bar{h}_0$ for parallel flow configuration (PF); reproduced based on data in Fraas (2019)

$5.0 < x/D \leq 9.0$, only the dissipation of the existing coherent structures can be observed.

For the blowing ratio $BR = 1.0$, a larger spread between the Ω_{CV} legs at $x/D = 5.0$ for the low coolant channel Reynolds number (Figure 4.3a versus Figure 4.4a) leads to a closer attachment of the jet to the surface (see also Figure 4.1a compared to Figure 4.1b). This leads to an initially improved coverage in terms of the adiabatic film cooling effectiveness as seen in Figure 4.10a. Song et al. (2017) investigated vortex generators downstream of cylindrical holes to induce an Ω_{ACV} pair. They reported a significant increase of the adiabatic film cooling effectiveness for attached cooling jets due to the 'downwash' effect of the additional Ω_{ACV} pair.
At the lowest blowing ratio $BR = 1.0$, the Ω_{ACV} pair between the Ω_{CV} legs is most pronounced (Figure 4.3a). The apparent positive effect of the Ω_{ACV} pair is countered by an increased mixing with the hot gas due to the additional interfaces and, hence, a faster consumption of the available cooling potential for the low coolant channel Reynolds number. Therefore, the distributions of the laterally averaged adiabatic film cooling effectiveness converge in streamwise direction when comparing the high and low coolant channel Reynolds number at $BR = 1.0$.
For the blowing ratio $BR = 3.0$, the initial spread between the Ω_{CV} legs is identical at $x/D = 5.0$ (Figure 4.3c versus Figure 4.4c) and so is $\bar{\eta}_{a,w}$ as shown in Figure 4.10a. For the high coolant channel Reynolds number, the wall-normal distance is slightly larger at $x/D = 5.0$. This small difference in wall-normal distance is less relevant initially but allows for more hot gas entrainment further downstream. This, in turn, leads to a comparatively stronger increase in wall-normal distance of the Ω_{CV} pair for the high coolant channel Reynolds number and, therefore,

a faster reduction of $\bar{\eta}_{a,w}$. The initially identical distributions of the laterally averaged adiabatic film cooling effectiveness at $x/D = 5.0$, hence, diverge in downstream direction for the blowing ratio $BR = 3.0$.

The trends in the laterally averaged ratio of heat transfer coefficients with and without film cooling $\bar{h}_f/\bar{h}_0$ observed in Figure 4.10b are related to the discussed far field structures as well. Similarly to the adiabatic film cooling effectiveness $\eta_{a,w}$, all spatial distributions of the ratio of heat transfer coefficients with and without film cooling h_f/h_0 are qualitatively similar and present with a single maximum in lateral direction and a decay in streamwise direction (see Figure A.38 for details).
For $BR = 1.0$ and 2.0, a significantly higher laterally averaged ratio of heat transfer coefficients with and without film cooling $\bar{h}_f/\bar{h}_0$ is observed for the low coolant channel Reynolds number. For $BR = 3.0$, the heat transfer augmentation is very similar for both coolant channel Reynolds numbers within $5.0 \leq x/D \leq 10.0$ but remains significantly higher for the large coolant channel Reynolds number for $x/D \geq 10$.
As shown in Figure 2.3, film cooling impacts the thermal and aerodynamic boundary layer. For $BR = 1.0$ and 2.0 and the low coolant channel Reynolds number, the additional Ω_{ACV} pair with a further spread Ω_{CV} pair compared to just a single, narrower Ω_{CV} pair has multiple effects. The additional interfaces between the Ω_{ACV} and Ω_{CV} pair likely lead to an increased lateral exchange and every vortex leg itself would be associated with a thinning of the boundary layer right below it. Higher values for the ratio of heat transfer coefficients with and without film cooling are, hence, observed for those PF cases, where the Ω_{ACV} pair plays a significant role ($BR = 1.0$ and 2.0 at $Re_{D,cc} = 5 \times 10^3$).
For $BR = 3.0$, the Ω_{CV} pairs are initially similar for the low and high coolant channel Reynolds number which also explains the very similar initial values of h_f/h_0. For $x/D \geq 8.8$, no flow field data is available, but as mentioned in subsection 4.2.1, the dissipation of the Ω_{CV} pair for $BR = 3.0$ at the high coolant channel Reynolds number is slower compared to all other cases. Due to the increased wall-normal distance, the Ω_{CV} pair is damped less, can sustain longer and is therefore likely responsible for the consistently higher heat transfer augmentation observed in Figure 4.10b.

Based on the previous analysis, it can be concluded that there is excellent agreement between the flow field data and the thermal film cooling quantities from different measurement campaigns at the same film cooling test facility. This emphasises the repeatability of the test facility and the reliability of the measurement data. In the following, the initially mentioned single lateral maximum in the $\eta_{a,w}$ and h_f/h_0 distributions is revisited. For this purpose, a few relevant previous investigations are briefly discussed first.

Baldauf (2001, pg. 103, Fig. 7.1) observed a change in h_f/h_0 pattern on the downstream surface with an increase in blowing ratio for a cylindrical cooling hole. For low blowing ratios, two lateral h_f/h_0 maxima are observed downstream of the film cooling hole exit. Towards higher blowing ratios, the two lateral maxima regions convert to a single maximum along the centreline. Baldauf (2001) assumes that the two lateral maxima appear as long as the Ω_{CV} pair is close enough to the surface. In such cases, the effect of heat transfer augmentation due to boundary layer thinning is prevalent. After crossing a certain wall-normal distance, additional coherent structures

like wake vortices Ω_{WV} develop in the jet wake and lead to a single laterally centred maximum. At full jet lift-off, a low h_f/h_0 region is observed immediately downstream of the ejection due to the boundary layer separation followed by a high h_f/h_0 region due to reattachment. The h_f/h_0 data discussed in Baldauf (2001) was gathered at a low turbulence intensity of $Tu = 1.5\,\%$ and moderate and high density ratios of $DR = 1.2$ and 1.8.
Saumweber (2005) investigated a fan-shaped cooling hole with a large lateral opening angle of 14°. He observed two lateral maxima in $\eta_{a,w}$ for all investigated blowing ratios at a low turbulence intensity of $Tu = 2.0\,\%$. For an increase of turbulence intensity to $Tu = 7.5\,\%$, the two lateral maxima were less pronounced at low blowing ratios, but equally significant at high blowing ratios. When considering the effect of unsteady wakes on the adiabatic film cooling effectiveness at $Tu = 2.0\,\%$ with increasing wake Strouhal numbers, the two lateral maxima transformed to a single maximum for low blowing ratios and were generally less pronounced at high blowing ratios. According to Saumweber (2005), the two lateral maxima are desired for lateral spreading of the coolant and occur due to a flow separation on the downstream wall of the diffuser. For a decrease in the lateral opening angle from 14° to 10° and 7°, the two lateral maxima eventually converge to a single maximum for low and high blowing ratios. This transition happens more quickly for high blowing ratios. An increase in the hole length of the cylindrical part of the cooling hole also favoured the transition from two lateral maxima to a single maximum in $\eta_{a,w}$ for all blowing ratios. Spatial distributions of h_f/h_0 were not provided.
For a laidback fan-shaped hole with identical opening angles as in the present work, Kampe et al. (2012) also observed two lateral maxima in wall-normal velocity near the hole exit. Information on the thermal film cooling quantities beyond lateral averages were not provided.
McClintic et al. (2019) investigated a laidback fan-shaped cooling hole with a smaller opening angle of 7° at high turbulence intensities $Tu = 7.0\,\%$. They observed homogeneous dimensionless temperature fields at the diffuser exit for low and moderate density ratios $DR = 1.1$ and 1.4.
For the same laidback fan-shaped cooling hole, Haydt and Lynch (2021) observed a single lateral maximum in $\eta_{a,w}$ for low and high blowing ratios. For h_f/h_0, two lateral maxima were observed at low blowing ratios but a single lateral maximum at high blowing ratios. Their investigations were carried out at low turbulence intensities and density ratios of $Tu = 1.5\,\%$ and $DR = 1.0$, respectively.

Based on the observations in the present work and the discussed literature, the following conclusions are drawn: Two lateral jet cores observed for cylindrical, laidback and laidback fan-shaped cooling holes may or may not correspond to two lateral maxima in the thermal film cooling quantities. For both, $\eta_{a,w}$ and h_f/h_0, an increase of turbulence intensity, unsteady wake frequency or hole length as well as a decrease in opening angle correlate with a transition from two lateral maxima to a single lateral maximum in the thermal film cooling quantities. When both, $\eta_{a,w}$ and h_f/h_0 are presented, the two lateral maxima in h_f/h_0 seem to be more robust. No investigation reports two lateral maxima in $\eta_{a,w}$ where no two lateral maxima in h_f/h_0 are observed, however, the opposite is possible. Little to no understanding of the reasons for this behaviour are discussed in any of the previous literature.
As mentioned initially, all PF cases of the laidback fan-shaped cooling hole in the present work, presented with a single lateral maximum in $\eta_{a,w}$ and h_f/h_0 as shown in Figure A.37 and A.38, re-

spectively. While the aforementioned relevant parameters turbulence intensity, hole length and opening angle would suggest this outcome for the present work, it remains unclear, as to why this is the case. A separation of the coherent flow structure from the wall as hypothesised in Baldauf (2001) can not be the reason, as the Ω_{CV} and Ω_{ACV} pairs in Figure 4.3 and 4.4 stay very close to the wall.

Flow field characteristics that are typically associated with an increase in heat transfer coefficients are boundary layer thinning and an increased turbulence intensity. With respect to boundary layer thinning, stagnation or reattachment points yield an increase and flow separations a decrease in the local heat transfer coefficients (Hale et al., 2000). To understand the local relation between the coherent structures and the heat transfer augmentation for film cooling JiCs, the lateral distributions of h_f/h_0 in Figure 4.3 and 4.4 are revisited.
The lateral maximum of h_f/h_0 is located in between the Ω_{CV} and Ω_{ACV} pair for all PF cases. The magnitude of the observed local maximum in h_f/h_0 below the dominant coherent structure compared to the h_f/h_0 magnitude below the Ω_{CV} or Ω_{ACV} legs suggests different drivers for the heat transfer augmentation than boundary layer thinning or turbulence intensity. Compared to the values of h_f/h_0 below the dominant Ω_{CV} legs, the central maximum is approximately 100 % to 300 % larger. Aga and Abhari (2011) also report that the maxima in streamwise vorticity below the dominant coherent structure do not necessarily coincide with the maxima in h_f/h_0. In fact, for certain operating conditions, the local extrema in near-wall vorticity and h_f/h_0 show opposing trends. This is particularly the case at locations where an interaction between the coherent structures of neighbouring cooling holes is expected. Aga and Abhari (2011) do not provide an explanation for this observation. Kohli and Bogard (1998), Bernsdorf et al. (2008), and Straußwald et al. (2018) point out that the steady-state assumption for the thermal film cooling quantities may be inaccurate or even incorrect. According to Bernsdorf et al. (2008), the steady state assumption is only valid at low pulsation amplitudes. The same time-averaged flow field could, hence, yield different results for the adiabatic film cooling effectiveness $\eta_{a,w}$ and the ratio of heat transfer coefficients with and without film cooling h_f/h_0.
As mentioned in section 3.4, Stichling et al. (2021) and Stichling and Bauer (2022a,b) discuss unsteady effects in the film cooling ejection. Compared to the data analysed in the present work, different operating conditions or geometries and only the streamwise symmetry plane was analysed. Stichling et al. (2021) and Stichling and Bauer (2022b) qualitatively describe an intermittency of the coolant ejection using a method called Proper Orthogonal Decomposition (POD) and PIV raw data visualisations, respectively. An increase in blowing ratio yields a reduction in the intermittency of the coolant jet. Similarly to Schreivogel et al. (2016) and Abram et al. (2016), rather than forming a continuous jet, 'coolant lumps' are observed. They periodically exit the cooling hole and penetrate deep into the hot gas cross-flow. Stichling and Bauer (2022b) consider the intermittency of the coolant jet as the main reason for the comparatively lower adiabatic film cooling effectiveness of the laidback fan-shaped cooling hole with low pitch compared to a slot geometry.
Based on the same POD algorithm used by Stichling et al. (2021), Stichling and Bauer (2022a) reported a POD mode associated with the lateral fluctuation of the Ω_{CV} pair for the same laidback fan-shaped cooling hole as in the present work. Straußwald et al. (2020) observed a similar

'meandering' effect of the coolant jet.

A lateral unsteadiness of the Ω_{CV} pair position would induce a reciprocating flow in the vicinity of the interface between the vortex legs. For channel flows, Ye et al. (2021) have shown that the increase in heat transfer due to reciprocating flows scales with the oscillation frequency and amplitude. This agrees well with the conclusions of Bernsdorf et al. (2008) about the invalidity of the steady-state assumption for large fluctuation amplitudes. Furthermore, a lateral unsteadiness can explain the single maximum of h_f/h_0 and the significant difference in the absolute values of h_f/h_0 below the Ω_{CV} legs and the Ω_{CV} pair.

4.2.4 Concluding Remarks on the Formation of Coherent Structures and their Relation to the Thermal Film Cooling Quantities

The coherence between the thermal film cooling quantities and the comprehensive flow field measurements conducted for the PF configuration highlights the capabilities of the film cooling test facility and the combined analysis in the present work.

The formation process of the counter-rotating vortex pair (Ω_{CV} pair) in a laidback fan-shaped film cooling hole at engine-realistic operating conditions with parallel coolant cross-flow, is strongly dependent on the local cooling hole exit velocity distribution. It is shown that maxima of x-vorticity in the x-plane laterally align well with the centres of the dominant vortical structures for all PF cases (see Figure 4.3 and 4.4). Depending on the local velocity ratio VR_{local}, two formation processes are observed for the Ω_{CV} pair.

For cases with low local velocity ratios $VR_{local} \leq 1.0$ over the entire cooling hole exit (as for $BR = 1.0$ and 2.0), the formation is dominated by hairpin vortices as suggested by Tyagi and Acharya (2003) and Fawcett et al. (2013). When more than one maximum of wall-normal velocity exists in lateral direction, each of them is accompanied by its own Ω_{CV} pair, where the formation process for each is still dominated by hairpin vortices. This results in an Ω_{ACV} pair in between of the classical Ω_{CV} pair as described in Figure 2.1a. The maxima in wall-normal velocity essentially represent separate jet cores where each is subject to the interaction with the cross-flow.

For cases with regions of local velocity ratios $VR_{local} > 1.0$ at the cooling hole exit (as in $BR \geq 3.0$), a significant in-hole vorticity appears to be a major contributor to the Ω_{CV} pair formation. The commonly suggested mechanisms of vorticity 'tilting and folding' (Andreopoulos and Rodi, 1984; Kelso et al., 1996; Fric, 1990) could not be confirmed for the laidback fan-shaped geometry. As the blowing ratio of the coolant ejection is known to fluctuate over time (Stichling et al., 2021; Straußwald et al., 2018), local velocity ratios of $VR_{local} \leq 1.0$ may still be present at instantaneous points in time. At those times, the formation of hairpin vortices Ω_{HpV} can make minor contributions to the time-averaged Ω_{CV} pair observed in the plane orthogonal to the hot gas cross-flow.

Irrespective of the exact formation process of the Ω_{CV} pair, the local cooling hole exit velocity profile plays a major role in the wall-normal and lateral position and spreading of the Ω_{CV} pair and whether or not an Ω_{ACV} pair is present. The streamwise location and lateral number of jet cores is decisive for the initiation location and the number of Ω_{CV} pairs, respectively.

Since the hole exit velocity distributions are strongly dependent on the inlet flow phenomena, the previous sections undeniably show the significance of considering engine-realistic inflow conditions and, more specifically, coolant cross-flow for film cooling investigations and fundamental JiC research. The influence of orthogonal coolant cross-flow is even more significant, as will be shown in section 4.3.

Aside from the Ω_{CV} and Ω_{ACV} pair and the shear layer vortices Ω_{SV}, indications of a steady wake vortex Ω_{sWV} pair are found for the PF case with the single, most upstream wall-normal velocity maximum ($BR = 3.0$, $Re_{D,\mathrm{cc}} = 5 \times 10^3$). Due to the single, dominant jet core, the blockage of the cross-flow is much stronger compared to all other PF cases. The Ω_{sWV} resembles the time-averaged separation related to the wake vortices much like in a Kármán vortex street. As mentioned in section 2.1, the formation of wake vortices in a JiC is different from those in a Kármán vortex street. In a JiC, the Ω_{WV} originate from boundary layer fluid, not cross-flow fluid. While the same PF case presents with the highest heat transfer augmentation at $x/D \leqq 5.0$ downstream of the ejection, it is unclear whether this is related to the Ω_{sWV}, as the thermal film cooling quantities are not available upstream of $x/D = 5.0$.

Although frequently discussed in the context of film cooling, the horseshoe vortex (Ω_{HV}) is not observed for any of the PF cases, not even for the case causing a significant blockage of the cross-flow ($BR = 3.0, Re_{D,\mathrm{cc}} = 5 \times 10^3$).

Despite the fact that multiple jet cores are observed at the cooling hole exit for some PF cases, the distributions of the adiabatic film cooling effectiveness $\eta_{\mathrm{a,w}}$ and the ratio of heat transfer coefficients with and without film cooling h_{f}/h_0 both show a single peak in lateral direction. This is plausible given the trends indicated by the previously discussed investigations. An increased spreading for the PF cases with an Ω_{ACV} pair leads to reduced lift for the Ω_{CV} pair and an improved adiabatic film cooling effectiveness. For all PF cases that contain both a Ω_{CV} and an Ω_{ACV} pair, a significantly higher heat transfer augmentation is observed. In general, two opposing effects play a role. Stronger vortical structures such as the Ω_{CV} pair close to the wall decrease the boundary layer thickness leading to a heat transfer augmentation. An increased spreading, on the one hand, yields an overall weaker Ω_{CV} pair, while, at the same time, leading to an additional Ω_{ACV} pair, which, in turn, leads to additional local boundary layer thinning.

The reason for seeing only one lateral maximum in both, the adiabatic film cooling effectiveness and the ratio of heat transfer coefficients with and without film cooling was previously explained based on coherent structures in the jet wake that are thought to increasingly appear when the coolant jet is detached from the surface (Baldauf et al., 1999b; Baldauf, 2001). Flow field data for film cooling JiCs to corroborate this hypothesis is not available. For the laidback fan-shaped cooling hole in the present work, a Ω_{CV} pair or Ω_{CV}-Ω_{ACV} pair combination close to the wall is observed for all but one PF case, with no indication of a significant jet wake due to lift-off. As discussed in Fraas et al. (2019a) and Fraas (2019) based on the thermal film cooling quantities only, no lift-off is expected even for the highest blowing ratio. A possible explanation for the single lateral maximum of the ratio of heat transfer coefficients with and without film cooling is proposed based on indications of a lateral fluctuation of the dominant coherent structure (Stichling and Bauer, 2022a). The steady-state assumption for the thermal film cooling quantities should, hence, be revisited.

4.3 Coherent Structures with Orthogonal Coolant Cross-Flow

In the previous section, the secondary flow field and the corresponding coherent structures at the cooling hole exit are discussed for parallel coolant cross-flow. It is shown that the qualitative and quantitative appearance of the coherent structures varies, given a change in coolant channel Reynolds number $Re_{D,\mathrm{cc}}$. For a change in blowing ratio BR, only the quantitative appearance of the flow field is altered. Based on the changes observed in the thermal film cooling quantities in Fraas et al. (2019a), a significantly more drastic change is expected for the overall flow field when moving from parallel to orthogonal coolant cross-flow configuration. In general, a change in blowing ratio BR at orthogonal coolant cross-flow is expected to also impact the qualitative rather than just the quantitative appearance of the secondary flow field. Previous investigations have reported changes in the lateral direction, towards which the distributions of $\eta_{\mathrm{a,w}}$ and h_{f}/h_0 are biased at different blowing ratios (Saumweber et al., 2001; Gritsch et al., 2003; Saumweber and Schulz, 2008a).
In the following sections, the far-field coherent structures observed for the orthogonal coolant cross-flow (OF) configuration at varying blowing ratios are characterised. Inconsistencies in the common explanation for the asymmetries in the coolant jet are discussed. Most importantly, the relation to the observed trends in the adiabatic film cooling effectiveness $\eta_{\mathrm{a,w}}$ and the ratio of heat transfer coefficients with and without film cooling h_{f}/h_0 is emphasised.

4.3.1 Far Field Coherent Structures

In Figure 4.11 and 4.12, the time-averaged lateral and wall-normal velocity components are shown in an x-plane at $x/D = 5.0$ with a background contour of normalised x-vorticity ω_x for the low and high coolant channel Reynolds number $Re_{D,\mathrm{cc}}$, respectively. The white iso-line of turbulent kinetic energy corresponds to the iso-surface depicted in Figure 4.2. The black lines below the horizontal axis indicate the downstream edges of the cooling hole diffuser exit geometry. The blue line represents the lateral distribution of the ratio of heat transfer coefficients with and without film cooling h_{f}/h_0 at $x/D = 5.0$ based on data from Fraas (2019). The x-axis corresponds to $h_{\mathrm{f}}/h_0 = 1.0$.
For the OF cases with high coolant channel Reynolds number (Figure 4.12), the heat transfer augmentation is significantly lower. Therefore, the value range of h_{f}/h_0 is reduced accordingly. When comparing the OF cases with high coolant channel Reynolds number quantitatively to the other OF or PF cases, this has to be considered. Detailed spatial distributions of h_{f}/h_0 for all OF cases can be found in Figure A.41.

For a variation of the blowing ratio BR, qualitatively similar secondary flows are observed for a fixed coolant channel Reynolds number $Re_{D,\mathrm{cc}}$ and the respective OF cases. Given the results for the thermal film cooling quantities in Fraas et al. (2019a) showing the same lateral bias within one coolant channel Reynolds number, this was expected for the specific geometry and operating conditions. As mentioned previously, the lateral bias does not generally have the same direction for a change in operating conditions (Saumweber et al., 2001; Gritsch et al., 2003; Saumweber and Schulz, 2008a) and could be a coincidence in the results of the present work.

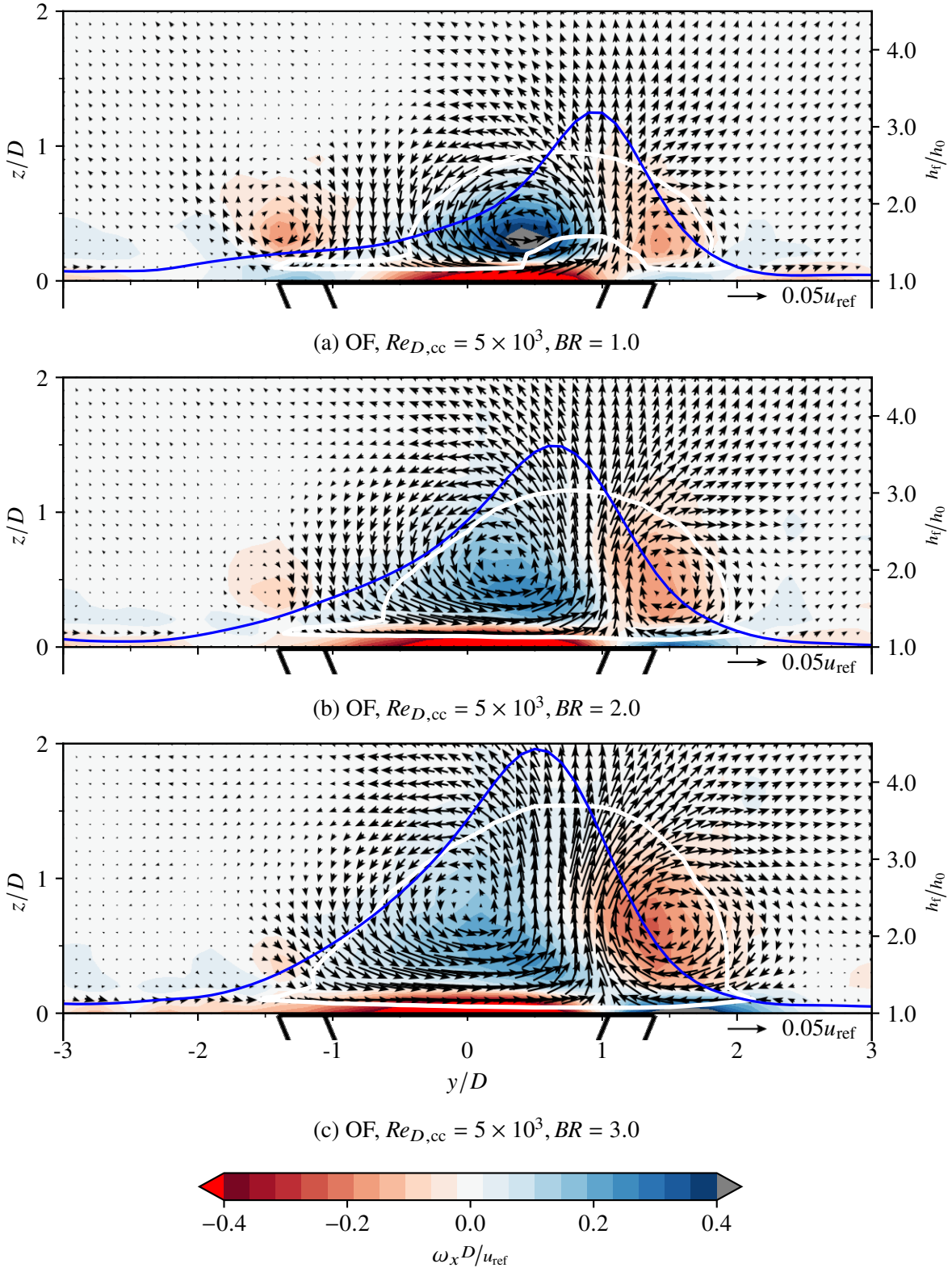

(a) OF, $Re_{D,\mathrm{cc}} = 5 \times 10^3$, $BR = 1.0$

(b) OF, $Re_{D,\mathrm{cc}} = 5 \times 10^3$, $BR = 2.0$

(c) OF, $Re_{D,\mathrm{cc}} = 5 \times 10^3$, $BR = 3.0$

Figure 4.11: Steady coherent flow structures and their relation to h_f/h_0 at $x/D = 5.0$ and $Re_{D,\mathrm{cc}} = 5{\times}10^3$. White iso-line corresponds to the iso-surface of k_t shown in Figure 4.2. The coolant cross-flow is in negative y/D direction.

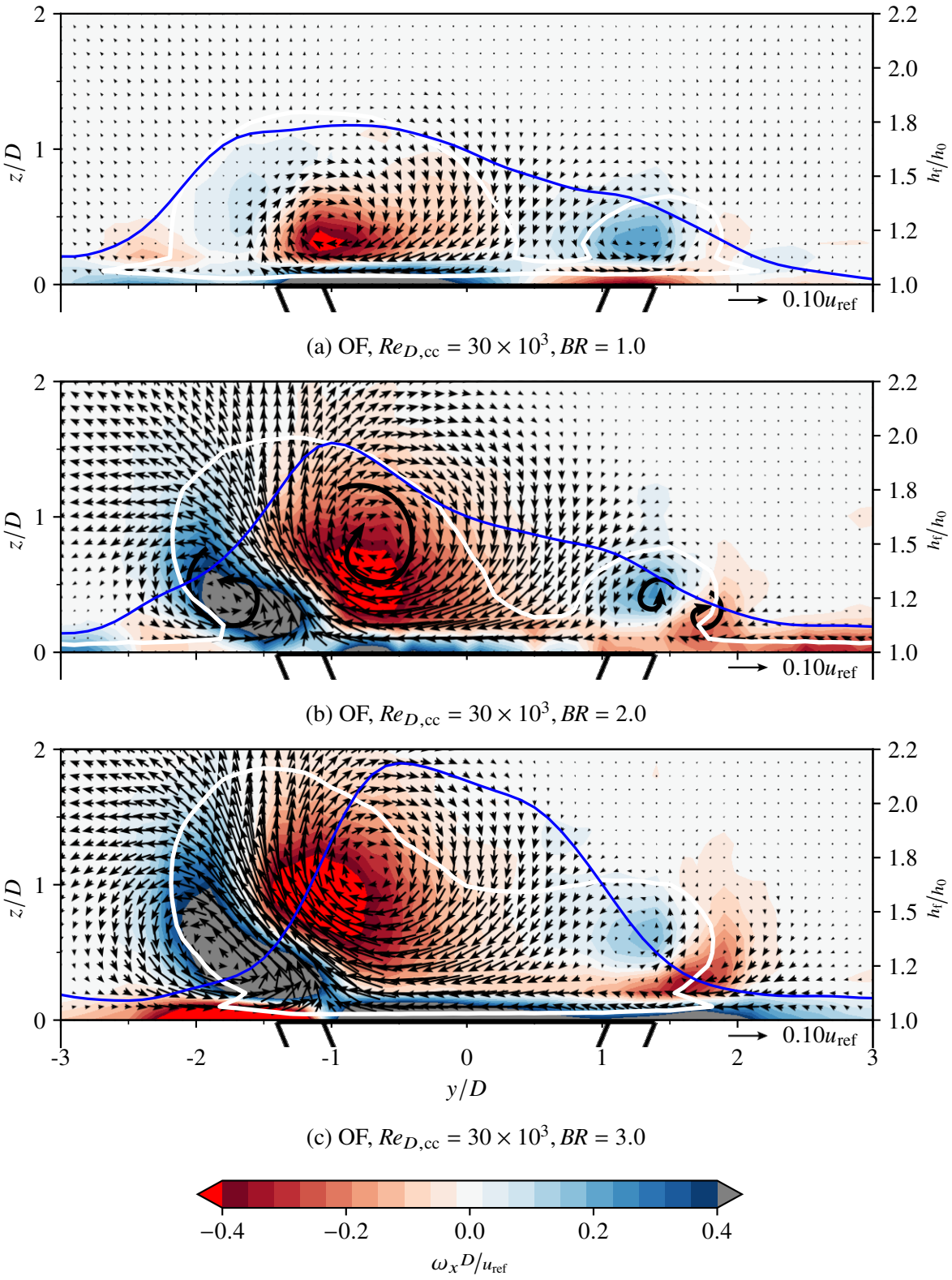

(a) OF, $Re_{D,\mathrm{cc}} = 30 \times 10^3$, $BR = 1.0$

(b) OF, $Re_{D,\mathrm{cc}} = 30 \times 10^3$, $BR = 2.0$

(c) OF, $Re_{D,\mathrm{cc}} = 30 \times 10^3$, $BR = 3.0$

Figure 4.12: Steady coherent flow structures and their relation to h_f/h_0 at $x/D = 5.0$ and $Re_{D,\mathrm{cc}} = 30 \times 10^3$. White iso-line corresponds to the iso-surface of k_t shown in Figure 4.2. The coolant cross-flow is in negative y/D direction.

In contrast to the PF configuration, the secondary flow field is much stronger and asymmetric for both coolant channel Reynolds numbers at the OF configuration. To emphasise the significant difference in x-vorticities, it should be noted that the value range of the x-vorticity contour is chosen three times larger in the OF cases compared to the PF cases. The unit vector scaling was also adapted. For the secondary flows of the PF cases, the order of magnitude was 1 % to 5 % of u_{ref}. For the OF cases, the overall secondary flow fields are stronger, especially for the high coolant channel Reynolds number, with magnitudes of up to 10 % of u_{ref}.

For all OF cases, the most dominant secondary flow structure is a Ω_{CV} pair. Like for the PF cases, the Ω_{CV} pair is located downstream of the wall-normal velocity maximum at the cooling hole exit (see section A.9 for details on the local wall-normal velocity distribution).
For the low coolant channel Reynolds number (Figure 4.11), the dominant secondary flow is biased towards positive y/D values, while for the high coolant channel Reynolds number (Figure 4.12), a clear bias towards negative y/D values is present. This can also be observed in the iso-surfaces of normalised turbulent kinetic energy shown in Figure 4.2.

For the low coolant channel Reynolds number (Figure 4.11), the Ω_{CV} pair itself is relatively symmetric in terms of x-vorticity magnitude, shape and position of the Ω_{CV} legs, especially towards the higher blowing ratios $BR = 2.0$ and 3.0. The Ω_{CV} pair is accompanied by a second, much weaker, single vortex. For the low blowing ratio $BR = 1.0$ (Figure 4.11a), this vortex is visible at $y/D \approx -1.4$. With increasing blowing ratios towards $BR = 2.0$ and 3.0 (Figure 4.11b and 4.11c), this single vortex still exists further upstream at $x/D = 4.0$ (not shown) but is nearly completely dissipated at $x/D = 5.0$.

For the high coolant channel Reynolds number (Figure 4.12), the legs of the dominant Ω_{CV} pair still show increasing symmetry in terms of shape, size and vorticity magnitude (not position) towards increasing blowing ratios, but are overall much less symmetric compared to the low coolant channel Reynolds number in terms of shape, position and x-vorticity magnitude. Compared to the low coolant channel Reynolds number, the dominant coherent structure is associated with significantly larger x-vorticity magnitudes when comparing the same blowing ratio. This is due to the fact that, for the low coolant channel Reynolds number, the wall-normal velocity distributions close to the hole exit are comparatively more homogeneous. An example of this is shown for the blowing ratio $BR = 2.0$ in Figure 4.13. Despite the same blowing ratio, the velocity maximum is significantly larger for the high coolant channel Reynolds number.
For the low blowing ratio $BR = 1.0$, it is not clear at all from the flow field at $x/D = 5.0$ that the dominant secondary flow structure origins from a Ω_{CV} pair at all. Further upstream at $x/D = 4.0$ (not shown), the second but much weaker Ω_{CV} leg is visible, but nearly completely dissipated at $x/D = 5.0$.

As observed for the low coolant channel Reynolds number, the Ω_{CV} pair at the high coolant channel Reynolds number is accompanied by a second, weaker coherent structure on the laterally opposite side at $y/D \approx 1.4$. Compared to the low coolant channel Reynolds number, this additional structure is more significant with larger x-vorticity magnitudes. Instead of a single vortex, it appears as a secondary, weaker Ω_{CV} pair. This is especially apparent from the blowing ratios $BR = 2.0$ and 3.0 (see Figure 4.12b and 4.12c). The primary and secondary Ω_{CV} pair is exemplarily indicated using black arrows for $BR = 2.0$ in Figure 4.12b. The line of constant

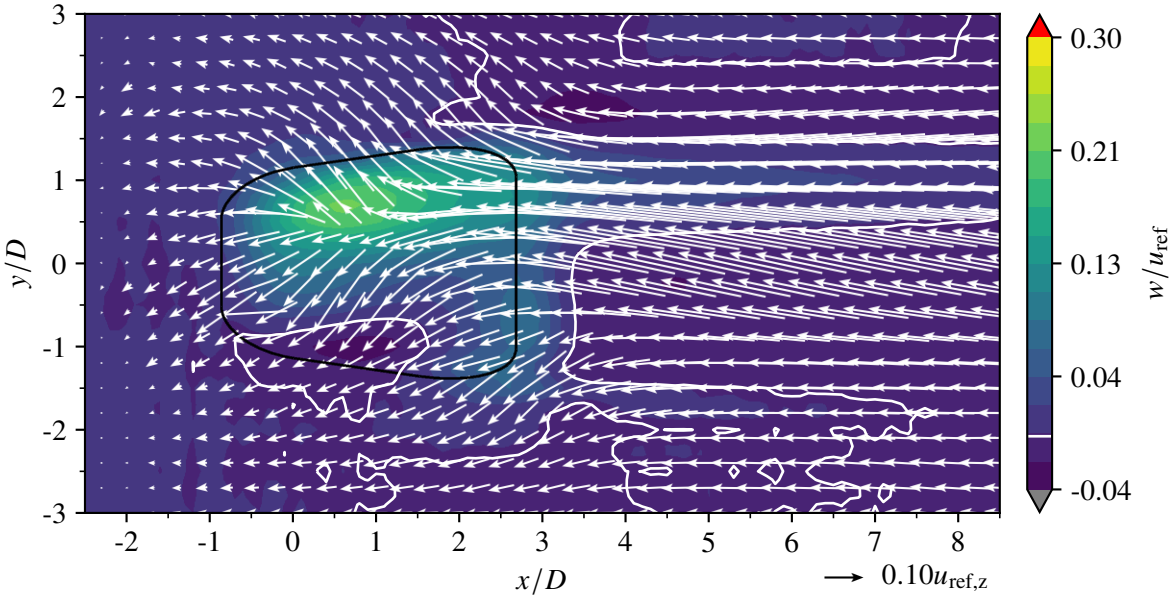

(a) OF, $Re_{D,\mathrm{cc}} = 5 \times 10^3$, $BR = 2.0$

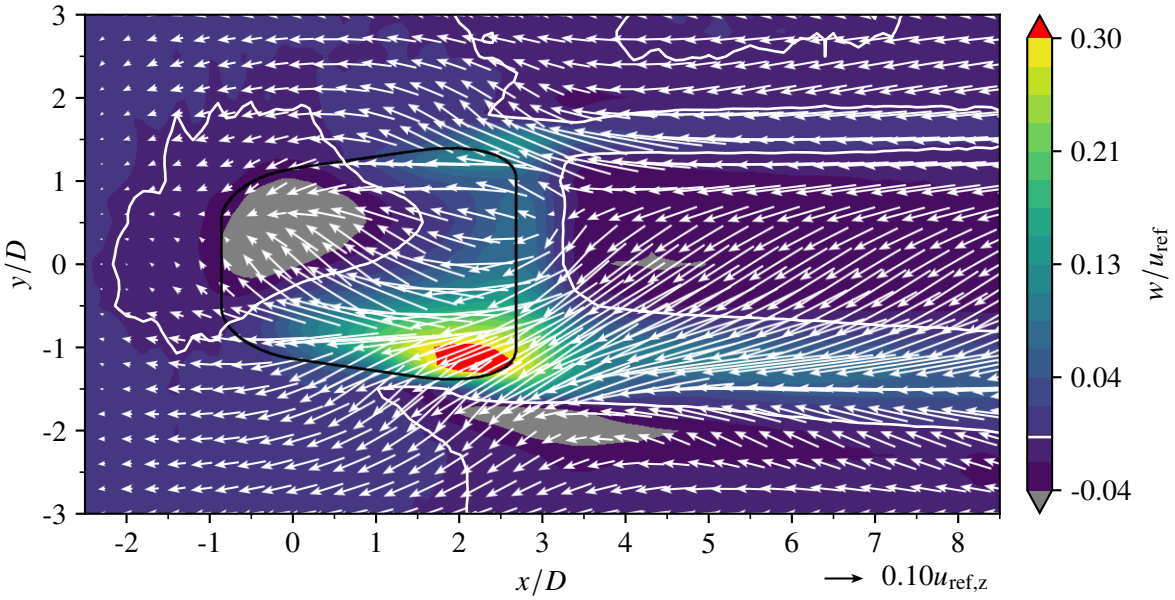

(b) OF, $Re_{D,\mathrm{cc}} = 30 \times 10^3$, $BR = 2.0$

Figure 4.13: Impact of the coolant ejection on the near-wall wall-normal velocity, w, and in-plane velocity field, $\left(\left(u - u_{\mathrm{ref,z}}\right), v\right)$, at $z/D = 0.3$.

normalised turbulent kinetic energy k_t therefore, envelopes two distinct local maxima in lateral direction. The two Ω_{CV} pairs are laterally clearly separated at $BR = 1.0$ but start influencing each other towards the higher blowing ratios $BR = 2.0$ and 3.0, as the strong and weak Ω_{CV} pair increase in size.

For all OF cases, except $BR = 1.0$, the Ω_{CV} pair lifts further away from the wall in downstream direction. Details on the progression of the coherent structures for all OF cases from $x/D = 0$ to 8.0 are provided in section A.10.

4.3.2 Origin of the Asymmetries in the Secondary Flow Field

The main reason for the more complex and strongly asymmetric secondary flow field of the OF configuration compared to the PF configuration are the more complex flow conditions at the hole inlet. Aside from flow separations that vary in strength depending on coolant channel Reynolds number and blowing ratio, the orthogonal coolant cross-flow is expected to cause a swirling flow in the cooling hole as suggested in Saumweber and Schulz (2008a). Due to the inclination angle of the hole and the cross-flow direction, the rotational direction of the swirl is positive along the hole axis, where the hole axis points towards the cooling hole exit. This is confirmed by the results of McClintic et al. (2019)[3]. The swirl and the wake of a possible inlet flow separation propagate to the diffuser and, finally, cause an asymmetric cooling hole exit velocity distribution. A detailed overview of the resulting local velocity distributions close to the hole exit at $z/D = 0.3$ are provided in section A.7, A.8 and A.9 for all velocity components. While refraining from a detailed discussion, it should be pointed out that more or less significant backflow regions into the hole are observed for all OF cases. These regions are characterised by significant negative wall-normal velocities w, such as in Figure 4.13. This is consistent with predictions made by Kohli and Thole (1998) for fan-shaped cooling holes. No backflow regions were observed for any of the PF cases.

In contrast to the possible inlet flow phenomena shown in Figure 4.7 for the PF cases, a flow separation for the OF cases is, if existent, always located on the upstream side of the cooling hole inlet. Without measurement data in the cooling hole, it is not possible to determine the inlet velocity ratio VR_{inlet} at which significant inlet flow separations would occur. An increase in VR_{inlet}, however, always leads to a stronger inlet flow separation and swirl in the cooling hole. A stronger flow separation leads to a more inhomogeneous in-hole velocity profile with an off-centre velocity maximum. Assuming that the number of revolutions n_{rev} of the fluid in the cooling hole caused by the induced swirl is purely dependent on the inlet velocity ratio and the hole length (Saumweber, 2005), the distance along the hole axis required for one full revolution l and the number of revolutions possible n_{rev} for a given inlet velocity ratio and hole length L are given as

$$l_{\text{rev}} \simeq 2D\, VR_{\text{inlet}} \quad \text{and} \quad n_{\text{rev}} = L/l. \tag{4.1}$$

In Table 4.2, the number of revolutions n_{rev} of the in-hole swirl is calculated for all cases according to Equation 4.1 based on either the full hole length L or the length of the cylindrical part of the hole L_{cyl} only. Integer values of n_{rev} suggest that the in-hole velocity profile has completed one full rotation about the hole axis and is merely shifted in positive direction along the hole axis. A possible velocity maximum due to the jetting effect would have regained its initial location in the cross-sectional flow field. Based on Equation 4.1, a decrease of the blowing ratio from $BR = 3.0$ to 1.0 and an increase of the coolant channel Reynolds number from $Re_{D,\text{cc}} = 5 \times 10^3$ to 30×10^3 yield an increase of n_{rev} by a factor of 3 and 6, respectively.

Saumweber and Schulz (2008a) and Fraas (2019) suggest that velocity maxima due to the jetting

[3]McClintic et al. (2019) conducted a measurement of the velocity field in a plane orthogonal to the hole axis coinciding with the upstream edge of the diffuser. For a high inlet velocity ratio, the in-hole swirl was still detectable in an in-hole plane close to the diffuser exit.

Table 4.2: Number of revolutions of the in-hole swirl for all cases according to Equation 4.1 based on the full hole length L or the length of the cylindrical part of the hole L_{cyl}

L_{cyl} / L	n_{rev}	
	$Re_{D,\mathrm{cc}} = 5 \times 10^3$	$Re_{D,\mathrm{cc}} = 30 \times 10^3$
$BR = 1.0$	0.5/1.0	3.0/5.9
$BR = 2.0$	0.3/0.5	1.5/2.9
$BR = 3.0$	0.2/0.3	1.0/1.9

effect caused by the wake of a possible inlet flow separation in combination with the in-hole swirl are the reason for the asymmetries observed in the thermal film cooling quantities. The velocity maxima are transported to different lateral edges of the diffuser, depending on how many revolutions are possible at a given inlet velocity ratio VR_{inlet} and the hole length. Depending on the exact location of the velocity maximum, the flow in the diffuser separates from either of the lateral edges. While this explanation seems intuitive, the calculation of the number of revolutions in Table 4.2 for the laidback fan-shaped hole in the present work contradicts with this theory.
As mentioned before and seen in Figure 4.11 and 4.12, the flow field is biased towards the same lateral direction for a constant coolant channel Reynolds number. The approximated values for the number of revolutions n_{rev} in Table 4.2 would suggest otherwise. For both investigated coolant channel Reynolds numbers, the lateral edge at which the flow separation occurs should change at least once when increasing the blowing ratio from $BR = 1.0$ to 3.0. This is, of course, inconsistent. The only exception is the high coolant channel Reynolds number if the full hole length L is used for the calculation as it nearly produces integer values for n_{rev} only. Even if the assumption in Equation 4.1 was inaccurate as to the exact value of n_{rev}, it would still require the resulting n_{rev} to be close to a half or full rotation for all blowing ratios of the same coolant channel Reynolds number to produce the observed lateral biases.
Fraas et al. (2019b) suggested a modification of the inlet cooling hole geometry to attenuate the detrimental effect of the cross-flow on the diffuser aerodynamics. To reduce the size of a possible inlet flow separation, they proposed a rounded inlet geometry with $r_{\mathrm{inlet}} = 0.5D$. For the low coolant channel Reynolds number, the resulting adiabatic film cooling effectiveness is slightly improved but qualitatively similar compared to that of the reference geometry. For the high coolant channel Reynolds number, the qualitative and quantitative distributions of the adiabatic film cooling effectiveness change drastically (Fraas, 2019). This suggests that the expected adverse effect of the inlet flow separation is secondary compared to the in-hole swirl at the low coolant channel Reynolds number. This might be because no inlet flow separation occurs or because it is insignificantly small for the low coolant channel Reynolds number. In such cases, where the inlet flow separation is less relevant (low coolant channel Reynolds number), the in-hole swirl appears to be more relevant to the diffuser aerodynamics and critical for the one-sided flow separation in the diffuser.
Given the in-hole swirl direction, backflow into the diffuser would be favoured for $y/D \leq 0$ lead-

ing to the majority of coolant leaving the cooling hole at the opposite lateral side $y/D \geq 0$. An increase in inlet velocity ratio VR_{inlet} would lead to an increasing in-hole swirl, yielding larger positive and negative wall-normal velocities at the cooling hole exit. This is consistent with the wall-normal velocity distributions provided in section A.9.
Given the number of revolutions n_{rev} calculated based on the full hole length L for the high coolant channel Reynolds number, the velocity maximum might, by coincidence, stay on the same side. Hence, the same bias for all investigated blowing ratios would be observed.
As mentioned for the PF cases in subsection 4.2.2, the measurement data of the present work constitutes excellent validation data for numerical flow simulations. A LES validated using the flow field data of the present work could provide more insights into the in-hole flow field and the exact reason for the observed phenomena. Film cooling flows, however, constitute a challenging task for numerical flow simulations. As shown in the present work for the PF configuration, a change in inlet velocity ratio and corresponding size and position of the inlet flow separation leads to significant changes in the near-wall velocity distributions. An accurate prediction of the size and position of the inlet flow separation is, therefore, decisive for the usability of the simulation data. Experimental flow field investigations at the hole inlet could provide additional validation data for numerical simulations to potentially minimise the unknown error of the prediction of the in-hole flow field.

4.3.3 Influence of Coherent Structures on Thermal Film Cooling Quantities $\eta_{\text{a,w}}$ and h_{f}/h_0

In accordance with Saumweber et al. (2001), Gritsch et al. (2003), and Saumweber and Schulz (2008a), a detrimental effect of the orthogonal coolant cross-flow on the cooling performance was reported by Fraas et al. (2019a) and Fraas (2019) for the laidback fan-shaped film cooling hole investigated in the present work. The lateral bias of the coherent structures observed in Figure 4.11 and 4.12 agrees well with the bias of the lateral maximum in the spatial distribution of the adiabatic film cooling effectiveness discussed in Fraas et al. (2019a) and Fraas (2019). A summary of the thermal film cooling quantities for the laidback fan-shaped geometry with orthogonal coolant cross-flow is provided in subsection A.13.4. For a detailed analysis of the thermal data, the reader is referred to Fraas et al. (2019a) and Fraas (2019).
The position of the maxima of $\eta_{\text{a,w}}$ and h_{f}/h_0 are nearly coincident. The position of the maximum in h_{f}/h_0 in Figure 4.11 and 4.12 is, therefore, qualitatively representative for the $\eta_{\text{a,w}}$ maximum as well. The match between lateral bias in the flow field and $\eta_{\text{a,w}}$ implies that a majority of the coolant is transported by the dominant secondary flow structure.
As discussed previously, the dominant coherent structure is a Ω_{CV} pair for all OF cases. For the low coolant channel Reynolds number, the lateral maximum of the adiabatic film cooling effectiveness at $x/D = 5.0$ is found between the dominant Ω_{CV} legs for all blowing ratios. For the high coolant channel Reynolds number and the blowing ratios $BR = 1.0$ and 3.0, the maximum of the adiabatic film cooling effectiveness is found below the dominant vortex with negative x-vorticity at $y/D = -0.8$. For $BR = 2.0$, the lateral maximum of the adiabatic film cooling effectiveness is in between of the Ω_{CV} pair vortex legs at $y/D = -1.0$.

The laterally averaged adiabatic film cooling effectiveness $\bar{\eta}_{a,w}$ is shown in Figure 4.14a. For the high coolant channel Reynolds number, the laterally averaged adiabatic film cooling effectiveness is nearly identical for the blowing ratios $BR = 2.0$ and 3.0. This is plausible, as the secondary flow field is qualitatively identical but with higher x-vorticity magnitudes at the high blowing ratio $BR = 3.0$ (see Figure 4.12b and 4.12c). The larger amount of coolant available for the $BR = 3.0$ is, therefore, compensated by the stronger Ω_{CV} pair which carries the coolant jet further away from the wall and entrains hot gas more quickly. For $BR = 1.0$, the effectiveness is initially higher, identical at $x/D = 14$ and lower downstream, compared to that of the higher blowing ratios. The overall significantly weaker secondary flows allow the coolant to remain closer to the wall. Due to the lower amount of coolant, the streamwise reduction of the adiabatic film cooling effectiveness is much stronger compared to the higher blowing ratios.
For the low coolant channel Reynolds number and $BR = 1.0$, the laterally averaged adiabatic film cooling effectiveness is identical to that of the high coolant channel Reynolds number. For $BR = 2.0$ and 3.0, the $\bar{\eta}_{a,w}$ is much higher compared to all other OF cases. It is initially identical for both blowing ratios but reduces slightly less for the highest blowing ratio $BR = 3.0$. This drastic change of the laterally averaged adiabatic film cooling effectiveness is clearly related to the strength of the secondary flows. For the low blowing ratio $BR = 1.0$, similar x-vorticity magnitudes can be observed in the secondary flow field for both coolant channel Reynolds numbers (see Figure 4.11a and 4.12a). This suggests a similar entrainment of hot gas and, hence, a similar adiabatic wall temperature. Given that $\bar{\eta}_{a,w}$ for both coolant channel Reynolds numbers remains

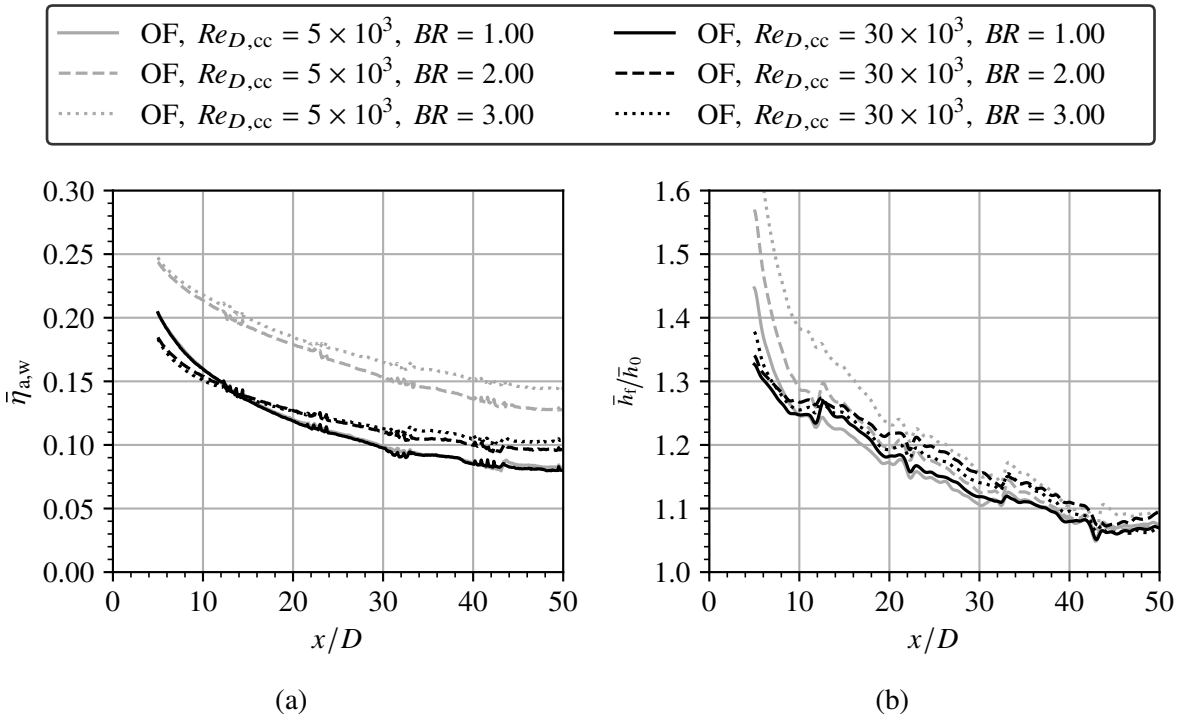

Figure 4.14: Laterally averaged (a) adiabatic film cooling effectiveness $\bar{\eta}_{a,w}$ and (b) ratio of heat transfer coefficients with and without film cooling $\bar{h}_f/\bar{h}_0$ for orthogonal flow configuration (OF); reproduced based on data in Fraas (2019)

identical along the entire downstream distance for $BR = 1.0$, it is reasonable to assume that the secondary flow field dissipates similarly quickly for both coolant channel Reynolds numbers. For the two cases at the low coolant channel Reynolds number and blowing ratio $BR = 2.0$ and 3.0, the x-vorticity magnitude is much lower compared to all other OF cases, approximately by a factor of 4 to 5. The vorticity magnitudes are, hence, closer to what is observed for the PF configuration. Due to the much lower vorticity, the hot gas entrainment is proportionally lower and the laterally averaged adiabatic film cooling effectiveness significantly higher. Due to the larger amount of available coolant at the high blowing ratio $BR = 3.0$, the laterally averaged adiabatic film cooling effectiveness remains higher in downstream direction compared to $BR = 2.0$.

According to Fraas et al. (2019a), the maximum of the ratio of heat transfer coefficients with and without film cooling h_f/h_0 appears to be laterally shifted at $x/D = 5.0$ but is close to the centreline further downstream. They assumed that a single vortex, much like observed for compound angle holes, was responsible for carrying the coolant further in lateral direction and increasing the ratio of heat transfer coefficients with and without film cooling closer to the centreline. As shown in subsection 4.3.1, the secondary flow field contains at least one dominant Ω_{CV} pair.
To really understand the connection between local heat transfer augmentation and the coherent flow structures, the local lateral distribution of the ratio of heat transfer coefficients with and without film cooling h_f/h_0 displayed by the blue lines in Figure 4.11 and 4.12 is revisited.
For the low coolant channel Reynolds number, an increase of the maximum ratio of heat transfer coefficients with and without film cooling is observed for an increase in blowing ratio at $x/D = 5.0$. The laterally averaged values of the ratio of heat transfer coefficients with and without film cooling follow the same trend as shown in Figure 4.14. The maximum of the ratio of heat transfer coefficients with and without film cooling is located in between the two Ω_{CV} legs for all cases. As for the PF configuration this is despite the fact that the Ω_{CV} pair seems reasonably close to the wall for all OF cases at the low coolant channel Reynolds number. As observed for the PF cases, a lateral fluctuation of the Ω_{CV} pair location is likely causing the single lateral maximum in contrast to what is observed in Baldauf et al. (1999b) and Baldauf (2001).
At the same time, the effect of boundary layer thinning is apparent for all blowing ratios, as the lateral distribution remains slightly increased for $y/D \leq 0$, especially for the low blowing ratio $BR = 1.0$. This is due to the secondary coherent structures at $y/D \approx -1.4$ and due to the stagnation point created between the dominant Ω_{CV} pair and the secondary coherent structure. It is, however, surprising at first that even the much larger x-vorticity magnitudes with the closest proximity to the wall for $BR = 1.0$ only yield a single lateral maximum in of h_f/h_0 located below the Ω_{CV} pair. As suggested for the PF cases already, this is thought to be related to a lateral fluctuation of the Ω_{CV} pair, leading to a reciprocating flow in between the two vortex legs. As mentioned previously, a reciprocating flow can yield significant increases in heat transfer augmentation (Ye et al., 2021).
For the high coolant channel Reynolds number, the relation between the lateral distribution of the ratio of heat transfer coefficients with and without film cooling is more convoluted but follows the same rules. An increase of h_f/h_0 is observed for stagnation areas and below coherent structures with high x-vorticities, but the observed maxima do not exactly align with either of these two as for the OF cases with low coolant channel Reynolds number. Despite the much larger

x-vorticities, the local heat transfer augmentation is much lower compared to the low coolant channel Reynolds number. This also reflects in the laterally averaged ratio of heat transfer coefficients with and without film cooling in Figure 4.14b. The reason for this is twofold. Firstly, as shown for all PF cases (see Figure 4.3 and 4.4) and the OF cases at the low coolant channel Reynolds number (see Figure 4.11), the contribution of the boundary layer thinning of the Ω_{CV} pair is evident but not prevalent. The more significant contribution is always in between the Ω_{CV} pairs and not below each Ω_{CV}. This might be related to the strong asymmetry in the wall-normal distance of the Ω_{CV} legs of the dominant pair. This can reduce the impact of a lateral unsteadiness of the Ω_{CV} pair on h_f/h_0. Secondly, the wall-normal distance of the Ω_{CV} pair is increased compared to the low coolant channel Reynolds number, which further reduces the heat transfer augmentation below the Ω_{CV} legs as long as the jet is attached to the wall.

In terms of the laterally averaged h_f/h_0 $\bar{h}_f/\bar{h}_0$, all OF cases at the high coolant channel Reynolds number show a similar and relatively lower laterally averaged ratio of heat transfer coefficients with and without film cooling compared to the cases at the low coolant channel Reynolds number. This is plausible given the previously discussed relations between the dominant coherent structures and the h_f/h_0.
For the high coolant channel Reynolds number, it can be observed in 4.12 that the distance of the Ω_{CV} pair(s) to the wall increases with an increase in blowing ratio. This is not observed for the low coolant channel Reynolds number. Although similar, the highest values of $\bar{h}_f/\bar{h}_0$ at $x/D = 5.0$ are present for the high coolant channel Reynolds number at the blowing ratio $BR = 3.0$. This suggests that the increased wall-normal distance of the Ω_{CV} pair from the wall is overcompensated by the higher x-vorticity magnitudes.
As mentioned previously, the increased wall-normal distance one of the Ω_{CV} legs reduces the impact of lateral fluctuations of the Ω_{CV} pair on the heat transfer augmentation as the reciprocating effect on the boundary layer between the vortex legs is attenuated.

The spatially and laterally averaged ratio of heat transfer coefficients with and without film cooling observed for the low coolant channel Reynolds number confirms these considerations. The ratio of heat transfer coefficients with and without film cooling increases with an increase in blowing ratio and is initially much higher for all cases compared to the high coolant channel Reynolds number. The wall-normal distance of the Ω_{CV} legs increases only slightly with an increase in blowing ratio.

4.3.4 Concluding Remarks on the Coherent Structures and their Relation to the Thermal Film Cooling Quantities $\eta_{a,w}$ and h_f/h_0

For orthogonal coolant cross-flow, the secondary flows due to the interaction of hot gas and coolant are much stronger and asymmetric. This asymmetry is typically explained as a consequence of the wake of the inlet flow separation that is transported to different locations by the in-hole swirl (Saumweber and Schulz, 2008a; Fraas, 2019). The estimated number of revolutions n_{rev}, however, suggests that, rather than the wake of the inlet flow separation, the swirl itself at the hole exit might be the primary cause for the observed flow separation in the diffuser at the low coolant channel Reynolds number.

In terms of thermal film cooling quantities, the same asymmetry is found in the spatial distributions of the adiabatic film cooling effectiveness and the ratio of heat transfer coefficients with and without film cooling. As for the PF configuration, the maximum values of the ratio of heat transfer coefficients with and without film cooling are mostly observed below the centre of the Ω_{CV} pair. Regions with the largest near-wall vorticities do, like in Aga and Abhari (2011), not coincide with the maxima in the ratio of heat transfer coefficients with and without film cooling.

4.4 Heat Flux Reduction and Coherent Structures for Parallel and Orthogonal Coolant Cross-Flow

To understand the combined effects of the adiabatic film cooling effectiveness $\eta_{a,w}$ and the ratio of heat transfer coefficients with and without film cooling h_f/h_0, the heat flux reduction Γ as defined in Equation 2.11 is used. Γ is essentially a modified version of the adiabatic film cooling effectiveness $\eta_{a,w}$ scaled by the ratio of heat transfer coefficients with and without film cooling h_f/h_0.

In Figure 4.15, the laterally averaged heat flux reduction $\overline{\Gamma}$ for the PF and OF configuration is presented. For the PF configuration (Figure 4.15a), the overall qualitative relation between the different operating conditions is similar compared to the results of the laterally averaged adiabatic film cooling effectiveness $\bar{\eta}_{a,w}$ presented in Figure 4.10a. A change in coolant channel

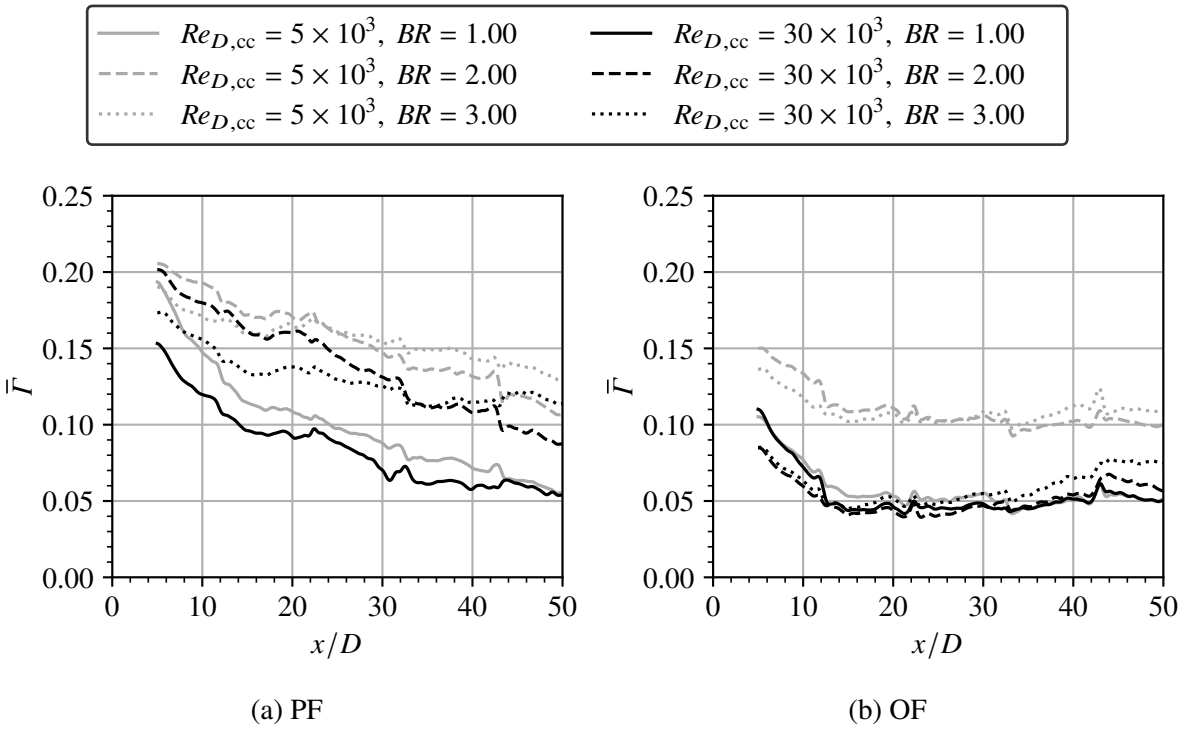

(a) PF (b) OF

Figure 4.15: Laterally averaged heat flux reduction $\overline{\Gamma}$ for (a) parallel cross-flow configuration (PF) and (a) orthogonal cross-flow configuration (OF); produced based on measurement data in Fraas (2019)

Reynolds number at constant blowing ratio does not entail any qualitative change in the laterally averaged heat flux reduction $\overline{\Gamma}$ compared to $\bar{\eta}_{\mathrm{a,w}}$. The same is true when comparing the results of the blowing ratios $BR = 1.0,\ 2.0$ and 3.0 at the low coolant channel Reynolds number. For the high coolant channel Reynolds number, a significant change in the qualitative relation for $\overline{\Gamma}$ compared to $\bar{\eta}_{\mathrm{a,w}}$ can be observed when comparing blowing ratios $BR = 2.0$ and 3.0. For both, $\overline{\Gamma}$ and $\bar{\eta}_{\mathrm{a,w}}$, the high blowing ratio $BR = 3.0$ shows lower values initially, but higher values after a certain downstream distance. This switch happens at $x/D \approx 14$ for $\bar{\eta}_{\mathrm{a,w}}$ but much later at $x/D \approx 32$ for $\overline{\Gamma}$. This can be explained by the missing Ω_{ACV} pair due to the single jet core at the cooling hole exit, leading to a more persistent Ω_{CV} pair due to its increased wall-normal distance pointed out in subsection 4.2.2. Consequently, the laterally averaged ratio of heat transfer coefficients with and without film cooling $\bar{h}_{\mathrm{f}}/\bar{h}_0$ for $BR = 3.0$ at the high coolant channel Reynolds number (see Figure 4.10b) remains higher compared to the other cases.

For the OF configuration in Figure 4.15b, the qualitative changes observed for a change in coolant channel Reynolds number at constant blowing ratio are similar as for $\bar{\eta}_{\mathrm{a,w}}$ in Figure 4.14a. The main overall difference compared to $\bar{\eta}_{\mathrm{a,w}}$ is that downstream of $x/D \approx 32$, $\overline{\Gamma}$ starts increasing again due to the continued reduction of $\bar{h}_{\mathrm{f}}/\bar{h}_0$ (see Figure 4.14b). At the high coolant channel Reynolds number, the qualitative change between the heat flux reduction for the different blowing ratios is the same as for $\bar{\eta}_{\mathrm{a,w}}$. For the low coolant channel Reynolds number, the qualitative change in $\overline{\Gamma}$ and $\bar{\eta}_{\mathrm{a,w}}$ is different when comparing the blowing ratios $BR = 2.0$ and 3.0. For $\bar{\eta}_{\mathrm{a,w}}$, the values are nearly identical at $x/D = 5.0$ but diverge downstream with a higher $\bar{\eta}_{\mathrm{a,w}}$ for the high blowing ratio $BR = 3.0$. For the laterally averaged heat flux reduction $\overline{\Gamma}$, lower values are observed for $BR = 3.0$ initially, compared to $BR = 2.0$. Downstream of $x/D \approx 27$, the laterally averaged heat flux reduction $\bar{\eta}_{\mathrm{a,w}}$ is higher for $BR = 2.0$. The reason for this is, again, the increased wall-normal distance of the Ω_{CV} pair for $BR = 3.0$ compared to $BR = 2.0$. This results in a higher $\bar{h}_{\mathrm{f}}/\bar{h}_0$ for $x \leq 20$ compared to all other cases of the OF configuration (see Figure 4.14b).

To compare the cooling performance of a specific hole geometry at various operating conditions, the area-averaged heat flux reduction $\overline{\overline{\Gamma}}$ is used. In Fraas (2019), the area-average is conducted for the entire streamwise distance where temperature data is available such that $x/D \in [5, 50]$. As can be seen in the laterally averaged heat flux reduction $\overline{\Gamma}$ in Figure 4.15, the streamwise distance along which the averaging is conducted, impacts the result. This is emphasised by the area-averaged data for all blowing ratios presented in Figure 4.16. The area-average in the present work is conducted for two different streamwise distances of $x/D \in [5, 10]$ and $x/D \in [5, 50]$ in Figure 4.16a and 4.16b, respectively. These very different ranges are chosen, as the streamwise distance between separate film cooling hole rows can vary strongly in gas turbines and jet engines. The design process is usually iterative and there are additional constraints like the airfoil aerodynamics and the internal cooling passages influencing the placement of the film cooling rows.

The area-averaged heat flux reduction $\overline{\overline{\Gamma}}$ is overall lower for a larger streamwise averaging distance. The area-averaged adiabatic film cooling effectiveness $\bar{\bar{\eta}}_{\mathrm{a,w}}$ and ratio of heat transfer coefficients with and without film cooling $\bar{\bar{h}}_{\mathrm{f}}/\bar{\bar{h}}_0$ are both reducing in streamwise direction. The comparison of Figure 4.16a and 4.16b, hence, shows that the impact of a reduced adiabatic

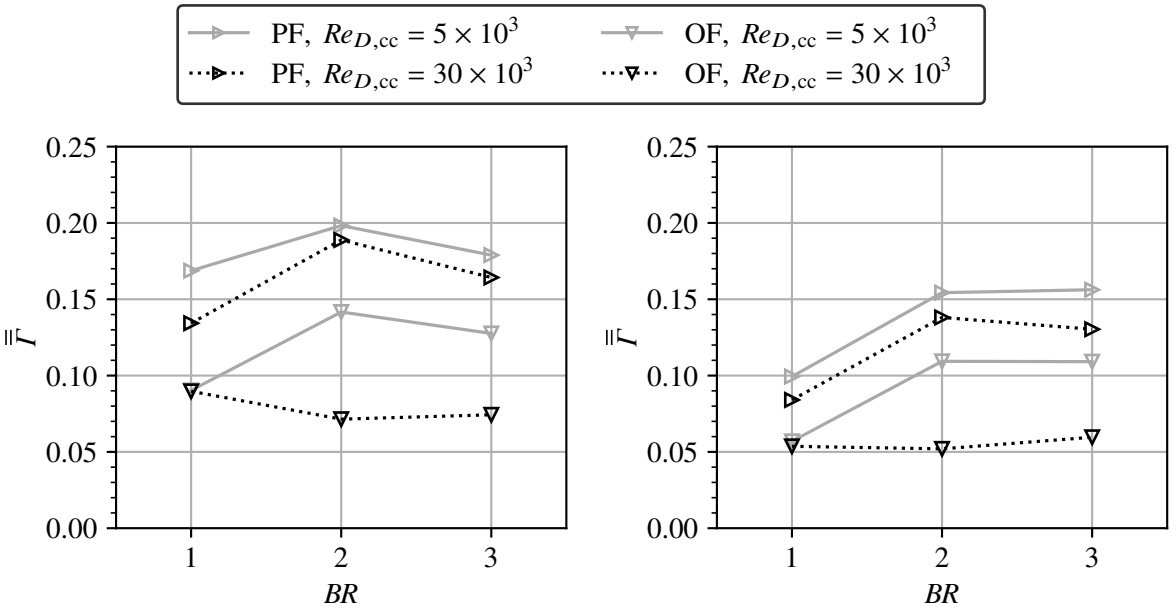

(a) $x \in [5, 10]$ (b) $x \in [5, 50]$

Figure 4.16: Area-averaged heat flux reduction $\overline{\overline{\Gamma}}$ for (a) $x/D \in [5, 10]$ and (b) $x/D \in [5, 50]$; produced based on measurement data in Fraas (2019)

film cooling effectiveness is increasingly significant for the heat flux reduction in streamwise direction. The observed reduction in $\overline{\Gamma}$ is stronger for the PF configuration compared to the OF configuration. The results presented in section 4.2 and 4.3 also show that the dominant secondary flow structures are attenuated quickly in streamwise direction. For the OF configuration, the attenuation is, however, less quick compared to the PF configuration. This is also reflected in the previously presented laterally averaged $\overline{\overline{h}}_f/\overline{\overline{h}}_0$ in Figure 4.10b and 4.14b for the PF and OF configuration, respectively. For both coolant cross-flow directions, understanding the coherent structures in the flow and their relation to the heat transfer augmentation is, therefore, more relevant when the streamwise distance between film cooling rows on the turbine blade or vane decreases. Based on $\overline{h}_f/\overline{h}_0$, the relevant downstream region in the present work extends by approximately a factor of two from $0 \leq x/D \lesssim 20$ to $0 \leq x/D \lesssim 40$ for the PF and OF configuration, respectively, when using a heat transfer augmentation of $\leq 10\,\%$ as the threshold. The optimal choice of blowing ratio BR to maximise the area-averaged heat flux reduction $\overline{\overline{\Gamma}}$ for a specific coolant channel Reynolds number and cross-flow direction changes for some configurations when comparing Figure 4.16a and 4.16b. The $\overline{\overline{\Gamma}}$-$BR$ relation appears rotated in clockwise direction from Figure 4.16a to Figure 4.16b such that a shorter streamwise averaging distance always benefits the lower blowing ratios. For the larger streamwise averaging distance of $x/D \in [5, 50]$, the change in heat flux reduction from blowing ratio $BR = 2.0$ to $BR = 3.0$ is mostly small while for $x/D \in [5, 10]$, the blowing ratio $BR = 2.0$ is clearly the optimal choice in terms of maximising the area-averaged heat flux reduction for all configurations, except for the PF configuration with the high coolant channel Reynolds number.

While it is not possible to give a generalised guideline for the design process, the information

on the coherent structures presented in section 4.1, 4.2 and 4.3 combined with the heat flux reduction Γ provides valuable insights into the relation between the coherent structures driving the heat transfer augmentation and the overall cooling performance.

5 Conclusion and Outlook

Film cooling constitutes an essential cooling method used in gas turbines and jet engines to maintain the integrity of the components under exceedingly high temperatures. From a fluid dynamics perspective, film cooling is a special case of the generic jet in cross-flow (JiC). The vast amount of fundamental research on the flow field and the coherent structures in a generic JiC is not directly transferable to a film cooling JiC as the operating conditions vary significantly. Major differences include engine-realistic temperature ratios, hot gas cross-flow turbulence intensities and coolant channel Reynolds number and cross-flow direction. Despite the well-known significant influence, the coolant (or inlet) cross-flow is neglected in the majority of fundamental and application-oriented research. In addition, the majority of application-oriented research is focused on the thermal film cooling quantities only. The flow field data that is available is mostly inconclusive and insufficient with regard to characterising the coherent structures in the film cooling JiC. Furthermore, the connection between the local coherent structures and the local ratio of heat transfer coefficients with and without film cooling has never been discussed.
The present work aimed at gathering, understanding and providing a combined data set including both, the thermal film cooling quantities and detailed information on the flow field of the cooling jet interacting with the hot gas cross-flow at engine-realistic operating conditions. The focus of this work was to characterise the dominant coherent flow structures of the JiC at parallel and orthogonal coolant cross-flow and their relation to the resulting thermal film cooling quantities, the adiabatic film cooling effectiveness $\eta_{a,w}$ and the ratio of heat transfer coefficients with and without film cooling h_f/h_0 on the adjacent wall.

For this purpose, a unique film cooling test facility at the Institute of Thermal Turbomachinery was used. It was previously build for extensive experimental investigations on the thermal film cooling quantities with a focus on fully engine-realistic operating conditions. Most importantly, this included engine-realistic temperature and blowing ratios, turbulence intensities and the mostly neglected effects of parallel and orthogonal coolant cross-flow with different coolant channel Reynolds numbers. Extensive measurements using stereoscopic Particle Image Velocimetry were conducted in the present work to complement the thermal film cooling quantities with highly resolved quasi-volumetric velocity data of the entire mixing region of the film cooling jet and the hot gas cross-flow. The investigations in the present work were focused on a laidback fan-shaped cooling hole geometry. In total, 12 different cases were investigated, varying the blowing ratio, coolant channel Reynolds number and the cross-flow direction. While the theoretical dimensionless parameters were well-defined for all investigated cases, the effective local blowing ratio or velocity ratio varied strongly at the film cooling hole exit.

For all investigated cases, irrespective of the coolant cross-flow direction, the dominant coherent flow structure appeared to be a single or double counter-rotating vortex (Ω_{CV}) pair in the plane orthogonal to the hot gas cross-flow direction.

With regard to the formation of the dominant coherent structure, the flow field data in the present work indicated differences depending on the local velocity ratio at the cooling hole exit.
For cases with local velocity ratios $VR_{local} \leq 1.0$, the direction of the shear layer vorticity in the streamwise, wall-normal centre plane was positive. The streamwise vorticity distributions

downstream of the cooling hole exit suggested that the Ω_{CV} pair observed in the plane orthogonal to the hot gas cross-flow was actually the streamwise part of the hairpin vortices Ω_{HpV}. In the plane orthogonal to the hot gas cross-flow, a Ω_{HpV} is indistinguishable from a Ω_{CV} pair.
For cases with regions of local velocity ratios $VR_{local} > 1.0$, a significant in-hole vorticity appeared to contribute largely to the formation of the Ω_{CV} pair. The negative shear layer vorticity in the streamwise, wall-normal centre plane indicated that hairpin vortices Ω_{HpV} are not dominating the resulting time-averaged flow field.

For the parallel coolant cross-flow configuration, the Ω_{CV} pair was symmetric. A single Ω_{CV} pair was present for the high coolant channel Reynolds number, while for the small coolant channel Reynolds number, two Ω_{CV} pairs were visible. In the latter case, the inner legs appeared as an additional but weaker anti counter-rotating vortex Ω_{ACV} pair located in between the Ω_{CV} pair in the plane orthogonal to the hot gas cross-flow. A significant change in the lateral and wall-normal position of the Ω_{CV} pair was observed when comparing the low and high coolant channel Reynolds number. The lateral spreading of the Ω_{CV} pair at the low coolant channel Reynolds number was significantly increased compared to the high coolant channel Reynolds number. The increased lateral spreading was responsible for keeping the coherent structures closer to the wall, leading to a higher adiabatic film cooling effectiveness $\eta_{a,w}$ and an increased ratio of heat transfer coefficients with and without film cooling h_f/h_0. Whether or not an Ω_{ACV} pair is formed was related to the local velocity distribution at the film cooling hole exit. Every significant velocity maximum at the cooling hole exit corresponded to a separate jet core. When two lateral jet cores were present, one Ω_{CV} pair was observed to develop around each jet core, irrespective of the formation process. For the low coolant channel Reynolds number, two jet cores were present resulting in two Ω_{CV} pairs, where the inner legs of each pair appeared as the Ω_{ACV} pair in the plane orthogonal to the hot gas cross-flow. The additional Ω_{ACV} pair for the parallel flow configuration at the low coolant channel Reynolds number was accompanied by a higher adiabatic film cooling effectiveness $\eta_{a,w}$ and an increase in the ratio of heat transfer coefficients with and without film cooling h_f/h_0 compared to the cases with the high coolant channel Reynolds number.
For the orthogonal coolant cross-flow configuration, the strong asymmetry of the Ω_{CV} pair was observed to agree well with the direction of asymmetry in the adiabatic film cooling effectiveness $\eta_{a,w}$ and the ratio of heat transfer coefficients with and without film cooling h_f/h_0. This asymmetry is typically explained as a consequence of the position of the in-hole velocity maximum or minimum resulting from the inlet flow separation transported along the hole by the in-hole swirl. In the present work, an estimate of the number of rotations of the coolant in the cooling hole due to the in-hole swirl was conducted. It suggested that the asymmetries observed in the flow field and the thermal film cooling quantities at the low coolant channel Reynolds number may be related to the in-hole swirl direction at the cooling hole exit.
For both, the PF and the OF cases, the streamwise location where the initiation of the Ω_{CV} pair started was directly correlated to the streamwise location of the velocity maximum at the cooling hole exit. The number of Ω_{CV} pairs observed was dependent on the number of lateral wall-normal velocity maxima at the cooling hole exit.

In terms of local heat transfer augmentation, a single, very significant lateral maximum of the

ratio of heat transfer coefficients with and without film cooling h_f/h_0 was located in between the Ω_{CV} pair for all cases where both Ω_{CV} legs had a similar wall-normal position. This was the case for all parallel flow cases and the orthogonal flow case with the low coolant channel Reynolds number. Contrary to the usual claims, the position of the lateral maximum of h_f/h_0 coincided with neither the axis of the secondary flow structures, nor the location of the maximum streamwise vorticity, nor the regions subjected to downwash and impingement of the secondary flows onto the wall where boundary layer thinning is expected. The location of the lateral maximum of h_f/h_0 did, however, coincide with the separation region of the secondary flow between the Ω_{CV} legs. As a possible explanation for the strong increase in h_f/h_0 in a separation region while no jet detachment occurs, the lateral fluctuation of the Ω_{CV} pair observed in previous studies leading up to this work was discussed. This lateral fluctuation would lead to a reciprocating boundary layer near the wall between the Ω_{CV} legs. A reciprocating boundary layer is known to increase the heat transfer significantly.
For the orthogonal coolant cross-flow case with high coolant channel Reynolds number, the maximum value of h_f/h_0 was lower by a factor of ≈ 2.0 compared to the low coolant channel Reynolds number. The lateral maximum in h_f/h_0 was biased towards the centre of the film cooling hole and located approximately below the centre of the Ω_{CV} which was further away from the wall. For these cases, the wall-normal position of the Ω_{CV} pair was not symmetric, such that one Ω_{CV} leg was significantly further away from the wall than the other. A weaker but distinguishable second lateral maximum of h_f/h_0 was present. This secondary maximum was located below regions where the secondary flow field lead to an impingement of the flow onto the wall.

For the first time, the present work provides a combined data set of the flow field and the thermal film cooling quantities of a film cooling JiC at engine-realistic operating conditions. A detailed characterisation of the coherent flow structures around and downstream of a laidback fan-shaped film cooling hole was provided and their formation discussed. It was clearly shown that quasi-volumetric flow field data is required to correctly characterise the resulting coherent structures and their formation, especially for the orthogonal coolant cross-flow configuration. Widely accepted concepts of the prevalent coherent structures based on flow field investigations on generic JiC investigations are revisited.
Unique and partially unexpected relations between the local distribution of the ratio of heat transfer coefficients with and without film cooling and the dominant coherent flow structures were observed. The results of the present work in combination with previous flow field investigations suggest that the most significant heat transfer augmentation is related to an unsteady component of the Ω_{CV} pair. The usually discussed reasons for heat transfer augmentation are observed to play a comparatively minor role. These results question the quasi-steady modelling approach for the heat transfer augmentation due to film cooling. Furthermore, the significance of understanding the impact of the dominant coherent flow structures on the heat flux reduction for the design of film cooled airfoils was outlined to provide impulses for the design process of film cooling.
Hence, the present work contributes to both, the application-oriented film cooling research field, and the fundamental understanding of the significant drivers for heat transfer augmentation in jets in cross-flow.

In future works, a more detailed analysis of the flow phenomena driving heat transfer augmen-

tation downstream of JiCs should be conducted. The analysis should focus on getting a more detailed understanding of the impact of reciprocating boundary layers on the ratio of heat transfer coefficients with and without film cooling. Furthermore, the relevance of the fluctuation frequency and amplitude to the heat transfer augmentation should be analysed to gain an optimal understanding of how to minimise the heat transfer augmentation due to film cooling. Furthermore, the limits to the steady-state assumption in terms of fluctuation frequency and amplitude in film cooling should be investigated thoroughly.
Inconsistencies in the commonly used explanation for the location of the flow separation in the diffuser based on the position of the wake of the inlet separation at the diffuser inlet were observed in the present work. To better understand the relation between the hole inlet and exit flow fields, additional PIV measurements covering the hole inlet should be conducted. Based on the (S)PIV data, numerical simulations using LES should be conducted and validated. When a good agreement is achieved, the simulation data could be used to better understand the corresponding in-hole effects and how to influence the flow field to improve the thermal film cooling quantities.

Bibliography

Abram, C., Schreivogel, P., Fond, B., Straußwald, M., Pfitzner, M., and Beyrau, F. (2016). „Investigation of Film Cooling Flows using Thermographic Particle Image Velocimetry at a 6 kHz Repetition Rate“. In: *18th International Symposium on the Application of Laser and Imaging Techniques to Fluid Mechanics*.

ACARE (2022). *Fly the Green Deal*. Tech. rep. Advisory Council for Aviation Researchand Innovation in Europe. URL: https://www.acare4europe.org/news/fly-the-green-deal/ (accessed on 30/11/2023).

Acarlar, M. S. and Smith, C. R. (1987). „A study of hairpin vortices in a laminar boundary layer. Part 2. Hairpin vortices generated by fluid injection“. In: *Journal of Fluid Mechanics*, Band 175, Heft -1, p. 43. DOI: 10.1017/s0022112087000284.

Acharya, S. and Leedom, D. H. (2012). „Large Eddy Simulations of Discrete Hole Film Cooling With Plenum Inflow Orientation Effects“. In: *Journal of Heat Transfer*, Band 135, Heft 1. DOI: 10.1115/1.4007667.

Adrian, R. J. and Westerweel, J. (2011). *Particle image velocimetry*. 30. Cambridge University Press. ISBN: 978-0-521-44008-0.

Aga, V. and Abhari, R. S. (2011). „Influence of Flow Structure on Compound Angled Film Cooling Effectiveness and Heat Transfer“. In: *Journal of Turbomachinery*, Band 133, Heft 3. DOI: 10.1115/1.4002420.

Aga, V., Rose, M., and Abhari, R. S. (2008). „Experimental Flow Structure Investigation of Compound Angled Film Cooling“. In: *Journal of Turbomachinery*, Band 130, Heft 3. DOI: 10.1115/1.2775491.

Anderson, J. B., Wilkes, E. K., McClintic, J. W., and Bogard, D. G. (2016). „Effects of Freestream Mach Number, Reynolds Number, and Boundary Layer Thickness on Film Cooling Effectiveness of Shaped Holes“. In: *Volume 5C: Heat Transfer*. American Society of Mechanical Engineers. DOI: 10.1115/gt2016-56152.

Andreopoulos, J. and Rodi, W. (1984). „Experimental investigation of jets in a crossflow“. In: *Journal of Fluid Mechanics*, Band 138, pp. 93–127. DOI: 10.1017/s0022112084000057.

Baldauf, S., Scheurlen, M., Schulz, A., and Wittig, S. (2002b). „Heat Flux Reduction From Film Cooling and Correlation of Heat Transfer Coefficients From Thermographic Measurements at Enginelike Conditions“. In: *Journal of Turbomachinery*, Band 124, Heft 4, pp. 699–709. DOI: 10.1115/1.1505848.

Baldauf, S., Schulz, A., and Wittig, S. (1999a). „High-Resolution Measurements of Local Effectiveness From Discrete Hole Film Cooling“. In: *Journal of Turbomachinery*, Band 123, Heft 4, pp. 758–765. DOI: 10.1115/1.1371778.

Baldauf, S., Schulz, A., and Wittig, S. (1999b). „High-Resolution Measurements of Local Heat Transfer Coefficients From Discrete Hole Film Cooling“. In: *Journal of Turbomachinery*, Band 123, Heft 4, pp. 749–757. DOI: 10.1115/1.1387245.

Baldauf, S. (2001). „Filmkühlung thermisch höchstbelasteter Oberflächen: Korrelation thermographischer Messungen“. Dissertation. Institut für Thermische Strömungsmaschinen, Karlsruher Institut für Technologie. ISBN: 978-3-89722-639-5.

Baldauf, S. and Scheurlen, M. (1996). „CFD Based Sensitivity Study of Flow Parameters for Engine Like Film Cooling Conditions“. In: *Volume 4: Heat Transfer; Electric Power; Industrial and Cogeneration*. American Society of Mechanical Engineers. DOI: 10.1115/96-gt-310.

Bauen, A., Bitossi, N., German, L., Harris, A., and Leow, K. (2020). „Sustainable Aviation Fuels“. In: *Johnson Matthey Technology Review*. DOI: 10.1595/205651320x15816756012040.

Beresh, S. J. (2021). „Time-resolved particle image velocimetry“. In: *Measurement Science and Technology*, Band 32, Heft 10, p. 102003. DOI: 10.1088/1361-6501/ac08c5.

Berkooz, G., Holmes, P., and Lumley, J. L. (1993). „The proper orthogonal decomposition in the analysis of turbulent flows“. In: *Annual review of fluid mechanics*, Band 25, Heft 1, pp. 539–575. DOI: 10.1146/annurev.fl.25.010193.002543.

Bernsdorf, S., Rose, M. G., and Abhari, R. S. (2005). „Modeling of Film Cooling—Part I: Experimental Study of Flow Structure“. In: *Journal of Turbomachinery*, Band 128, Heft 1, pp. 141–149. DOI: 10.1115/1.2098768.

Bernsdorf, S., Rose, M. G., and Abhari, R. S. (2008). „Experimental Validation of Quasisteady Assumption in Modeling of Unsteady Film-Cooling“. In: *Journal of Turbomachinery*, Band 130, Heft 1. DOI: 10.1115/1.2720878.

BMWK (2022). *Jahreswirtschaftsbericht 2022*. Tech. rep. Bundsministerium für Wirtschaft und Klimaschutz. URL: https://www.bundesregierung.de/breg-de/suche/jahreswirtschaftsbericht-2022-2001422 (accessed on 30/11/2023).

Bogard, D. G. and Thole, K. A. (2006). „Gas Turbine Film Cooling“. In: *Journal of Propulsion and Power*, Band 22, Heft 2, pp. 249–270. DOI: 10.2514/1.18034.

Brandes, J., Haun, M., Wrede, D., Jürgens, P., Kost, C., and Henning, H.-M. (2021). *Wege zu einem klimaneutralen Energiesytem*. Tech. rep. Fraunhofer-Institut für Solare Energiesysteme. URL: https://www.ise.fraunhofer.de/de/veroeffentlichungen/studien/wege-zu-einem-klimaneutralen-energiesystem.html (accessed on 30/11/2023).

Brittingham, R. A. and Leylek, J. H. (1997). „A Detailed Analysis of Film Cooling Physics: Part IV— Compound-Angle Injection With Shaped Holes“. In: *Journal of Turbomachinery*, Band 122, Heft 1, pp. 133–145. DOI: 10.1115/1.555419.

Brizzi, L.-E. (1994). „Contribution à l'étude de l'instabilité générée par un jet cylindrique débouchant perpendiculairement à un écoulement transversal“. thèse. Université de Poitiers.

Cambonie, T. and Aider, J.-L. (2014). „Transition scenario of the round jet in crossflow topology at low velocity ratios“. In: *Physics of Fluids*, Band 26, Heft 8, p. 084101. DOI: 10.1063/1.4891850.

Cardone, G., Meola, C., and Carlomagno, G. M. (1998). „Convective heat transfer to a jet in cross-flow“. In: *Proc. QIRT*. Vol. 98, pp. 278–83. DOI: 10.21611/qirt.1998.044.

Carlomagno, G. M. (2006). „Colours in a complex fluid flow“. In: *Optics & Laser Technology*, Band 38, Heft 4-6, pp. 230–242. DOI: 10.1016/j.optlastec.2005.06.016.

Carlomagno, G. M., Nese, F. G., and Astarita, T. (2004a). „PIV and wall convective heat transfer measurements in a round jet in cross-flow“. In: *24th International Congress of the Aeronautical Sciences*.

Carlomagno, G. M., Nese, F. G., Cardone, G., and Astarita, T. (2004b). „Thermo-fluid-dynamics of a complex fluid flow“. In: *Infrared Physics & Technology*, Band 46, Heft 1-2, pp. 31–39. DOI: 10.1016/j.infrared.2004.03.005.

Charonko, J. J. and Vlachos, P. P. (2013). „Estimation of uncertainty bounds for individual particle image velocimetry measurements from cross-correlation peak ratio“. In: *Measurement Science and Technology*, Band 24, Heft 6, p. 065301. DOI: 10.1088/0957-0233/24/6/065301.

Choe, H., Kays, W., and Moffat, R. (1974). „The superposition approach to film-cooling“. In: *American Society of Mechanical Engineers, Winter Annual Meeting*.

Coleman, H. W. and Steele, W. G. (2018). *Experimentation, Validation, and Uncertainty Analysis for Engineers*. Wiley Sons, Incorporated, John, p. 384. ISBN: 9781119417705. DOI: 10.1002/9781119417989.

Dai, C., Jia, L., Zhang, J., Shu, Z., and Mi, J. (2016). „On the flow structure of an inclined jet in crossflow at low velocity ratios“. In: *International Journal of Heat and Fluid Flow*, Band 58, pp. 11–18. DOI: 10.1016/j.ijheatfluidflow.2015.12.001.

David, L., Fraticelli, R., Calluaud, D., and Borée, J. (2004). „Cross flow investigation by stereoscopic PIV measurements“. In: *12th international symposium on application of laser techniques to fluid mechanics*, pp. 12–15.

Eberly, M. K. and Thole, K. A. (2013). „Time-Resolved Film-Cooling Flows at High and Low Density Ratios“. In: *Journal of Turbomachinery*, Band 136, Heft 6. DOI: 10.1115/1.4025574.

Fawcett, R. J., Wheeler, A. P. S., He, L., and Taylor, R. (2011). „Experimental Investigation Into Unsteady Effects on Film Cooling“. In: *Journal of Turbomachinery*, Band 134, Heft 2. DOI: 10.1115/1.4003053.

Fawcett, R. J., Wheeler, A. P., He, L., and Taylor, R. (2013). „Experimental investigation into the impact of crossflow on the coherent unsteadiness within film cooling flows“. In: *International Journal of Heat and Fluid Flow*, Band 40, pp. 32–42. DOI: 10.1016/j.ijheatfluidflow.2013.01.001.

Fearn, R. and Weston, R. P. (1974). „Vorticity Associated with a Jet in a Cross Flow“. In: *AIAA Journal*, Band 12, Heft 12, pp. 1666–1671. DOI: 10.2514/3.49576.

Foster, N. W. and Lampard, D. (1975). „Effects of density and velocity ratio on discrete hole film cooling“. In: *AIAA Journal*, Band 13, Heft 8, pp. 1112–1114. DOI: 10.2514/3.6960.

Fraas, M. (2019). „Der Einfluss der Eintrittsgeometrie auf die Kühlwirkung einer konturierten Filmkühlbohrung mit kühlluftseitiger Queranströmung“. Dissertation. Institut für Thermische Strömungsmaschinen, Karlsruher Institut für Technologie. ISBN: 978-3-8325-4970-1.

Fraas, M., Glasenapp, T., Schulz, A., and Bauer, H.-J. (2017). „Introducing a New Test Rig for Film Cooling Measurements With Realistic Hole Inflow Conditions“. In: *Volume 5C: Heat Transfer*. American Society of Mechanical Engineers. DOI: 10.1115/gt2017-63585.

Fraas, M., Glasenapp, T., Schulz, A., and Bauer, H.-J. (2019a). „Film Cooling Measurements for a Laidback Fan-Shaped Hole: Effect of Coolant Crossflow on Cooling Effectiveness and Heat Transfer“. In: *Journal of Turbomachinery*, Band 141, Heft 4, p. 041006. DOI: 10.1115/1.4041655.

Fraas, M., Glasenapp, T., Schulz, A., and Bauer, H.-J. (2019b). „Optimized inlet geometry of a laidback fan-shaped film cooling hole – Experimental study of film cooling performance“. In: *International Journal of Heat and Mass Transfer*, Band 128, pp. 980–990. DOI: 10.1016/j.ijheatmasstransfer.2018.09.035.

Fric, T. F. and Roshko, A. (1988). „Views of the Transverse Jet near Field“. In: *Physics of Fluids*, Band 31, Heft 9, pp. 2390–2390. DOI: 10.1063/1.4738825.

Fric, T. F. and Roshko, A. (1991). „Structure in the Near Field of the Transverse Jet“. In: *Turbulent Shear Flows 7*. Springer, pp. 225–237. DOI: 10.1007/978-3-642-76087-7_17.

Fric, T. F. and Roshko, A. (1994). „Vortical structure in the wake of a transverse jet“. In: *Journal of Fluid Mechanics*, Band 279, pp. 1–47. DOI: 10.1017/s0022112094003800.

Fric, T. F. (1990). „Structure in the near field of the transverse jet“. en. PhD thesis. California Institute of Technology. DOI: 10.7907/JVHG-E582.

Gelhausen, M. C., Berster, P., and Wilken, D. (2021). „Post-COVID-19 Scenarios of Global Airline Traffic until 2040 That Reflect Airport Capacity Constraints and Mitigation Strategies“. In: *Aerospace*, Band 8, Heft 10, p. 300. DOI: 10.3390/aerospace8100300.

Gogineni, S., Sutkus, D., Goss, L., and Glezer, A. (1995). „Investigation of a jet in a cross flow using PIV“. In: *33rd Aerospace Sciences Meeting and Exhibit*. American Institute of Aeronautics and Astronautics. DOI: 10.2514/6.1995-790.

Gogineni, S., Pestian, D., Rivir, R., and Goss, L. (1996). „PIV measurements of flat plate film cooling flows with high free stream turbulence“. In: *34th Aerospace Sciences Meeting and Exhibit*. American Institute of Aeronautics and Astronautics. DOI: 10.2514/6.1996-617.

Goldstein, R. J. (1971). „Film Cooling“. In: *Advances in Heat Transfer*. Elsevier, pp. 321–379. DOI: 10.1016/s0065-2717(08)70020-0.

Gritsch, M., Baldauf, S., Martiny, M., Schulz, A., and Wittig, S. (1999). „The Superposition Approach to Local Heat Transfer Coefficients in High Density Ratio Film Cooling Flows“. In: *Volume 3: Heat Transfer Electric Power Industrial and Cogeneration*. American Society of Mechanical Engineers. DOI: 10.1115/99-gt-168.

Gritsch, M., Schulz, A., and Wittig, S. (2003). „Effect of Internal Coolant Crossflow on the Effectiveness of Shaped Film-Cooling Holes“. In: *Journal of Turbomachinery*, Band 125, Heft 3, pp. 547–554. DOI: 10.1115/1.1580523.

Hada, S., Yuri, M., Masada, J., Ito, E., and Tsukagoshi, K. (2012). „Evolution and Future Trend of Large Frame Gas Turbines: A New 1600 Degree C, J Class Gas Turbine“. In: *Volume 3: Cycle Innovations Education Electric Power Fans and Blowers Industrial and Cogeneration*. American Society of Mechanical Engineers. DOI: 10.1115/gt2012-68574.

Hale, C. A. (1999). „An experimental and numerical study of the hydrodynamics and surface heat transfer associated with short film cooling holes fed by a narrow plenum“. PhD thesis. Purdue University.

Hale, C. A., Plesniak, M. W., and Ramadhyani, S. (2000). „Structural features and surface heat transfer associated with a row of short-hole jets in crossflow“. In: *International Journal of Heat and Fluid Flow*, Band 21, Heft 5, pp. 542–553. DOI: 10.1016/s0142-727x(00)00043-6.

Hancock, G. J. (1987). „A review of the aerodynamics of a jet in a cross flow“. In: *The Aeronautical Journal*, Band 91, Heft 905, pp. 201–213. DOI: 10.1017/s0001924000021254.

Haydt, S. and Lynch, S. (2018). „Flowfield of a Shaped Film Cooling Hole Over a Range of Compound Angles“. In: *Volume 5C: Heat Transfer*. American Society of Mechanical Engineers. DOI: 10.1115/gt2018-75728.

Haydt, S. and Lynch, S. (2021). „Heat Transfer Coefficient Augmentation for a Shaped Film Cooling Hole at a Range of Compound Angles“. In: *Journal of Turbomachinery*, Band 143, Heft 5. DOI: 10.1115/1.4046964.

Haydt, S., Lynch, S., and Lewis, S. (2018). „The Effect of Area Ratio Change Via Increased Hole Length for Shaped Film Cooling Holes With Constant Expansion Angles“. In: *Journal of Turbomachinery*, Band 140, Heft 5. DOI: 10.1115/1.4038871.

ICAO (2022). *Innovation for a Green Transition - 2022 Environmental Report*. Tech. rep. International Civil Aviation Organization. URL: https://www.icao.int/environmental-protection/Pages/envrep2022.aspx (accessed on 30/11/2023).

JCGM (2008). *Evaluation of measurement data—Guide to the expression of uncertainty in measurement*. Tech. rep. Joint Committee for Guides in Metrology, p. 134. URL: https://www.iso.org/sites/JCGM/GUM-JCGM100.htm (accessed on 30/11/2023).

Jessen, W., Schröder, W., and Klaas, M. (2007). „Evolution of jets effusing from inclined holes into crossflow“. In: *International Journal of Heat and Fluid Flow*, Band 28, Heft 6, pp. 1312–1326. DOI: 10.1016/j.ijheatfluidflow.2007.06.010.

Jessen, W., Konopka, M., and Schroeder, W. (2011). „Particle-Image Velocimetry Measurements of Film Cooling in an Adverse Pressure Gradient Flow“. In: *Journal of Turbomachinery*, Band 134, Heft 2. DOI: 10.1115/1.4003175.

Johnson, B., Tian, W., Zhang, K., and Hu, H. (2014). „An experimental study of density ratio effects on the film cooling injection from discrete holes by using PIV and PSP techniques“. In: *International Journal of Heat and Mass Transfer*, Band 76, pp. 337–349. DOI: 10.1016/j.ijheatmasstransfer.2014.04.028.

Johnson, B., Zhang, K., Tian, W., and Hu, H. (2013). „An Experimental Study on Film Cooling Effectiveness by Using PIV and PSP Techniques“. In: *51st AIAA Aerospace Sciences Meeting including the New Horizons Forum and Aerospace Exposition*. American Institute of Aeronautics and Astronautics. DOI: 10.2514/6.2013-603.

Jovanović, M., Lange, H. de, and Steenhoven, A. van (2006). „Influence of hole imperfection on jet cross flow interaction“. In: *International Journal of Heat and Fluid Flow*, Band 27, Heft 1, pp. 42–53. DOI: 10.1016/j.ijheatfluidflow.2005.06.003.

Kalghatgi, P. and Acharya, S. (2014). „Modal Analysis of Inclined Film Cooling Jet Flow“. In: *Journal of Turbomachinery*, Band 136, Heft 8. DOI: 10.1115/1.4026374.

Kampe, T. auf dem, Völker, S., Sämel, T., Heneka, C., Ladisch, H., Schulz, A., and Bauer, H.-J. (2012). „Experimental and Numerical Investigation of Flow Field and Downstream Surface Temperatures of Cylindrical and Diffuser Shaped Film Cooling Holes“. In: *Journal of Turbomachinery*, Band 135, Heft 1, p. 011026. DOI: 10.1115/1.4006336.

Karagozian, A. R. (2014). „The jet in crossflow“. In: *Physics of Fluids*, Band 26, Heft 10, p. 101303. DOI: 10.1063/1.4895900.

Keane, R. D. and Adrian, R. J. (1990). „Optimization of particle image velocimeters. I. Double pulsed systems“. In: *Measurement Science and Technology*, Band 1, Heft 11, pp. 1202–1215. DOI: 10.1088/0957-0233/1/11/013.

Kelso, R. M., Lim, T. T., and Perry, A. E. (1996). „An experimental study of round jets in cross-flow“. In: *Journal of Fluid Mechanics*, Band 306, pp. 111–144. DOI: 10.1017/s0022112096001255.

Kelso, R. M. and Smits, A. J. (1995). „Horseshoe vortex systems resulting from the interaction between a laminar boundary layer and a transverse jet“. In: *Physics of Fluids*, Band 7, Heft 1, pp. 153–158. DOI: 10.1063/1.868736.

Kline, S. J. (1953). „Describing uncertainty in single sample experiments“. In: *Mech. Engineering*, Band 75, pp. 3–8.

Kohli, A. and Bogard, D. G. (1998). „Effects of Very High Free-Stream Turbulence on the Jet–Mainstream Interaction in a Film Cooling Flow“. In: *Journal of Turbomachinery*, Band 120, Heft 4, pp. 785–790. DOI: 10.1115/1.2841790.

Kohli, A. and Thole, K. A. (1998). „Entrance Effects on Diffused Film-Cooling Holes“. In: *Volume 4: Heat Transfer; Electric Power; Industrial and Cogeneration*. American Society of Mechanical Engineers. DOI: 10.1115/98-gt-402.

Leboeuf, F. and Sgarzi, O. (2001). „Film Cooling in Turbines: A Review of the Behavior of Discrete Three-Dimensional Jets“. In: *Turbomachinery Fluid Dynamics and Heat Transfer*, pp. 161–177. DOI: 10.1201/9780203734919-7.

Lee, D., Fahey, D., Skowron, A., Allen, M., Burkhardt, U., Chen, Q., Doherty, S., Freeman, S., Forster, P., Fuglestvedt, J., Gettelman, A., León, R. D., Lim, L., Lund, M., Millar, R., Owen, B., Penner, J., Pitari, G., Prather, M., Sausen, R., and Wilcox, L. (2021). „The contribution of global aviation to anthropogenic climate forcing for 2000 to 2018“. In: *Atmospheric Environment*, Band 244, p. 117834. DOI: 10.1016/j.atmosenv.2020.117834.

Li, P., Eckels, S. J., Mann, G. W., and Zhang, N. (2014). „Experimental Measurements in Near-Wall Regions by Particle Image Velocimetry (PIV)“. In: American Society of Mechanical Engineers. DOI: 10.1115/fedsm2014-21918.

Lugt, H. J. (1985). „Vortices and Vorticity in Fluid Dynamics: The development of vortices may serve as a paradigm to illustrate how patterns in nature become organized“. In: *American Scientist*, Band 73, Heft 2, pp. 162–167. ISSN: 00030996. URL: http://www.jstor.org/stable/27853158 (accessed on 15/2/2023).

Mahesh, K. (2013). „The Interaction of Jets with Crossflow“. In: *Annual Review of Fluid Mechanics*, Band 45, Heft 1, pp. 379–407. DOI: 10.1146/annurev-fluid-120710-101115.

Margason, R. J. (1993). *Fifty Years of Jet in Cross Flow Research*. Tech. rep. NASA Ames Research Center. URL: https://ui.adsabs.harvard.edu/abs/1993ceaj.agar.....M/abstract (accessed on 30/11/2023).

McClintic, J. W., Fox, D. W., Jones, F. B., Bogard, D. G., Dyson, T. E., and Webster, Z. D. (2019). „Flow Physics of Diffused-Exit Film Cooling Holes Fed by Internal Crossflow“. In: *Journal of Turbomachinery*, Band 141, Heft 3. DOI: 10.1115/1.4042166.

McNamara, L. J. (2019). „Scaling film cooling adiabatic effectiveness with mass transfer and thermal experimental techniques“. PhD thesis. Air Force Institute of Technology.

Megerian, S., Davitian, J., Alves, L. S. D. B., and Karagozian, A. R. (2007). „Transverse-jet shear-layer instabilities. Part 1. Experimental studies“. In: *Journal of Fluid Mechanics*, Band 593, pp. 93–129. DOI: 10.1017/s0022112007008385.

Mersch, O. (2020). „Durchführung von Particle Image Velocimetry Messungen an einem Filmkühlversuchsstand sowie Analyse der Messdaten mit Schwerpunkt auf der Proper Orthogonal Decomposition“. Master. Institut für Thermische Strömungsmaschinen, Karlsruher Institut für Technologie. Superviser: Prof. Hans-Jörg Bauer, Co-Superviser: Katharina Stichling, M. Sc.

Metzger, D. E., Carper, H. J., and Swank, L. R. (1968). „Heat Transfer With Film Cooling Near Nontangential Injection Slots“. In: *Journal of Engineering for Power*, Band 90, Heft 2, pp. 157–162. DOI: 10.1115/1.3609155.

Metzger, D. E., Takeuchi, D. I., and Kuenstler, P. A. (1973). „Effectiveness and Heat Transfer With Full-Coverage Film Cooling“. In: *Journal of Engineering for Power*, Band 95, Heft 3, pp. 180–184. DOI: 10.1115/1.3445720.

Metzger, D. E. and Fletcher, D. D. (1971). „Evaluation of heat transfer for film-cooled turbine components“. In: *Journal of Aircraft*, Band 8, Heft 1, pp. 33–38. DOI: 10.2514/3.44223.

Muppidi, S. and Mahesh, K. (2007). „Direct numerical simulation of round turbulent jets in crossflow“. In: *Journal of Fluid Mechanics*, Band 574, pp. 59–84. DOI: 10.1017/s0022112006004034.

Ochs, M., Horbach, T., Schulz, A., Koch, R., and Bauer, H.-J. (2009). „A novel calibration method for an infrared thermography system applied to heat transfer experiments“. In: *Measurement Science and Technology*, Band 20, Heft 7, p. 075103. DOI: 10.1088/0957-0233/20/7/075103.

Ochs, M., Schulz, A., and Bauer, H.-J. (2010). „High dynamic range infrared thermography by pixelwise radiometric self calibration“. In: *Infrared Physics & Technology*, Band 53, Heft 2, pp. 112–119. DOI: 10.1016/j.infrared.2009.10.002.

Peterson, S. D. (2003). „Structural Features of Jets-in-Crossflow for Film-Cooling Applications“. In: *41st Aerospace Sciences Meeting and Exhibit*. American Institute of Aeronautics and Astronautics. DOI: 10.2514/6.2003-303.

Peterson, S. D. and Plesniak, M. W. (2002). „Short-hole jet-in-crossflow velocity field and its relationship to film-cooling performance“. In: *Experiments in Fluids*, Band 33, Heft 6, pp. 889–898. DOI: 10.1007/s00348-002-0493-9.

Peterson, S. D. and Plesniak, M. W. (2004). „Evolution of jets emanating from short holes into crossflow“. In: *Journal of Fluid Mechanics*, Band 503, pp. 57–91. DOI: 10.1017/s0022112003007407.

Plesniak, M. W. (2005). „Noncanonical Short Hole Jets-in-Crossflow for Turbine Film Cooling“. In: *Journal of Applied Mechanics*, Band 73, Heft 3, pp. 474–482. DOI: 10.1115/1.2130359.

Raffel, M., Willert, C. E., Scarano, F., Kähler, C. J., Wereley, S. T., and Kompenhans, J. (2018). *Particle Image Velocimetry*. Springer International Publishing. DOI: 10.1007/978-3-319-68852-7.

Renze, P., Schröder, W., and Meinke, M. (2007a). „Large-eddy Simulation of Film Cooling Flows with Variable Density Jets“. In: *Flow, Turbulence and Combustion*, Band 80, Heft 1, pp. 119–132. DOI: 10.1007/s10494-007-9080-8.

Renze, P., Jessen, W., and Schröder, W. (2008). „Numerical and Experimental Analysis of Cylindrical Film Cooling Holes in a Shallow Cavity“. In: *46th AIAA Aerospace Sciences Meeting and Exhibit*. American Institute of Aeronautics and Astronautics. DOI: 10.2514/6.2008-570.

Roach, P. (1987). „The generation of nearly isotropic turbulence by means of grids“. In: *International Journal of Heat and Fluid Flow*, Band 8, Heft 2, pp. 82–92. DOI: 10.1016/0142-727x(87)90001-4.

Rydholm, H. A. (1998). „An Experimental Investigation of the Velocity and Temperature Fields of Cold Jets Injected Into a Hot Crossflow“. In: *Journal of Turbomachinery*, Band 120, Heft 2, pp. 320–326. DOI: 10.1115/1.2841409.

Saha, A. K. and Yaragani, C. B. (2011). „Three-dimensional numerical study of jet-in-crossflow characteristics at low Reynolds number“. In: *Heat and Mass Transfer*, Band 48, Heft 2, pp. 391–411. DOI: 10.1007/s00231-011-0895-4.

Sau, R. and Mahesh, K. (2008). „Dynamics and mixing of vortex rings in crossflow“. In: *Journal of Fluid Mechanics*, Band 604, pp. 389–409. DOI: 10.1017/s0022112008001328.

Saumweber, C. (2005). „Filmkuehlung thermisch hochbelasteter Gasturbinenschaufeln: Moeglichkeiten und Grenzen des Einsatzes von Diffusorbohrungen“. Dissertation. Institut für Thermische Strömungsmaschinen, Karlsruher Institut für Technologie. ISBN: 3832510796.

Saumweber, C. and Schulz, A. (2008a). „Comparison the Cooling Performance of Cylindrical and Fan-Shaped Cooling Holes With Special Emphasis on the Effect of Internal Coolant Cross-Flow“. In: *Volume 4: Heat Transfer, Parts A and B*. ASMEDC. DOI: 10.1115/gt2008-51036.

Saumweber, C. and Schulz, A. (2008b). „Effect of Geometry Variations on the Cooling Performance of Fan-Shaped Cooling Holes“. In: *Volume 4: Heat Transfer, Parts A and B*. ASMEDC. DOI: 10.1115/gt2008-51038.

Saumweber, C. and Schulz, A. (2012). „Free-Stream Effects on the Cooling Performance of Cylindrical and Fan-Shaped Cooling Holes“. In: *Journal of Turbomachinery*, Band 134, Heft 6. DOI: 10.1115/1.4006287.

Saumweber, C., Schulz, A., and Wittig, S. (2003). „Free-Stream Turbulence Effects on Film Cooling With Shaped Holes“. In: *Journal of Turbomachinery*, Band 125, Heft 1, pp. 65–73. DOI: 10.1115/1.1515336.

Saumweber, C., Schulz, A., Wittig, S., and Gritsch, M. (2001). „Effects of Entrance Crossflow Directions to Film Cooling Holes“. In: *Annals of the New York Academy of Sciences*, Band 934, Heft 1, pp. 401–408. DOI: 10.1111/j.1749-6632.2001.tb05876.x.

Scarano, F. and Riethmuller, M. L. (2000). „Advances in iterative multigrid PIV image processing“. In: *Experiments in Fluids*, Band 29, Heft 7, S051–S060. DOI: 10.1007/s003480070007.

Scharnowski, S., Bross, M., and Kähler, C. J. (2018). „Accurate turbulence level estimations using PIV/PTV“. In: *Experiments in Fluids*, Band 60, Heft 1. DOI: 10.1007/s00348-018-2646-5.

Schreivogel, P., Abram, C., Fond, B., Straußwald, M., Beyrau, F., and Pfitzner, M. (2016). „Simultaneous kHz-rate temperature and velocity field measurements in the flow emanating from angled and trenched film cooling holes“. In: *International Journal of Heat and Mass Transfer*, Band 103, pp. 390–400. DOI: 10.1016/j.ijheatmasstransfer.2016.06.092.

Schripp, T., Anderson, B. E., Bauder, U., Rauch, B., Corbin, J. C., Smallwood, G. J., Lobo, P., Crosbie, E. C., Shook, M. A., Miake-Lye, R. C., Yu, Z., Freedman, A., Whitefield, P. D., Robinson, C. E., Achterberg, S. L., Köhler, M., Oßwald, P., Grein, T., Sauer, D., Voigt, C., Schlager, H., and LeClercq, P. (2022). „Aircraft engine particulate matter emissions from sustainable aviation fuels: Results from ground-based measurements during the NASA/DLR campaign ECLIF2/ND-MAX“. In: *Fuel*, Band 325, p. 124764. DOI: 10.1016/j.fuel.2022.124764.

Schroeder, R. P. and Thole, K. A. (2014). „Adiabatic Effectiveness Measurements for a Baseline Shaped Film Cooling Hole“. In: *Volume 5B: Heat Transfer*. American Society of Mechanical Engineers. DOI: 10.1115/gt2014-25992.

Schroeder, R. P. and Thole, K. A. (2016a). „Effect of High Freestream Turbulence on Flowfields of Shaped Film Cooling Holes“. In: *Journal of Turbomachinery*, Band 138, Heft 9, p. 091001. DOI: 10.1115/1.4032736.

Schroeder, R. P. and Thole, K. A. (2016c). „Thermal Field Measurements for a Shaped Hole at Low and High Freestream Turbulence Intensity“. In: *Journal of Turbomachinery*, Band 139, Heft 2. DOI: 10.1115/1.4034798.

Sciacchitano, A. (2019). „Uncertainty quantification in particle image velocimetry“. In: *Measurement Science and Technology*, Band 30, Heft 9, p. 092001. DOI: 10.1088/1361-6501/ab1db8.

Sciacchitano, A., Neal, D. R., Smith, B. L., Warner, S. O., Vlachos, P. P., Wieneke, B., and Scarano, F. (2015). „Collaborative framework for PIV uncertainty quantification: comparative assessment of methods“. In: *Measurement Science and Technology*, Band 26, Heft 7, p. 074004. DOI: 10.1088/0957-0233/26/7/074004.

Sciacchitano, A., Wieneke, B., and Scarano, F. (2013). „PIV uncertainty quantification by image matching“. In: *Measurement Science and Technology*, Band 24, Heft 4, p. 045302. DOI: 10.1088/0957-0233/24/4/045302.

Sen, B., Schmidt, D. L., and Bogard, D. G. (1996). „Film Cooling With Compound Angle Holes: Heat Transfer“. In: *Journal of Turbomachinery*, Band 118, Heft 4, pp. 800–806. DOI: 10.1115/1.2840937.

Sherif, S. and Pletcher, R. (1990). „The physical and thermal characteristics of the subsonic jet in a cross stream - a review“. In: *Mixed Convection Environ. Flows*, Band 152, pp. 83–94.

Shoji, T., Harris, E. W., Besnard, A., Schein, S. G., and Karagozian, A. R. (2020). „On the origins of transverse jet shear layer instability transition“. In: *Journal of Fluid Mechanics*, Band 890. DOI: 10.1017/jfm.2020.127.

Smith, B. L. and Oberkampf, W. L. (2014). „Limitations of and Alternatives to Traditional Uncertainty Quantification for Measurements“. In: American Society of Mechanical Engineers. DOI: 10.1115/fedsm2014-22068.

Song, L., Zhang, C., Song, Y., Li, J., and Feng, Z. (2017). „Experimental investigations on the effects of inclination angle and blowing ratio on the flat-plate film cooling enhancement using the vortex generator downstream“. In: *Applied Thermal Engineering*, Band 119, pp. 573–584. DOI: 10.1016/j.applthermaleng.2017.03.089.

Stichling, K. and Bauer, H.-J. (2022a). „Aerothermal Analysis of Film Cooling Flows“. en. In: *Proceedings of the 25th ISABE Conference, Ottawa, CAN, September 25-30, 2022*. International Society of Air-Breathing Engines (ISABE). DOI: 10.5445/IR/1000156259.

Stichling, K. and Bauer, H.-J. (2022b). „Aerothermal comparison of a diffuser hole and a slot geometry: thermal performance and jet stability“. In: *Proceedings of GPPS Forum 22, Chania, GR, September 12-14, 2022*. DOI: 10.33737/jgpps/163087.

Stichling, K., Elfner, M., and Bauer, H.-J. (2020). „Investigation of Film Cooling Using Time-Resolved Stereo Particle Image Velocimetry“. In: *Volume 7B: Heat Transfer*. American Society of Mechanical Engineers. DOI: 10.1115/gt2020-14403.

Stichling, K., Elfner, M., and Bauer, H.-J. (2021). „Investigation of Film Cooling Using Time-Resolved Stereo Particle Image Velocimetry“. In: *Journal of Turbomachinery*, Band 143, Heft 7, p. 071014. DOI: 10.1115/1.4050391.

Straußwald, M., Abram, C., Sander, T., Beyrau, F., and Pfitzner, M. (2020). „Time-resolved temperature and velocity field measurements in gas turbine film cooling flows with mainstream turbulence“. In: *Experiments in Fluids*, Band 62, Heft 1. DOI: 10.1007/s00348-020-03087-2.

Straußwald, M., Sander, T., Bakhtiari, A., and Pfitzner, M. (2018). „High-Speed Velocity Measurements of Film Cooling Applications at High-Turbulence Main Flow Conditions“. In: *Volume 5C: Heat Transfer*. American Society of Mechanical Engineers. DOI: 10.1115/gt2018-76458.

Stripf, M. (2007). „Einfluss der Oberflächenrauigkeit auf die transitionale Grenzschicht an Gasturbinenschaufeln: experimentelle Untersuchungen und Entwicklung eines Berechnungsverfahrens“. Dissertation. Institut für Thermische Strömungsmaschinen, Karlsruher Institut für Technologie.

Taherian, M. and Mohammadian, A. (2021). „Buoyant Jets in Cross-Flows: Review, Developments, and Applications“. In: *Journal of Marine Science and Engineering*, Band 9, Heft 1, p. 61. DOI: 10.3390/jmse9010061.

Takeishi, K. (2017). „Progress Of Film Cooling In Industrial Gas Turbine Vanes And Blades“. In: *12th European Conference on Turbomachinery Fluid dynamics Thermodynamics*.

Takeishi, K., Oda, Y., Egawa, Y., and Kitamura, T. (2010). „Film cooling with swirling coolant flow“. In: *Advanced Computational Methods and Experiments in Heat Transfer XI*. WIT Press. DOI: 10.2495/ht100171.

Takeishi, K., Komiyama, M., Oda, Y., and Egawa, Y. (2013). „Aerothermal Investigations on Mixing Flow Field of Film Cooling With Swirling Coolant Flow“. In: *Journal of Turbomachinery*, Band 136, Heft 5. DOI: 10.1115/1.4023909.

Takeishi, K., Komiyama, M., Oda, Y., Mori, S., and Kitamura, T. (2011). „Study on the Thermal and Flow Fields of Shaped Film-Cooling Holes“. In: *Heat Transfer Research*, Band 42, Heft 1, pp. 83–100. DOI: 10.1615/heattransres.v42.i1.70.

Thole, K. A., Gritsch, M., Schulz, A., and Wittig, S. (1997). „Effect of a Crossflow at the Entrance to a Film-Cooling Hole“. In: *Journal of Fluids Engineering*, Band 119, Heft 3, pp. 533–540. DOI: 10.1115/1.2819277.

Tyagi, M. and Acharya, S. (2003). „Large Eddy Simulation of Film Cooling Flow From an Inclined Cylindrical Jet“. In: *Journal of Turbomachinery*, Band 125, Heft 4, pp. 734–742. DOI: 10.1115/1.1625397.

UN (2016). *The Paris Agreement*. Tech. rep. United Nations. URL: https://unfccc.int/process-and-meetings/the-paris-agreement/the-paris-agreement (accessed on 30/11/2023).

Wernet, M. P., Wroblewski, A. C., and Locke, R. J. (2016). *A Dual-Plane PIV Study of Turbulent Heat Transfer Flows*. Tech. rep. Glenn Research Center.

Wieneke, B. (2015). „PIV uncertainty quantification from correlation statistics“. In: *Measurement Science and Technology*, Band 26, Heft 7, p. 074002. DOI: 10.1088/0957-0233/26/7/074002.

Wieneke, B. (2017). „PIV Uncertainty Quantification and Beyond“. en. In: DOI: 10.13140/RG.2.2.26244.42886.

Wiese, C. J. and Rutledge, J. L. (2021). „The Effects of Specific Heat and Viscosity on Film Cooling Behavior“. In: *Journal of Turbomachinery*, Band 143, Heft 4. DOI: 10.1115/1.4049785.

Wright, L. M., Gao, Z., Varvel, T. A., and Han, J.-C. (2005). „Assessment of Steady State PSP, TSP, and IR Measurement Techniques for Flat Plate Film Cooling“. In: *Heat Transfer: Volume 3*. ASMEDC. DOI: 10.1115/ht2005-72363.

Wright, L. M., McClain, S. T., Brown, C. P., and Harmon, W. V. (2013). „Assessment of a Double Hole Film Cooling Geometry Using S-PIV and PSP“. In: *Volume 3B: Heat Transfer*. American Society of Mechanical Engineers. DOI: 10.1115/gt2013-94614.

Wright, L. M., McClain, S. T., and Clemenson, M. D. (2011a). „Effect of Freestream Turbulence Intensity on Film Cooling Jet Structure and Surface Effectiveness Using PIV and PSP“. In: *Journal of Turbomachinery*, Band 133, Heft 4, p. 041023. DOI: 10.1115/1.4003051.

Wright, L. M., McClain, S. T., and Clemenson, M. D. (2011b). „PIV Investigation of the Effect of Freestream Turbulence Intensity on Film Cooling From Fanshaped Holes“. In: *Volume 5: Heat Transfer, Parts A and B*. ASMEDC. DOI: 10.1115/gt2011-46127.

Ye, Q., Zhang, Y., and Wei, J. (2021). „A comprehensive review of pulsating flow on heat transfer enhancement“. In: *Applied Thermal Engineering*, Band 196, p. 117275. DOI: 10.1016/j.applthermaleng.2021.117275.

Zamiri, A., You, S. J., and Chung, J. T. (2020). „Large eddy simulation of unsteady turbulent flow structures and film-cooling effectiveness in a laidback fan-shaped hole“. In: *Aerospace Science and Technology*, Band 100, p. 105793. DOI: 10.1016/j.ast.2020.105793.

Zhou, W. and Hu, H. (2015). „An Experimental Study on Film Cooling Performance Behind Barchan Dune-Shaped Ramps Using PSP and PIV Techniques“. In: *Volume 5B: Heat Transfer*. American Society of Mechanical Engineers. DOI: 10.1115/gt2015-43781.

Zhou, W. and Hu, H. (2016a). „An Experimental Study of Barchan-Dune-Shaped Injection Compounds for Improved Film Cooling Effectiveness“. In: *32nd AIAA Aerodynamic Measurement Technology and Ground Testing Conference*. American Institute of Aeronautics and Astronautics. DOI: 10.2514/6.2016-3407.

Zhou, W. and Hu, H. (2016b). „Improvements of film cooling effectiveness by using Barchan dune shaped ramps“. In: *International Journal of Heat and Mass Transfer*, Band 103, pp. 443–456. DOI: 10.1016/j.ijheatmasstransfer.2016.07.066.

Zhou, W. and Hu, H. (2017). „A novel sand-dune-inspired design for improved film cooling performance“. In: *International Journal of Heat and Mass Transfer*, Band 110, pp. 908–920. DOI: 10.1016/j.ijheatmasstransfer.2017.03.091.

Zhou, W., Johnson, B., and Hu, H. (2014). „An Experimental Study of Momentum-Preserving Shaped Holes for Film Cooling Using PSP and PIV“. In: *52nd Aerospace Sciences Meeting*. American Institute of Aeronautics and Astronautics. DOI: 10.2514/6.2014-0280.

Zhou, W., Johnson, B., and Hu, H. (2017). „Effects of Flow Compressibility and Density Ratio on Film Cooling Performance“. In: *Journal of Propulsion and Power*, Band 33, Heft 4, pp. 964–974. DOI: 10.2514/1.b36275.

Relevant Supervised Student Projects

Mersch, O. (2020). „Durchführung von Particle Image Velocimetry Messungen an einem Filmkühlversuchsstand sowie Analyse der Messdaten mit Schwerpunkt auf der Proper Orthogonal Decomposition“. Master. Institut für Thermische Strömungsmaschinen, Karlsruher Institut für Technologie. Superviser: Prof. Hans-Jörg Bauer, Co-Superviser: Katharina Stichling, M. Sc.

Previous Publications of the Author

Bicat, D., Stichling, K., Elfner, M., Bauer, H.-J., and Lehmann, K. (2022). „Experimental investigation of the influence of film cooling hole diameter on the total cooling effectiveness for cyclone-cooled turbine blades“. In: *Proceedings of Global Power and Propulsion Society*. GPPS. DOI: 10.33737/gpps22-tc-32.

Jackowski, T., Elfner, M., Bauer, H.-J., Stichling, K., and Hahn, M. (2021). „Experimental Study of Impingement Effusion Cooled Double-Wall Combustor Liners: Aerodynamic Analysis with Stereo-PIV“. In: *Energies*, Band 14, Heft 19, p. 6191. DOI: 10.3390/en14196191. URL: https://www.mdpi.com/1996-1073/14/19/6191.

Okraschevski, M., Hoffmann, S., Stichling, K., Koch, R., and Bauer, H.-J. (2021). „Fluid dynamics beyond the continuum: A physical perspective on large-eddy simulation“. In: *Physical Review Fluids*, Band 6, Heft 10, p. l102601. DOI: 10.1103/physrevfluids.6.l102601.

Stichling, K. and Bauer, H.-J. (2022a). „Aerothermal Analysis of Film Cooling Flows“. en. In: *Proceedings of the 25th ISABE Conference, Ottawa, CAN, September 25-30, 2022*. International Society of Air-Breathing Engines (ISABE). DOI: 10.5445/IR/1000156259.

Stichling, K. and Bauer, H.-J. (2022b). „Aerothermal comparison of a diffuser hole and a slot geometry: thermal performance and jet stability“. In: *Proceedings of GPPS Forum 22, Chania, GR, September 12-14, 2022*. DOI: 10.33737/jgpps/163087.

Stichling, K., Elfner, M., and Bauer, H.-J. (2020). „Investigation of Film Cooling Using Time-Resolved Stereo Particle Image Velocimetry“. In: *Volume 7B: Heat Transfer*. American Society of Mechanical Engineers. DOI: 10.1115/gt2020-14403.

Stichling, K., Elfner, M., and Bauer, H.-J. (2021). „Investigation of Film Cooling Using Time-Resolved Stereo Particle Image Velocimetry“. In: *Journal of Turbomachinery*, Band 143, Heft 7, p. 071014. DOI: 10.1115/1.4050391.

Appendix

A.1 Supplementary Bibliography on Flow Field Measurements in Film Cooling Flows

In the following, an extensive list of previous flow field investigations on film cooling jets in cross-flow not mentioned in subsection 2.2.3 is provided. To the best knowledge of the author, this list includes all existing additional flow field investigations related to film cooling JiCs.

Aga, V. (2009). „Experimental investigation of the influence of flow structure on compound angled film cooling performance“. en. PhD thesis. ETH Zurich. DOI: 10.3929/ETHZ-A-006015291.

Berger, P. A. and Liburdy, J. A. (1998). „A Near-Field Investigation Into the Effects of Geometry and Compound Angle on the Flowfield of a Row of Film Cooling Holes“. In: *Volume 4: Heat Transfer Electric Power Industrial and Cogeneration*. American Society of Mechanical Engineers. DOI: 10.1115/98-gt-279.

Bernsdorf, S. (2005). „Experimental investigation of film cooling flow structure“. en. Dissertation. ETH Zurich. DOI: 10.3929/ETHZ-A-005122587.

Borghi, M. R., Poinsatte, P., Thurman, D., and Engblom, W. (2017). „Preliminary Numerical and Experimental Evaluation of Turbulent Mixing from Thin-Film Cooling“. In: *55th AIAA Aerospace Sciences Meeting*. American Institute of Aeronautics and Astronautics. DOI: 10.2514/6.2017-1004.

Böttger, M., Lange, M., Mailach, R., and Vogeler, K. (2020). „Experimental Study on the Influence of Film Cooling Hole Extraction on Heat Transfer and Flow Field in Internal Ribbed Cooling Channels of Turbine Blades“. In: *Journal of Turbomachinery*, Band 142, Heft 10. DOI: 10.1115/1.4047608.

Castán, C. P. M. (2018). „Film cooling aerodynamic performance. Flow structures and aerodynamic losses in an airfoil with pressure side injection“. MA thesis. Delft University of Technology.

Figueiredo, A. J. C., Jones, R., Pountney, O. J., Scobie, J. A., Lock, G. D., Sangan, C. M., and Cleaver, D. J. (2018). „Volumetric Velocimetry Measurements of Film Cooling Jets“. In: *Journal of Engineering for Gas Turbines and Power*, Band 141, Heft 3. DOI: 10.1115/1.4041206.

Getsinger, D. R., Dees, J. E., and Rodebaugh, G. P. (2015). „Flowfield and Film Performance Measurements of Axial Shaped Cooling Holes on a Flat Plate“. In: *45th AIAA Fluid Dynamics Conference*. American Institute of Aeronautics and Astronautics. DOI: 10.2514/6.2015-2929.

Haven, B. A. and Kurosaka, M. (1997). „Kidney and anti-kidney vortices in crossflow jets“. In: *Journal of Fluid Mechanics*, Band 352, pp. 27–64. DOI: 10.1017/s0022112097007271.

Hodges, J., Fernandes, C. P., Fernandez, E., and Kapat, J. S. (2019). „Flow Statistics and Visualization of Multirow Film Cooling Boundary Layers Emanating From Cylindrical and Diffuser Shaped Holes“. In: *Journal of Turbomachinery*, Band 141, Heft 6. DOI: 10.1115/1.4041867.

Hu, H., Zhou, W., and Johnson, B. (2015). „An Experimental Study of Compressibility Effects on the Film Cooling Effectiveness Using PSP and PIV Techniques“. In: *53rd AIAA Aerospace*

Sciences Meeting. American Institute of Aeronautics and Astronautics. DOI: 10.2514/6.2015-0352.

Jovanović, M. (2006). „Film cooling through imperfect holes“. en. PhD thesis. Eindhoven University of Technology. ISBN: 90-386-2888-9. DOI: 10.6100/IR613186.

Lange, H. C. de (2014). „Jet in crossflow: Experiments on the interaction of flow-structure and cooling efficiency“. In: *International Conference on Heat Transfer, Fluid Mechanics and Thermodynamics*. International Conference on Heat Transfer, Fluid Mechanics and Thermodynamics.

Lenzi, T., Palanti, L., Picchi, A., Bacci, T., Mazzei, L., Andreini, A., and Facchini, B. (2020a). „Time-Resolved Flow Field Analysis of Effusion Cooling System With Representative Swirling Main Flow“. In: *Journal of Turbomachinery*, Band 142, Heft 6. DOI: 10.1115/1.4046181.

Lenzi, T., Picchi, A., Bacci, T., Andreini, A., and Facchini, B. (2020b). „Unsteady Flow Field Characterization of Effusion Cooling Systems with Swirling Main Flow: Comparison Between Cylindrical and Shaped Holes“. In: *Energies*, Band 13, Heft 19, p. 4993. DOI: 10.3390/en13194993.

Natsui, G. (2015). „Multi-Row Film Cooling Boundary Layers“. PhD thesis. University of Central Florida. URL: https://stars.library.ucf.edu/etd/1464/.

Natsui, G., Voet, M. T., Little, Z., Fernandez, E., Kapat, J., and Dees, J. E. (2016b). „Hydrodynamic Measurements Throughout a Flat Plate Multi-Row Film Cooling Array With Inclined Holes“. In: *Volume 5C: Heat Transfer*. American Society of Mechanical Engineers. DOI: 10.1115/gt2016-56184.

Rouina, S., Miranda, M., and Barigozzi, G. (2016). „Experimental Investigation of the Unsteady Flow Behavior on a Film Cooling Flat Plate“. In: *Energy Procedia*, Band 101, pp. 726–733. DOI: 10.1016/j.egypro.2016.11.092.

Schroeder, R. P. and Thole, K. A. (2016b). „Effect of In-Hole Roughness on Film Cooling From a Shaped Hole“. In: *Journal of Turbomachinery*, Band 139, Heft 3. DOI: 10.1115/1.4034847.

Shyam, V., Thurman, D. R., Poinsatte, P. E., Ameri, A. A., and Culley, D. E. (2018). *Toward Cooling Uniformity: Investigation of Spiral, Sweeping Holes, and Unconventional Cooling Paradigms*. Tech. rep. Glenn Research Center.

Stephan, M., Lee, H., Albert, B., Dreizler, A., and Böhm, B. (2016). „Simultaneous planar gas-phase temperature and velocity measurements within a film cooling configuration using thermographic phosphors“. In: *18th International Symposium on the Application of Laser and Imaging Techniques to Fluid Mechanics*.

Straußwald, M., Sander, T., Abram, C., and Pfitzner, M. (2022). „Investigating the Influence of Mainstream Turbulence and Large Vortices on Gas Turbine Trenched Film Cooling Flows Using Planar Temperature-Velocity Imaging“. In: *Journal of Turbomachinery*, Band 144, Heft 10. DOI: 10.1115/1.4054215.

Takeishi, K., Oda, Y., Mori, S., and Krewinkel, R. (2020). „Effect of main stream turbulence on the film cooling effectiveness of a circular and a fan-shaped film cooling hole“. In: *Mechanical Engineering Journal*, Band 7, Heft 4, pp. 20–00176–20–00176. DOI: 10.1299/mej.20-00176.

Thurman, D., Poinsatte, P., Ameri, A., Culley, D., Raghu, S., and Shyam, V. (2016). „Investigation of Spiral and Sweeping Holes“. In: *Journal of Turbomachinery*, Band 138, Heft 9. DOI: 10.1115/1.4032839.

Voet, M. T., Fernandes, C. P., Little, Z., Fernandez, E., and Kapat, J. (2017). „Effect of Density Ratio on Multi-Row Film Cooling Performance“. In: *Volume 5C: Heat Transfer*. American Society of Mechanical Engineers. DOI: 10.1115/gt2017-64097.

Watson, T. B., Nahang-Toudeshki, S., Wright, L. M., Crites, D. C., Morris, M. C., and Riahi, A. (2016). „Application of S-PIV for Investigation of Round and Shaped Film Cooling Holes at High Density Ratios“. In: American Society of Mechanical Engineers. DOI: 10.1115/gt2016-56209.

Wright, L. M., McClain, S. T., and Clemenson, M. D. (2010). „Effect of Freestream Turbulence Intensity on Film Cooling Jet Structure and Surface Effectiveness Using PIV and PSP“. In: *Volume 4: Heat Transfer, Parts A and B*. ASMEDC. DOI: 10.1115/gt2010-23054.

Zhou, W. (2016). „Novel cooling strategies for improved protection ofgas turbine blades“. PhD thesis. Iowa State University.

A.2 PF: Velocity Distributions at Hole Outlet: Streamwise Velocity Component u

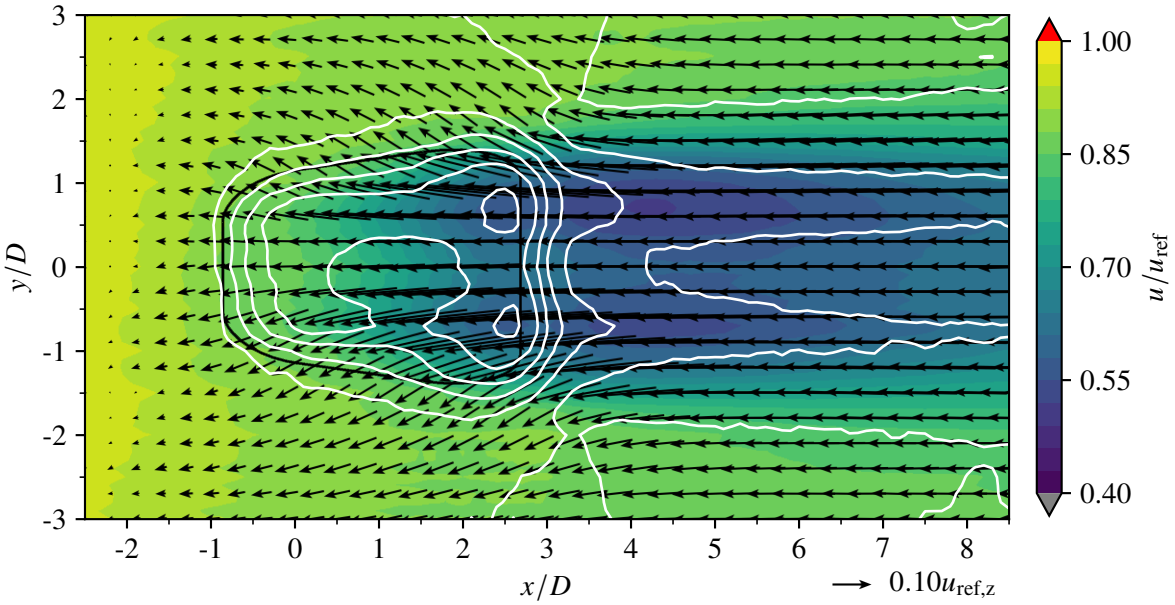

(a) PF, $Re_{D,\mathrm{cc}} = 5 \times 10^3$, $BR = 1.0$

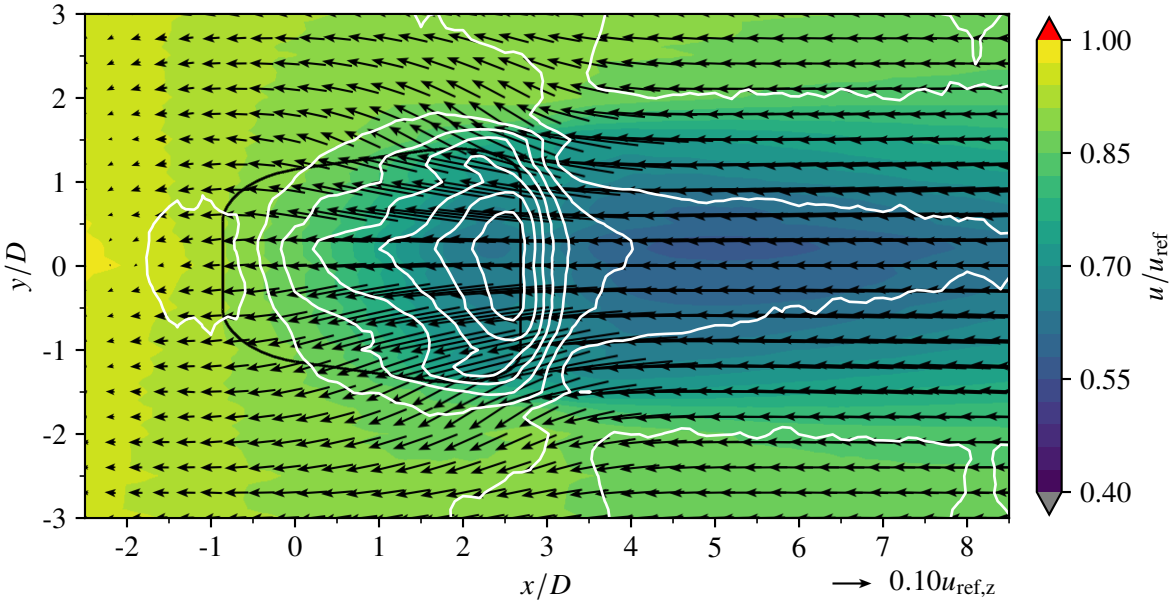

(b) PF, $Re_{D,\mathrm{cc}} = 30 \times 10^3$, $BR = 1.0$

Figure A.1: Impact of the coolant ejection on the near-wall streamwise velocity, u, and in-plane velocity field, $\left(\left(u - u_{\mathrm{ref,z}}\right), v\right)$, at $z/D = 0.3$ for $BR = 1.0$. The white lines correspond to the contours of wall-normal velocity w shown in section A.4.

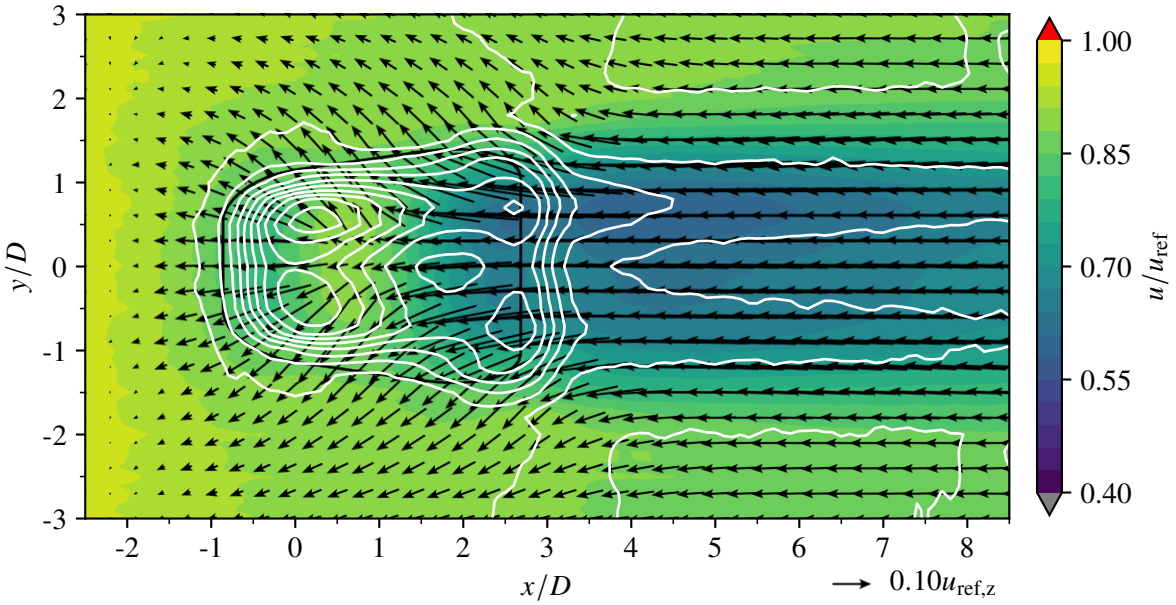

(a) PF, $Re_{D,\mathrm{cc}} = 5 \times 10^3$, $BR = 2.0$

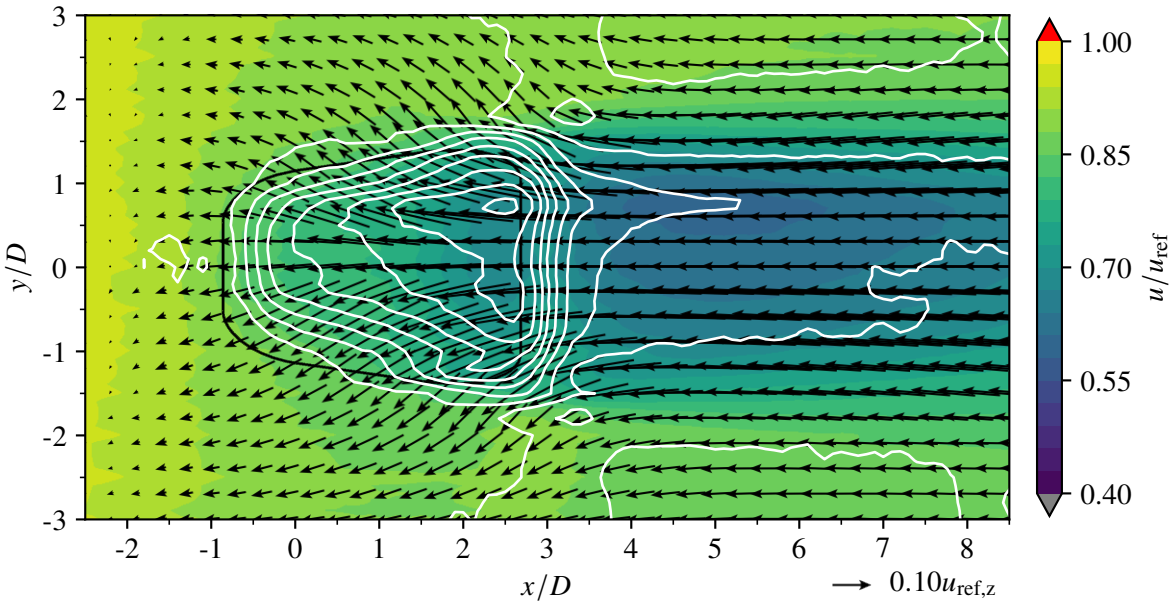

(b) PF, $Re_{D,\mathrm{cc}} = 30 \times 10^3$, $BR = 2.0$

Figure A.2: Impact of the coolant ejection on the near-wall streamwise velocity, u, and in-plane velocity field, $\left(\left(u - u_{\mathrm{ref,z}}\right), v\right)$, at $z/D = 0.3$ for $BR = 2.0$. The white lines correspond to the contours of wall-normal velocity w shown in section A.4.

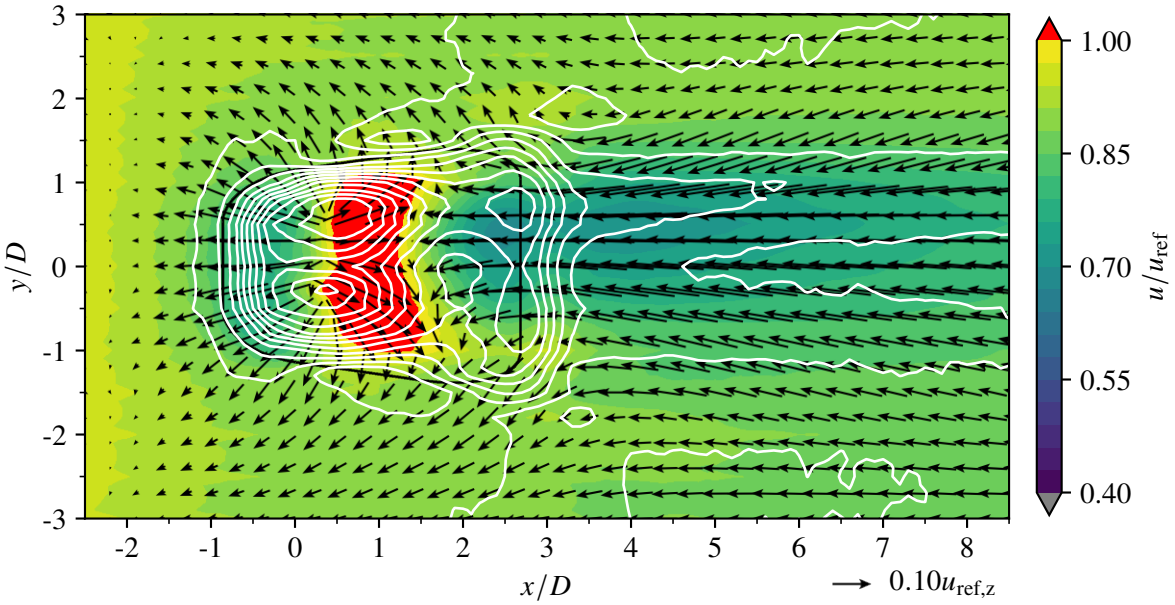

(a) PF, $Re_{D,\mathrm{cc}} = 5 \times 10^3$, $BR = 3.0$

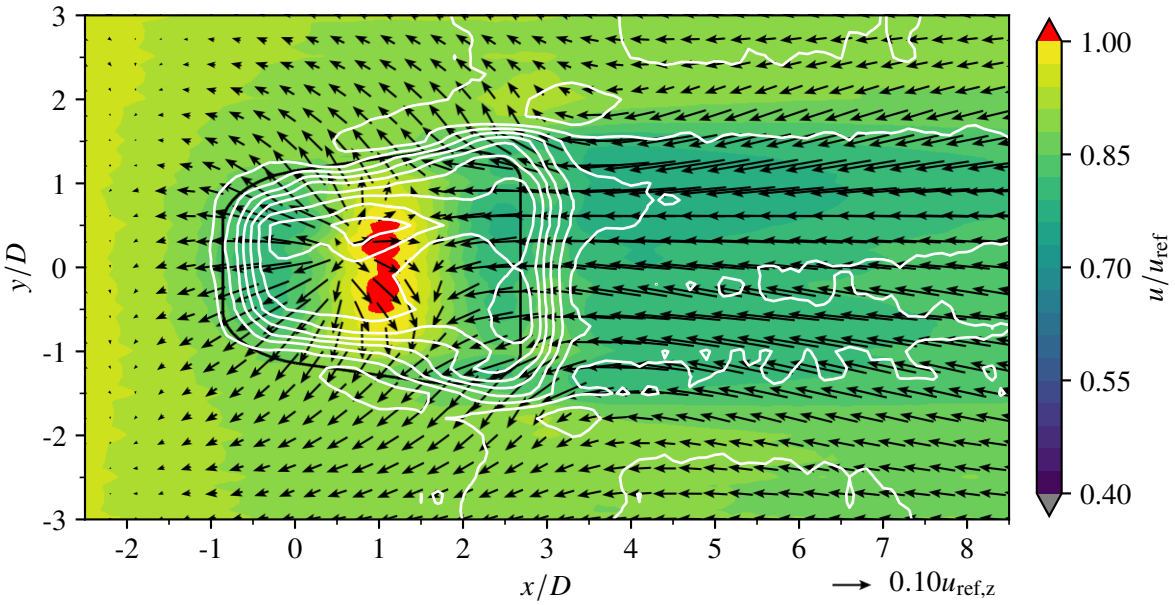

(b) PF, $Re_{D,\mathrm{cc}} = 30 \times 10^3$, $BR = 3.0$

Figure A.3: Impact of the coolant ejection on the near-wall streamwise velocity, u, and in-plane velocity field, $\left(\left(u - u_{\mathrm{ref,z}}\right), v\right)$, at $z/D = 0.3$ for $BR = 3.0$. The white lines correspond to the contours of wall-normal velocity w shown in section A.4.

A.3 PF: Velocity Distributions at Hole Outlet: Lateral Velocity Component v

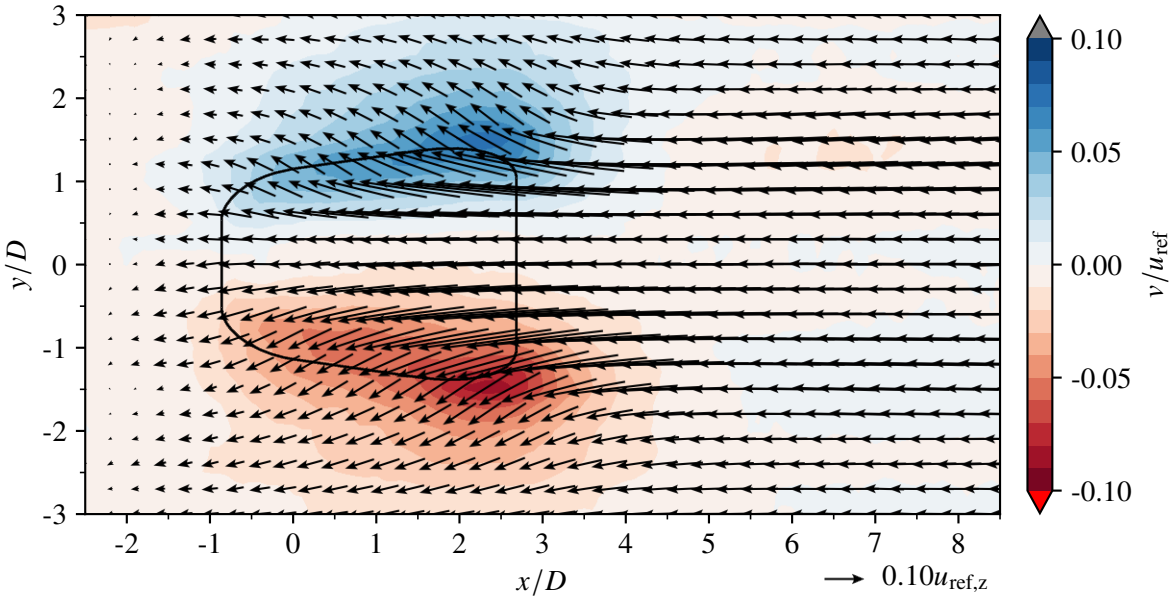

(a) PF, $Re_{D,\mathrm{cc}} = 5 \times 10^3$, $BR = 1.0$

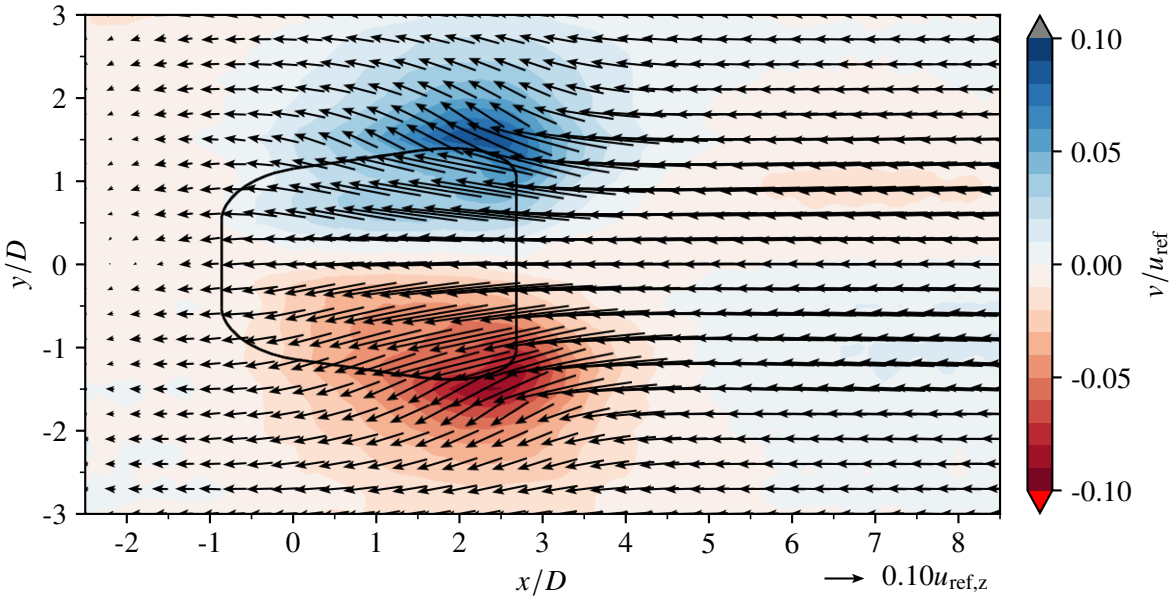

(b) PF, $Re_{D,\mathrm{cc}} = 30 \times 10^3$, $BR = 1.0$

Figure A.4: Impact of the coolant ejection on the near-wall lateral velocity, v, and in-plane velocity field, $\left(\left(u - u_{\mathrm{ref,z}}\right), v\right)$, at $z/D = 0.3$ for $BR = 1.0$.

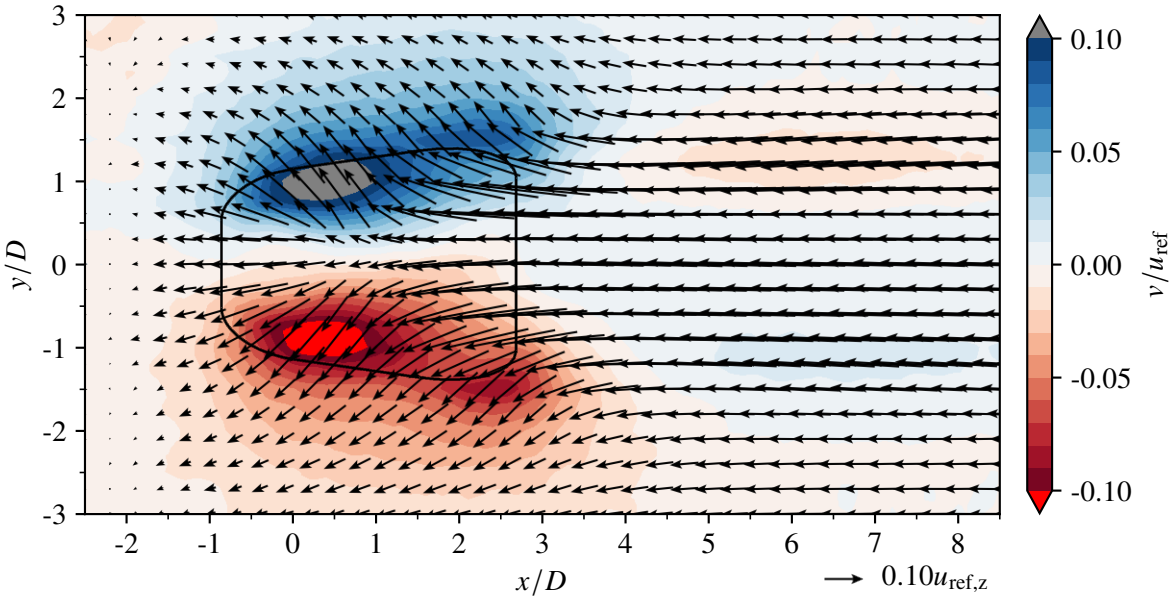

(a) PF, $Re_{D,\mathrm{cc}} = 5 \times 10^3$, $BR = 2.0$

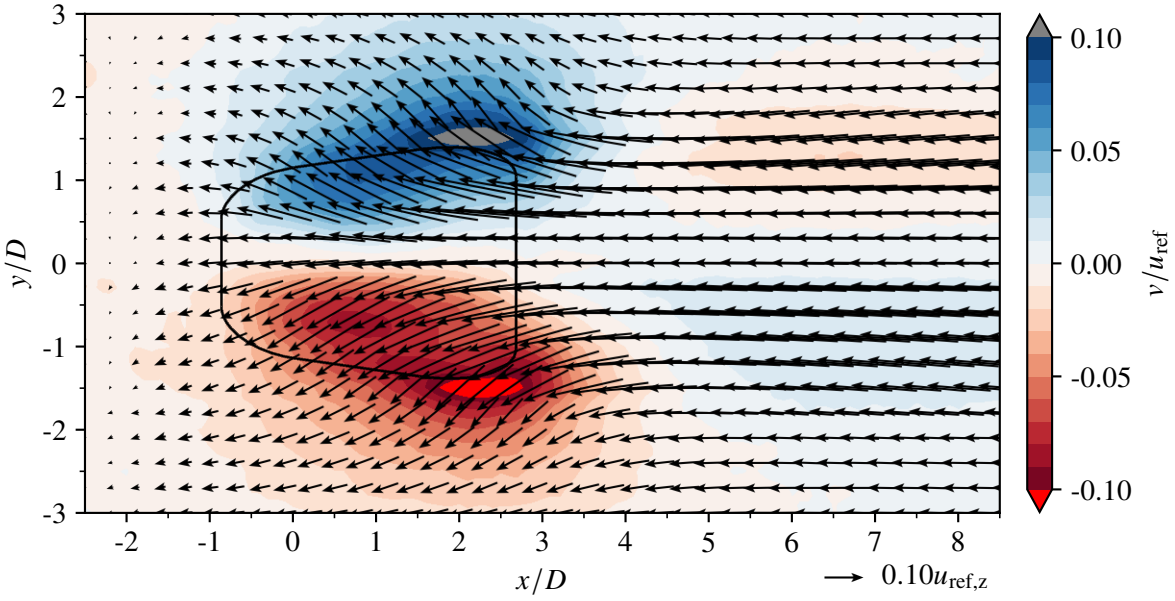

(b) PF, $Re_{D,\mathrm{cc}} = 30 \times 10^3$, $BR = 2.0$

Figure A.5: Impact of the coolant ejection on the near-wall lateral velocity, v, and in-plane velocity field, $\left(\left(u - u_{\mathrm{ref,z}}\right), v\right)$, at $z/D = 0.3$ for $BR = 2.0$.

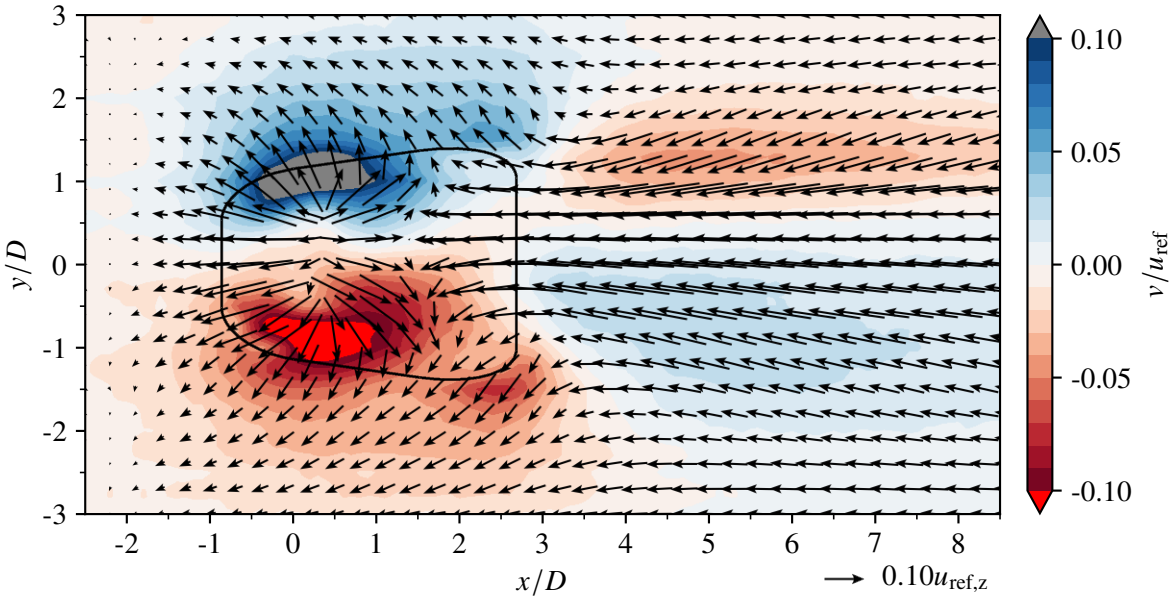

(a) PF, $Re_{D,\mathrm{cc}} = 5 \times 10^3$, $BR = 3.0$

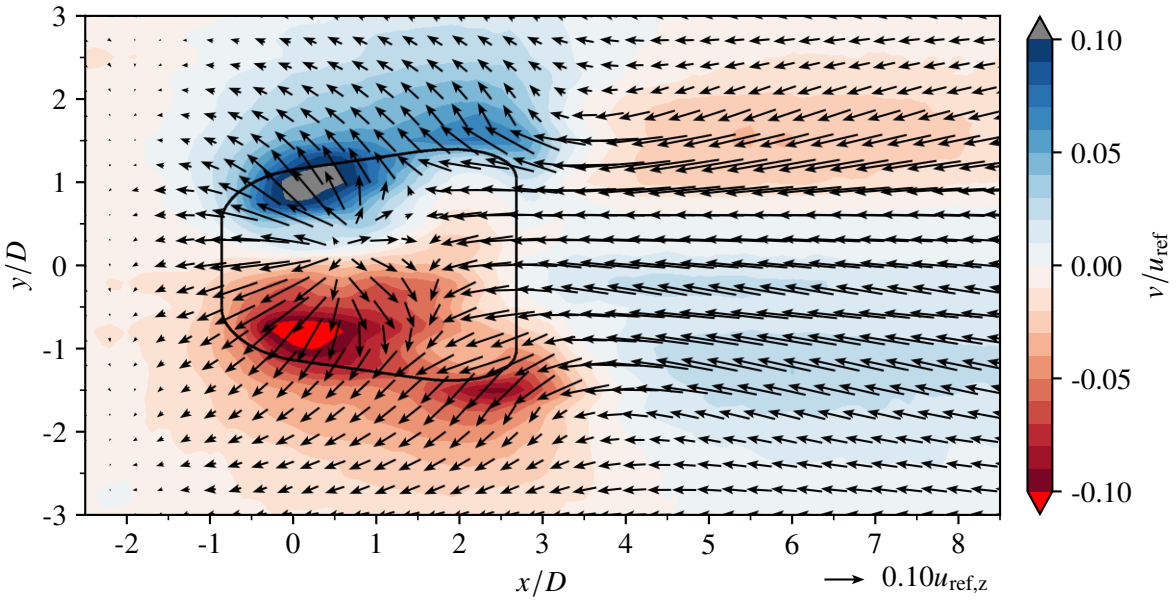

(b) PF, $Re_{D,\mathrm{cc}} = 30 \times 10^3$, $BR = 3.0$

Figure A.6: Impact of the coolant ejection on the near-wall lateral velocity, v, and in-plane velocity field, $\left(\left(u - u_{\mathrm{ref,z}}\right), v\right)$, at $z/D = 0.3$ for $BR = 3.0$.

A.4 PF: Velocity Distributions at Hole Outlet: Wall-Normal Velocity Component w

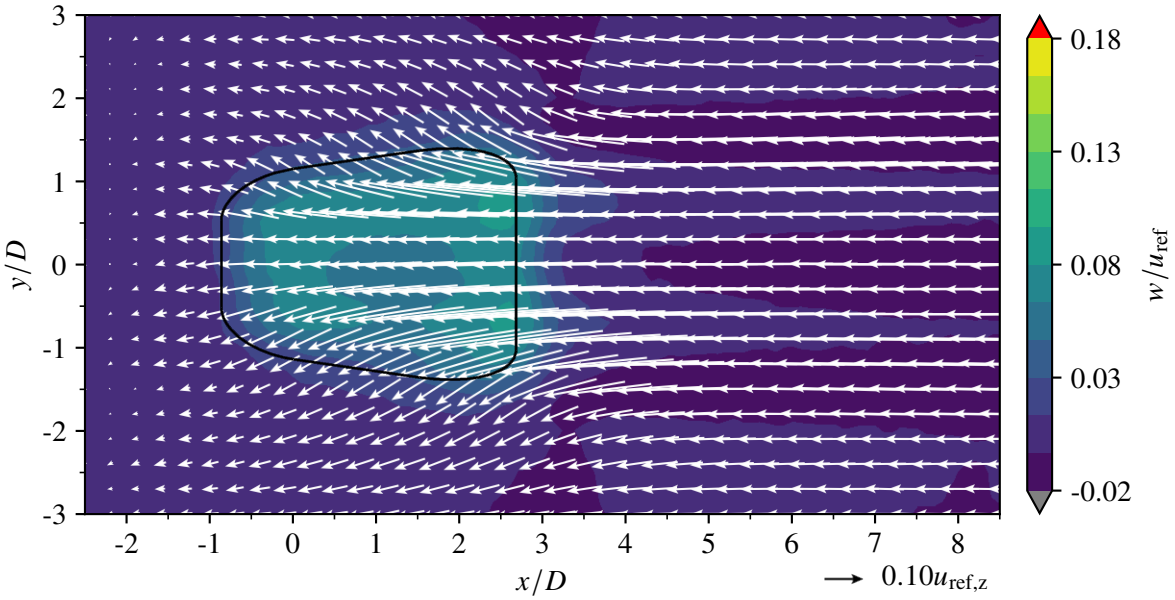

(a) PF, $Re_{D,\mathrm{cc}} = 5 \times 10^3$, $BR = 1.0$

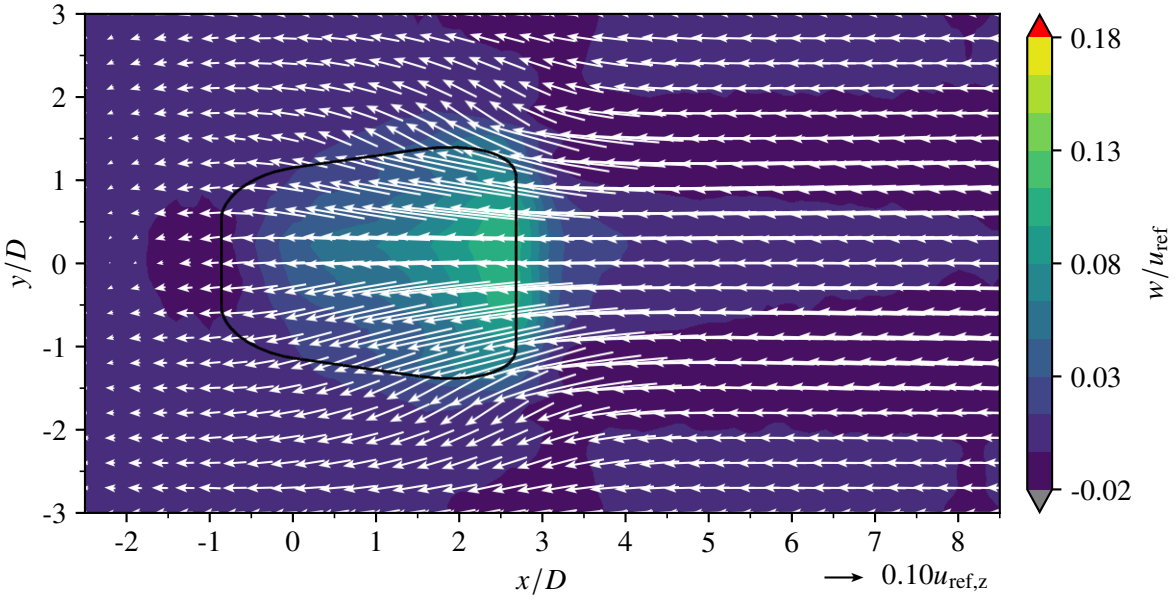

(b) PF, $Re_{D,\mathrm{cc}} = 30 \times 10^3$, $BR = 1.0$

Figure A.7: Impact of the coolant ejection on the near-wall wall-normal velocity, w, and in-plane velocity field, $\left(\left(u - u_{\mathrm{ref,z}}\right), v\right)$, at $z/D = 0.3$ for $BR = 1.0$.

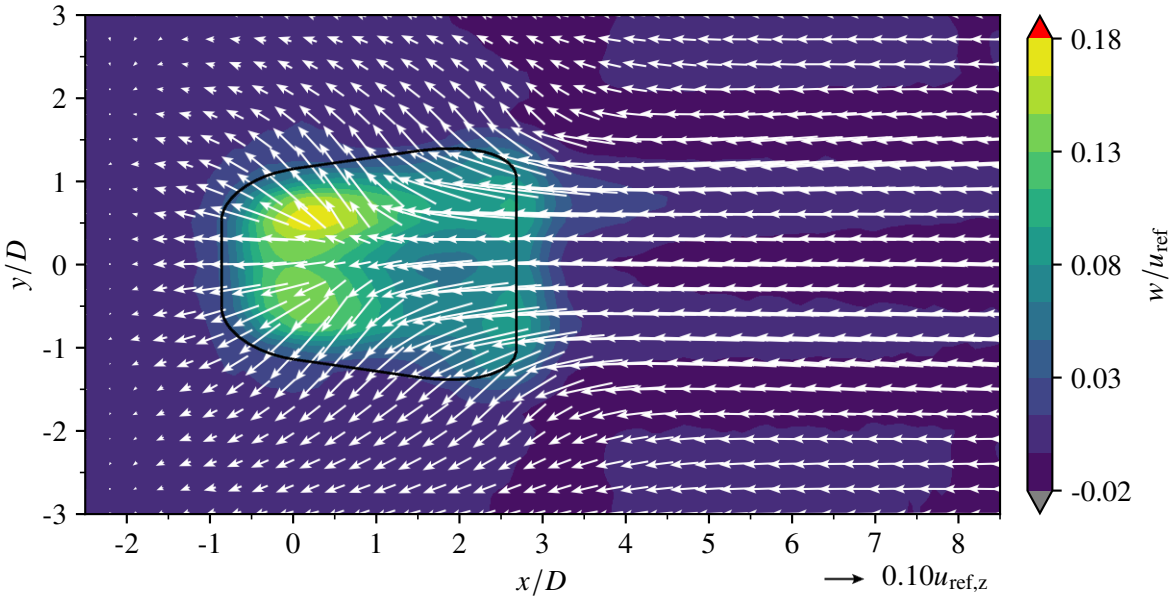

(a) PF, $Re_{D,\mathrm{cc}} = 5 \times 10^3$, $BR = 2.0$

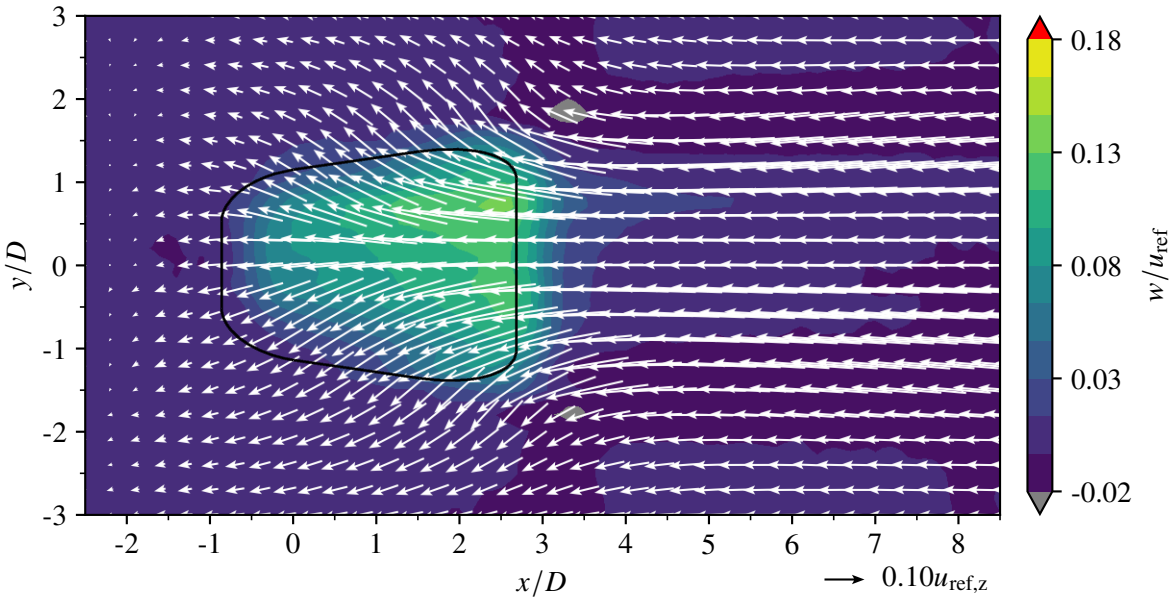

(b) PF, $Re_{D,\mathrm{cc}} = 30 \times 10^3$, $BR = 2.0$

Figure A.8: Impact of the coolant ejection on the near-wall wall-normal velocity, w, and in-plane velocity field, $\left(\left(u - u_{\mathrm{ref,z}}\right), v\right)$, at $z/D = 0.3$ for $BR = 2.0$.

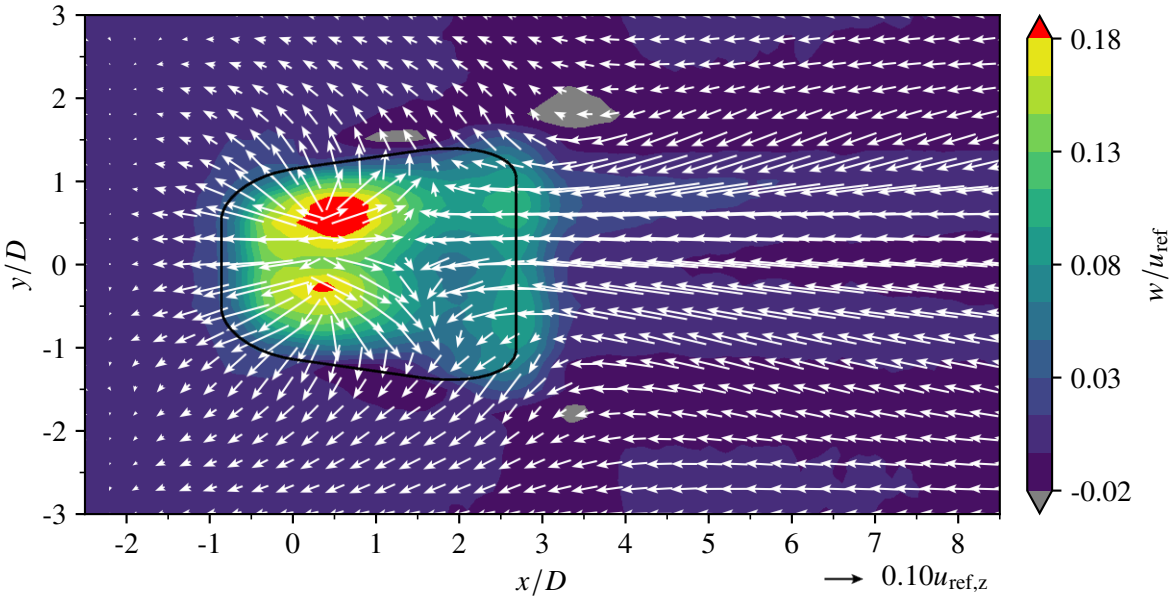

(a) PF, $Re_{D,\mathrm{cc}} = 5 \times 10^3$, $BR = 3.0$

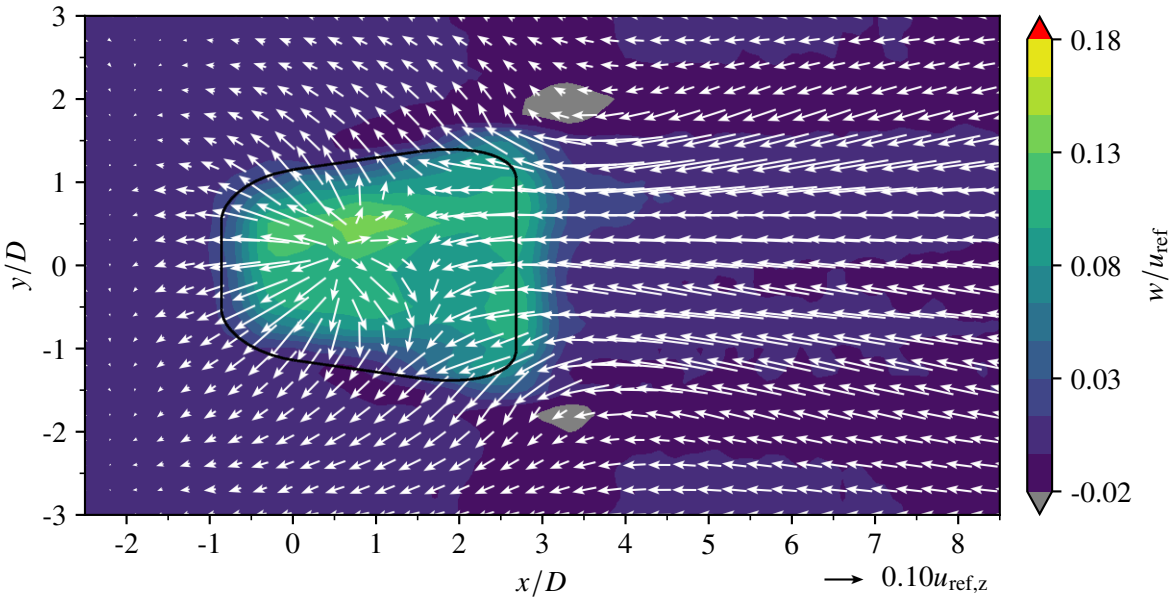

(b) PF, $Re_{D,\mathrm{cc}} = 30 \times 10^3$, $BR = 3.0$

Figure A.9: Impact of the coolant ejection on the near-wall wall-normal velocity, w, and in-plane velocity field, $\left(\left(u - u_{\mathrm{ref,z}}\right), v\right)$, at $z/D = 0.3$ for $BR = 3.0$.

A.5 Vorticity Distributions at Hole Outlet: Streamwise Vorticity ω_x

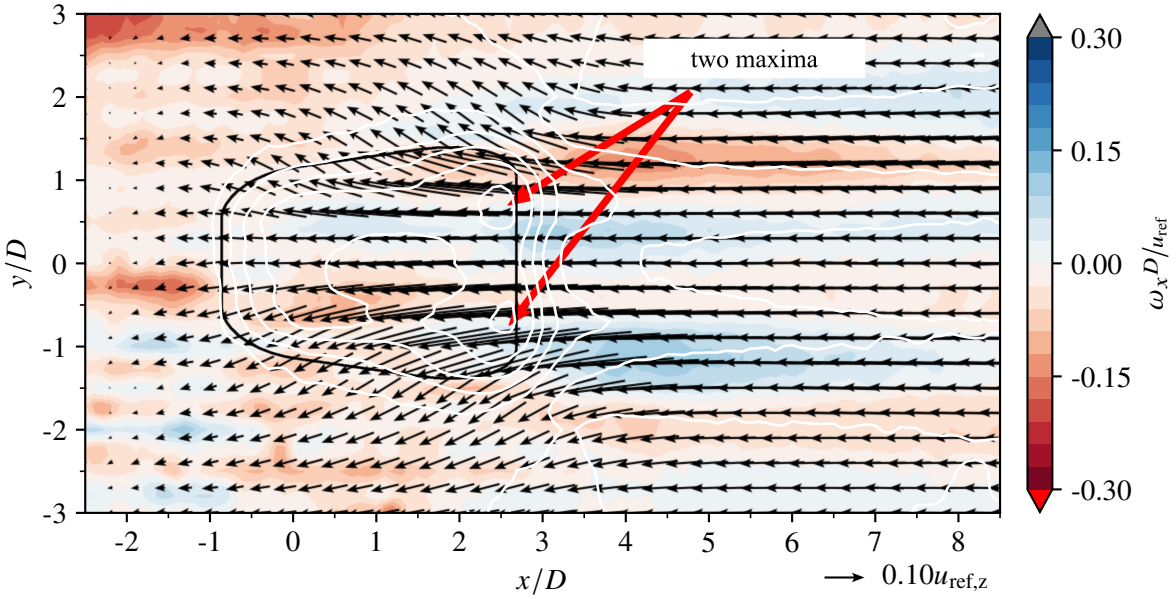

(a) PF, $Re_{D,cc} = 5 \times 10^3$, $BR = 1.0$

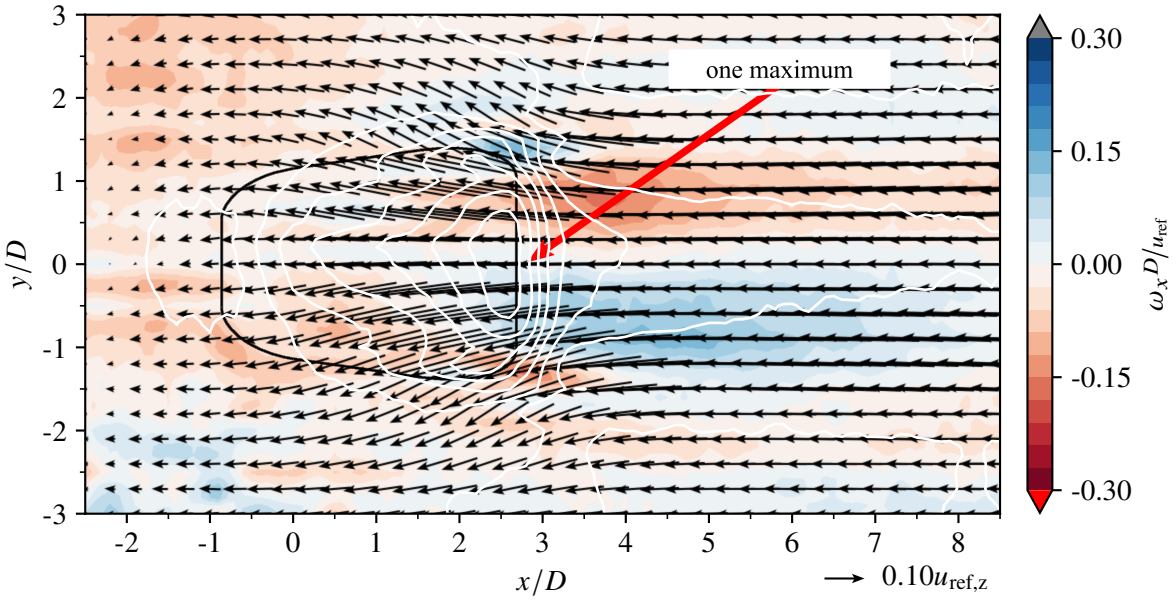

(b) PF, $Re_{D,cc} = 30 \times 10^3$, $BR = 1.0$

Figure A.10: Impact of the coolant ejection on the near-wall x-vorticity, ω_x, and in-plane velocity field, $\left(\left(u - u_{ref,z}\right), v\right)$, at $z/D = 0.3$ for $BR = 1.0$. The white lines correspond to the contours of wall-normal velocity w shown in section A.4.

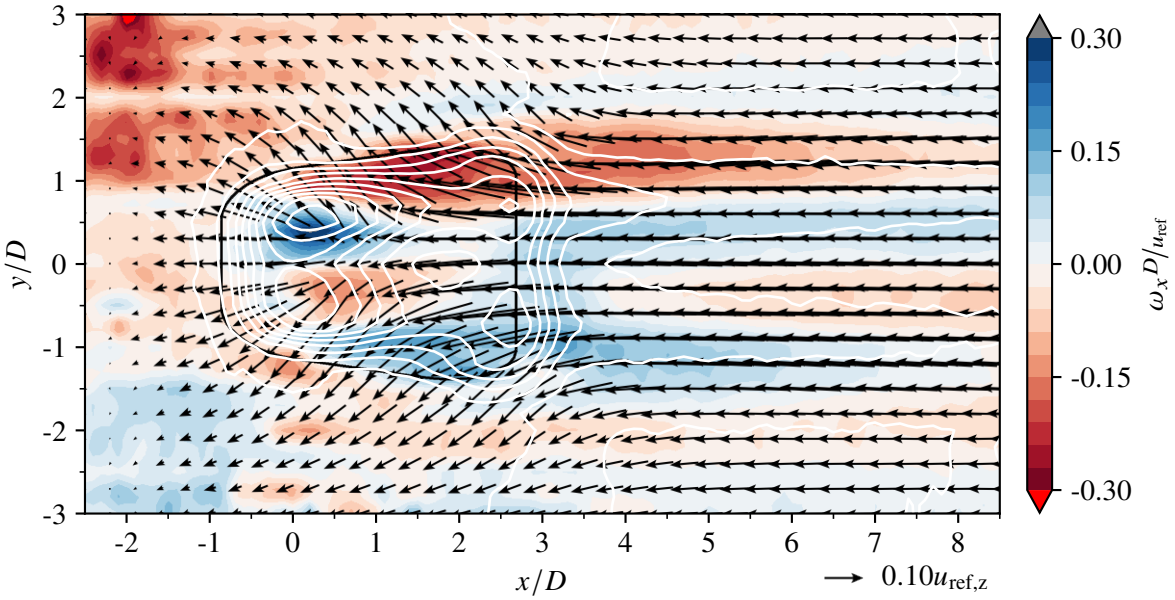

(a) PF, $Re_{D,\mathrm{cc}} = 5 \times 10^3$, $BR = 2.0$

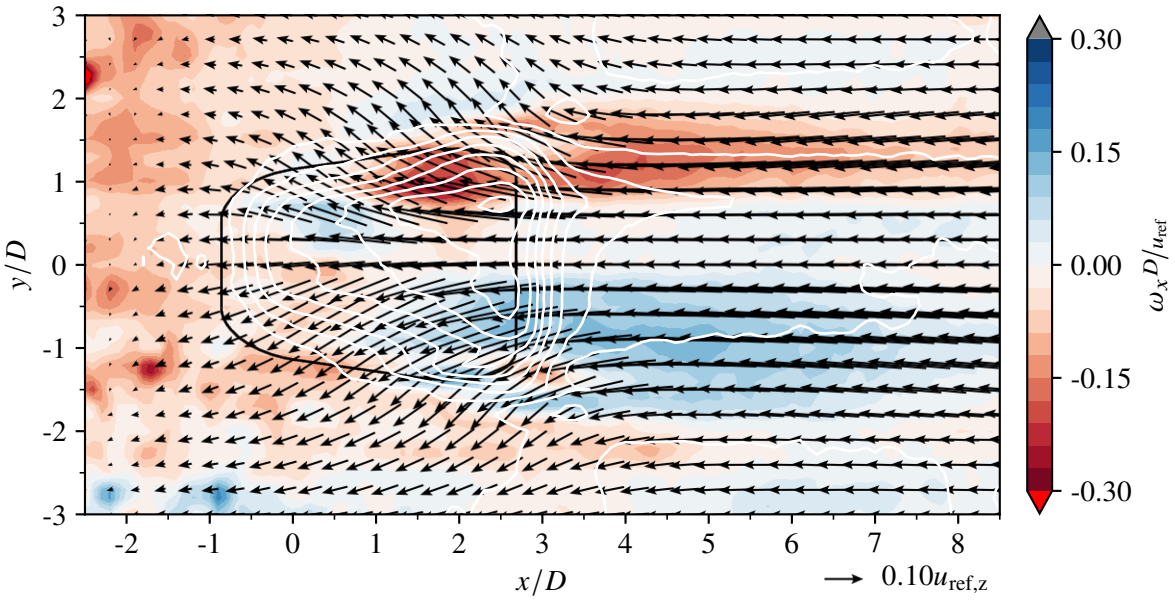

(b) PF, $Re_{D,\mathrm{cc}} = 30 \times 10^3$, $BR = 2.0$

Figure A.11: Impact of the coolant ejection on the near-wall x-vorticity, ω_x, and in-plane velocity field, $\left(\left(u - u_{\mathrm{ref,z}}\right), v\right)$, at $z/D = 0.3$ for $BR = 2.0$. The white lines correspond to the contours of wall-normal velocity w shown in section A.4.

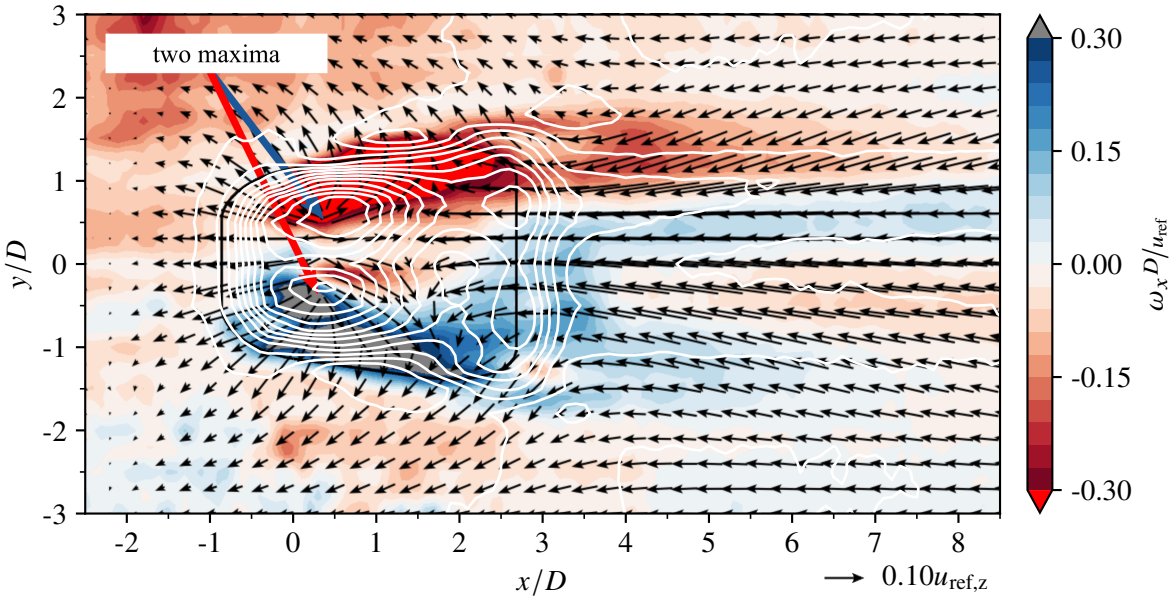

(a) PF, $Re_{D,\mathrm{cc}} = 5 \times 10^3$, $BR = 3.0$

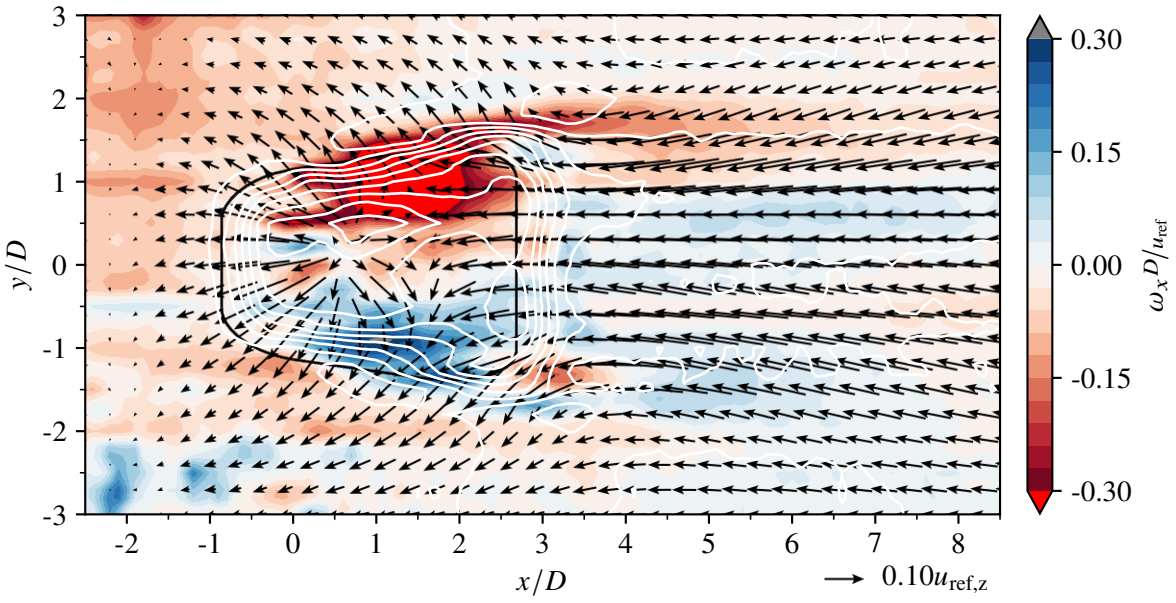

(b) PF, $Re_{D,\mathrm{cc}} = 30 \times 10^3$, $BR = 3.0$

Figure A.12: Impact of the coolant ejection on the near-wall x-vorticity, ω_x, and in-plane velocity field, $\left(\left(u - u_{\mathrm{ref,z}}\right), v\right)$, at $z/D = 0.3$ for $BR = 3.0$. The white lines correspond to the contours of wall-normal velocity w shown in section A.4.

A.6 Vorticity Distributions at Hole Outlet: Wall-Normal Vorticity ω_z

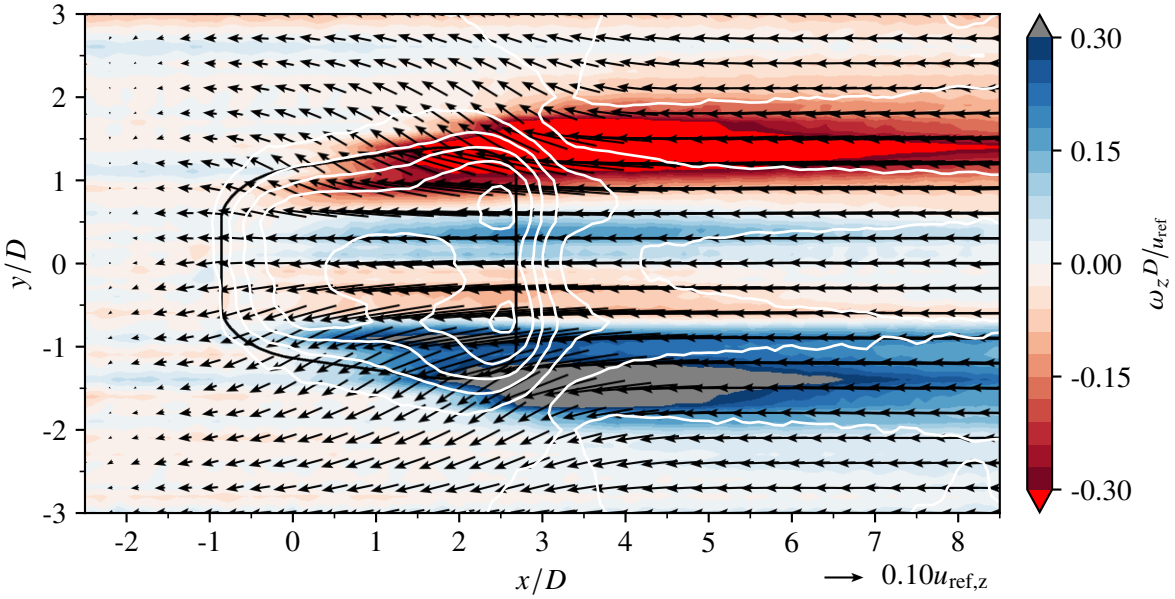

(a) PF, $Re_{D,\mathrm{cc}} = 5 \times 10^3$, $BR = 1.0$

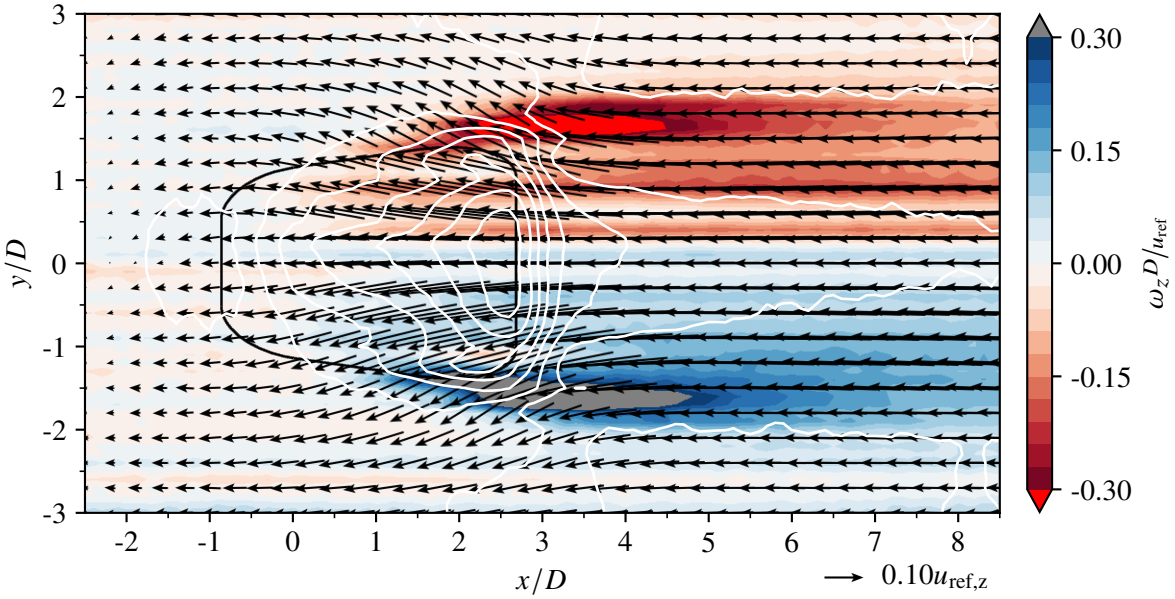

(b) PF, $Re_{D,\mathrm{cc}} = 30 \times 10^3$, $BR = 1.0$

Figure A.13: Impact of the coolant ejection on the near-wall z-vorticity, ω_z, and in-plane velocity field, $\left(\left(u - u_{\mathrm{ref,z}}\right), v\right)$, at $z/D = 0.3$ for $BR = 1.0$. The white lines correspond to the contours of wall-normal velocity w shown in section A.4.

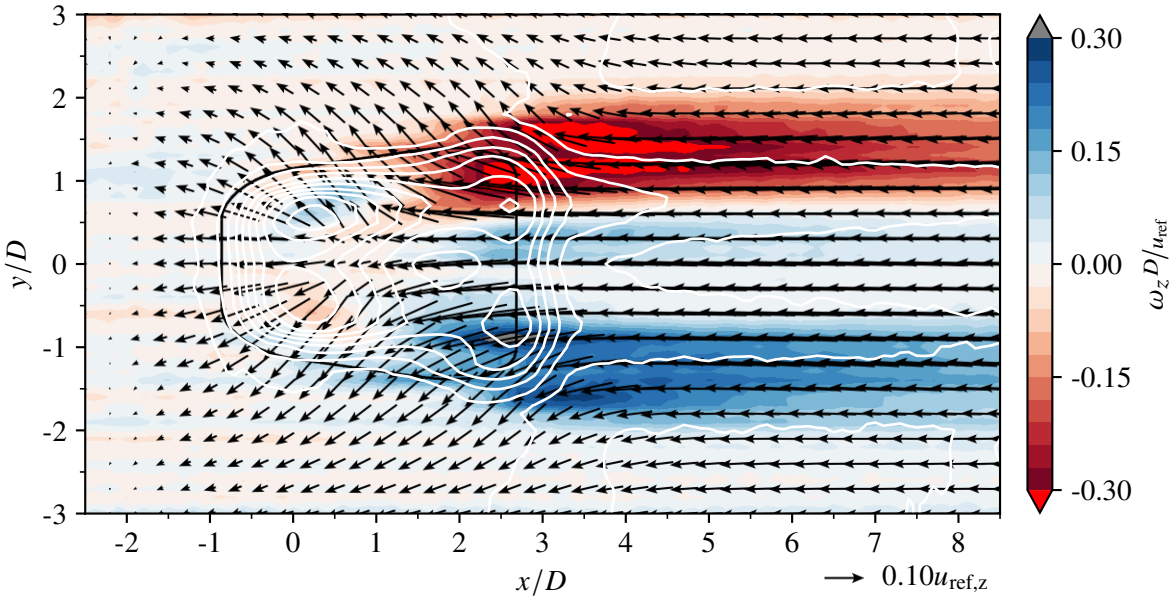

(a) PF, $Re_{D,\mathrm{cc}} = 5 \times 10^3$, $BR = 2.0$

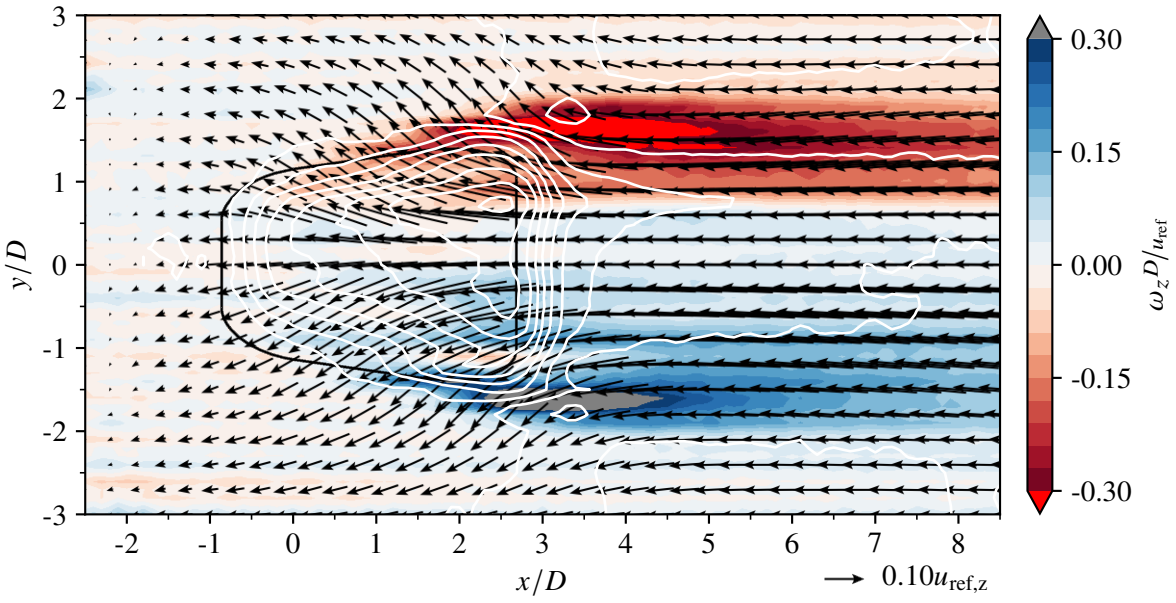

(b) PF, $Re_{D,\mathrm{cc}} = 30 \times 10^3$, $BR = 2.0$

Figure A.14: Impact of the coolant ejection on the near-wall z-vorticity, ω_z, and in-plane velocity field, $\left(\left(u - u_{\mathrm{ref,z}}\right), v\right)$, at $z/D = 0.3$ for $BR = 2.0$. The white lines correspond to the contours of wall-normal velocity w shown in section A.4.

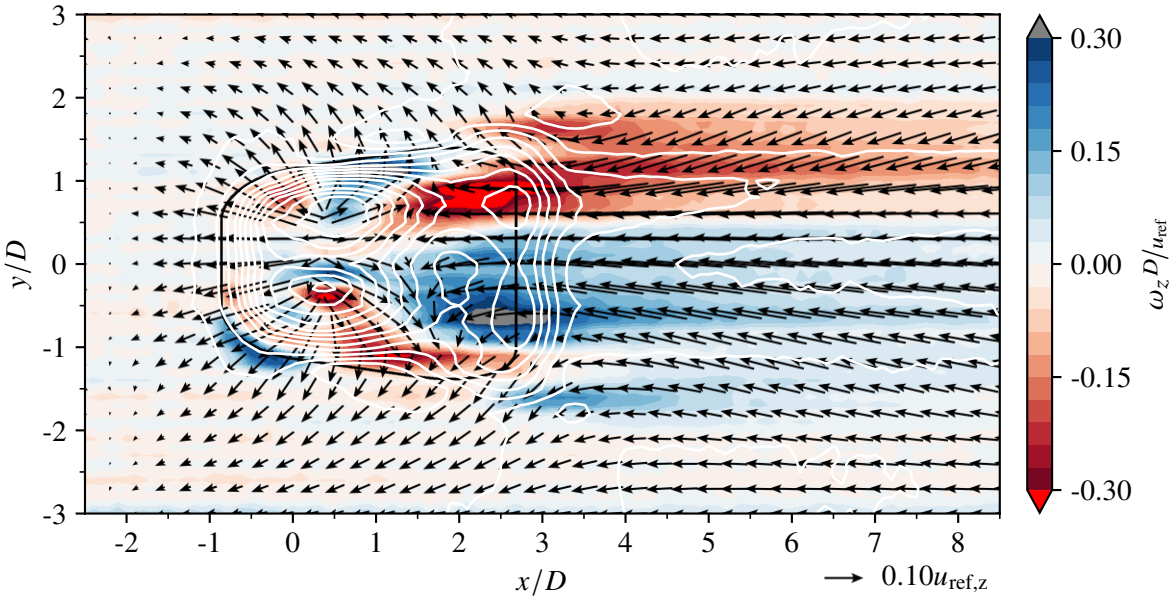

(a) PF, $Re_{D,\mathrm{cc}} = 5 \times 10^3$, $BR = 3.0$

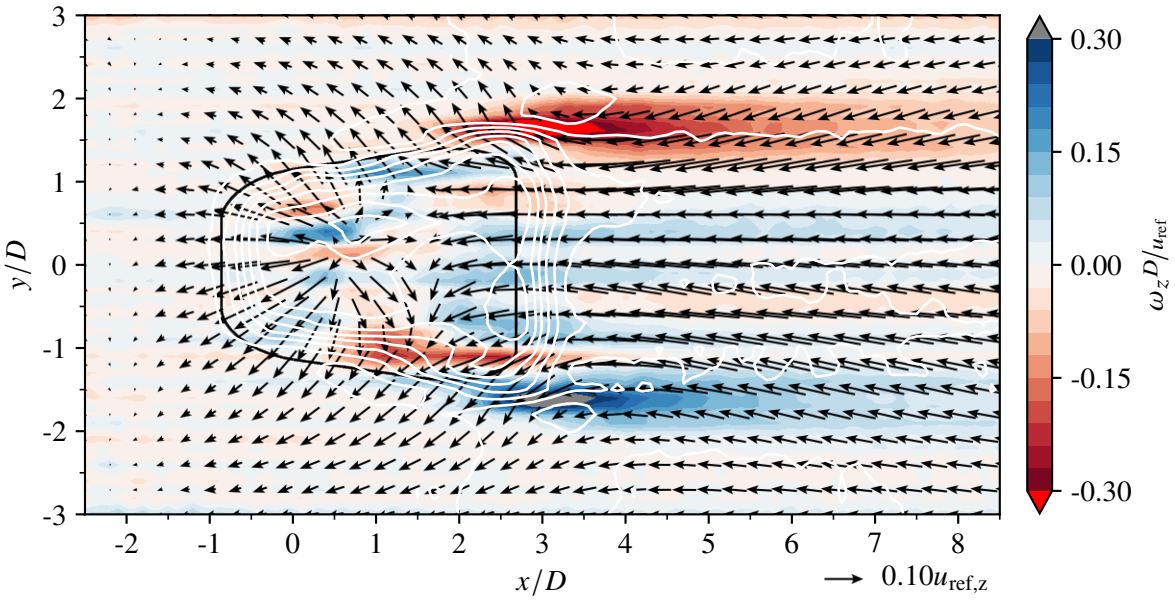

(b) PF, $Re_{D,\mathrm{cc}} = 30 \times 10^3$, $BR = 3.0$

Figure A.15: Impact of the coolant ejection on the near-wall z-vorticity, ω_z, and in-plane velocity field, $\left(\left(u - u_{\mathrm{ref,z}}\right), v\right)$, at $z/D = 0.3$ for $BR = 3.0$. The white lines correspond to the contours of wall-normal velocity w shown in section A.4.

A.7 OF: Velocity Distributions at Hole Outlet: Streamwise Velocity Component u

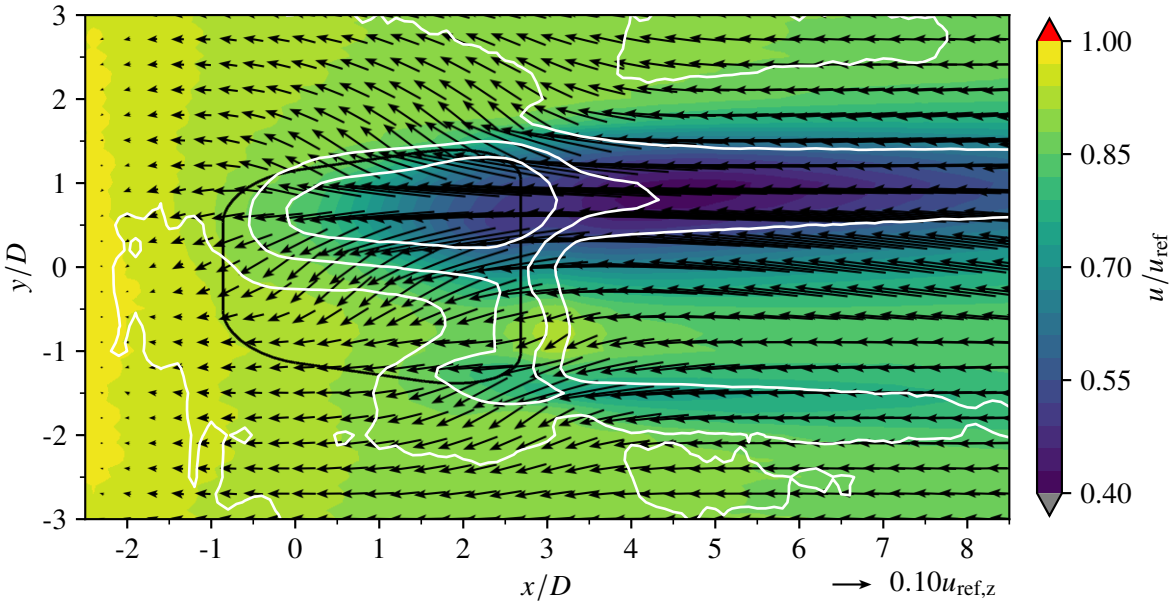

(a) OF, $Re_{D,\mathrm{cc}} = 5 \times 10^3$, $BR = 1.0$

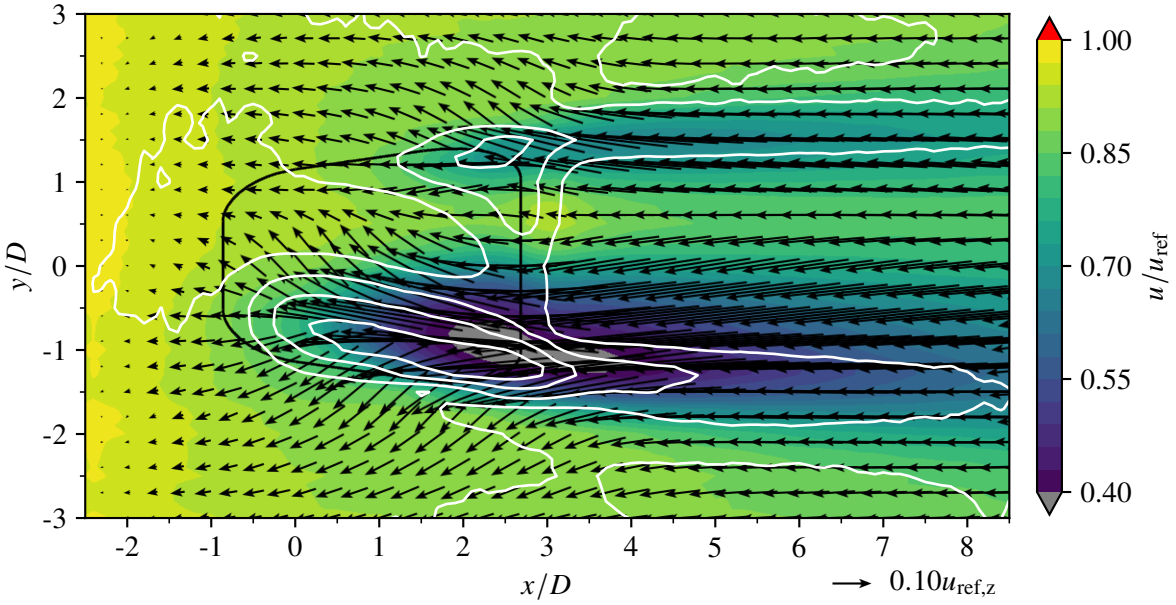

(b) OF, $Re_{D,\mathrm{cc}} = 30 \times 10^3$, $BR = 1.0$

Figure A.16: Impact of the coolant ejection on the near-wall streamwise velocity, u, and in-plane velocity field, $\left(\left(u - u_{\mathrm{ref,z}}\right), v\right)$, at $z/D = 0.3$ for $BR = 1.0$. The white lines correspond to the contours of wall-normal velocity w shown in section A.9.

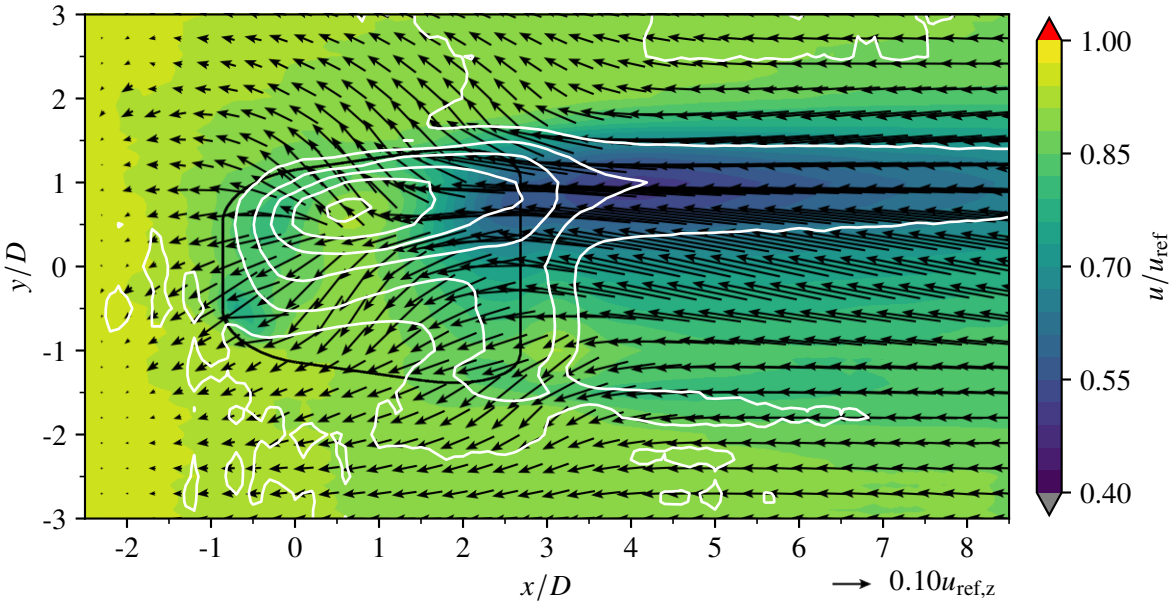

(a) OF, $Re_{D,\mathrm{cc}} = 5 \times 10^3$, $BR = 2.0$

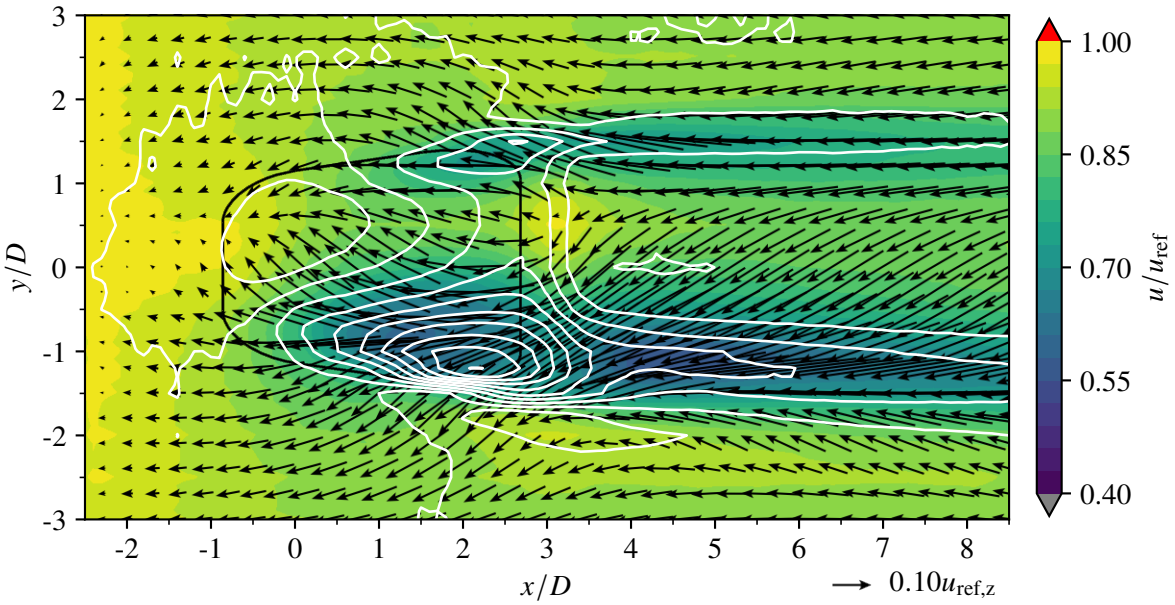

(b) OF, $Re_{D,\mathrm{cc}} = 30 \times 10^3$, $BR = 2.0$

Figure A.17: Impact of the coolant ejection on the near-wall streamwise velocity, u, and in-plane velocity field, $\left(\left(u - u_{\mathrm{ref,z}}\right), v\right)$, at $z/D = 0.3$ for $BR = 2.0$. The white lines correspond to the contours of wall-normal velocity w shown in section A.9.

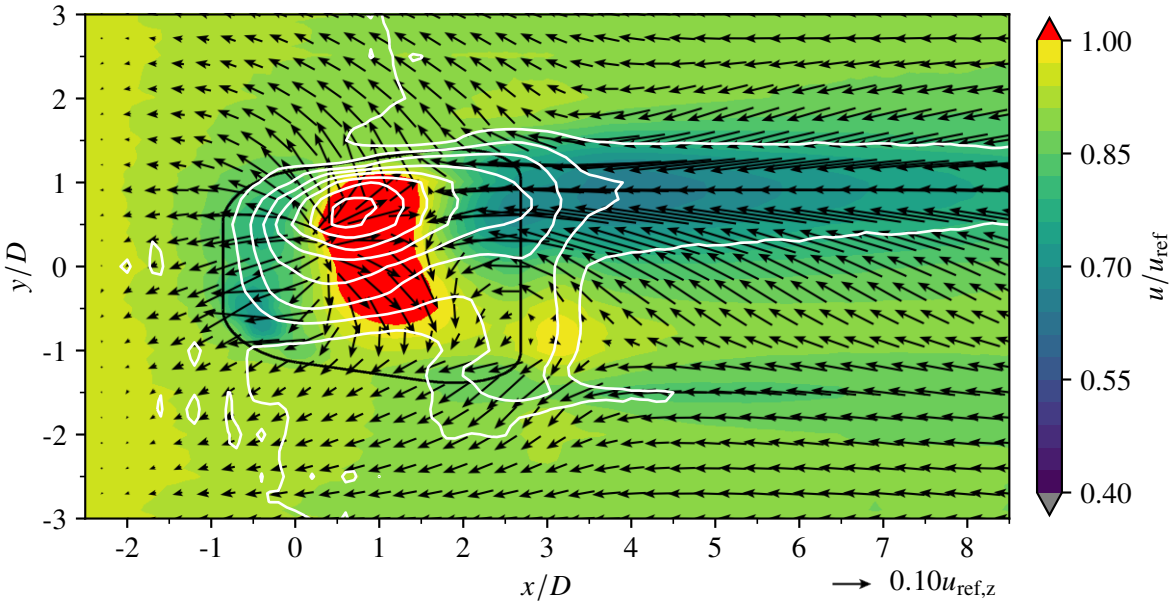

(a) OF, $Re_{D,\mathrm{cc}} = 5 \times 10^3$, $BR = 3.0$

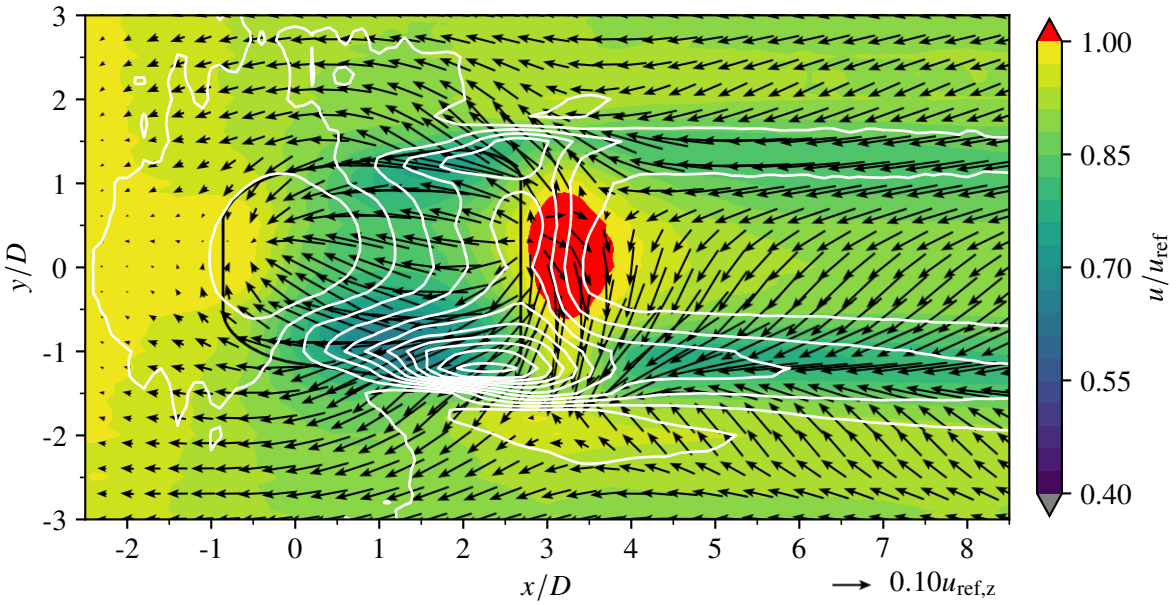

(b) OF, $Re_{D,\mathrm{cc}} = 30 \times 10^3$, $BR = 3.0$

Figure A.18: Impact of the coolant ejection on the near-wall streamwise velocity, u, and in-plane velocity field, $\left(\left(u - u_{\mathrm{ref,z}}\right), v\right)$, at $z/D = 0.3$ for $BR = 3.0$. The white lines correspond to the contours of wall-normal velocity w shown in section A.9.

A.8 OF: Velocity Distributions at Hole Outlet: Lateral Velocity Component v

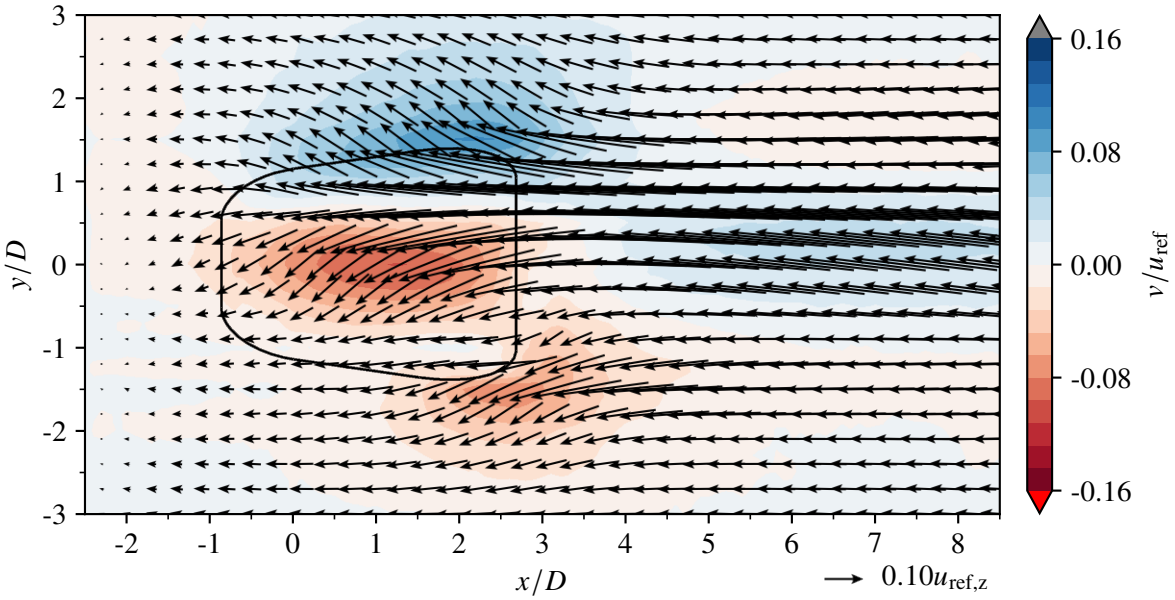

(a) OF, $Re_{D,\mathrm{cc}} = 5 \times 10^3$, $BR = 1.0$

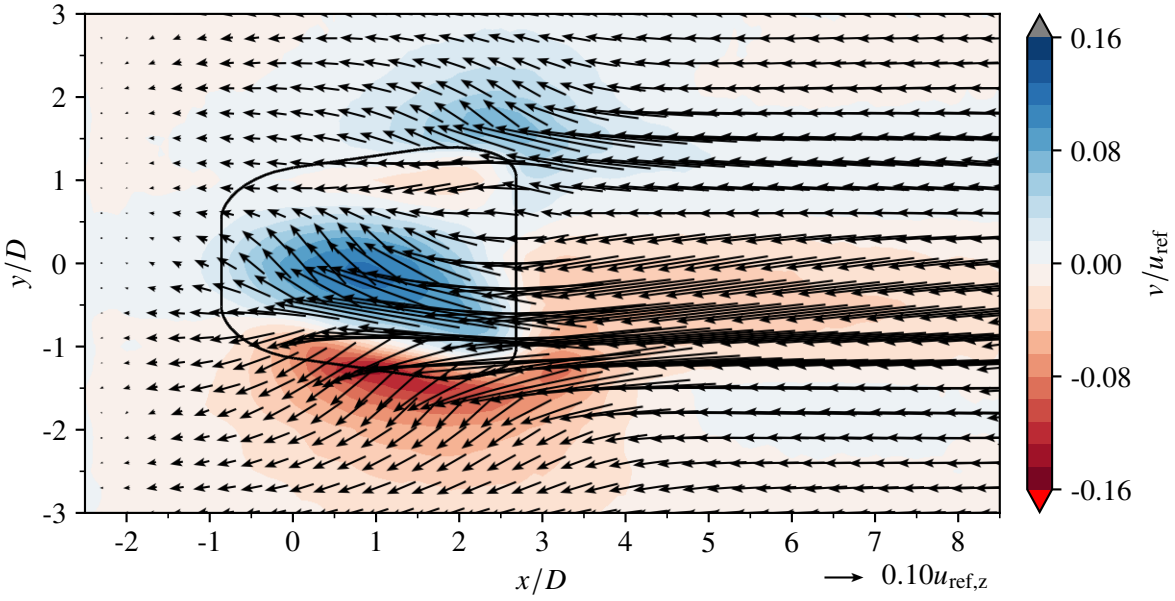

(b) OF, $Re_{D,\mathrm{cc}} = 30 \times 10^3$, $BR = 1.0$

Figure A.19: Impact of the coolant ejection on the near-wall lateral velocity, v, and in-plane velocity field, $\left(\left(u - u_{\mathrm{ref,z}}\right), v\right)$, at $z/D = 0.3$ for $BR = 1.0$.

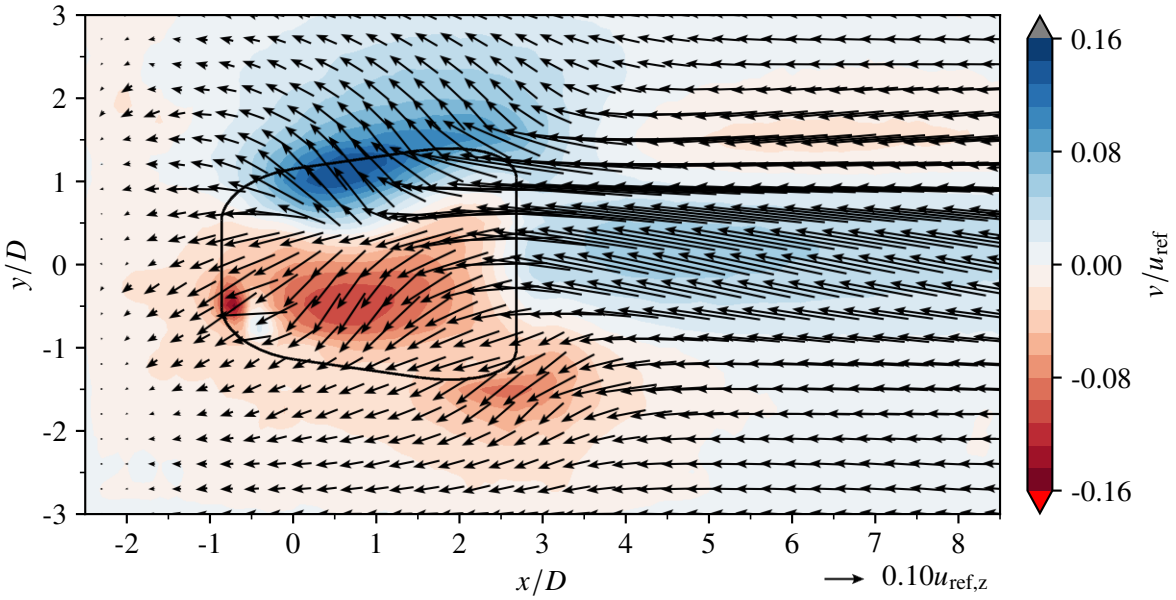

(a) OF, $Re_{D,\mathrm{cc}} = 5 \times 10^3$, $BR = 2.0$

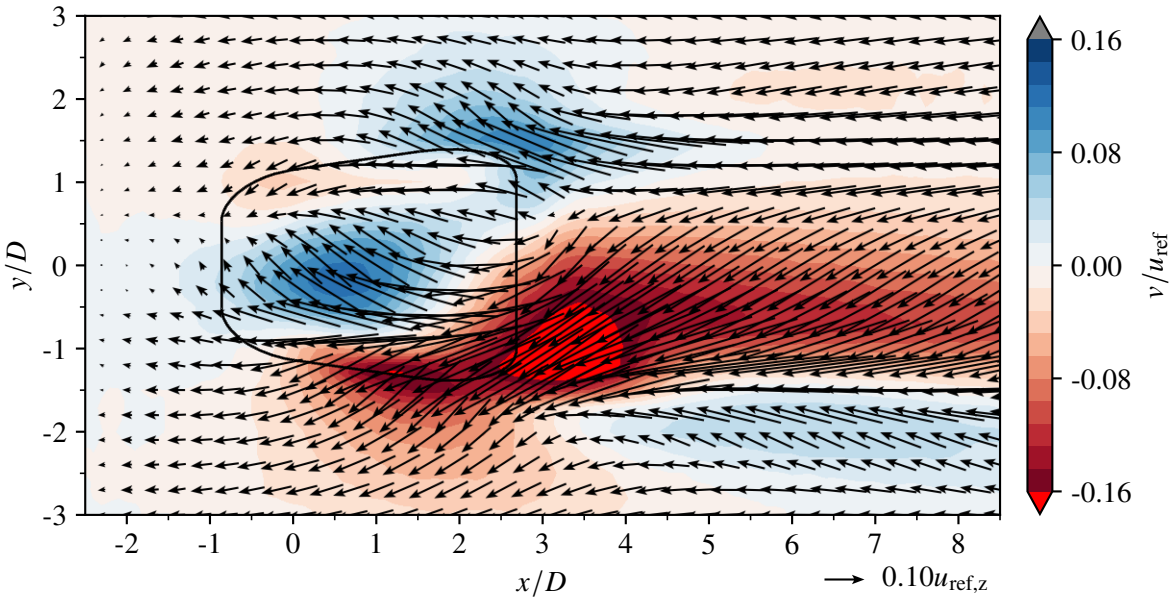

(b) OF, $Re_{D,\mathrm{cc}} = 30 \times 10^3$, $BR = 2.0$

Figure A.20: Impact of the coolant ejection on the near-wall lateral velocity, v, and in-plane velocity field, $\left(\left(u - u_{\mathrm{ref,z}}\right), v\right)$, at $z/D = 0.3$ for $BR = 2.0$.

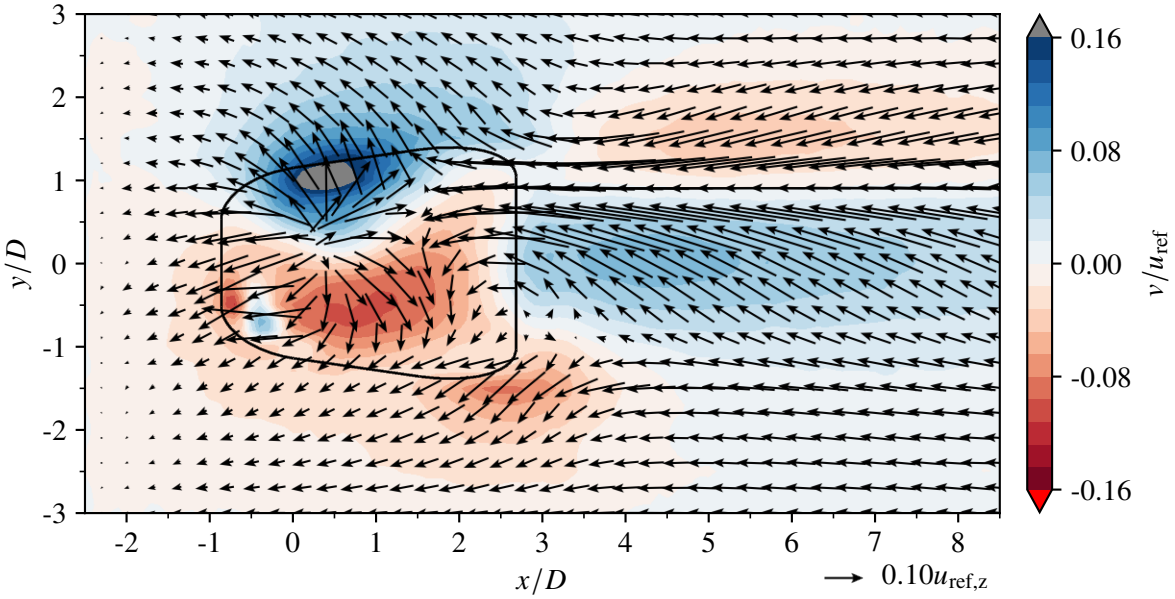

(a) OF, $Re_{D,\mathrm{cc}} = 5 \times 10^3$, $BR = 3.0$

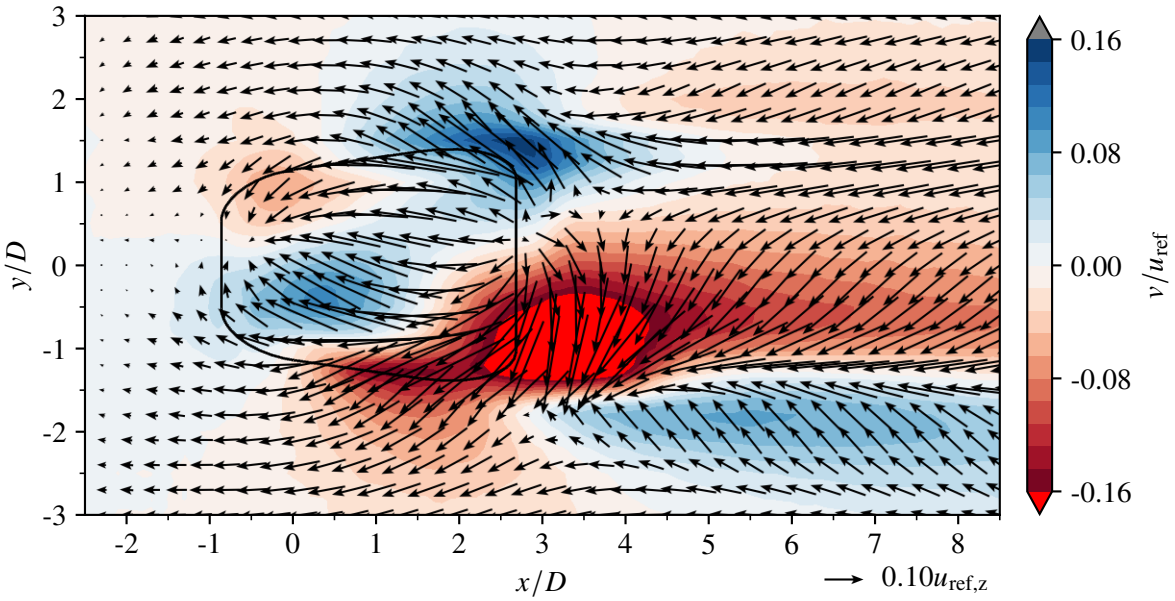

(b) OF, $Re_{D,\mathrm{cc}} = 30 \times 10^3$, $BR = 3.0$

Figure A.21: Impact of the coolant ejection on the near-wall lateral velocity, v, and in-plane velocity field, $\left(\left(u - u_{\mathrm{ref,z}}\right), v\right)$, at $z/D = 0.3$ for $BR = 3.0$.

A.9 OF: Velocity Distributions at Hole Outlet: Wall-Normal Velocity Component w

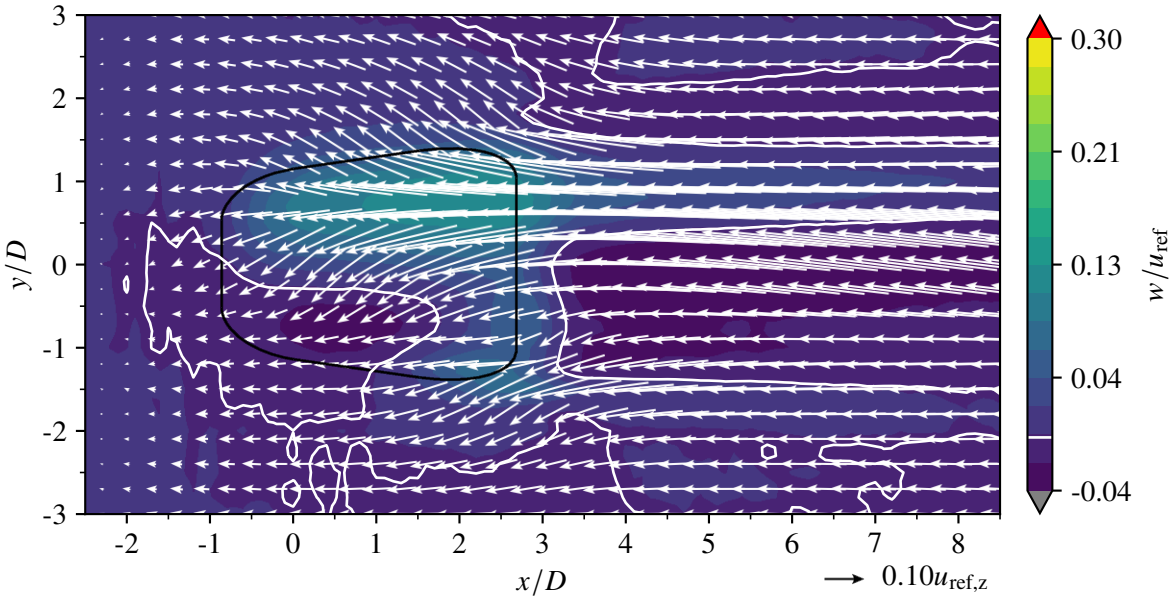

(a) OF, $Re_{D,\mathrm{cc}} = 5 \times 10^3$, $BR = 1.0$

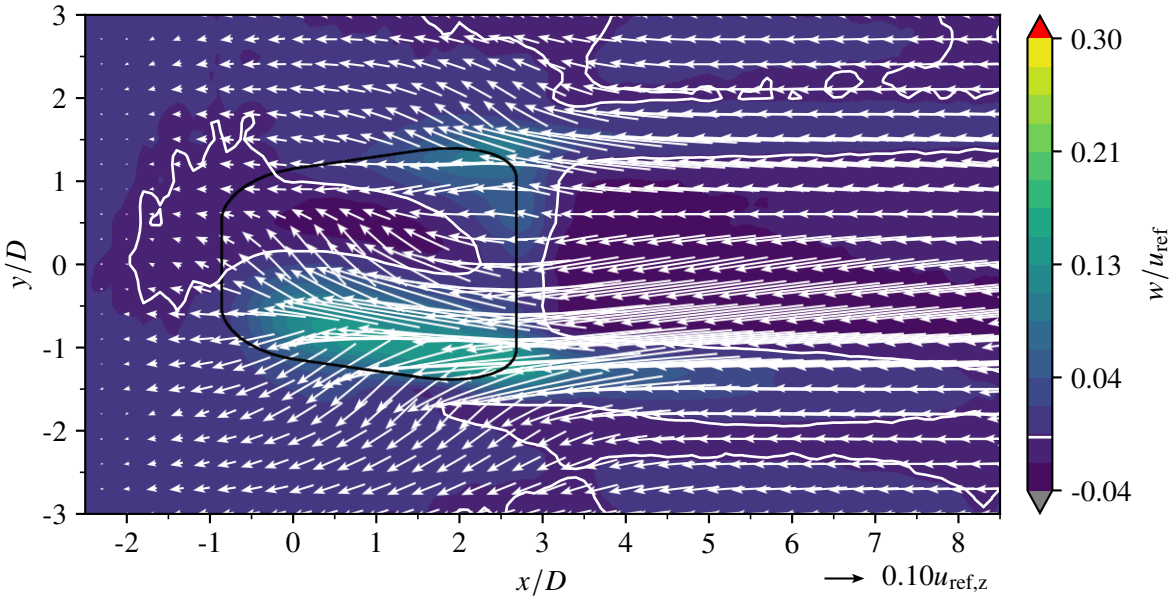

(b) OF, $Re_{D,\mathrm{cc}} = 30 \times 10^3$, $BR = 1.0$

Figure A.22: Impact of the coolant ejection on the near-wall wall-normal velocity, w, and in-plane velocity field, $\left(\left(u - u_{\mathrm{ref,z}}\right), v\right)$, at $z/D = 0.3$ for $BR = 1.0$.

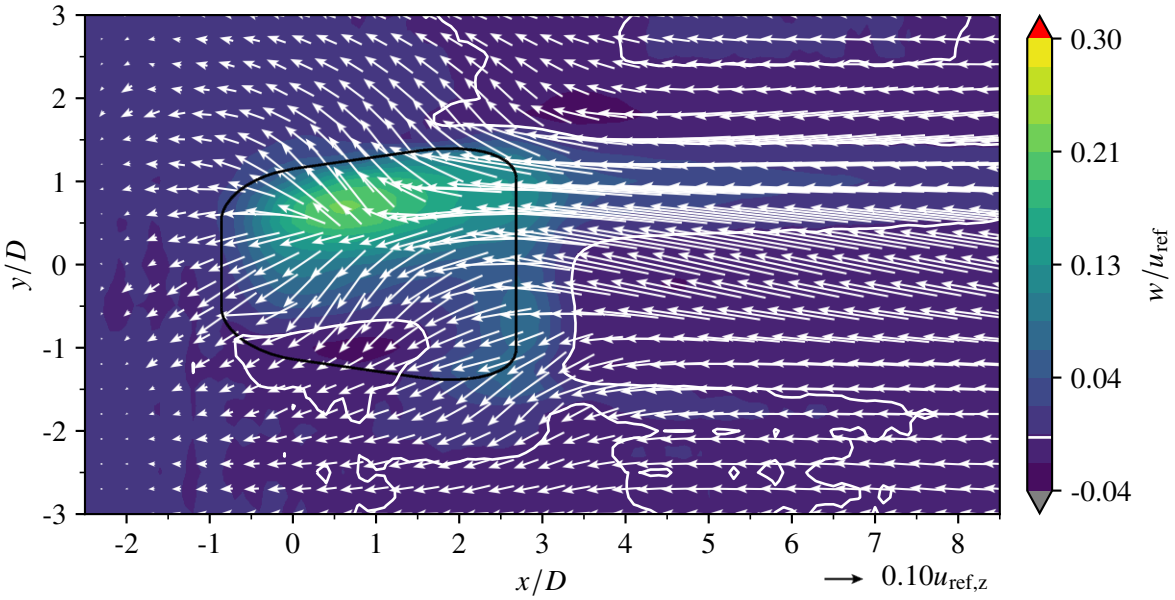

(a) OF, $Re_{D,\mathrm{cc}} = 5 \times 10^3$, $BR = 2.0$

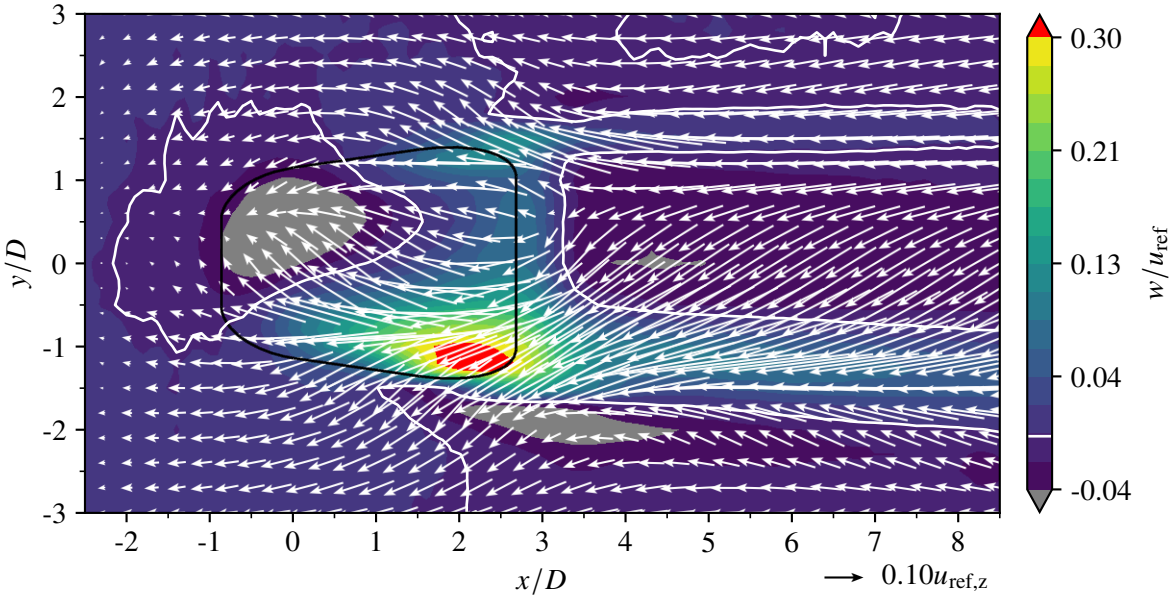

(b) OF, $Re_{D,\mathrm{cc}} = 30 \times 10^3$, $BR = 2.0$

Figure A.23: Impact of the coolant ejection on the near-wall wall-normal velocity, w, and in-plane velocity field, $\left(\left(u - u_{\mathrm{ref,z}}\right), v\right)$, at $z/D = 0.3$ for $BR = 2.0$.

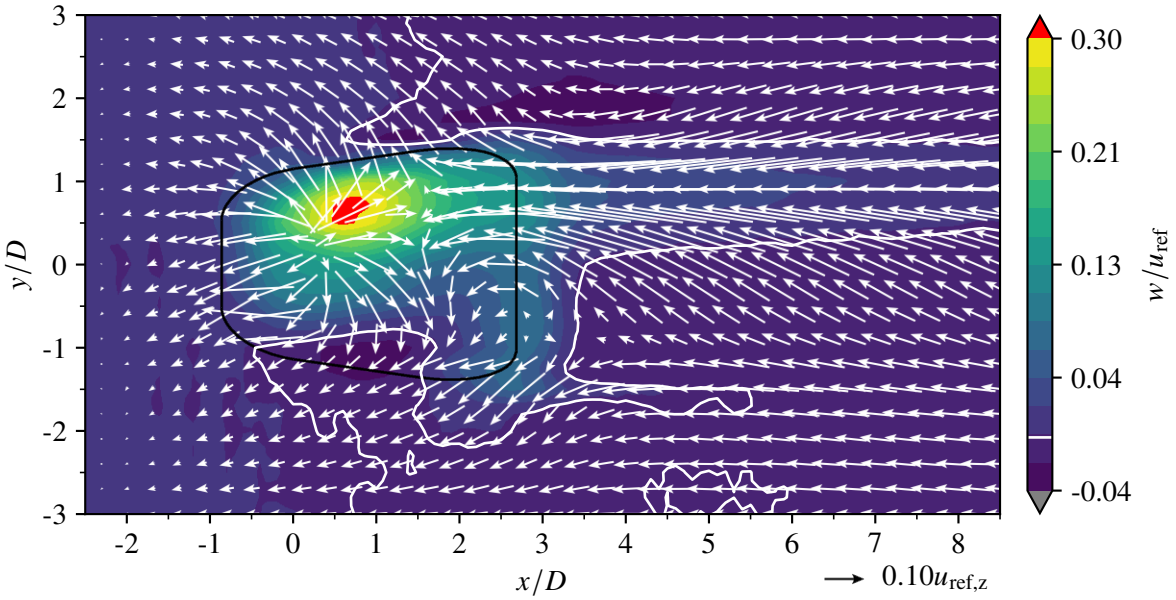

(a) OF, $Re_{D,\mathrm{cc}} = 5 \times 10^3$, $BR = 3.0$

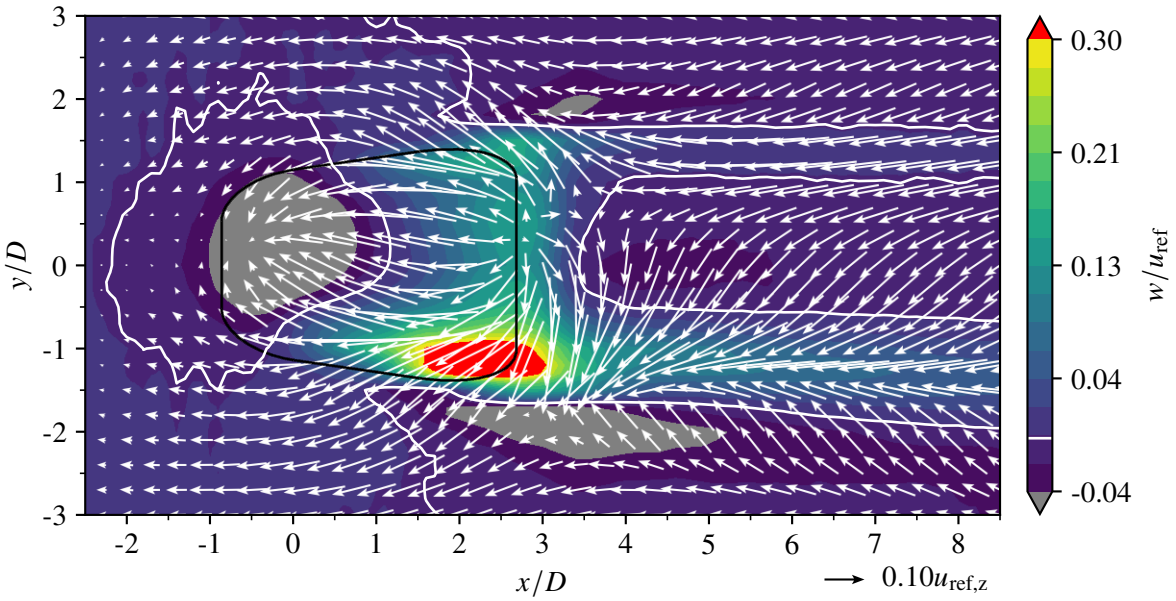

(b) OF, $Re_{D,\mathrm{cc}} = 30 \times 10^3$, $BR = 3.0$

Figure A.24: Impact of the coolant ejection on the near-wall wall-normal velocity, w, and in-plane velocity field, $\left(\left(u - u_{\mathrm{ref,z}}\right), v\right)$, at $z/D = 0.3$ for $BR = 3.0$.

A.10 OF: Evolution of Coherent Structures in x-Planes based on the In-Plane Velocity Field and the x-Vorticity ω_x

In this section, the evolution of the coherent structures in x-direction is visualised for the OF configuration to improve the intuitive understanding of the secondary flow field. The time-averaged lateral and wall-normal velocity components are shown in x-planes at $x/D = 0,\ 3.0,\ 5.0$ and 8.0 with a background contour of normalised x-vorticity ω_x for the low and high coolant channel Reynolds number $Re_{D,\mathrm{cc}}$. The black lines below the horizontal axis indicate the downstream edges of the cooling hole diffuser exit geometry. The white line in the third figure of each subset is an iso-line of turbulent kinetic energy corresponding to the iso-surfaces depicted in Figure 4.2. The blue or green lines represent the lateral distribution of the ratio of heat transfer coefficients with and without film cooling h_f/h_0 at $x/D = 5.0$ and 8.0 based on data from Fraas (2019). No quantitative scale for h_f/h_0 is added to the figures as only the relative distribution is relevant in the present work. Detailed information on the quantitative distribution of h_f/h_0 is provided in section A.13 and by Fraas (2019). The x-axis corresponds to $h_\mathrm{f}/h_0 = 1.0$. The relative distribution is to scale, linear and equal for all blue lines for all cases. The ratio of heat transfer coefficients with and without film cooling is, hence, quantitatively directly comparable for all cases, except for the OF cases with high coolant channel Reynolds number (green lines in Figure A.28, A.29 and A.30). For those cases, the heat transfer augmentation is significantly lower and a factor of two is applied to h_f/h_0. This is indicated by the different colour choices for the lines - green instead of blue. When comparing the OF cases with high coolant channel Reynolds number quantitatively to the other cases, this has to be considered.

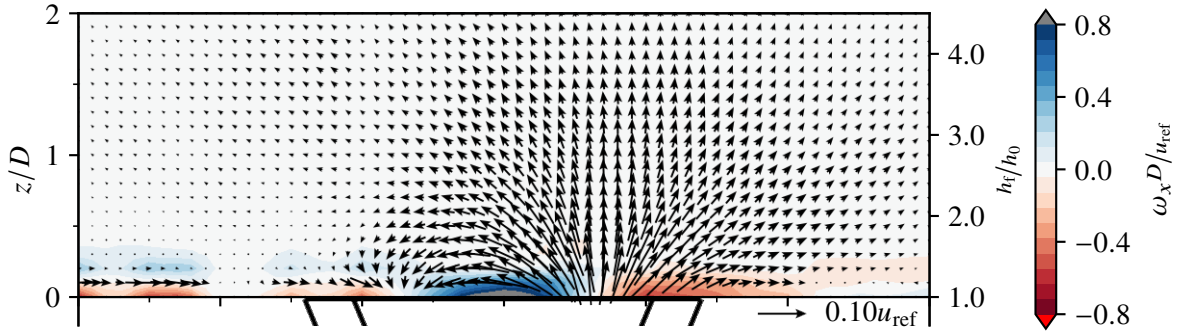

(a) OF, $Re_{D,\mathrm{cc}} = 5 \times 10^3$, $BR = 1.0$: $x/\mathrm{D} = 0.0$

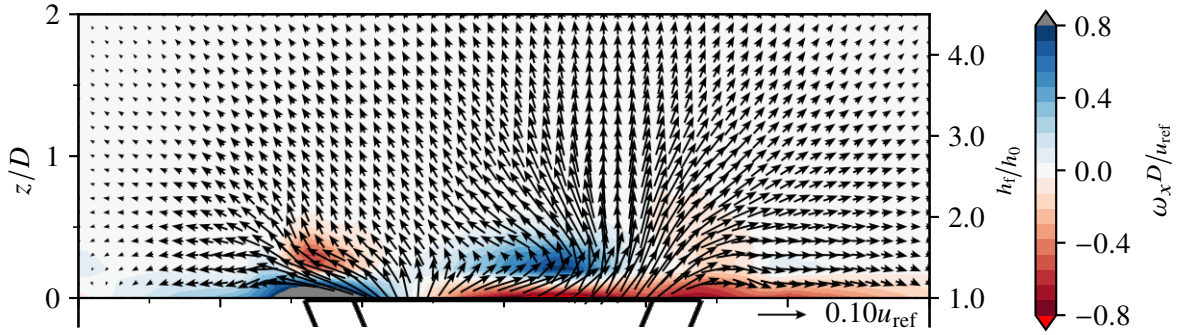

(b) OF, $Re_{D,\mathrm{cc}} = 5 \times 10^3$, $BR = 1.0$, $x/D = 3.0$

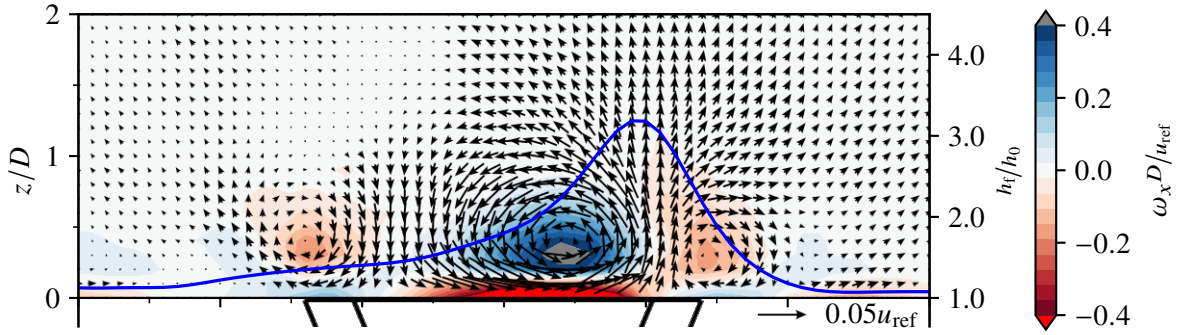

(c) OF, $Re_{D,\mathrm{cc}} = 5 \times 10^3$, $BR = 1.0$, $x/D = 5.0$

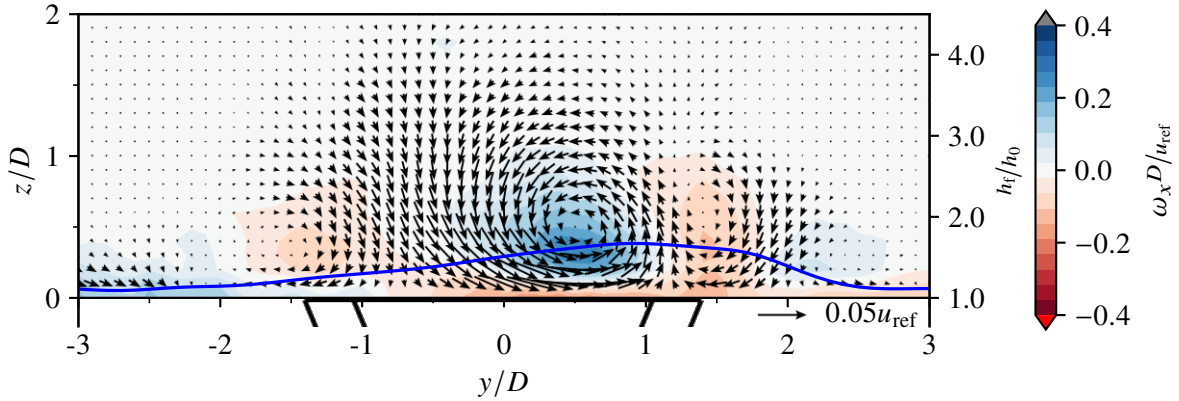

(d) OF, $Re_{D,\mathrm{cc}} = 5 \times 10^3$, $BR = 1.0$, $x/D = 8.0$

Figure A.25: Evolution of coherent structures and h_f/h_0 in the x-plane for $Re_{D,\mathrm{cc}} = 5{\times}10^3$ and $BR = 1.0$

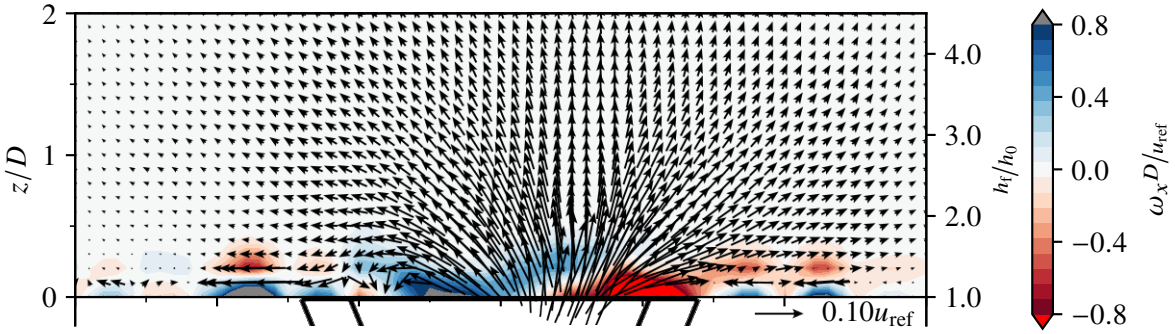

(a) OF, $Re_{D,\mathrm{cc}} = 5 \times 10^3$, $BR = 2.0$: $x/D = 0.0$

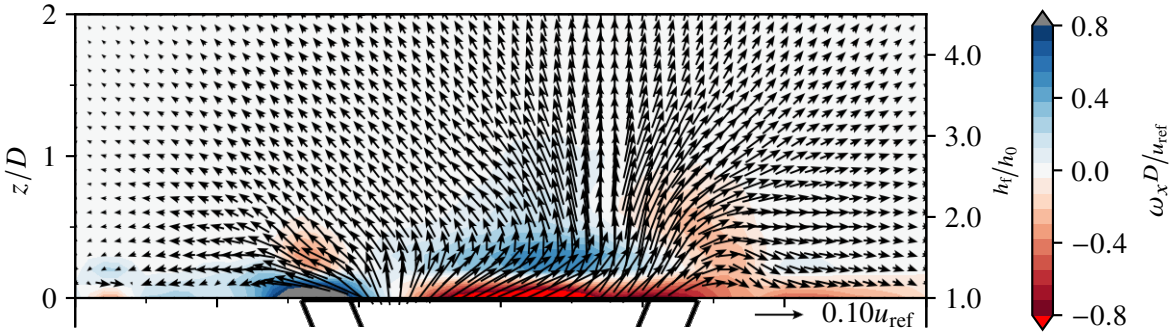

(b) OF, $Re_{D,\mathrm{cc}} = 5 \times 10^3$, $BR = 2.0$, $x/D = 3.0$

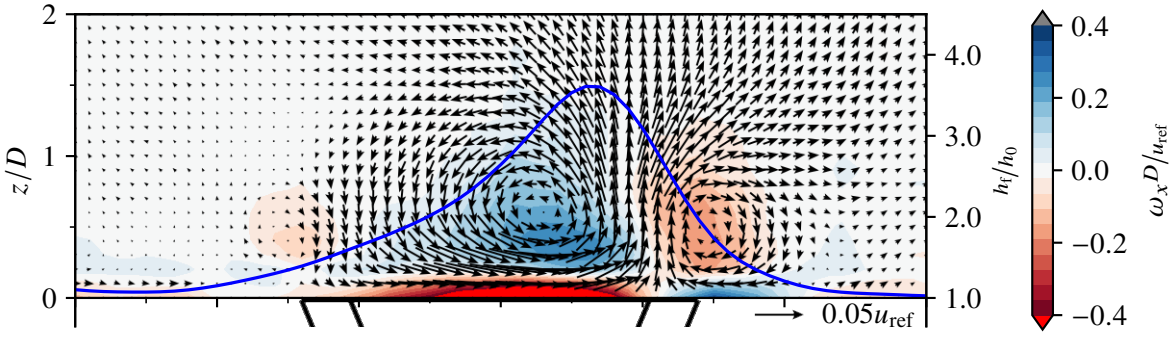

(c) OF, $Re_{D,\mathrm{cc}} = 5 \times 10^3$, $BR = 2.0$, $x/D = 5.0$

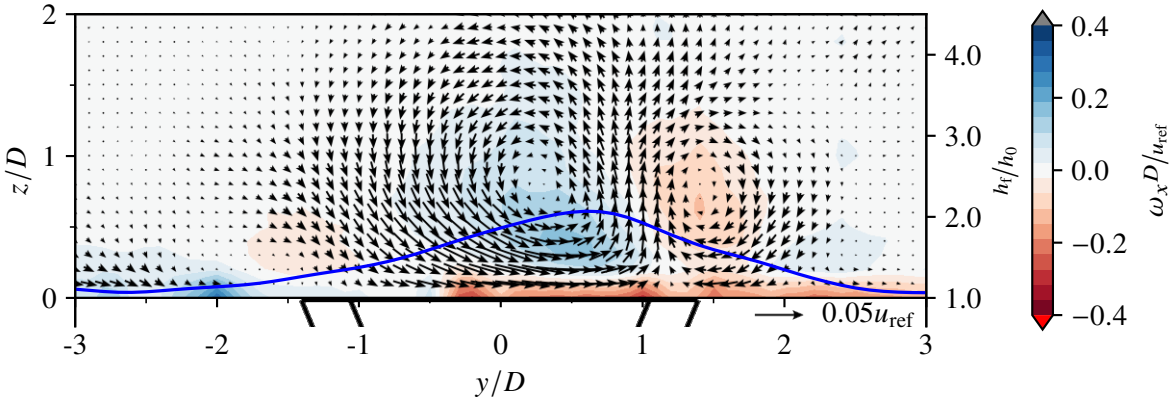

(d) OF, $Re_{D,\mathrm{cc}} = 5 \times 10^3$, $BR = 2.0$, $x/D = 8.0$

Figure A.26: Evolution of coherent structures and h_f/h_0 in the x-plane for $Re_{D,\mathrm{cc}} = 5{\times}10^3$ and $BR = 2.0$

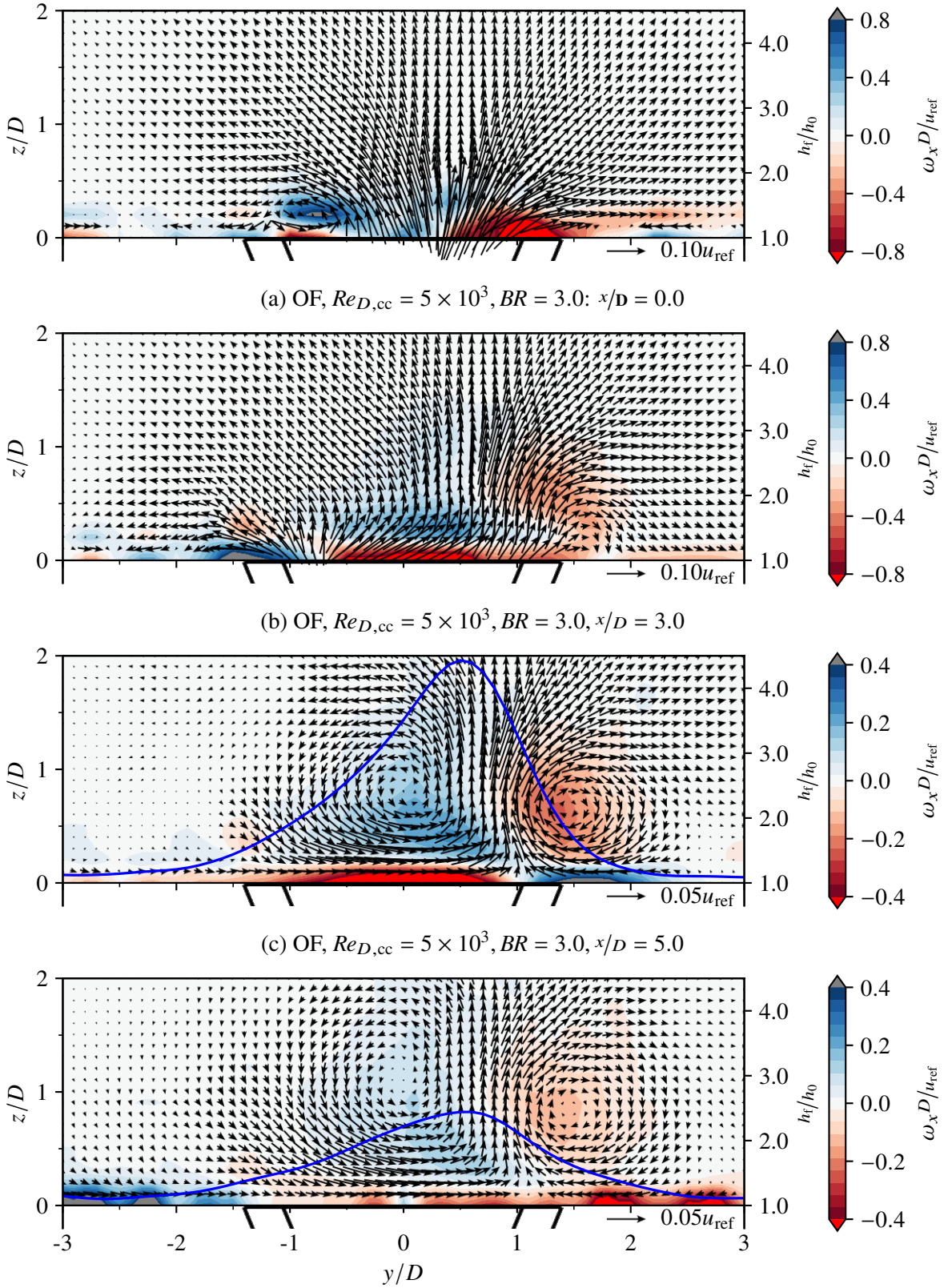

(a) OF, $Re_{D,cc} = 5 \times 10^3$, $BR = 3.0$: $x/D = 0.0$

(b) OF, $Re_{D,cc} = 5 \times 10^3$, $BR = 3.0$, $x/D = 3.0$

(c) OF, $Re_{D,cc} = 5 \times 10^3$, $BR = 3.0$, $x/D = 5.0$

(d) OF, $Re_{D,cc} = 5 \times 10^3$, $BR = 3.0$, $x/D = 8.0$

Figure A.27: Evolution of coherent structures and h_f/h_0 in the x-plane for $Re_{D,cc} = 5{\times}10^3$ and $BR = 3.0$

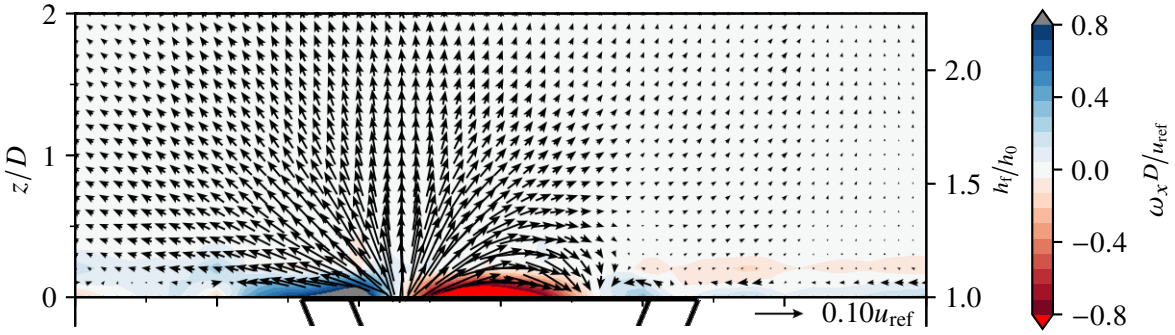

(a) OF, $Re_{D,\mathrm{cc}} = 30 \times 10^3$, $BR = 1.0$: $x/\mathrm{D} = 0.0$

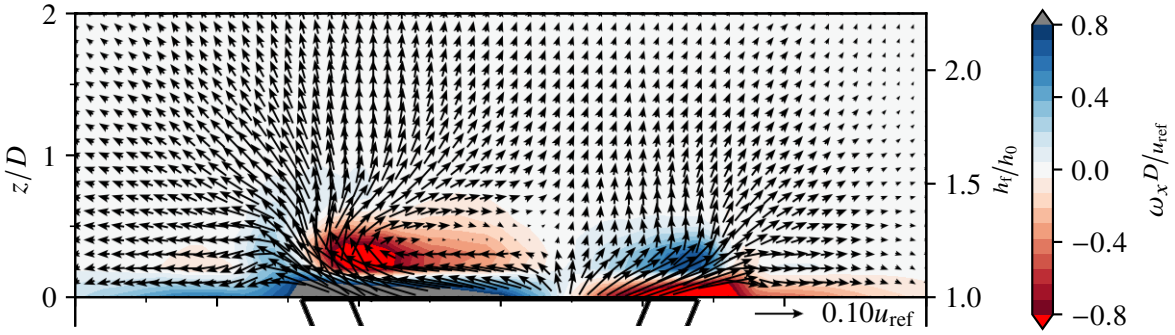

(b) OF, $Re_{D,\mathrm{cc}} = 30 \times 10^3$, $BR = 1.0$, $x/D = 3.0$

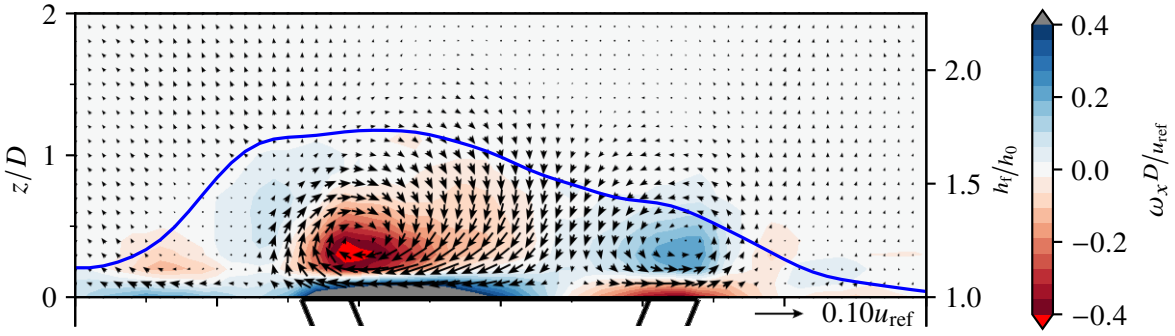

(c) OF, $Re_{D,\mathrm{cc}} = 30 \times 10^3$, $BR = 1.0$, $x/D = 5.0$

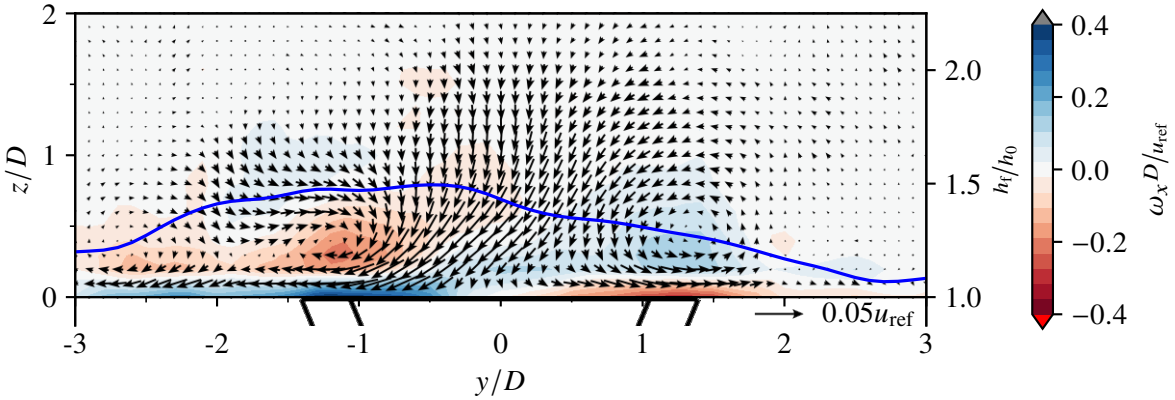

(d) OF, $Re_{D,\mathrm{cc}} = 30 \times 10^3$, $BR = 1.0$, $x/D = 8.0$

Figure A.28: Evolution of coherent structures and h_f/h_0 in the x-plane for $Re_{D,\mathrm{cc}} = 30 \times 10^3$ and $BR = 1.0$

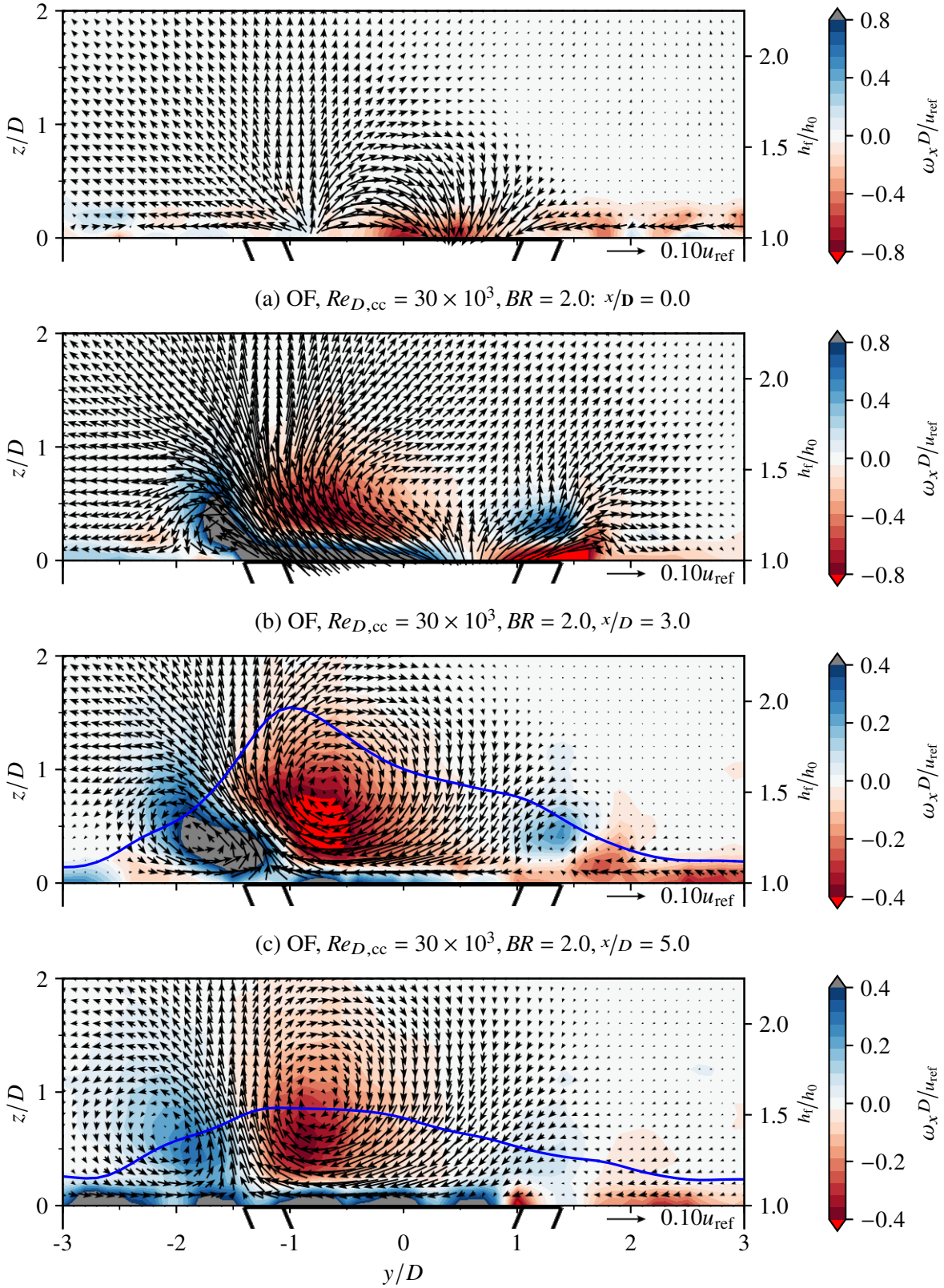

(a) OF, $Re_{D,\mathrm{cc}} = 30 \times 10^3$, $BR = 2.0$: $x/\mathrm{D} = 0.0$

(b) OF, $Re_{D,\mathrm{cc}} = 30 \times 10^3$, $BR = 2.0$, $x/D = 3.0$

(c) OF, $Re_{D,\mathrm{cc}} = 30 \times 10^3$, $BR = 2.0$, $x/D = 5.0$

(d) OF, $Re_{D,\mathrm{cc}} = 30 \times 10^3$, $BR = 2.0$, $x/D = 8.0$

Figure A.29: Evolution of coherent structures and h_f/h_0 in the x-plane for $Re_{D,\mathrm{cc}} = 30 \times 10^3$ and $BR = 2.0$

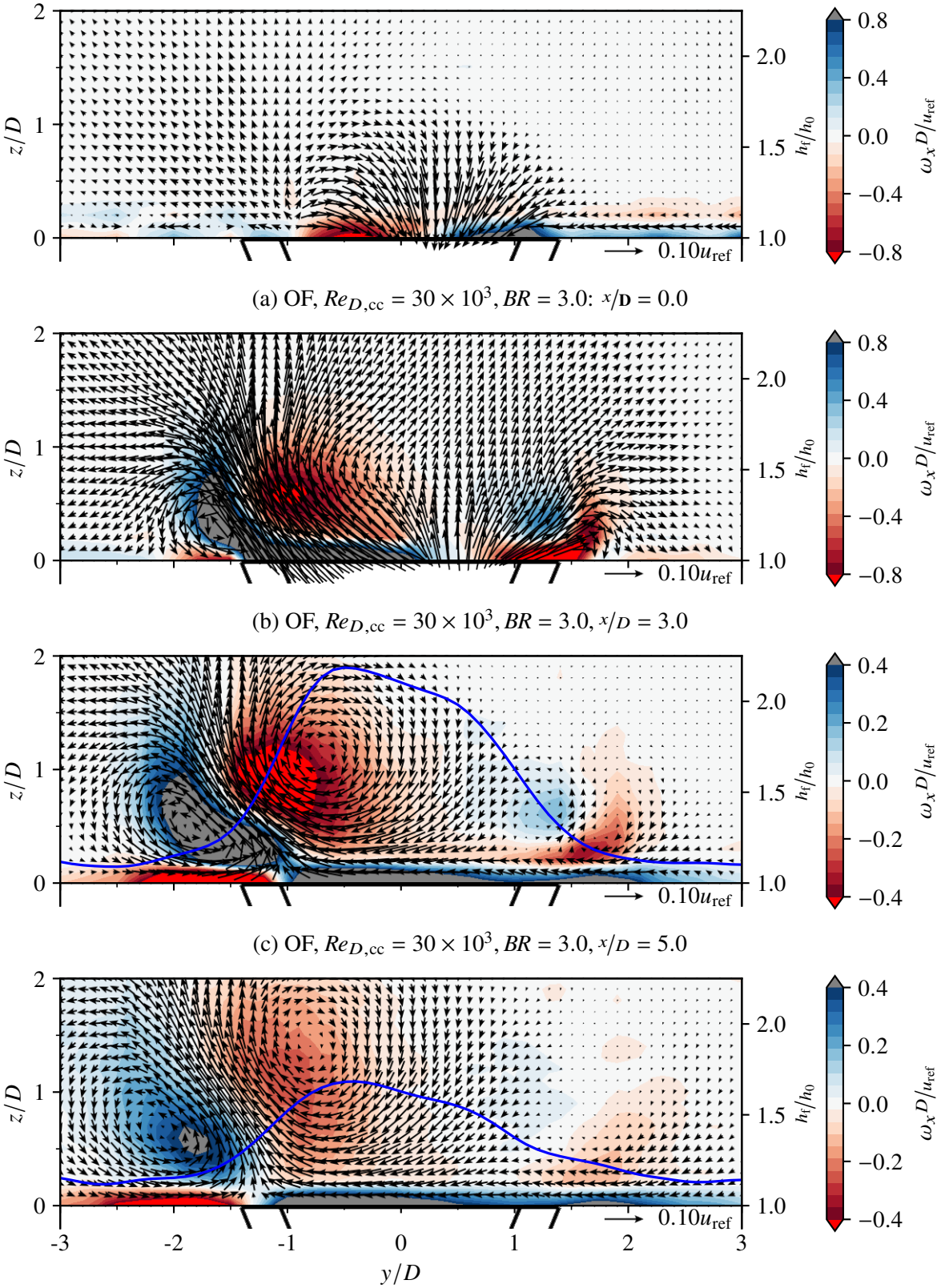

(a) OF, $Re_{D,\mathrm{cc}} = 30 \times 10^3$, $BR = 3.0$: $x/\mathrm{D} = 0.0$

(b) OF, $Re_{D,\mathrm{cc}} = 30 \times 10^3$, $BR = 3.0$, $x/D = 3.0$

(c) OF, $Re_{D,\mathrm{cc}} = 30 \times 10^3$, $BR = 3.0$, $x/D = 5.0$

(d) OF, $Re_{D,\mathrm{cc}} = 30 \times 10^3$, $BR = 3.0$, $x/D = 8.0$

Figure A.30: Evolution of coherent structures and h_f/h_0 in the x-plane for $Re_{D,\mathrm{cc}} = 30 \times 10^3$ and $BR = 3.0$

A.11 Vorticity Distributions at Hole Outlet: Streamwise Vorticity ω_x

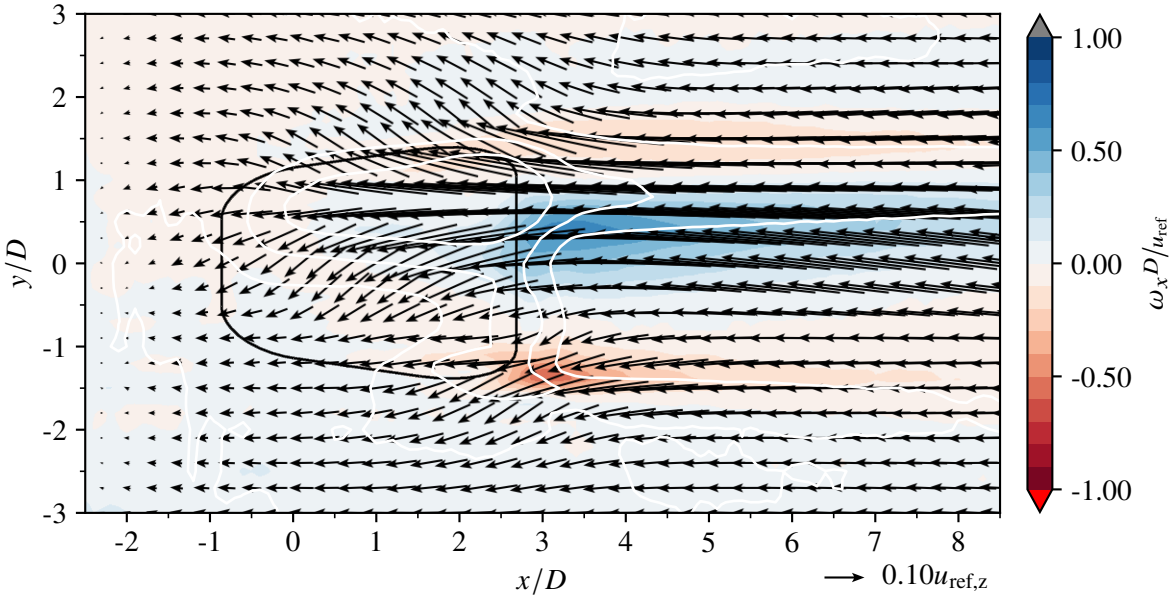

(a) OF, $Re_{D,\mathrm{cc}} = 5 \times 10^3$, $BR = 1.0$

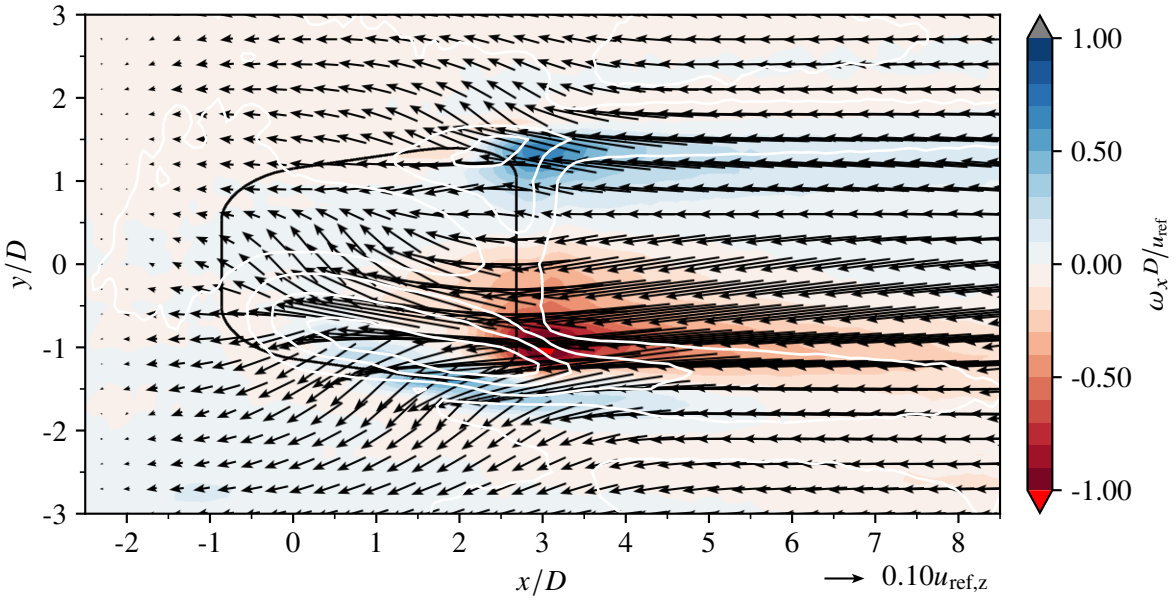

(b) OF, $Re_{D,\mathrm{cc}} = 30 \times 10^3$, $BR = 1.0$

Figure A.31: Impact of the coolant ejection on the near-wall x-vorticity, ω_x, and in-plane velocity field, $\left(\left(u - u_{\mathrm{ref,z}}\right), v\right)$, at $z/D = 0.3$ for $BR = 1.0$. The white lines correspond to the contours of wall-normal velocity w shown in section A.4.

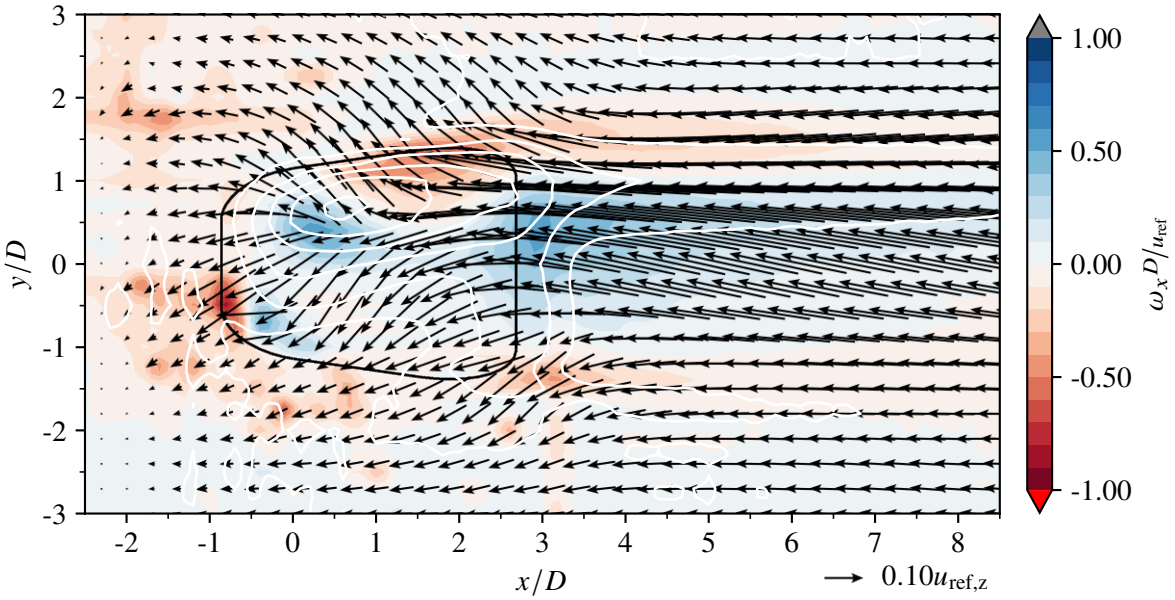

(a) OF, $Re_{D,\mathrm{cc}} = 5 \times 10^3$, $BR = 2.0$

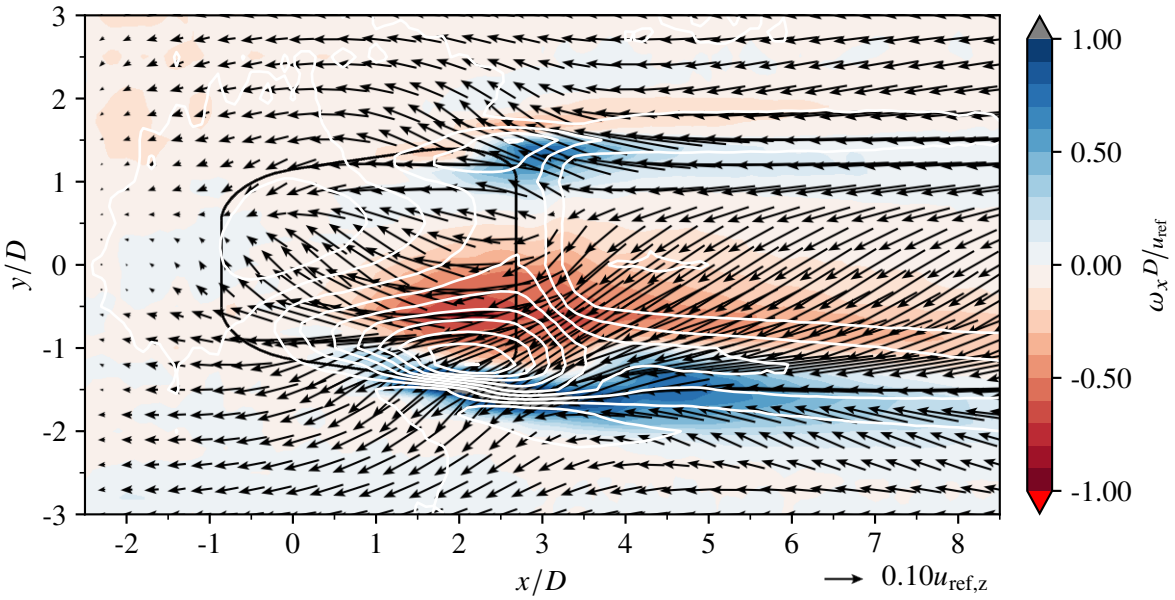

(b) OF, $Re_{D,\mathrm{cc}} = 30 \times 10^3$, $BR = 2.0$

Figure A.32: Impact of the coolant ejection on the near-wall x-vorticity, ω_x, and in-plane velocity field, $\left(\left(u - u_{\mathrm{ref,z}}\right), v\right)$, at $z/D = 0.3$ for $BR = 2.0$. The white lines correspond to the contours of wall-normal velocity w shown in section A.4.

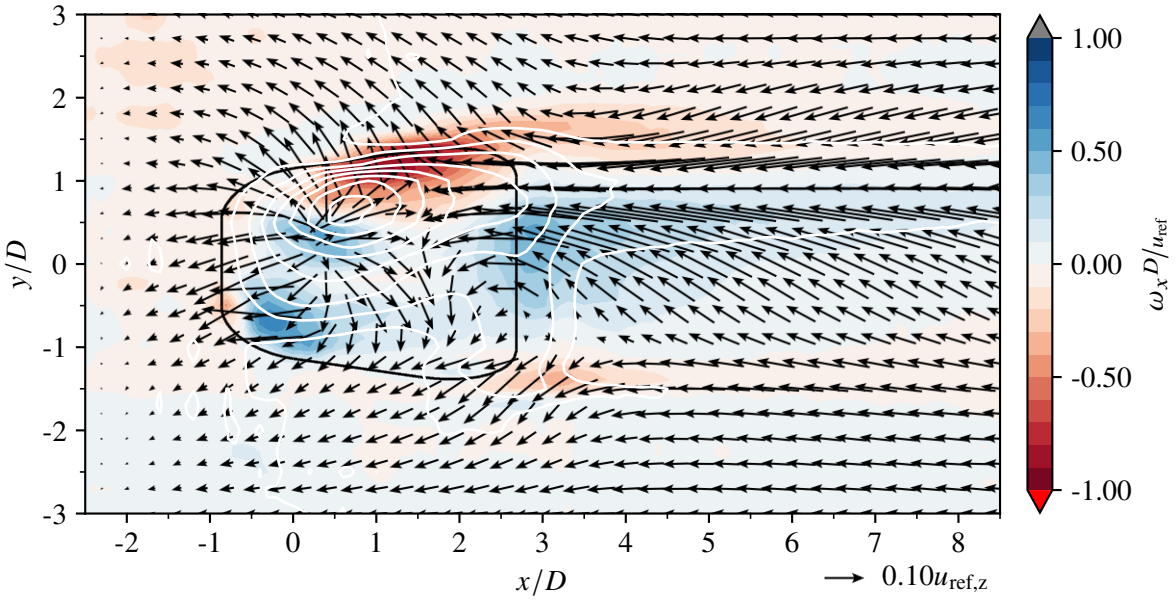

(a) OF, $Re_{D,\mathrm{cc}} = 5 \times 10^3$, $BR = 3.0$

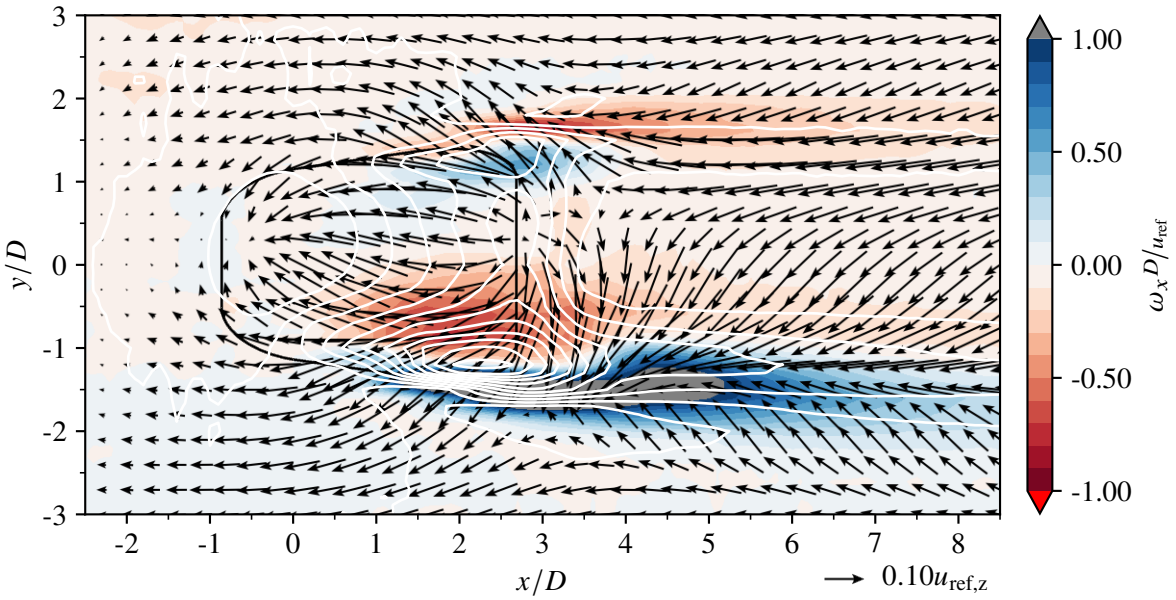

(b) OF, $Re_{D,\mathrm{cc}} = 30 \times 10^3$, $BR = 3.0$

Figure A.33: Impact of the coolant ejection on the near-wall x-vorticity, ω_x, and in-plane velocity field, $\left(\left(u - u_{\mathrm{ref,z}}\right), v\right)$, at $z/D = 0.3$ for $BR = 3.0$. The white lines correspond to the contours of wall-normal velocity w shown in section A.4.

A.12 Vorticity Distributions at Hole Outlet: Wall-Normal Vorticity ω_z

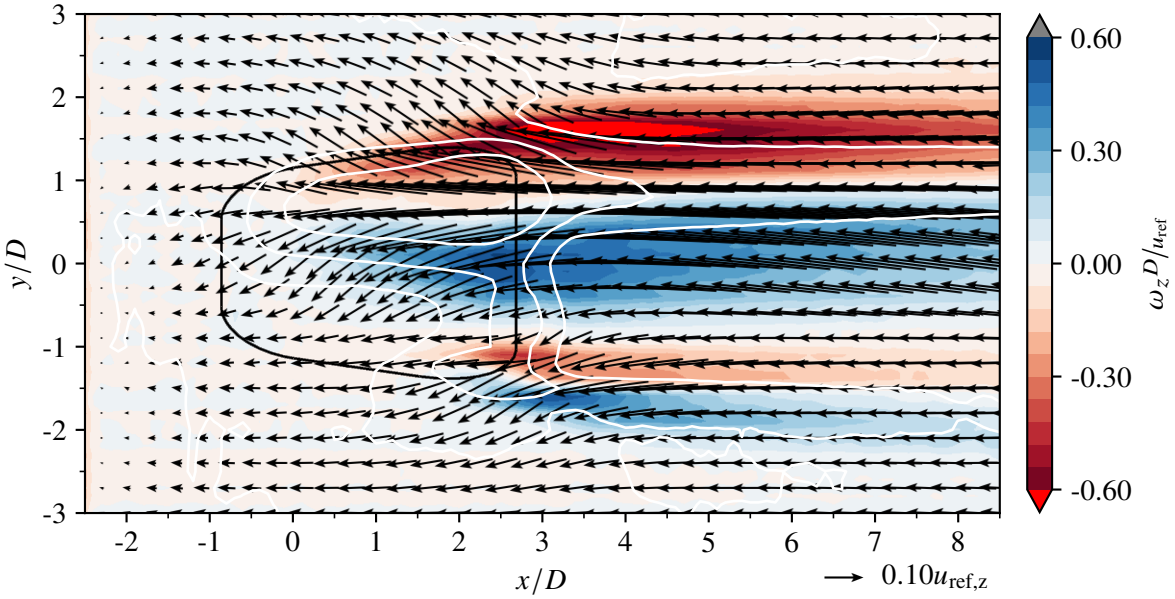

(a) OF, $Re_{D,\mathrm{cc}} = 5 \times 10^3$, $BR = 1.0$

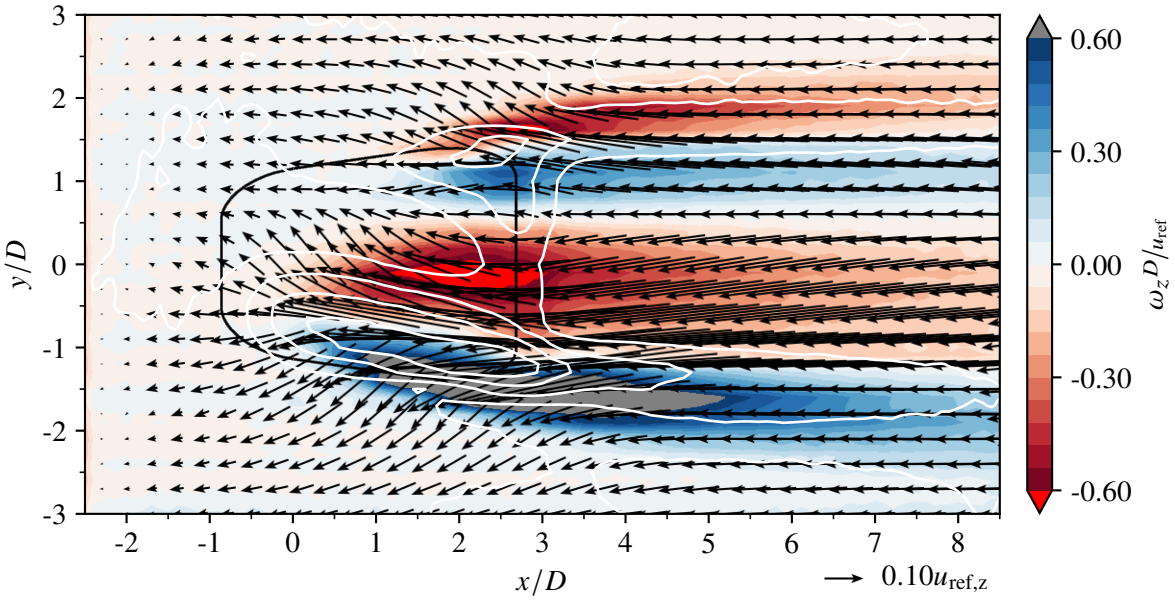

(b) OF, $Re_{D,\mathrm{cc}} = 30 \times 10^3$, $BR = 1.0$

Figure A.34: Impact of the coolant ejection on the near-wall z-vorticity, ω_z, and in-plane velocity field, $\left(\left(u - u_{\mathrm{ref,z}}\right), v\right)$, at $z/D = 0.3$ for $BR = 1.0$. The white lines correspond to the contours of wall-normal velocity w shown in section A.4.

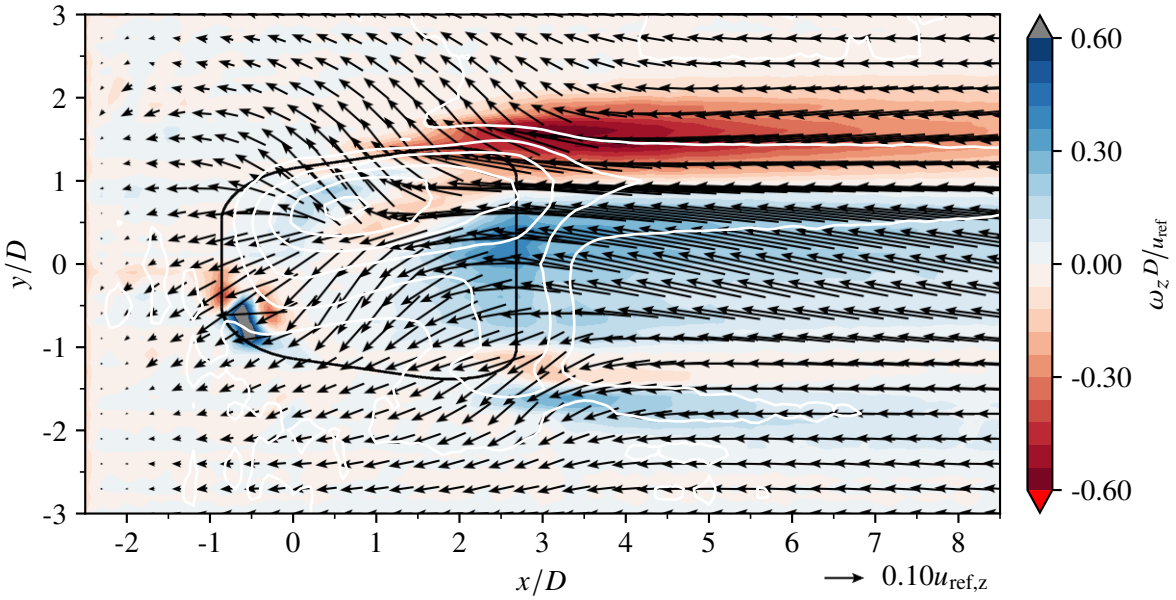

(a) OF, $Re_{D,\mathrm{cc}} = 5 \times 10^3$, $BR = 2.0$

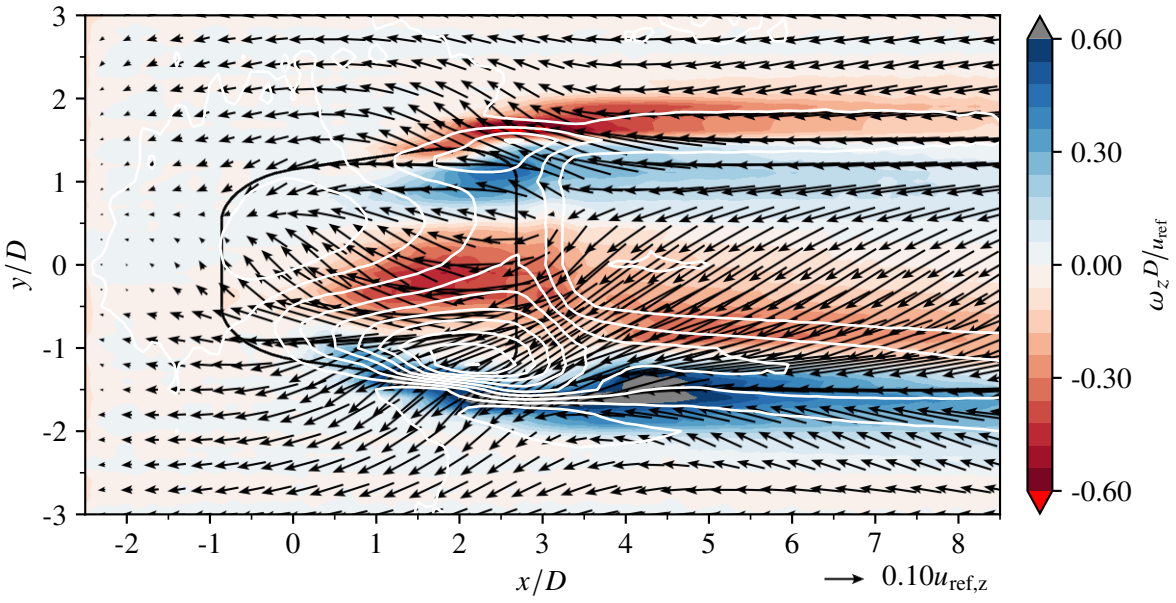

(b) OF, $Re_{D,\mathrm{cc}} = 30 \times 10^3$, $BR = 2.0$

Figure A.35: Impact of the coolant ejection on the near-wall z-vorticity, ω_z, and in-plane velocity field, $\left(\left(u - u_{\mathrm{ref,z}}\right), v\right)$, at $z/D = 0.3$ for $BR = 2.0$. The white lines correspond to the contours of wall-normal velocity w shown in section A.4.

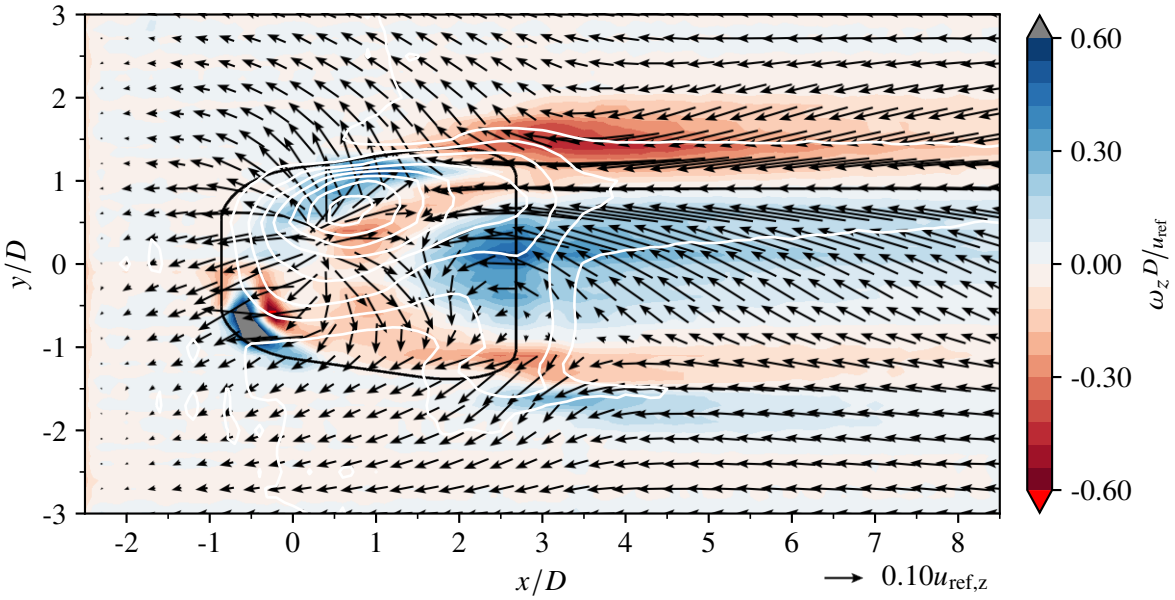

(a) OF, $Re_{D,\mathrm{cc}} = 5 \times 10^3$, $BR = 3.0$

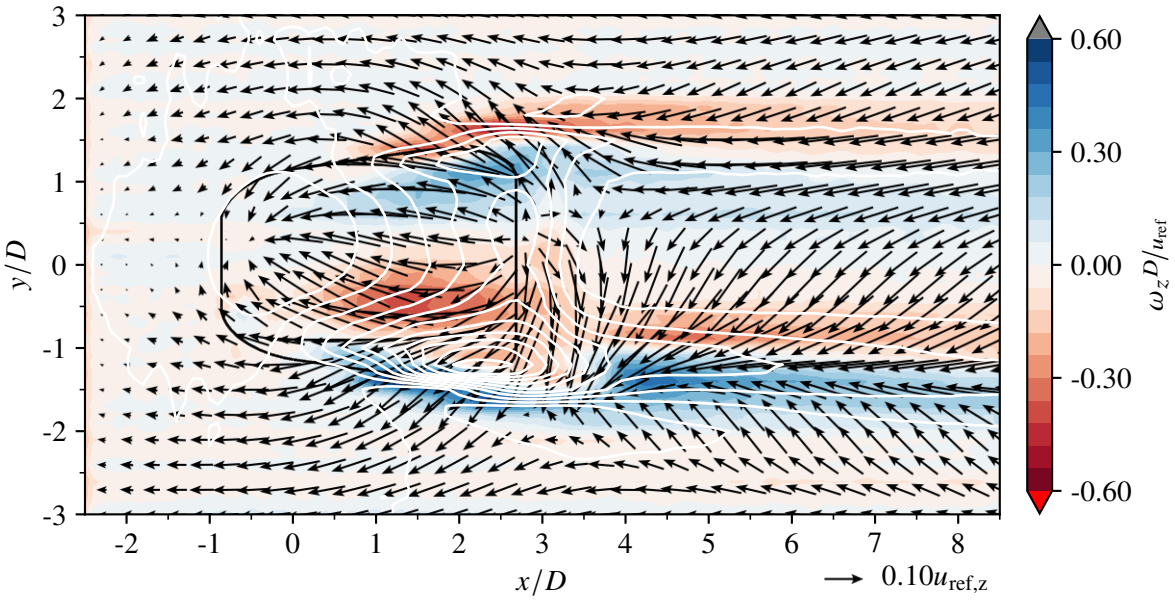

(b) OF, $Re_{D,\mathrm{cc}} = 30 \times 10^3$, $BR = 3.0$

Figure A.36: Impact of the coolant ejection on the near-wall z-vorticity, ω_z, and in-plane velocity field, $\left(\left(u - u_{\mathrm{ref,z}}\right), v\right)$, at $z/D = 0.3$ for $BR = 3.0$. The white lines correspond to the contours of wall-normal velocity w shown in section A.4.

A.13 Summary of Thermal Film Cooling Quantities for Parallel and Orthogonal Coolant Cross-flow

A.13.1 PF: Adiabatic Film Cooling Effectiveness $\eta_{a,w}$

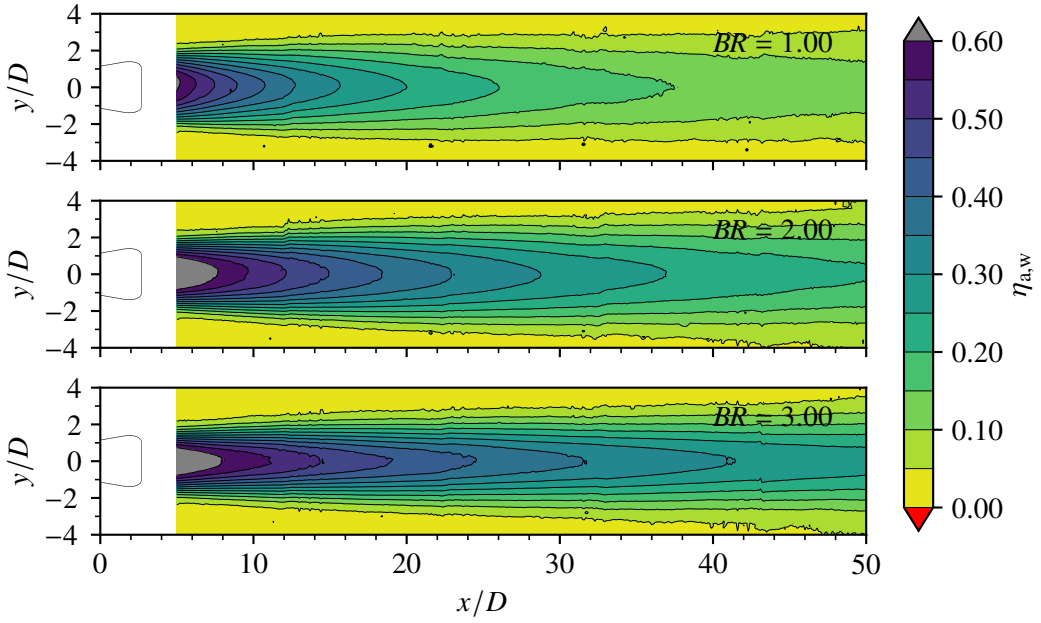

(a) $Re_{D,cc} = 5 \times 10^3$

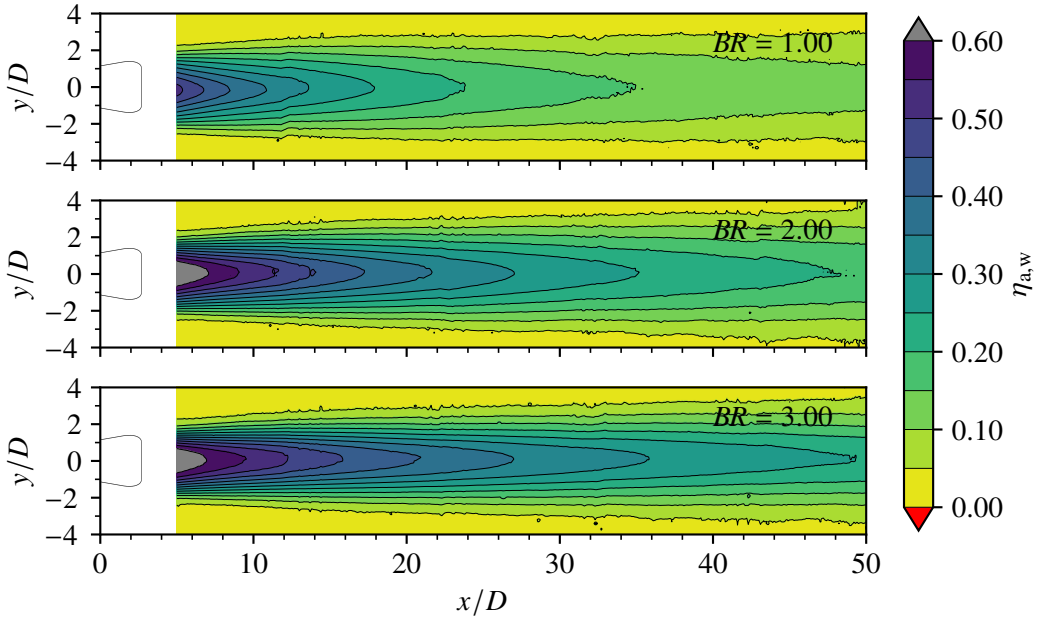

(b) $Re_{D,cc} = 30 \times 10^3$

Figure A.37: Adiabatic film cooling effectiveness $\eta_{a,w}$ for (a) low and (b) high coolant channel Reynolds number; produced based on data in Fraas (2019).

A.13.2 PF: Ratio of Heat Transfer Coefficients With and Without Film Cooling h_f/h_0

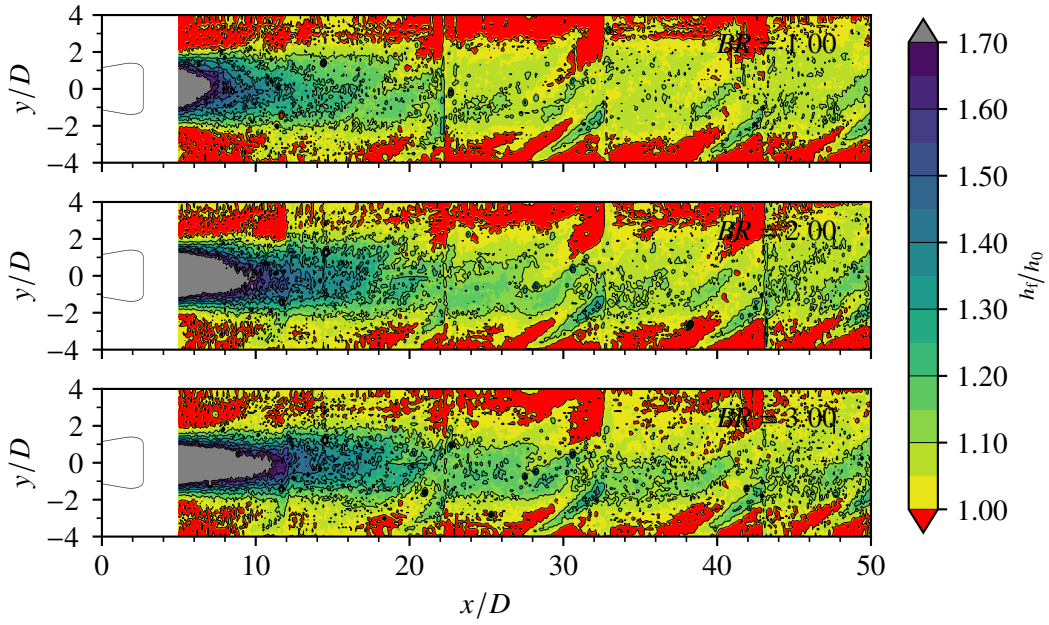

(a) $Re_{D,cc} = 5 \times 10^3$

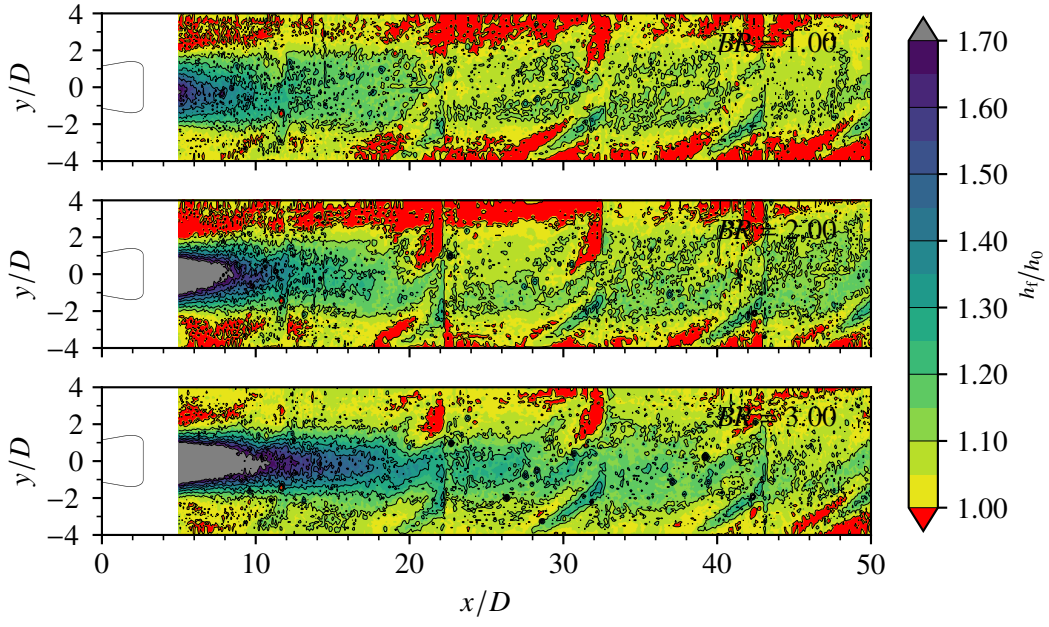

(b) $Re_{D,cc} = 30 \times 10^3$

Figure A.38: Adiabatic film cooling effectiveness $\eta_{a,w}$ for (a) low and (b) high coolant channel Reynolds number; reproduced based on data in Fraas (2019)

A.13.3 PF: Heat Flux Reduction Γ acc. to Baldauf et al. (2002)

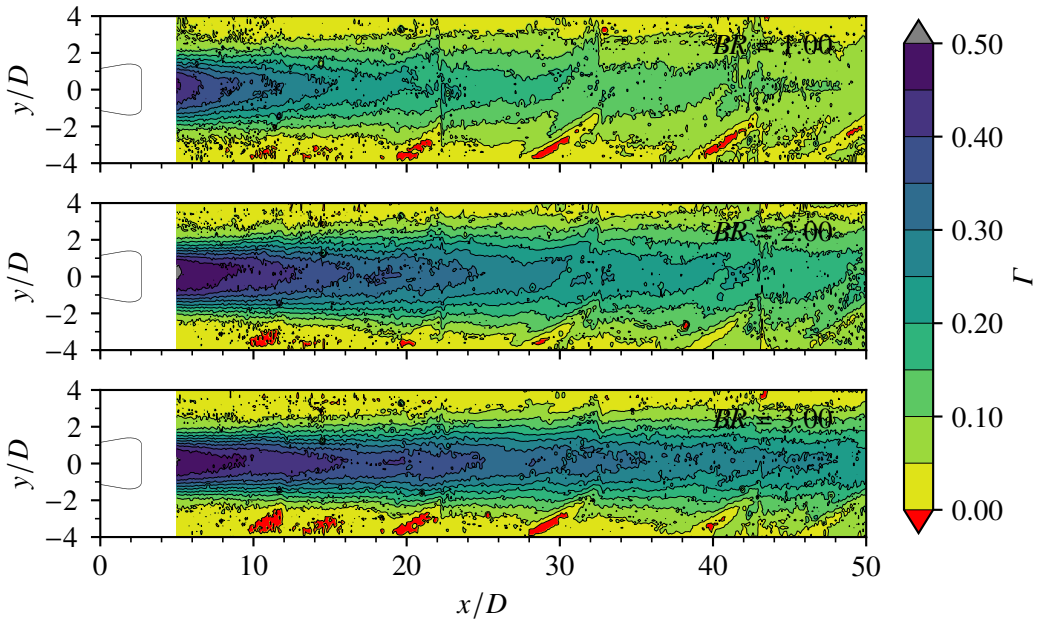

(a) $Re_{D,\mathrm{cc}} = 5 \times 10^3$

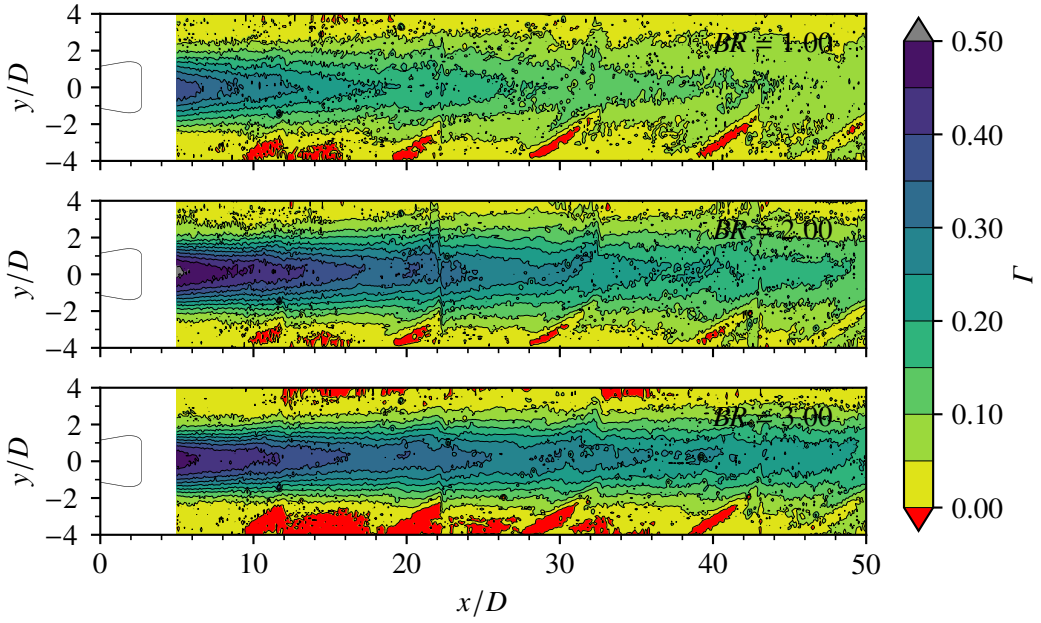

(b) $Re_{D,\mathrm{cc}} = 30 \times 10^3$

Figure A.39: Heat flux reduction Γ for (a) low and (b) high coolant channel Reynolds number according to Baldauf et al. (2002b); produced based on data in Fraas (2019).

A.13.4 OF: Adiabatic Film Cooling Effectiveness $\eta_{a,w}$

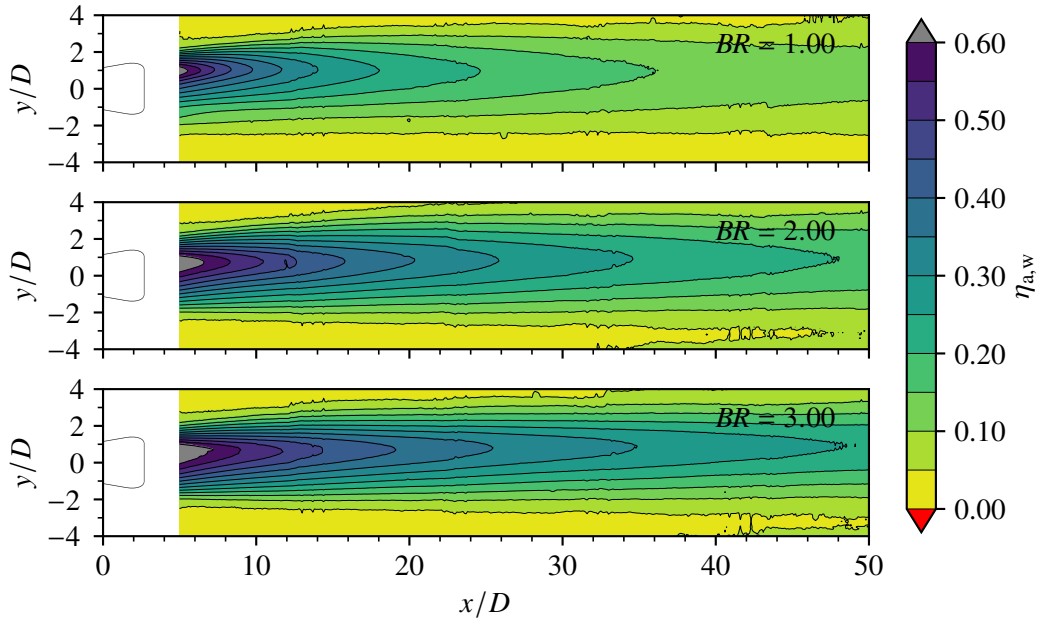

(a) $Re_{D,cc} = 5 \times 10^3$

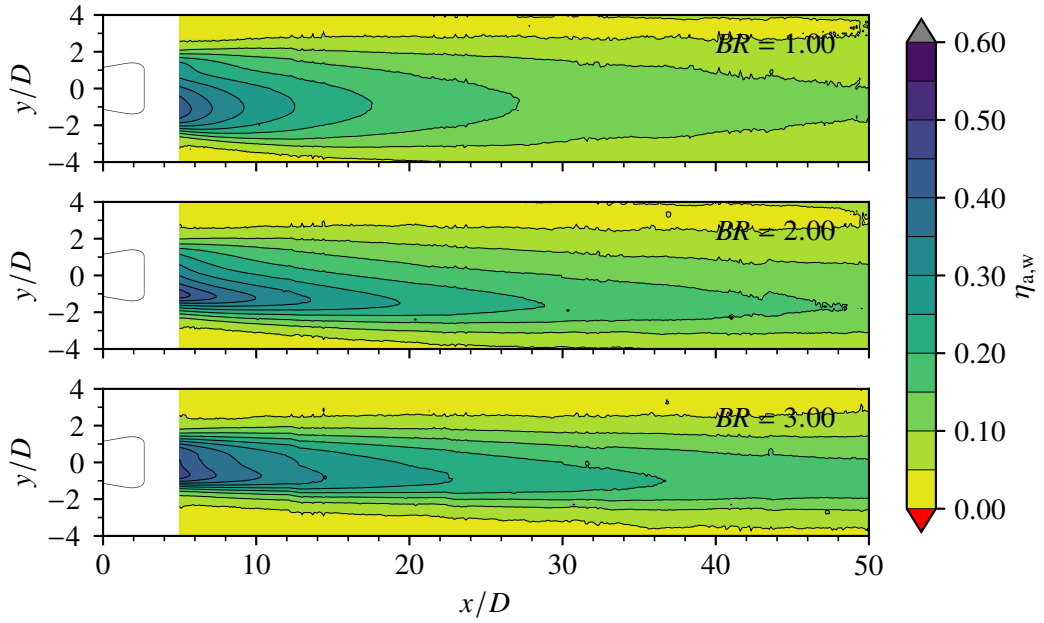

(b) $Re_{D,cc} = 30 \times 10^3$

Figure A.40: Adiabatic film cooling effectiveness $\eta_{a,w}$ for (a) low and (b) high coolant channel Reynolds number. Reproduced based on data in Fraas (2019). Coolant cross-flow direction is in negative y/D direction.

A.13.5 OF: Ratio of Heat Transfer Coefficients With and Without Film Cooling h_f/h_0

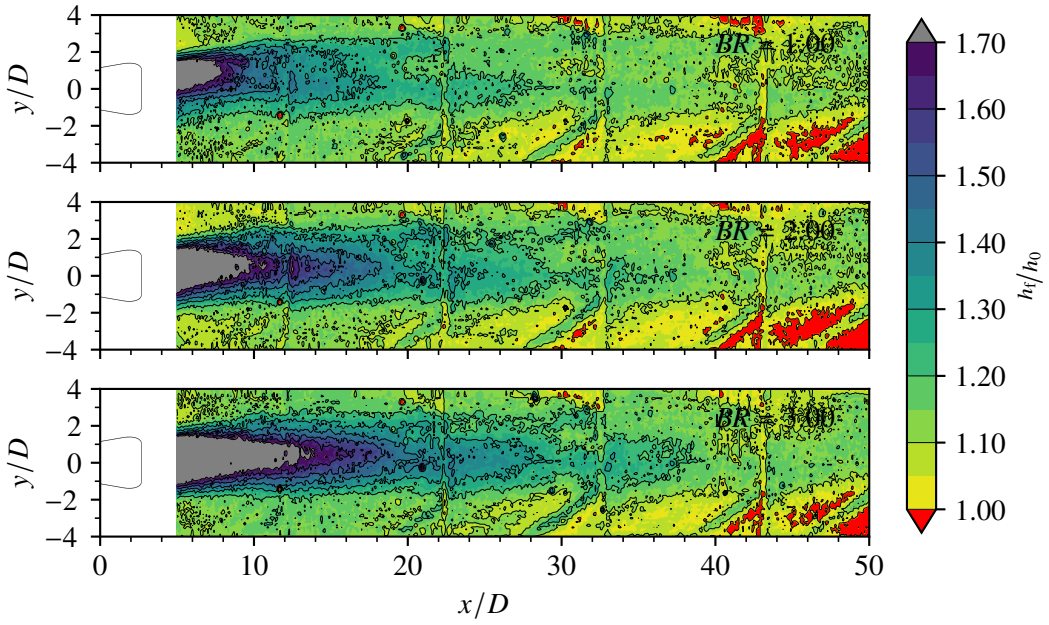

(a) $Re_{D,cc} = 5 \times 10^3$

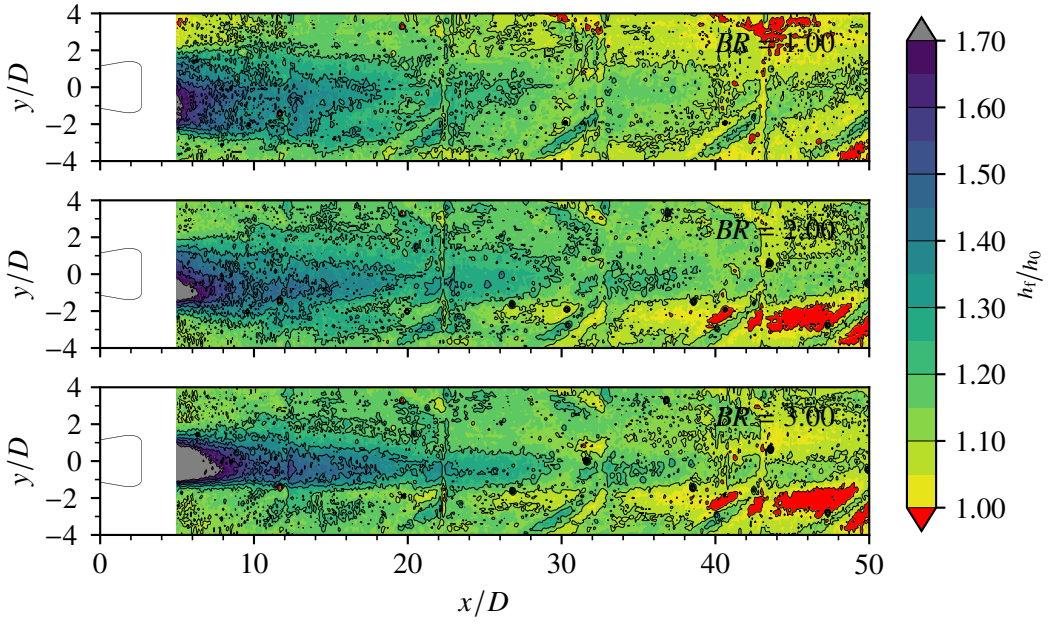

(b) $Re_{D,cc} = 30 \times 10^3$

Figure A.41: Adiabatic film cooling effectiveness $\eta_{a,w}$ for (a) low and (b) high coolant channel Reynolds number. Reproduced based on data in Fraas (2019). Coolant cross-flow direction is in negative y/D direction.

A.13.6 OF: Heat Flux Reduction Γ acc. to Baldauf et al. (2002)

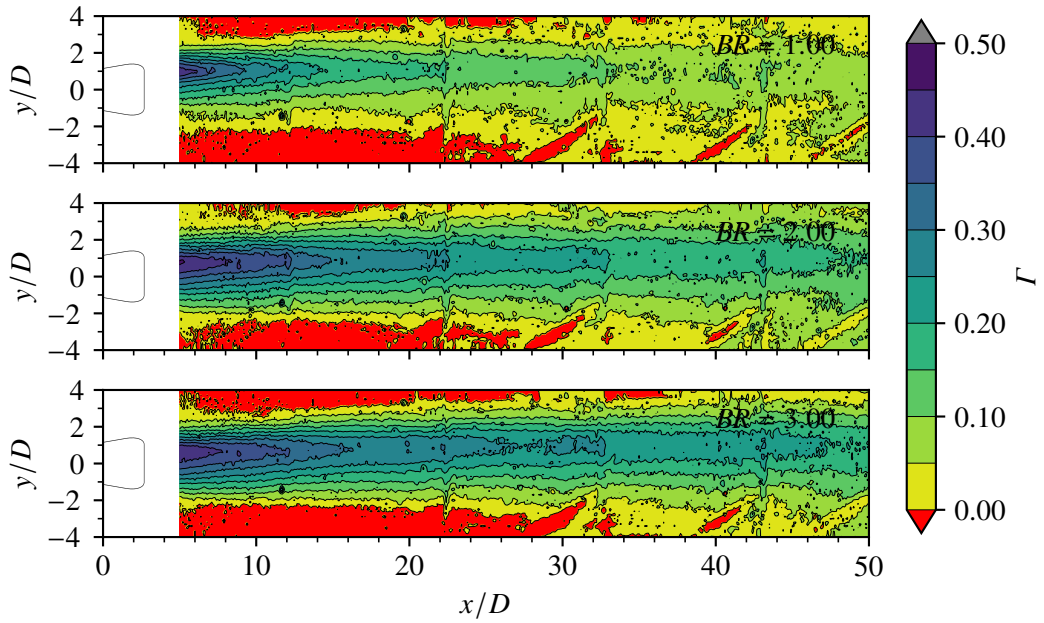

(a) $Re_{D,\mathrm{cc}} = 5 \times 10^3$

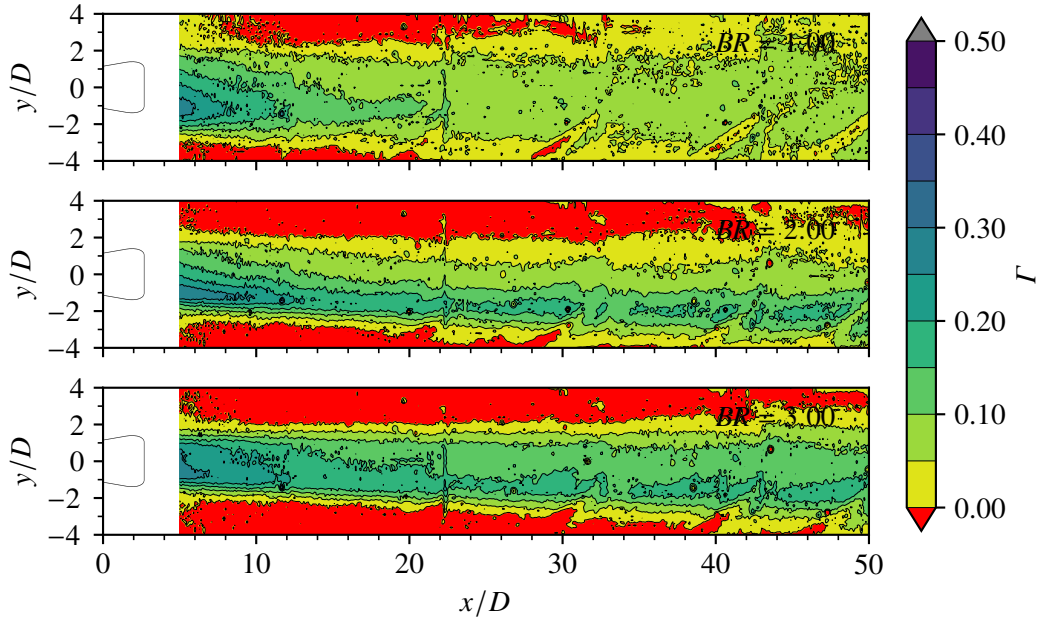

(b) $Re_{D,\mathrm{cc}} = 30 \times 10^3$

Figure A.42: Heat flux reduction Γ for (a) low and (b) high coolant channel Reynolds number according to Baldauf et al. (2002b); produced based on data in Fraas (2019)

A.13.7 Laterally Averaged Adiabatic Film Cooling Effectiveness $\bar{\eta}_{a,w}$ and Ratio of Heat Transfer Coefficients With and Without Film Cooling $\bar{h}_f/\bar{h}_0$

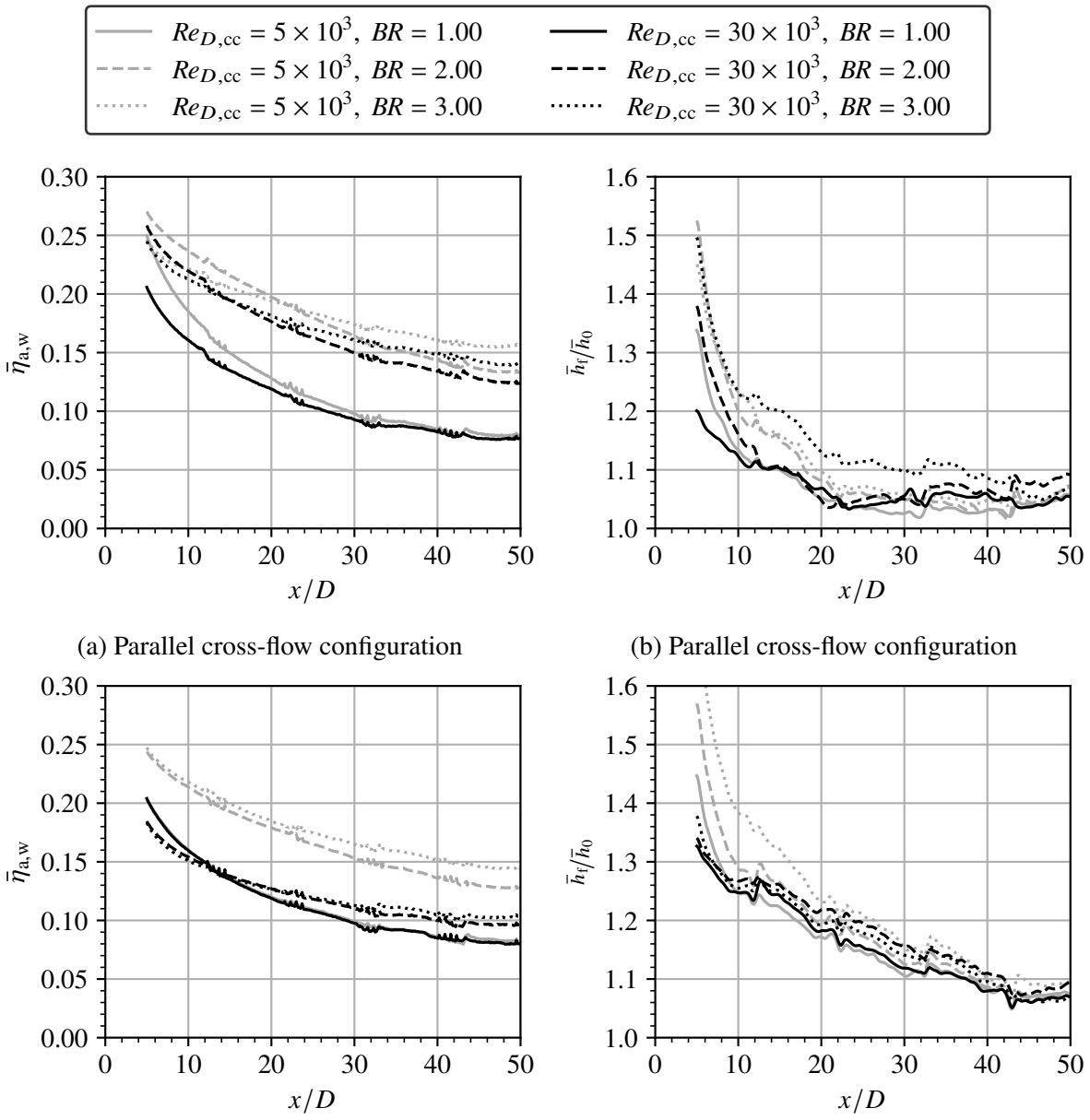

(a) Parallel cross-flow configuration

(b) Parallel cross-flow configuration

(c) Orthogonal cross-flow configuration

(d) Orthogonal cross-flow configuration

Figure A.43: Laterally averaged adiabatic film cooling effectiveness $\bar{\eta}_{a,w}$ and ratio of heat transfer coefficients with and without film cooling $\bar{h}_f/\bar{h}_0$ for parallel ((a) and (b)) and orthogonal coolant cross-flow configuration ((c) and (d)); reproduced based on data in Fraas (2019)

A.13.8 Laterally Averaged Heat Flux Reduction $\overline{\Gamma}$ acc. to Baldauf et al. (2002)

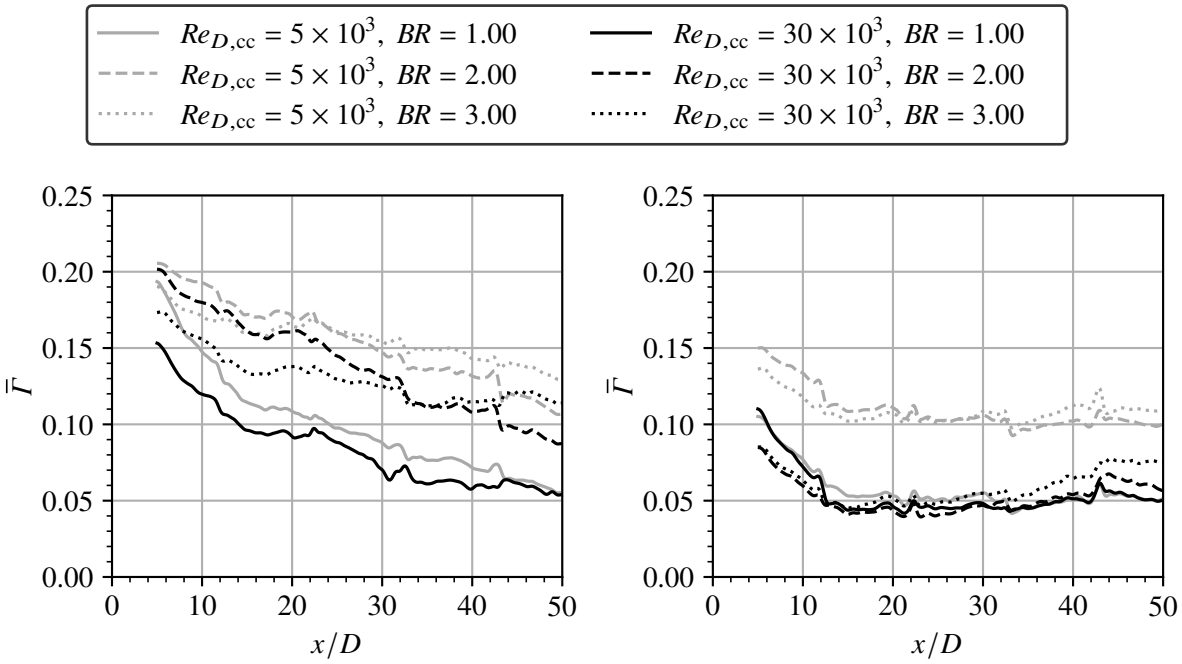

(a) Parallel cross-flow configuration

(b) Orthogonal cross-flow configuration

Figure A.44: Laterally averaged heat flux reduction $\overline{\Gamma}$ for (a) parallel and (b) orthogonal coolant cross-flow configuration; produced based on data in Fraas (2019)